UNIVERSIDADE FEDERAL DE PERNAMBUCO - UFPE

CENTRO DE CIÊNCIAS EXATAS E DA NATUREZA – CCEN

PROGRAMA DE PÓS-GRADUAÇÃO EM CIÊNCIA DE MATERIAIS

MANOEL LEONARDO DA SILVA NETO

EVALUATING OPTICAL NONLINEARITIES AND APPLICATIONS OF PHOTONIC NANOMATERIALS

Recife

2021

MANOEL LEONARDO DA SILVA NETO

EVALUATING OPTICAL NONLINEARITIES AND APPLICATIONS OF PHOTONIC NANOMATERIALS

Tese apresentada ao Programa de Pós-Graduação em Ciência de Materiais da Universidade Federal de Pernambuco, como requisito parcial para a obtenção do título de Doutor em Ciência de Materiais. Área de concentração: Materiais não metálicos.

Orientador: Prof. Dr. Cid Bartolomeu de Araújo

Coorientador: Prof. Dr. Edilson Lucena Falcão Filho

Coorientador externo: Prof. Dr. Anderson Stevens Leônidas Gomes

Recife

2021

Catalogação na fonte
Bibliotecária Monick Raquel Silvestre da S. Portes, CRB4-1217

S586e Silva Neto, Manoel Leonardo da
Evaluating optical nonlinearities and applications of photonic nanomaterials / Manoel Leonardo da Silva Neto. – 2021.
196 f.: il., fig., tab.

Orientador: Cid Bartolomeu de Araújo.
Tese (Doutorado) – Universidade Federal de Pernambuco. CCEN, Ciência de Materiais, Recife, 2021.
Inclui referências e apêndices.

1. Materiais não metálicos. 2. Nanomateriais. I. Araújo, Cid Bartolomeu de (orientador). II. Título.

620.19 CDD (23. ed.) UFPE- CCEN 2021 - 172

MANOEL LEONARDO DA SILVA NETO

EVALUATING OPTICAL NONLINEARITIES AND APPLICATIONS OF PHOTONIC NANOMATERIALS

Tese apresentada ao Programa de Pós - Graduação em Ciência de Materiais da Universidade Federal de Pernambuco, como requisito para a obtenção do título de Doutor em Ciência de Materiais.

Aprovada em: 19/07/2021.

BANCA EXAMINADORA

_____
Prof. Dr. Cid Bartolomeu de Araújo (Orientador)
Universidade Federal de Pernambuco

_____
Prof. Dr. Eduardo Henrique Lago Falcão (Examinador Interno)
Universidade Federal de Pernambuco

_____
Prof. Dr. Eduardo Padrón Hernandez (Examinador Interno)
Universidade Federal de Pernambuco

_____
Profª. Dra. Isabel Cristina dos Santos Carvalho (Examinadora Externa)
Pontifícia Universidade Católica do Rio de Janeiro PUC-RIO

_____
Prof. Dr. Lino Misoguti (Examinador Externo)
Universidade de São Paulo - USP

À minha família

AGRADECIMENTOS

Esta tese não seria possível sem a contribuição de muitas pessoas. Aqui vai meu agradecimento à cada uma delas.

Primeiro, nada disso seria possível sem o apoio incondicional da minha Família. Então, aqui agradeço à minha mãe, Raimunda, ao meu Pai, João e aos meus irmãos Francisco, Rosa, Pedro e João Paulo, por sempre me apoiarem nos estudos e na vida. Peço desculpas pelas ausências em diversas datas festivas. Aqui também agradeço à futura chefe de cozinha da Família, minha sobrinha Viviane, e ao meu sobrinho, João Vitor, pelos momentos de alegria que sempre me proporcionaram nos momentos que estivemos juntos.

Cursar uma pós-graduação não é uma tarefa simples; longe da família, esta tarefa pode se tornar muito mais difícil. Bom, para mim não foi tão difícil assim, graças ao incondicional apoio da minha esposa, Nágila, e do carinho (muitas vezes escondido em unhadas e mordidas) do meu gato, Caramelo. Muito obrigado por estarem sempre do meu lado, nos momentos fáceis e difíceis.

As minhas cunhadas Laiz e Paula Vitória, e a minha sogra, Osmarina por me proporcionarem momentos de alegria.

Ao meu orientador Prof. Cid Bartolomeu de Araújo, por ter me aceitado em seu laboratório, e por toda a paciência. A sua forma de supervisar estudantes e dá-lo liberdade de propor experimentos e modelos, com certeza moldam a carreira destes.

Gostaria de agradecer também ao meu co-orientador, Edilson Lucena, pelas discussões sobre experimentos, e pelo conhecimento repassado na área de lasers.

Ao Prof. Anderson Gomes, por abrir as portas do seu laboratório (e dos projetos de pesquisa em colaboração) para mim.

Ao Prof. Leonardo Menezes, com qual tive grande aprendizado, tanto no laboratório quanto em teoria.

Ao Prof. Lúcio Acioli, pelos ensinamentos em equipamentos eletrônicos e fotodetectores.

A todos os colegas e ex-colegas de laboratório Albert, Andréa, Cássia, Felipe, Maxwell, Renato, Rudson e Talita pelas discussões e ajuda no trabalho e pelos momentos de descontração.

Ao Prof. Albert novamente, pelas discussões sobre experimentos e teorias para explicá-los.

Ao Prof. Anderson Amaral pelas longas e proveitosas conversas sobre o trabalho.

Ao Prof. André Moura, pelas discussões e brincadeiras.

Ao colega Bismarck C. Lima, que tiver o prazer de trabalhar no OSA Student Chapter Recife.

Aos colegas e ex-colegas do Laboratório de fotônica, que aqui cito apenas alguns: Melissa, Edwin, Avishek, Arthur, Cecília e Pablo. Muito obrigado pelas discussões e pelos momentos de descontração.

Ao OSA Student Chapter Recife, e a todos os seus membros.

Às colaborações nacionais e internacionais, que aqui menciono: UFAL, PUC-RIO, MACKENZIE, AFRL – USA, Universidade de Angers – França, IACS – Índia.

Ao Prof. Eduardo Padrón, por ter aberto as portas de seu laboratório para a síntese das amostras em um projeto paralelo a este descrito aqui.

Ao Prof. Eduardo Falcão pela ajuda na passagem do mestrado para o doutorado direto.

Aos amigos externos ao ambiente acadêmico, que agradeço em nome Johnyefeson, Valquíria e Lesli, pelos momentos de descontração.

Aos técnicos do Departamento de Física, Maria Virgínia (Laboratório de Química), Sérgio Santos (Microscopia), Carlos Alberto (Setor Financeiro), Daniel (Oficina de Eletrônica), e à Secretaria do Programa de Pós – Graduação em Ciência de Materiais, em nome da secretária, Ingrid e à bolsista, Luana.

À FACEPE pela disponibilidade da bolsa.

“Be patient, for the world is broad and wide” (ABBOTT, 1952, p. 2)

ABSTRACT

The development of new materials is crucial for applications in various areas. In this sense, nanomaterials in their most diverse types, shape, and size have been synthesized. The miniaturization of materials where at least one dimension is below 100 nm brings interesting properties, which significantly increases their applicability. In this work we investigated the nonlinear optical properties of the four types of materials: Transition Metal Dichalcogenides (TMD's), Gold Nanoclusters (AuNC's), Graphene Quantum Dots (GQD's), and $NaNbO_3$ nanocrystals, using the techniques of Z-Scan, and Hyper-Rayleigh Scattering (HRS) and a random laser application was performed. Interesting properties have been found in TMD's. A high value for the first hyperpolarizability of $ZrTe_2$ monolayers suspended in acetonitrile (ACN) was measured using the HRS technique, and a dipolar behavior for the nonlinear polarization was demonstrated. It was characterized for the first time the nonlinear refraction index of $ZrTe_2$ monolayers suspended in ACN and, as an application of this material, we used it as a scatter for random laser. In NbS_2 monolayers suspended in ACN, a change in the signal of the nonlinear refraction index from negative to positive and the transition from two-photons absorption to a saturated behavior with the increase of intensity was shown. In MoS_2 monolayers, the fifth-order nonlinear refraction index was demonstrated for the first time. In MGC's with six atoms ($Au_6(GSH)_2(MPA)_2$) dissolved in water, the first hyperpolarizability was characterized using the HRS technique. Increase of the hyperpolarizability with decrease in the number of atoms, already demonstrated in the literature, was also seen in this work. For two different GQD's, the first hyperpolarizability was determined applying the HRS technique; a quadrupolar behavior was demonstrated from polarization measurements. Also, for GQD's the two-photon absorption cross-section was characterized by two-photon induced luminescence. Finally, $NaNbO_3$ nanocrystals prepared using different synthesis temperatures were characterized applying the HRS technique. An increase in the first hyperpolarizability with temperature was observed.

Keywords: nanomaterials; nonlinear optical properties; transition metal dichalcogenides; gold nanoclusters; graphene quantum dots; $NaNbO_3$ nanocrystals.

RESUMO

O desenvolvimento de novos materiais é crucial para aplicações nas mais diversas áreas. Neste sentido, nanomateriais nos seus mais diversos tipos, formas e tamanhos têm sido sintetizados. A miniaturização de materiais onde ao menos uma dimensão está abaixo dos 100 nm faz surgir interessantes propriedades, que eleva significativamente a aplicabilidade destes. Neste trabalho foram investigadas as propriedades ópticas não lineares dos quatro tipos de materiais: Dicalcogenetos de Metais de Transição (DMT's), nanoclusters de ouro, pontos quânticos de grafeno e nanocristais de $NaNbO_3$, utilizando as técnicas de Z-Scan, e Espalhamento Hiper-Rayleigh (HRS) e uma aplicação em laser aleatório foi realizada. Interessantes propriedades foram encontradas em DMT's. Um elevado valor para a primeira hiperpolarizabilidade de monocamadas de $ZrTe_2$ suspensas em acetonitrila (ACN) foi medido usando a técnica de HRS, e um comportamento dipolar para a polarização não linear foi demonstrado. Foi caracterizado pela primeira vez o índice de refração não linear de monocamadas de $ZrTe_2$ também suspensas em ACN e como aplicação deste material, utilizamos ele como espalhador para laser aleatório. Em monocamadas de NbS_2 suspenso em ACN, foi mostrado uma mudança no sinal do índice de refração não linear de negativo para positivo, e a transição de absorção de dois fótons para saturação da absorção de dois fótons com aumento da intensidade. Em monocamadas de MoS_2, o índice de refração não linear de quinta ordem foi demonstrado pela primeira vez. Em clusters de ouro metálicos com 6 átomos ($Au_6(GSH)_2(MPA)_2$) dissolvidos em água, a primeira hiperpolarizabilidade foi caracterizada usando a técnica de HRS. Um comportamento de aumento da hiperpolarizabilidade com a diminuição do número de átomos, que já tinha sido demonstrada na literatura, foi também visto neste trabalho. Em dois diferentes pontos quânticos de grafeno, foi calculada a primeira hiperpolarizabilidade a partir da técnica de HRS; um comportamento quadrupolar foi demonstrado para a polarização não linear. Também para pontos quânticos de grafeno foi caracterizada a seção de choque de absorção de dois fótons pela técnica de luminescência induzida pela absorção de dois fótons. Por último, nanocristais de $NaNbO_3$ preparados com diferentes temperaturas de síntese foram caracterizados usando a técnica de HRS. Um aumento na primeira hiperpolarizabilidade com a temperatura foi observado.

Palavras - chave: nanomateriais; propriedades ópticas não lineares; dicalcogenetos de metais de transição; nanoclusters metálicos; pontos quânticos de grafeno; nanocristais de $NaNbO_3$.

LIST OF FIGURES

LIST OF TABLES

CONTENTS

1 INTRODUCTION

Research on the properties of new materials for nonlinear nanophotonics is extremely important for the understanding of the physical and chemical phenomena that occur due to the high-intensity light-matter interaction. From understanding of fundamentals properties, the control of light-matter interaction leads to the development of ultrafast devices, such as sensors, photodetectors, nanolasers, and others.

In this sense, a large diversity of nanoparticles of different shapes and sizes as nanospheres, nanorods, nanoprisms, and nanowires (WANG et al, 2018; KHLEBTSOV et al, 2010) as well as mono- and multi-layered structures (WANG et al, 2012; YAN et al, 2018) have been extensively studied for the applications mentioned above. Other nanostructures that have been receiving large attention are metallic clusters and quantum dots. Clusters are aggregates of atoms embraced by molecules; these systems can be considered molecular-like materials. Clusters with a different number of atoms and different atomic species as Silver (Ag), Gold (Au) Cooper (Cu), and Ag-Au alloys were reported (PATRA et al, 2019; PATRA et al, 2018). Quantum Dots (QD's) are materials with high photoluminescence quantum yields and generally are composed of a metal and a chalcogen, e.g. CdS, CdSe, and CdTe (UNG et al, 2012 BERA et al, 2010). Due to the noncentrosymmetric crystalline phase, nanocrystals formed by an alkali metal and a transition metal oxide have a high Second Harmonic Generation (SHG); some examples are $BaTiO_3$, $PbTiO_3$, and $KNbO_3$ (LI et al, 2005; RODRIGUEZ et al, 2009).

Another class of materials that have aroused a lot of interest in the scientific community is the two-dimensional materials (2D materials), the best known of them is graphene, first isolated in 2004 by Andre Geim and Kostya Novoselov, who for this feat received the Nobel Prize in physics in 2010. Since 2004 there has been a huge increase in the number of publications in 2D materials, and besides graphene other materials have begun to be studied. Among the 2D materials the hexagonal boron nitride (h-BN), black phosphorus, and transition metal dichalcogenides (TMDs) are attracting large interest. Together, these materials have a high susceptibility in the electromagnetic spectrum, from microwave to ultraviolet (YOU et al, 2018). Many studies have sought to develop new devices with 2D materials, and one example is the development of a *Rectenna* that converts Wi-Fi signals into electricity using MoS_2 (ZHANG et al, 2019).

In particular, materials that have in the unit cell a transition metal located between two chalcogens (TMDs), have received a lot of attention due to their electronic properties that can

be tuned by modifying some parameters of the material. For example, by varying the number of layers we can change the luminescence intensity, the bandgap of the material, and the nonlinear susceptibility tensor (SPLENDIANI et al, 2010; DONG et al, 2016). The number of layers of the material can also change its crystalline structure (KOLOBOV and TOMINAGA, 2016) and may modify, for example, the electronic character of the material. NbS_2, for example, presents a superconducting state if the material has two layers, or a metallic state if the material has three layers. The behavior of these samples can vary significantly with the chalcogen (S, Se, and Te) that is bound to the transition metal.

Several nonlinear optical effects have already been demonstrated in TMDs. Because they are noncentrosymmetric materials, there is a generation of even and odd high harmonics (LIU et al, 2017), nonlinear refraction and nonlinear absorption are observed in MoX_2 (X = S, Se, and Te) at various wavelengths (WANG et al, 2014), and laser light generation by a hybrid structure consisting of WSe_2 monolayer/photonic crystal (WU et al, 2015). The electronic properties and consequently the optical properties of TMDs can be modified by increasing or decreasing the number of sample layers. In this sense, an increase in the photoluminescence efficiency is observed with a decrease in the number of MoS_2 layers; the signal of the nonlinear refractive index can be changed from positive to negative, with the increase in the number of layers. Materials with an even number of layers have higher second harmonic generation efficiency when compared to samples with an odd number of layers (SONG et al, 2018). Unlike metallic nanoparticles, where optical effects are mostly dominated by localized surface plasmons, in TMDs, optical effects are dominated by electron-hole pairs known as excitons. Excitonic transitions induce optical absorption in materials as MoS_2 and WS_2 for example (WANG et al, 2014).

Metallic Nanoclusters (MNC's) are a type of material that has been deserving large attention. The understanding and control of properties of these nanomaterials have large importance to possible applications in several fields like sensors, catalysis, and light-harvesting due to the fluorescence, low toxicity, and good photostability (MAITY et al, 2018). Characteristics like the number of atoms, stabilizing ligands, and valence state of the metal are significantly responsible for the luminescence properties of these materials. The nonlinear optical properties of MNC's are demonstrated in several works, and this included second and third-order phenomena like Incoherent Second Harmonic Generation (I-SHG) (RUSSIER-ANTOINE et al, 2014), nonlinear refraction, and nonlinear absorption (REYNA et al, 2018).

Graphene Quantum Dots (GQD's) are small pieces of graphene (carbon-based 2D material) with a lateral size smaller than 100 nm. The GQD's are characterized for good fluorescence quantum yield and have several applications in fluorescence microscopy, catalysis, and optoelectronics (YAN et al, 2019). In the last years, several authors have proposed to study experimental and theoretically optical nonlinearities in GQD's. The first-order hyperpolarizability is theoretically calculated by LI et al, 2019. Nonlinear refraction and nonlinear absorption measurements in commercial GQD's were performed by WANG et al, 2019. To increase the optical and electronic properties of GQD's, some authors prepared this nanomaterial with hydrogen and oxygen on the surfaces or using doping, as nitrogen substituting carbons atoms of the nanomaterial (LIU et al, 2013).

Lead-free and environmentally friendly nanomaterials have gained good attention in the last years due to several applications in different fields (YANG et al, 2020). Particularly, nanomaterials with perovskite crystalline structures have been identified as good candidates for the substitution of dangerous materials for the environment. For instance, Sodium Niobate nanocrystals ($NaNbO_3$ NCs) have demonstrated good potential for several applications. Their size dependence with the temperature allows control of the linear and nonlinear optical properties.

The objective of this thesis was the study of the second-, third- and fifth-order nonlinearities of different classes of photonic nanomaterials, and demonstrate an application of an LTMD'S as random laser scatterers. To perform this characterization three differents nonlinear optical techniques were employed, and a standard Random Laser characterization was also performed. For characterization of LTMD's, it was applied the technique of Hyper Rayleigh Scattering (HRS) (CLAYS and PERSOONS, 1991), for characterization of second-order nonlinearities, and the Z-Scan technique (SHEIK-BAHAE et al, 1990) for studies of self-focusing and self-defocusing. In the MNC's, GQD's, and $NaNbO_3$ NC's the HRS technique was applied for characterization of the first order hyperpolarizability. In GQD's the two-photon absorption induced luminescence was also applied to characterize the two-photon absorption cross-section.

The HRS technique is based on the detection of second-order parametric scattering I-SHG. This effect was reported for the first time in C_2Cl_4 molecules, in 1977 (SCHIMID and SCHRÖTTER, 1977). From the data obtained from the HRS experiment, it is possible to determine the orientational average of the first order hyperpolarizability, $\langle\beta(2\omega)\rangle$.

The Z-Scan technique (SHEIK-BAHAE et al, 1990) is based on the effects of self-focusing and defocusing of a light beam interacting with a nonlinear material. These effects correspond to a nonlinear spatial phase variation induced on the optical beam propagating along a nonlinear material. Z-scan is a useful technique for the characterization of intensity dependence refractive index (nonlinear refraction) and intensity dependence optical absorption (nonlinear optical absorption).

Two-photon absorption induced luminescence is a nonlinear optical process where two photons of frequency ω_{inc} are absorbed by a material and, after some time (that depends on the intrinsic properties of the material), occurs emission of light with frequency $\omega_{em} > \omega_{inc}$.

This thesis is organized as follows:

Chapter 1 gives an introduction describing the nanomaterials that are characterized in this thesis, and a brief explanation about the experiment used here.

Chapter 2 presents a theoretical description of the optical 1st, 2nd, and 3rd order susceptibilities. First, it is discussed the process of spontaneous emission and demonstrated the one and two-photon absorption cross-sections. The photoluminescence lifetime is also discussed. The classical treatment of the second and third-order susceptibility is shown and the processes of SHG, nonlinear refraction, and nonlinear absorption are introduced. A brief discussion of the conditions for laser emission and their different characteristics with respect to Random Lasers is made.

Chapter 3 describes details of the nonlinear optical techniques used for the characterization of the materials. The theoretical and the tools needs in the laboratory are shown in detail.

Chapter 4 is dedicated to show the results obtained from nonlinear optical experiments performed in the TMD's. Here, we demonstrated for the first time the results of I-SHG in Zirconium Ditelluride ($ZrTe_2$), nonlinear refraction in $ZrTe_2$. Unusual behavior of nonlinear refraction and absorption is demonstrated in NbS_2 samples and fifth-order nonlinearity is demonstrated in MoS_2 samples. In addition, it is performed the characterization of WS_2 samples, to compare with the fifth-order results in MoS_2 samples. Finally, $ZrTe_2$ samples are used as scatterers for operation of a dye-based (Rh6G) random laser. A small energy threshold was found, statistical studies were performed and a transition from paramagnetic to photonic spin glass states is reported.

The Chapter 5 presents the results of HRS for a Gold Cluster (GC) with six atoms, capped by glutathione ($C_{10}H_{17}N_3O_6S$) and 3-Mercaptopropionic acid ($C_3H_6O_2S$). The results show a high hyperpolarizability, $\langle\beta(2\omega)\rangle$, that corroborate predictions of an increase of $\langle\beta(2\omega)\rangle$ with the decrease of the number of atoms (RUSSIER-ANTOINE et al, 2014). Quantum mechanics calculations were performed to support the experimental results.

Chapter 6 shows measurements of the first-order hyperpolarizability of GQD's using the HRS method. Polarization resolved HRS measurements were performed to determine the origin of nonlinearity. Two-photon absorption cross-section is also determined using two-photon absorption induced luminescence and comparing the results with a known dye as reference.

Chapter 7 shows the results of HRS in $NaNbO_3$ samples. Five samples with nano- and submicron sizes were studied. One goal was the understanding of how the temperature of synthesis influence the $\langle\beta(2\omega)\rangle$ value. It was verified that the increase of temperature from 600 ºC to 1000 ºC, with intervals of 100 ºC contributes to the increasing $\langle\beta(2\omega)\rangle$. X-ray powder diffraction was performed and showed a change in the crystalline phase for temperature above 800 ºC that contributes for growth of the hyperpolarizability.

Chapter 8 presents a summary of the main conclusions and indicates possible future works to extend the results obtained along this thesis.

2 LIGHT-MATTER INTERACTION: LINEAR AND NONLINEAR PHENOMENA

2.1 LINEAR OPTICAL PHENOMENA

2.2.1 Linear optical absorption and emission

Linear Optical absorption is the phenomenon characterized as the absorption of one photon by an atomic entity. This process is possible when the photon energy is the same as the difference of energy between two energy levels.

Due to the purely quantum character of the spontaneous emission, it is necessary to describe this phenomenon using a quantum approach. The first step is to write the Schrodinger equation for the system:

$$i\hbar \frac{\partial \psi(\boldsymbol{r},t)}{\partial t} = \hat{H}\psi(\boldsymbol{r},t), \tag{2.1}$$

with $\hat{H} = \hat{H}_0 + \hat{V}(t)$ where $\hat{H}_0$ is the Hamiltonian of the free atom, and $\hat{V}(t) = -\hat{\mu}.\tilde{E}(t)$ is the interaction Hamiltonian of the system with the electromagnetic field. The electrical field for a monochromatic wave can be written as:

$$\vec{E}(t) = \vec{E}_0 e^{-i\omega t} + c.c. \tag{2.2}$$

When there is no external electric field applied, we have the solutions for the unperturbed Hamiltonian, $\hat{H} = \hat{H}_0$ and the solutions are energy eigenstates, having the form:

$$\psi(\boldsymbol{r},t) = u_n e^{-i\omega_n t}. \tag{2.3}$$

substituting (2.3) in (2.1) we obtain the spatial part of the wavefunction by solving the equation

$$\hat{H}_0 u_n(\boldsymbol{r}) = E_n u_n(\boldsymbol{r}), \tag{2.4}$$

where $E_n = \hbar\omega_n$, and the subscript n is used to distinguish the various eigenfunctions that form a complete set.

Then Eq. 1 assumes the form

$$i\hbar \frac{\partial \psi(\boldsymbol{r},t)}{\partial t} = \left(\hat{H}_0 + \hat{V}(t)\right)\psi(\boldsymbol{r},t), \tag{2.5}$$

and we can write $\psi(\boldsymbol{r},t)$ as a linear combination of the eigenfunctions $u_n(\boldsymbol{r})$**:**

$$\psi(\boldsymbol{r},t) = \sum_l a_l(t) u_l(\boldsymbol{r})\, e^{-i\omega_l t}, \tag{2.6}$$

So, applying $\psi(\boldsymbol{r},t)$ in the equation (2.5), we obtain:

$$i\hbar\left[\sum_l\left(\frac{da_l}{dt}u_l(\boldsymbol{r})e^{-i\omega_l t}-i\omega_l a_l(t)u_l(\boldsymbol{r})e^{-i\omega_l t}\right)\right]=\left[\sum_l\left(E_l+\hat{V}\right)a_l(t)u_l(\boldsymbol{r})e^{-i\omega_l t}\right] \quad (2.7)$$

where $E_l=\hbar\omega_l$. Further, using the orthonormality condition, we can simplify the expression (2.7):

$$i\hbar\frac{da_m}{dt}=\sum_l a_l(t)V_{lm}e^{-i\omega_{lm}t}, \quad (2.8)$$

where ~~this~~ the expression (2.8) is the matrix form of the Schrodinger equation and $\omega_{lm}=\omega_l-\omega_m$.

Equation (2.7) can be solved using the perturbation theory assuming:

$$a_m(t)=a_m^{(0)}(t)+\lambda a_m^{(1)}(t)+\lambda^2 a_m^{(2)}(t), \quad (2.9)$$

and matching the powers of λ in both sides of the equation (2.8),

$$\frac{da_m^{(N)}}{dt}=(i\hbar)^{-1}\sum_l a_l^{(N-1)}V_{lm}e^{-i\omega_{lm}t}, \quad (2.10)$$

where N is an integer and positive and $V_{lm}=-\mu_{lm}Ee^{-i\omega t}$. For two-photon absorption, we use $N=1$ and $N=2$, the probability amplitude $a_n^{(2)}(t)$, for an atom at level n in time t and therefore we obtain,

$$\frac{da_n^{(2)}(t)}{dt}=-(i\hbar)^{-1}\sum_m\frac{\mu_{nm}\mu_{mg}E^2}{\hbar(\omega_{mg}-\omega)}\left(e^{i(\omega_{mg}-2\omega)t}-e^{i(\omega_{nm}-\omega)t}\right). \quad (2.11)$$

Then, integrating the equation (2.11), we have:

$$a_n^{(2)}(t)=\sum_m\frac{\mu_{nm}\mu_{mg}E^2}{\hbar^2(\omega_{mg}-\omega)}\left[\frac{\left(e^{i(\omega_{mg}-2\omega)}-1\right)}{(\omega_{mg}-2\omega)}\right], \quad (2.12)$$

and calculating the probability of one atom be excited to level n for $t\to\infty$ we obtain

$$p_n^{(2)}(t)=\left|a_n^{(2)}(t)\right|^2=\left|\sum_m\frac{\mu_{nm}\mu_{mg}E^2}{\hbar^2(\omega_{mg}-\omega)}\right|^2 2\pi t\delta\left(\omega_{ng}-2\omega\right). \quad (2.13)$$

The expression (2.13) can be written in a more general form assuming that the level n is diffused in a density of states. Then, we have:

$$p_n^{(2)}(t)=\left|\sum_m\frac{\mu_{nm}\mu_{mg}E^2}{\hbar^2(\omega_{mg}-\omega)}\right|^2 2\pi t\rho_f\left(\omega_{ng}=2\omega\right), \quad (2.14)$$

where $\rho_f(\omega_{ng})$ is the atomic line shape. Here, $\rho_f(\omega_{ng}=2\omega)$ means that the density of the end states n, g must be evaluated at the 2ω frequency of the incident laser.

Now, we can define the rate transition for the two-photon absorption:

$$R_{ng}^{(2)} = \frac{p_n^{(2)}(t)}{t}, \tag{2.15}$$

and for easy manipulation, we can write the equation (2.15) in terms of the absorption cross-section:

$$R_{ng}^{(2)} = \sigma_{ng}^{(2)}(\omega) I^2. \tag{2.16}$$

with $I = 2n\varepsilon_0 c|E|^2$ being the light intensity. Consequently, Eq, (2.14), may be written as:

$$\sigma_{ng}^{(2)}(\omega) = \frac{1}{4n^2\varepsilon_0^2 c^2}\left|\sum_m \frac{\mu_{nm}\mu_{mg}E^2}{\hbar^2(\omega_{mg}-\omega)}\right|^2 2\pi t \rho_f\left(\omega_{ng} = 2\omega\right) \tag{2.17}$$

where the absorptions cross-section indicates the number of photons absorbed per second in one area of $1\ cm^2$, and has units of $fótons/cm^2 \cdot s$. Re-writing the equation (2.17) as an average of the absorption cross-section, we have:

$$\bar{\sigma}_{ng}^{(2)}(\omega) = \frac{\omega^2}{4n^2\varepsilon_0^2 c^2}\left|\sum_m \frac{\mu_{nm}\mu_{mg}E^2}{\hbar^2(\omega_{mg}-\omega)}\right|^2 2\pi t \rho_f\left(\omega_{ng} = 2\omega\right). \tag{2.18}$$

To estimate numerical values for absorption cross-section we need to assume that the summation in the equation (2.18) is dominated by only one level, such that $\omega_{mg} \approx \omega$ and for last, that the laser frequency is close to resonance, $(\rho_f\left(\omega_{ng} = 2\omega\right) \approx (2\pi\Gamma_n)^{-1})$, where Γ_n is the linewidth of the level n. Thus, the expression (2.18) can be approximate to:

$$\bar{\sigma}_{ng}^{(2)}(\omega) \approx \frac{\left|\mu_{nm}\mu_{mg}\right|^2}{4\hbar^2\varepsilon_0^2 c^2 \Gamma_n}, \tag{2.19}$$

and we can calculate the rate transitions:

$$R_{mg}^{(1)} = \left|\frac{\mu_{mg}E}{\hbar}\right|^2 2\pi\rho_f\left(\omega_{mg} - \omega\right), \tag{2.20}$$

for one-photon absorption, and

$$R_{ng}^{(2)} = \left|\frac{\mu_{nm}\mu_{mg}E^2}{\hbar^2(\omega_{mg}-\omega)}\right|^2 2\pi\rho_f\left(\omega_{mg} - 2\omega\right). \tag{2.21}$$

for two-photon absorption.

2.2.2 Emission lifetime

The emission lifetime is defined as the average time that one atomic entity in an excited state decay for a less energetic state, by a process that can be radiative (light emission) or nonradiative (energy transfer to another atom, vibrations, etc).

Considering a set of excited molecules, the rate decay is:

$$-\frac{dA}{dt} = (k_r^s + k_{nr}^s)A(t), \tag{2.22}$$

here $A(t)$ is the number of excited molecules in a time t, k_r^s is the radiative emission rate and k_{nr}^s is the nonradiative emission rate.

$$A(t) = A_0 e^{-\tau/\tau_s}, \tag{2.23}$$

where τ_s is the excited state lifetime and is described by:

$$\tau_s = \frac{1}{k_r^s + k_{nr}^s}, \tag{2.24}$$

thus, the fluorescence intensity is proportional to the population of the excited state and have an exponential behavior:

$$F(t) = A_0 k_r^s e^{-t/\tau}. \tag{2.25}$$

Therefore, the excited state lifetime is one important parameter obtained by fluorescence spectroscopy.

2.3 OPTICAL SUSCEPTIBILITIES

When low-intensity light interacts with a material, the phenomena that occur due to this interaction can be described, almost entirely, by the equations that are passed on in the course of electromagnetism. When we are working in this regime, we say that we are in the linear optics regime. The interaction of light with a material generates what we know as polarization (P), which in the case of linear optics can be written as (GRIFFITHS, 2011):

$$\boldsymbol{P} = \varepsilon_0 \chi \boldsymbol{E} \tag{2.26}$$

where, ε_0 is the vacuum electrical permittivity in, χ it is optical susceptibility and describes how much a material medium is susceptible to interact with $\boldsymbol{E}$. The vector $\boldsymbol{E}$ is the amplitude of the electric field that interacts with matter. When $\boldsymbol{E}$ has a small amplitude, $\boldsymbol{P}$ varies linearly with $\boldsymbol{E}$. However, when $\boldsymbol{E}$ has large amplitudes, equation (2.26) no longer describes the behavior of light-matter interaction.

Figure 1 - Responses of linear, quadratic, and cubic polarizations as a function of the applied field.

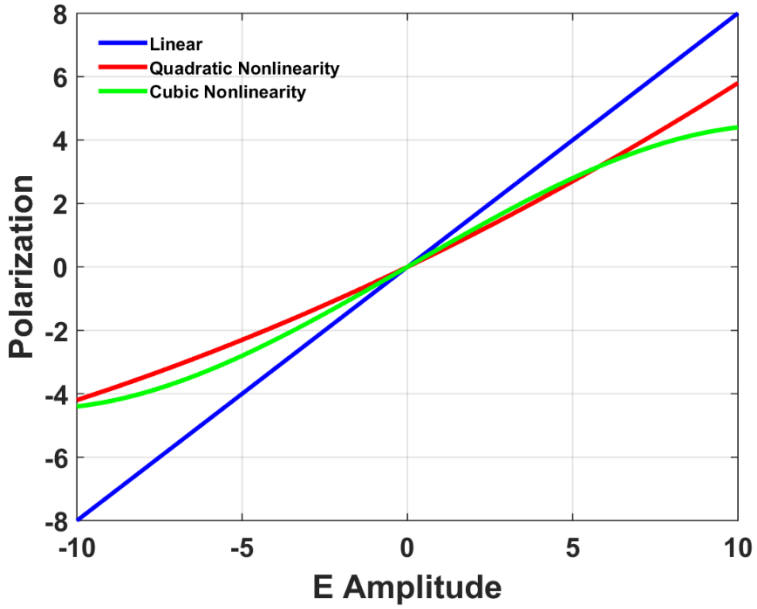

Source: The author (2021).

Figure 1 shows the behavior of polarization ($\boldsymbol{P}$) as a function of the amplitude of the electric field ($\boldsymbol{E}$). In blue we have only a polarization that depends linearly on $\boldsymbol{E}$, and in red and green, we have polarizations that depend on the amplitude of $\boldsymbol{E}$ to square and cubic power, respectively.

When we have the green and red cases shown in Figure 1, we are in the nonlinear optical regime, so the equation (2.26) will no longer describe the behavior of the light-matter

interaction. To correctly describe the behavior of $\boldsymbol{P}$ with $\boldsymbol{E}$ we must expand (2.26) in series of powers, obtaining the following equation (RESHEF et al, 2017):

$$\boldsymbol{P}(E) = \varepsilon_0 E \sum_j^{\infty} c_j \chi^{(j)} |E|^{j-1} , \tag{2.27}$$

in (2.27) $j \in \mathbb{R}, \mathbb{Z} \neq 0$, where c_j is a degeneracy factor. Being, $j = 1$ we recover the equation (2.26). The terms $j = 2$ give rise to various nonlinear effects, how, SHG and I-SHG, and effects like THG and nonlinear refraction are due $j = 3$. The question remains: how do we differentiate what effect is occurring when we have, $\chi^{(2)}$ for example? The answer is that $\chi^{(j)}$it is not a scalar, but an order tensor, $j + 1$ so the nonlinear effects that occur on materials are linked to different combinations of components of this tensor.

To see this in more detail, equation (2.27) can be written as follows:

$$P_i(E) = \varepsilon_0 \left(\sum_j \chi_{ij}^{(1)} E_j + \sum_{j,k} \chi_{ijk}^{(2)} E_j E_k + \sum_{j,k,l} \chi_{ijkl}^{(3)} E_j E_k E_l + \cdots \right), \tag{2.28}$$

the indexes $ijkl$ indicate the tensor components and can undergo permutations, thus, the 2nd order nonlinear susceptibility tensor has 27 components (3 indexes) and the third-order has 81 components (4 indexes). By use of symmetry properties, most of these components are null and in centrosymmetric materials (there is, materials with inversion symmetry), the even terms of expansion (2.28) are null. When the Kleinman symmetry is valid (BOYD, 2007), the relation between the coefficient, $d_{i,j}$ and the nonlinear optical susceptibility is $d_{i,j} = \frac{1}{2}\chi_{i,j}^{(2)}$. Thus, using the contracted notation ($d_{i,j}$), the second-order nonlinear susceptibility tensor, $d_{i,j}$ for a potassium phosphate monocrystal (or KH_2PO_4) simply KDP is (YARIV, 1989).

$$d_{i,j} = \begin{pmatrix} 0 & 0 & 0 & d_{1,4} & 0 & 0 \\ 0 & 0 & 0 & 0 & d_{1,4} & 0 \\ 0 & 0 & 0 & 0 & 0 & d_{3,6} \end{pmatrix}. \tag{2.29}$$

thus, for KDP, of the 18 tensor components $d_{i,j}$ only three are nonzero, of which two assume the same value. YARIV, 1989 shows all these values. Later we will return to treat the nonlinear susceptibility tensor, but now we will turn our attention to know its origin from a classical description.

2.4 CLASSICAL ORIGIN OF NONLINEAR SUSCEPTIBILITY

The appearance of non-linear optical effects due to the interaction between radiation and matter can be described with basis on quantum mechanics, but a classic treatment can be done to obtain many of the susceptibilities properties. Classically treating an electron in a potential well, is under the action of a force of the form.

$$\boldsymbol{F} = -\boldsymbol{\nabla} U, \tag{2.30}$$

where *U* is potential energy. The expression (2.30) is not new to us, we have already worked with it since the course of Physics I and is related to a restorative force, which in this case is acting on the electron. If we have electrons in a quadratic potential the restorative force acting on the electron is linear (a mass-spring harmonic oscillator), but if we include more terms in the potential, this oscillator will oscillate nonlinearly, and then an anharmonic oscillator appears, which is a perturbation in the harmonic oscillator.

Initially, we will consider an electron of electrical charge -*e* and mass *m* in a well of quadratic potential, being a characteristic frequency ω_0 and considering only linear interactions, the potential energy of the electron is:

$$U = \frac{1}{2} m\omega_0^2 X^2 \tag{2.31}$$

that is, the potential energy of the electron is quadratic in the X, where X is the displacement. Replacing (2.31) in (2.30), we obtain that:

$$F = -m\omega_0^2 X, \tag{2.32}$$

thus, in equation (2.32) we have the well-known Hook law, where the term $-m\omega_0^2$ would be an effective spring constant. To consider our model as close to reality as possible, we need to consider that electrons are not alone in material and that they interact with each other as well as with positive ions, suffering collisions that cause damping, which we will denote as γ. This term causes a damping force that is proportional to speed and can be written F_a as,

$$F_a = -m\gamma \frac{dX}{dt}, \tag{2.33}$$

Let us consider now that an *E* electric field interacts with electrons in a-material, and originate an electric force F_e by:

$$F_e = -eE(t), \tag{2.34}$$

Then, using Newton's second law to relate the forces involved in the interaction of the field with the matter, we have:

$$m\frac{d^2X}{dt^2} = -m\gamma\frac{dX}{dt} - m\omega_0^2 X - eE, \quad (2.35)$$

assuming a monochromatic and linearly polarized electrical field *E*, and writing in terms of its complex amplitude, $E = \frac{1}{2}Ae^{-i\omega t} + c.c$, we expect that X oscillates at the same frequency of the field, but out of phase:

$$X = \frac{1}{2}xe^{-i\omega t} + c.c. \quad (2.36)$$

where the phase offset is contained in *x*. Replacing (2.36) in (2.35) and solving the equation we obtain:

$$x = -\frac{eA}{mD(\omega)}, \quad (2.37)$$

where $D(\omega) = \omega_0^2 - \omega^2 - i\Gamma\omega$. Remembering that the expression for polarization is $P = -Nex$, and replacing x in it we are left with:

$$P = \frac{Ne^2A}{mD(\omega)}, \quad (2.38)$$

where *N* is the number of electronic oscillators. Replacing (2.38) in (2.27) and isolating $\chi^{(1)}$ we find an expression for linear optical susceptibility:

$$\chi^{(1)} = \frac{Ne^2A}{\varepsilon_0 mD(\omega)}. \quad (2.39)$$

We can the same procedure to calculate the nonlinear susceptibilities, but from now on, we will need to apply a perturbation to the system, so our oscillator will no longer be harmonic, but anharmonic.

We can rewrite the equation (2.31) to include more terms and have a better approximation:

$$U = \frac{1}{2}m\omega_0^2X^2 + \frac{1}{3}amX^3 + \frac{1}{4}bmX^4 + \cdots, \quad (2.40)$$

where a and b are coefficients of expansion that depend on the shape of the potential well where the electron is. Considering the first two corrections we can rewrite the equation for restoring force as:

$$F = -m\omega_0^2 X - maX^2 - mbX^3, \tag{2.41}$$

rewriting the equation (2.35) we have:

$$\frac{d^2X}{dt^2} + \gamma\frac{dX}{dt} + \omega_0^2 X + aX^2 + bX^3 = -\lambda\frac{eE}{m}, \tag{2.42}$$

being λ, adimensional parameter and equal to 1 and it is introduced to identify the order of the expansion in subsequent calculations. which is introduced to identify the order of the expansion. In order, to be able to write X in terms of power series it is necessary to consider small displacements:

$$X = \lambda X^{(1)} + \lambda^2 X^{(2)} + \lambda^3 X^{(3)} \tag{2.43}$$

Then, we can replace (2.43) in (2.42) to find the terms multiplying λ. Thus, separating the terms for different orders, $\lambda, \lambda^2. \lambda^3$ ...we have:

$$\lambda: \frac{d^2X^{(1)}}{dt^2} + \gamma\frac{dX^{(1)}}{dt} + \omega_0^2 X^{(1)} = -\frac{eE}{m}, \tag{2.44a}$$

$$\lambda^{(2)}: \frac{d^2X^{(2)}}{dt^2} + \gamma\frac{dX^{(2)}}{dt} + \omega_0^2 X^{(2)} + a(X^{(1)})^2 = 0, \tag{2.44b}$$

$$\lambda^{(3)}: \frac{d^2X^{(3)}}{dt^2} + \gamma\frac{dX^{(3)}}{dt} + \omega_0^2 X^{(3)} + 2aX^{(1)}X^{(2)} + b(X^{(1)})^3 = 0. \tag{2.44c}$$

Considering two fields of frequencies ω_1 and ω_2, we can solve these equations (2.44a), (2.44b), and (2.44c), so our incident field A is given by:

$$E = \frac{1}{2}A_1 e^{-i\omega_1 t} + \frac{1}{2}A_2 e^{-i\omega_2 t} + \text{c.c.}, \tag{2.45}$$

In the first order of λ the total offset is:

$$X^{(1)} = \frac{1}{2}x_1^{(1)} e^{-i\omega_1 t} + \frac{1}{2}x_2^{(1)} e^{-i\omega_2 t} + \text{c.c.}, \tag{2.46}$$

where $x_1^{(1)}$and $x_2^{(1)}$are complex amplitudes of linear displacement. Replacing (2.46) in (2.44b) we get:

$$\frac{d^2X^{(2)}}{dt^2} + \gamma\frac{dX^{(2)}}{dt}\omega_0^2 X^{(2)} + a\left(\frac{1}{2}x_1^{(1)} e^{-i\omega_1 t} + \frac{1}{2}x_2^{(1)} e^{-i\omega_2 t} + \text{c.c.}\right)^2 = 0 \tag{2.47}$$

in the last term of the equation (2.47), the linear displacement is squared, producing an inhomogeneous term, there are included the components of sum and difference of two frequencies.

Considering a frequency generated by the sum or difference of frequencies, that is, $\omega_3 = \omega_1 \pm \omega_2$ thus, we have:

$$\frac{d^2X^{(2)}}{dt^2} + \gamma\frac{dX^{(2)}}{dt} + \omega_0^2 X^{(2)} = -\left(a\frac{1}{2}x_1^{(1)}x_2^{(1)*}e^{-i\omega_3 t} + c.c.\right). \quad (2.48)$$

To solve the equation (2.48) we use the same procedure for linear displacements, like this:

$$X^{(2)} = \frac{1}{2}x^{(2)}e^{-i\omega_3 t} + c.c. \quad (2.49)$$

So, the solution of our equation is:

$$\left[\pm\omega_3^2 x^{(2)} \pm i\omega_3\gamma x^{(2)} + \omega_0^2 x^{(2)} + a x_1^{(1)}x_2^{(1)*}\right]e^{-i\omega_3 t} + c.c. = 0, \quad (2.50)$$

thus, the second-order solution for the complex amplitude is:

$$x^{(2)}(\omega_3) = \pm\frac{ae^2 A_1 A_2^*}{m^2 D(\omega_1)D^*(\omega_2)D(\omega_3)}, \quad (2.51)$$

Rewriting the polarization using only the term for the frequency difference we have:

$$P = \varepsilon_0\chi^{(2)}A_1A_2^* \quad (2.52)$$

and using (2.52) and the equation for polarization we obtain:

$$\chi^{(2)}(\omega_3;\ \omega_1, -\omega_2) = \frac{Nae^3}{\varepsilon_0 m^2 D(\omega_1)D^*(\omega_2)D(\omega_3)} \quad (2.53)$$

the notation $\chi^{(2)}(\omega_3;\ \omega_1, -\omega_2)$indicates a dependency with three frequencies; the first frequency corresponds to nonlinear polarization and the other two are the incident frequencies.

Considering now a centrosymmetric medium, that is, a medium with $\chi^{(2)} = 0$ we can follow the same procedure to find $\chi^{(3)}$. In this case the third-order response, $X^{(3)}$ is related to $(X^{(1)})^3$. Considering the case of two incident frequencies $\omega_1\ e\ \omega_2$and we are interested in a nonlinear displacement at the frequency, ω_1 and doing the same operations, we obtain to$(X^{(1)})^3$:

$$(X^{(1)})^3 = \frac{1}{8}\left(x_1^{(1)}e^{-i\omega_1 t} + \frac{1}{2}x_2^{(1)}e^{-i\omega_2 t} + \text{c.c.}\right) \times (x_1^{(1)}x_1^{(1)*}e^{-i(\omega_1-\omega_1)t} +$$
$$+x_2^{(1)}x_2^{(1)*}e^{-i(\omega_2-\omega_2)t}(x_1^{(1)})^2e^{-i(\omega_1+\omega_1)t} + (x_2^{(1)})^2e^{-i(\omega_1+\omega_1)t}2x_1^{(1)}x_2^{(1)}e^{-i(\omega_1+\omega_2)t} +$$
$$2x_1^{(1)}x_2^{(1)*}e^{-i(\omega_1-\omega_2)t} + \text{c.c.}). \quad (2.54)$$

Considering only the displacement in ω_1

$$(X^{(1)})^3 = \frac{1}{8}\left(3(x_1^{(1)})^2 x_1^{(1)*} + 6x_1^{(1)} x_2^{(1)} x_2^{(1)*}\right)e^{-i\omega_1 t} + c.c. \quad (2.55)$$

And replacing (2.55) at (2.44c) we come to:

$$\frac{d^2X^{(3)}}{dt^2} + \gamma\frac{dX^{(3)}}{dt} + \omega_0^2 X^{(3)} +$$

$$+\left(\frac{3b}{8}(x_1^{(1)})^2 x_1^{(1)*} + \frac{3b}{4}x_1^{(1)} x_2^{(1)} x_2^{(1)*} + c.c.\right)e^{-i\omega_1 t} = 0 \quad (2.56)$$

The solution of the above equation is:

$$x^{(3)}(\omega_1) = -\frac{3be^3 A_1}{8m^3 D^2(\omega_1)}\left[\frac{|A_1|^2}{D(\omega_1)D^*(\omega_1)} + 2\frac{|A_2|^2}{D(\omega_2)D^*(\omega_2)}\right] \quad (2.57)$$

and thus, we find an expression for third-order polarization:

$$P^{(3)}(\omega_1) = -\frac{3be^4 A_1}{8m^3 D^2(\omega_1)}\left[\frac{|A_1|^2}{D(\omega_1)D^*(\omega_1)} + 2\frac{|A_2|^2}{D(\omega_2)D^*(\omega_2)}\right] \quad (2.58)$$

Based on the expressions found for the second and third-order susceptibilities, we can make the same procedure for the fifth-order susceptibility (BESSE, et al, 2015). Therefore, we realize that in this expression we have two contributions of complex amplitudes. Optical processes due to the above expression will be detailed later.

Figure 2 shows the potential energy behavior of a harmonic oscillator in two distinct situations; in the first, in blue, we have the simple harmonic oscillator, described by the equation (2.31). In this curve we realize that there is symmetry on both sides, suggesting that a purely linear process occurs. In the green curve, which is described by the equation (2.40), an asymmetry is perceived in the potential energy curve. This behavior occurs due to the addition of terms in the equation (2.40).

Figure 2 - Behavior of the potential energy as a function of displacement, in blue the harmonic oscillator and in red the anharmonic oscillator.

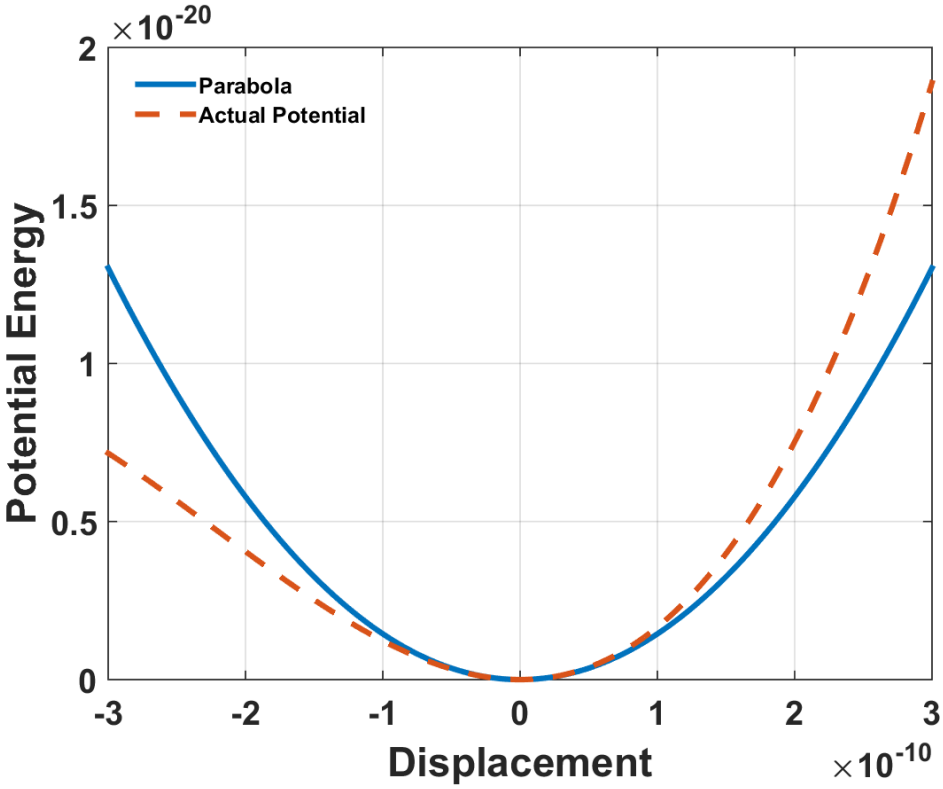

Source: The author (2021).

2.4.1 Second Harmonic Generation

Optical Second Harmonic Generation (SHG) was demonstrated for the first time in 1961 (FRANKEN, et al, 1961) and is of the most well-known phenomena in nonlinear optics. This process is due to the second-order nonlinear optical susceptibility $\chi^{(2)}$. SHG is perhaps the simplest of nonlinear optical processes and involves the interaction of three waves, two with frequencies ω, and one frequency 2ω. In this nonlinear process, a material is irradiated with wavelength λ, and radiation with half of the wavelength, $\frac{\lambda}{2}$, is generated. To mathematically describe this process, it is necessary to solve the wave equation in a nonlinear medium.

Considering only second-order processes we can write the equation (2.28) as:

$$\boldsymbol{P} = \varepsilon_0 \chi^{(1)} E + \boldsymbol{P}_{\boldsymbol{NL}}^{(\boldsymbol{2})} \ , \tag{2.59}$$

in which $P_{NL}^{(2)}$ is written in notation of contracted indexes, $(P_{NL}^{(2)}) = 2d_{ijk}E_jE_k$. Writing the nonlinear wave equation as (BOYD, 2008):

$$\nabla^2 \boldsymbol{E} = \mu_0 \sigma \frac{\partial \boldsymbol{E}}{\partial t} + \mu_0 \varepsilon \frac{\partial^2 \boldsymbol{E}}{\partial t^2} + \mu_0 \frac{\partial^2 \boldsymbol{P}_{NL}}{\partial t^2} , \tag{2.60}$$

considering only the one-dimensional case, with the direction of light propagation on the *z*-axis, we have that the interaction of three plane waves is:

$$E_i^{(\omega_1)}(z,t) = {}^1/_2\left[E_{1i}(z)e^{i(\omega_1 t - k_1 z)} + c.c.\right], \tag{2.61a}$$

$$E_j^{(\omega_2)}(z,t) = {}^1/_2\left[E_{2j}(z)e^{i(\omega_2 t - k_2 z)} + c.c.\right], \tag{2.61b}$$

$$E_k^{(\omega_3)}(z,t) = {}^1/_2\left[E_{3k}(z)e^{i(\omega_3 t - k_3 z)} + c.c.\right]. \tag{2.61c}$$

Considering a variation of the amplitude *z* of the complex field in the z-axis, and replacing (2.61) in (2.60) we find the solution to the wave equation:

$$\frac{dE_{1i}}{dz} = -\frac{\sigma_1}{2}\sqrt{\frac{\mu_0}{\varepsilon_1}}E_{1i} - i\omega_1\sqrt{\frac{\mu_0}{\varepsilon_1}}d'_{ijk}E_{2j}E^*_{3k}e^{-i(k_3-k_2-k_1)z}, \tag{2.62a}$$

$$\frac{dE^*_{2j}}{dz} = -\frac{\sigma_2}{2}\sqrt{\frac{\mu_0}{\varepsilon_2}}E^*_{2j} - i\omega_2\sqrt{\frac{\mu_0}{\varepsilon_2}}d'_{jik}E_{1i}E^*_{3k}e^{-i(k_1-k_3+k_2)z}, \tag{2.62b}$$

$$\frac{dE_{3j}}{dz} = -\frac{\sigma_3}{2}\sqrt{\frac{\mu_0}{\varepsilon_3}}E_{3j} - i\omega_3\sqrt{\frac{\mu_0}{\varepsilon_3}}d'_{kij}E_{1i}E_{2j}e^{-i(k_1+k_2+k_3)z}. \tag{2.62c}$$

The equations (2.62a - 2.62c) determine the processes of interaction of electric fields in the generation of new frequencies involving second-order nonlinear effects.

Figure 3 - SHG effect level diagram

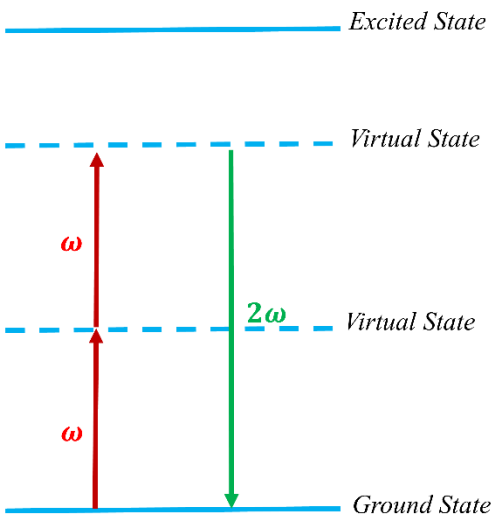

Source: The author (2021).

For the specific case of SHG, the interaction of three frequencies occurs, where two of these frequencies are equal, ($\omega_1$and ω_2) and ω_3= $2\omega_1$ or ω_3= $2\omega_2$. As we see, only two of the

three equations above participate in the SHG, the first (or second) and the third. Figure 3 shows the level diagram for an SHG process.

Two photons of frequency ω interact with the material and combine to generate a frequency 2ω. Considering a dielectric medium ($\sigma_3 = 0$) and that input beam loss are negligible, we can write:

$$\frac{dE_{3k}}{dz} = -2i\omega\sqrt{\frac{\mu_0}{\varepsilon}}\, d'_{ijk} E_{1i} E_{1j} e^{-i\Delta kz}, \tag{2.63}$$

in that $\omega_1 = \omega_2 = \omega_3/2$, and $\Delta k = k_3^k - k_1^i - k_1^j$. Whereas SHG does not occur at the first face of the crystal ($E_{3j}(0) = 0$), the solution to (2.63) in a crystal of length L is (YARIV and YEH, 1983):

$$E_{3j}^*(L) E_{3j}(L) = \frac{4\mu_0}{\varepsilon_0}\omega^2 (d'_{ijk})^2 E_{1i}^2 E_{1j}^2 L^2 \frac{sen^2(\Delta kL/2)}{(\Delta kL/2)^2} \tag{2.64}$$

The d'_{ijk} are the nonlinear coefficients and Δk is the phase difference between the fundamental beam and the harmonic generated.

Although the SHG process requires the participation of matter to occur, in the process neither energy absorption or luminescence occurs. What occurs is only a re-irradiation of a fraction of the incident light in the frequency of the generated harmonic. In real situations, there is the heating of the material that generates the harmonic, due to small absorptions induced by impurities or imperfections.

2.5 SELF – FOCUSING AND SELF–DEFOCUSING EFFECTS

The third-order polarization associated to $\chi^{(3)}$can be written as (POWERS and HAUS, 2017; BOYD, 2008):

$$P_x^{(3)}(\omega) = \frac{3\varepsilon_0}{4}\chi_{xxxx}^{(3)} |A_x|^2 A_x e^{i(k-k+k)z}, \tag{2.65}$$

Introducing the above equation in the wave equation, we obtain:

$$\frac{dA}{dz} = i\frac{3\omega}{8nc}\chi^{(3)}|A|^2 A \tag{2.66}$$

where in 2. 66 we suppress the x-indexes in χ and A. Writing amplitude, A as $A(z) = u(z)e^{i\phi(z)}$where $u(z)$ is a function with actual $\phi(z)$values. Replacing 2.66 in 2.65 we have:

$$\frac{du}{dz} + i\frac{d\phi}{dz} = i\frac{3\omega}{8nc}\chi^{(3)}u^3. \tag{2.67}$$

Assuming a lossless material, then $\chi^{(3)}$it is a real number, and we can divide the previous equation into two equations, one for the imaginary part $(du/dz) = 0$ and another equation for the real part:

$$\frac{d\phi}{dz} = \frac{3\omega}{8nc}\chi^{(3)}u^2. \tag{2.68}$$

Integrating the above equation, we find the phase displacement of the beam when interacting with a nonlinear material:

$$\Delta\phi = \frac{3\omega}{8nc}\chi^{(3)}u^2\Delta z. \tag{2.69}$$

In order to write the total phase, we should also add the term $\phi_l = ((n_0\omega/c)\Delta z)$ due to the linear propagation of the beam through the distance Δz. Thus, the total phase offset is given by:

$$\phi = \frac{\omega}{c}\left(n_0 + \frac{3}{8}\chi^{(3)}u^2\right)\Delta z, \tag{2.70}$$

Where $n_0$the linear refractive index of the material. The term u^2 is related to intensity, and we can rewrite:

$$n = n_0 + \frac{3}{4\varepsilon_0 n_0^2 c}\chi^{(3)}I = n_0 + n_2 I, \tag{2.71}$$

where

$$n_2^I = \frac{3}{4\varepsilon_0 n_0^2 c}\chi^{(3)}. \tag{2.72}$$

The dependence of the refractive index with the intensity is known as the Kerr effect or the quadratic electro-optical effect.

2.5.1 Nonlinear absorption

As the linear absorption depends on the imaginary part of the first-order susceptibility, the nonlinear absorption (in this case of two photons) depends on the imaginary part of the third-order susceptibility. This effect was theoretically predicted by Marie Goppert-Mayer, in 1931 (GOEPPERT-MAYER, 1931 (2009)) and demonstrated experimentally for the first time in 1961 (KAISER and GARRETT, 1961). Now, to fully describe the nonlinear coefficients associated with $\chi^{(3)}$ we must also consider the imaginary part of the third-order susceptibility.

Thus, the total susceptibility is $\chi^{(3)} = \Re e\left[\chi^{(3)}\right] + Im\left[\chi^{(3)}\right]$, then equation (2.67) can be rewritten as:

$$\frac{du}{dz} + iu\frac{d\phi}{dz} = i\frac{3\omega}{8nc}\Re e\left[\chi^{(3)}\right]u^3 - i\frac{3\omega}{8nc}Im\left[\chi^{(3)}\right]u^3, \tag{2.73}$$

Thus, we realize that the term du/dz is nonzero, and we may split the equation (2.73) as follows:

$$\frac{du}{dz} = -\frac{3\omega}{8nc}Im\left[\chi^{(3)}\right]u^3, \tag{2.74a}$$

$$\frac{d\phi}{dz} = -\frac{3\omega}{8nc}\Re e\left[\chi^{(3)}\right]u^2, \tag{2.74b}$$

The equation (2.74a) shows the dependence of nonlinear absorption with intensity. Considering that

$$I = \frac{\varepsilon_0 nc}{2}u^2, \tag{2.75}$$

we obtain that the rate at which the intensity changes with propagation, z is:

$$\frac{dI}{dz} = \varepsilon_0 nc\, u\frac{du}{dz} = -\frac{3\omega}{8c}\left[\varepsilon_0 c\frac{4}{n^2\varepsilon_0^2 c^2}I^2\right]Im\left[\chi^{(3)}\right] = -\frac{3\omega}{2n^2\varepsilon_0 c^2}I^2 Im\left[\chi^{(3)}\right] \tag{2.76}$$

Then, introducing $\beta = \left(\frac{3\omega}{2n^2\varepsilon_0 c^2}\right)Im\left[\chi^{(3)}\right]$ and adding the term due to the linear absorption we get:

$$\frac{dI}{dz} = -\alpha I - \beta I^2. \tag{2.77}$$

where α is the linear absorption coefficient, and β is the two-photon absorption coefficient.

Figure 4 shows the diagram of levels for illustration of the absorption of two photons (2PA). In this process, the material absorbs a pair of photons, whose sum of the energy of the two photons is equal to the transition energy between the fundamental and exciting levels of the material.

Figure 4 - Level diagram for nonlinear absorption of the two-photon absorption type.

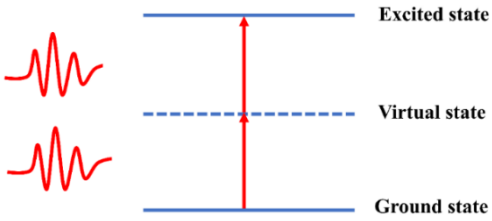

Source: The author (2021).

2.5.2 Saturated Absorption

Saturated absorption occurs when the light intensity is considerably high. In this case, the electrons of the fundamental state of the sample are excited to a higher level at such a large rate, that the population of the excited state becomes equal to that of the fundamental state. Therefore, even increasing the laser intensity there will be no increase in the number of photons absorbed.

The expression describing the saturated absorption coefficient in a homogeneously enlarged medium is given by:

$$\alpha = \frac{\alpha_0}{1+I/I_S}. \tag{2.78}$$

where α_0 is the absorption coefficient for low intensities, I is the intensity of the laser, and I_s is the saturation intensity.

2.6 STIMULATED EMISSION AND RANDOM LASERS

The energy transition between two states can be associated with the absorption or emission of a photon that has the same energy as the gap between these two states. When the difference of energy between the two states is $E_2 - E_1$, the relation between this difference and the frequency of the photon is:

$$E_2 - E_1 = h\nu \tag{2.79}$$

where h is Planck's constant and ν is the photon frequency. If a system is in thermal equilibrium, the states of low energy have a larger population when compared to higher energy states. However, it is possible to invert the population in such a way that the high energy state may have a larger population. Then, the presence of a photon of energy satisfying (2.79) may stimulate the emission of another photon with the same energy.

To understand the process of stimulated emission considers the following background. When an electromagnetic wave is in a cavity (isothermally closed) in thermal equilibrium the density radiation distribution, can be described by the equation:

$$u(\nu)d\nu = \frac{8\pi h\nu^3}{c^3}\frac{1}{(e^{h\nu/k_BT}-1)} \tag{2.80}$$

where $u(\nu)d\nu$ is the radiation density, k_B is the Boltzmann's constant, h is the Planck's constant, c is the speed of light and T is the temperature of the cavity. We can define a parameter from the equation (2.80), known as radiation modes density by unity volume and by unity frequency interval, $p_n = 8\pi\nu^2/c^3$. Another manner that we can refer to this parameter is the number of degrees of freedom by unity of volume and by unity of frequency interval.

From statistical mechanics, we can write an expression for a two-level system with a large number of similar atoms in thermal equilibrium as:

$$\frac{N_2}{N_1} = \frac{g_2}{g_1} exp\left(-\frac{(E_2-E_1)}{k_BT}\right) \tag{2.81}$$

The expression (2.81) is known as Boltzmann's ratio; g_1 and g_2 are degenerescences of the two-level system:

Figure 5 – Two energy levels with population N_1 and N_2 and degeneracies $g_1$and g_2.

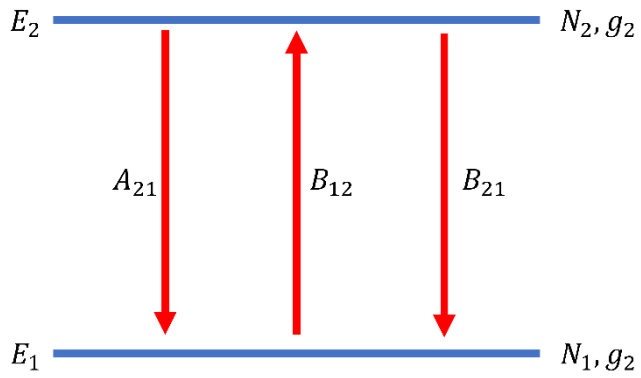

Source: The author (2021).

The populations N_1 and N_2 satisfy $N = N_1 + N_2$, the total number of atoms of the system. The arrows in Figure 5 describe three different processes that can occur due to the interaction radiation-matter. The first process is Absorption: this effect can occur if an electromagnetic wave of frequency ν_{12} interact with an atomic system, then, the population of lower energy level is depleted to a higher energy level, the rate of this transitions is:

$$\frac{\partial N_1}{\partial t} = -B_{12}u(\nu)N_1 \tag{2.82}$$

in the equation (2.82), B_{12} is a constant and $B_{12}u(\nu)$ is the probability to occur the transition by unity frequency.

The second process is known as Spontaneous Emission; this effect occurs after the atomic system absorbs the electromagnetic radiation, transit for a high energy level, and decays for a lower energy level. This process is spontaneous and does not depends on externals stimulus. The rate of this transition is described by:

$$\frac{\partial N_2}{\partial t} = -A_{21}N_2 \tag{2.83}$$

where the term A_{21} is a coefficient that describes the transition probability between the high energy level and the lower energy level. The solution of the equation (2.83) is:

$$N_2(t) = N_2(0)\exp(-t/\tau_{21}) \tag{2.84}$$

where τ_{21} is the spontaneous emission lifetime.

The last process is Stimulated Emission; unlike spontaneous emission, the stimulated emission occurs when an electromagnetic wave interacts with an atomic system and stimulates the system to decay from the higher energy state to a lower energy state; the difference of energy between the two states is emitted as light. The transition rate between the two levels is:

$$\frac{\partial N_2}{\partial t} = -B_{21}u(\nu_{21})N_2, \tag{2.85}$$

In this case, the radiation emitted by the system consists of two parts, (i) when the intensity is proportional to A_{21}, we have the spontaneous emission, (ii) when the intensity is proportional to $u(\nu_{21})B_{21}$, we have the stimulated emission. When occur the laser emission, we have the contributions of these two parts, the part (ii) is useful for the laser action; the photon emitted is in phase with the external field; part (ii) introduce a loss in the process, emitting photons out of phase with the external pump radiation.

We can combine the equations (2.83), (2.84), and (2.85) to express the change in the populations in the levels of our system. Using $N = N_1 + N_2$, we can write:

$$\frac{\partial N_1}{\partial t} = -\frac{\partial N_2}{\partial t} = B_{21}u(\nu)N_2 - B_{12}u(\nu)N_1 + A_{21}N_2\ . \tag{2.86}$$

For a system in the stationary state $\frac{\partial N_1}{\partial t} = \frac{\partial N_2}{\partial t} = 0$. Then, we can write:

$$B_{12}u(\nu)N_1 = A_{21}N_2 + N_2B_{21}u(\nu) \tag{2.87}$$

and using the Boltzmann equation (equation (2.81)) we can write:

$$u(\nu) = \frac{(A_{21}/B_{21})}{(B_{12}/B_{21})(g_1/g_2)(\exp{(h\nu/k_BT)}-1)} \tag{2.88}$$

the terms A_{21}, B_{12} and B_{21} are known as Einstein coefficients and the relation between them is:

$$\frac{A_{21}}{B_{21}} = \frac{8\pi h\nu^3}{c^3} \tag{2.89}$$

and

$$B_{21} = g_1 B_{21}/g_2. \tag{2.90}$$

If we consider a nondegenerate system, the equation (2.90) to $B_{21} = B_{12}$ and consequently, the probabilities for absorption and stimulated emission are equal.

As mentioned above an essential condition for LASER emission is the population inversion among the two levels involved in the process; in the equation (2.81) valid for a collection of atoms in thermal equilibrium there are always more atoms in lower energy level than the in higher energy level. In this way the difference $N_1 - N_2$ is always positive, which makes positive the absorption coefficient, and therefore the incident radiation is absorbed.

Figure 6 – a) Relative population in a two-level system in thermal equilibrium and b) population inversion for a laser system.

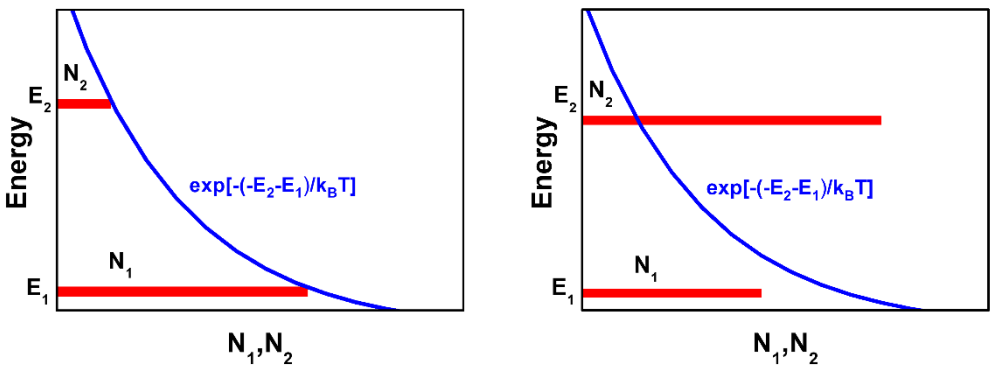

Source: The author (2021).

Figure 6 shows in red the population N_1 and N_2 in a two-level system and the blue represents the plot of the equation (2.81). In Figure 6 (a) we have the normal distribution for a system in thermal equilibrium. In Figure 6 (b) we have the case of population inversion; that is, the number of atoms in the lower energy level is smaller than the number of atoms in the high energy level; this is the necessary condition for laser emission.

In solid-state lasers, the atomic system (ions or molecules) is hosted inside a crystal or glass. For example, the first laser demonstrated was based on a ruby crystal (Al_2O_3 crystals doped with Cr^{3+} ions), as the gain medium (MAIMAN, 1960). But lasers system is not composed only by the gain medium; to operate a laser we need a cavity; the cavity is composed of two main parts, one is a gain media and the other is the optical resonator, is composed of two mirrors, one 100% reflector and other partially reflector. When the material is excited by an external source, the electrons of the gain media decay by stimulated emission emitting photons. The photons travel inside the cavity between the two mirrors. A certain number of the emitted photons are reflected by the mirrors and return to the gain medium, stimulating more electrons to decay and emit more photons. The emission of the photons is highly directional (photons *travel* in phase) along the axis of the cavity, and collimated (the beam divergence is small).

In addition to conventional lasers, there is another type of lasers, know as Random Lasers (RL's) that does not need a conventional optical cavity. Different from several other optical applications, where is not desirable materials that may produce scattering, RL's operate with basis on scattering materials. Proposed theoretically by Letokhov in 1968, the idea of generation of light using scatters particles is based in the diffusion of light when mean the free path of the photon inside the gain medium is smaller than the system (LETOKHOV, 1968).

Figure 7 – a) conventional versus b) random lasing. Whereas a conventional laser is usually composed of a two-mirror cavity that defines the optical modes, a random laser (panel b) exploits the confinement by multiple scattering to enhance the probability of stimulated emission.

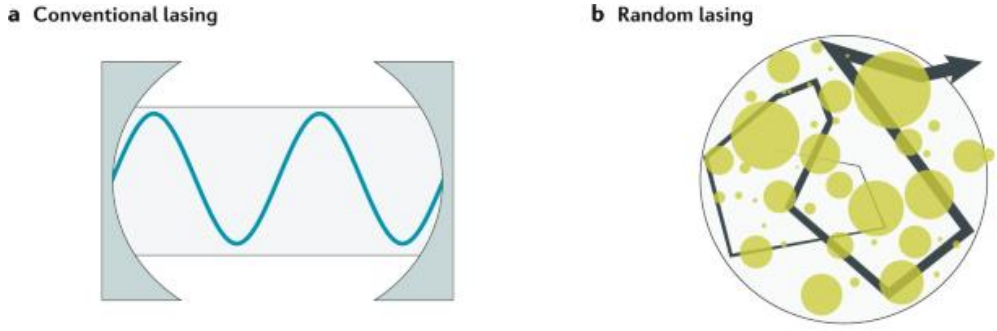

Source: Sapienza (2019).

The amplification of light by a scattering medium was shown for the first time experimentally at the end of the 1980s (MARKUSHEV, et al, 1986). The first material used to generate RL was a powder consisting of particles doped with Nd ions. After that, various other systems were exploited, as dyes (LAWANDY et al, 1994) and semiconductors powders (CAO et al, 1989). The RL's emission is described by analogy of conventional Lasers, with the difference that no mirrors are forming a cavity. Instead of a cavity, in the case of RL's the gain

medium scatter the light providing the necessary feedback to favor the stimulated emission. Successive scattering events of light among the particles act on as large number of “cavities” with different lengths that originate a large number of optical modes. When some of these modes have amplitude larger than the losses a laser threshold occurs and light is emitted in various directions. Then, it is observed spectral narrowing of the emitted light and nonlinear behavior of the emitted light amplitude versus the excitation intensity.

In the past seven years, beyond of the demonstration of RLs action in several types of materials, the intensity fluctuations of RLs were investigated from the point of view of Statistical Physics. Those studies allowed the characterization of photonic phase transitions by analogy with phenomena in magnetic materials (LIMA, 2019). These studies will be discussed in Chapter 4. Applications of RL’s take advantage of the speckle-free behavior for applications in imaging systems (BOSCHETTI et al, 2019).

3 NONLINEAR OPTICAL CHARACTERIZATION TECHNIQUES

To characterize the photonic nanomaterials, we use techniques widespread in the literature. This chapter, it is described the theoretical and experimental details of these techniques.

3.1 RANDOM LASER CHARACTERIZATION

Random Laser characterization was performed using the standard method. Rhodamine 6G (Rh6G) was employed as the gain medium and $ZrTe_2$ was used as the scatterer medium in both bulk and 2D form. The sample was excited at an angle of 45° and the signal was collected to 45º of the excitation beam.

Figure 8 – Experimental setup for RL characterization.

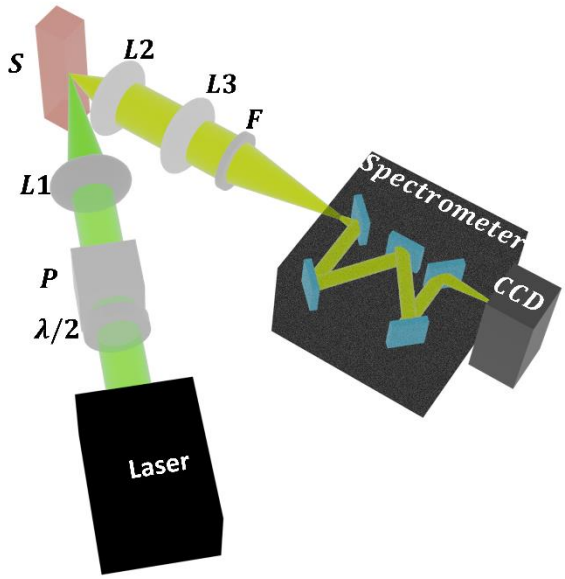

Source: The author (2021).

Figure 8 shows the experimental setup for RL characterization. The laser source employed was the second harmonic of an Nd: YAG Optical Parametric Oscillator (OPO) laser (532 nm, 5 ns, 5 Hz). A half-wave plate ($\lambda/2$) and a polarizer (P) are used for intensity control, a 15 cm focus lens ($L1$) is used to focus the laser radiation in the sample (S). A set of lens ($L2$) and ($L3$) is employed to collect the RL emission, a filter (F) is used to cut the excitation, CCD coupled to a spectrometer is used to collect the spectra.

3.1.1 Replica Symmetry Breaking (RSB)

Magnetic systems known as Spin Glass (SG) may, at low-temperature present disorder and frustration. The SG theory was introduced by Parisi and co-workers to solve the problem of spins in a magnetic system (MEZARD et al, 1987). An analogous effect occurs in RL's. The analogs of the spins in an RL system are the optical modes and the Excitation Pulse Energy (EPE) is the analog of the inverse of temperature (MOURA et al, 2020).

Below the RL threshold, the optical modes are uncorrelated, corresponding to what is called photonic paramagnetic phase. Around and closely above the threshold, the system presents a transition from a photonic paramagnetic phase to SG phase, and the optical modes become correlated.

The RSB implies that if identical systems are prepared with the same initial conditions the system may evolve to different states and this behavior is related to frustration in the presence of disorder. To verify this analogy, GHOFRANIHA *et.al*, 2015 considered a parameter that has an analogy with the Parisi order parameter, performing correlations between the intensity fluctuations from RL output spectra obtained under the same initial conditions.

$$q_{\gamma\beta} = \frac{\sum_k \Delta_\gamma(k)\Delta_\beta(k)}{\sqrt{\left[\sum_k \Delta_\gamma^2(k)\right]\left[\sum_k \Delta_\beta^2(k)\right]}}, \tag{3.1}$$

where $\gamma, \beta = 1,2,\dots,N_s$. The average intensity at the mode wavelength indexed by k reads $\bar{I}(k) = \sum_{\gamma=1}^{N_s} I_\gamma(k)/N_s$, and the intensity fluctuation is measured by $\Delta_\gamma(k) = I_\gamma(k) - \bar{I}(k)$.

3.2 HYPER RAYLEIGH SCATTERING (HRS)

The SHG effect was discussed in Chapter 2 in terms of a more common effect, the coherent SHG. In this case, for bulk materials, it is needed that the phase-matching condition be respected. For incoherent SHG (I-SHG), the phase-matching effect is not required, and the coherence length is considerably smaller than the wavelength (BRASSELET and ZYSS, 2010). The I-SHG in liquids occurs due to local fluctuations and was observed for the first time in 1965 and a brief theory about second-order parametric scattering was demonstrated (TERHUNE et al, 1965). To understand this behavior we express the changes of the polarization as:

$$\mu_i = \mu_P + \alpha_{ij}E_j + \beta_{ijk}E_jE_k, \tag{3.2}$$

where μ_i is the dipole moment induced in the solution, μ_P the permanent dipole moment, E_i is the component of the electrical field at the i direction, α_{ij} and β_{ijk} is the linear polarizability and the first-order hyperpolarizability, respectively. Note that the terms α_{ij} and β_{ijk} of equation (3.2) are the microscopic parameters that correspond to χ_{ij} and χ_{ijk}, that are the susceptibilities related to bulk materials.

For isotropic solutions, the time and spatial averages are null, and consequently, the average of the first-order hyperpolarizability is zero. However, if we made some considerations, only the average of the first-order hyperpolarizability is null and the variances are equal to second moments. The considerations are:

1 – There is no coupling between the neighboring volume elements;

2 – The rotational motion of the dissolved molecules is considerably slow when compared with the electromagnetic field at optical frequencies;

3 - The rotational motion of the dissolved molecules is considerably slow when compared with the envelope of the electromagnetic field at optical frequencies.

Therefore, the first-order hyperpolarizability is proportional to the number of molecules N and the product $\langle \beta_{uvw}\beta_{xyz}\rangle_{av}$; for an isotropic media, the transformation of the molecular axis, uvw is performed by averaging the products of the cosines directions over all directions (CYVIN, et al, 1965).

3.2.1 Orientational average of the dipole's moment

From a set with *N* scatters centers, the intensity of the generated harmonic is described by (ANDREWS et al, 1995):

$$I(2\omega) = D^{(2)}\left|\sum_{i=1}^{N}\beta_i{:}\,\boldsymbol{e}_{2\omega}\boldsymbol{e}_{\omega}\boldsymbol{e}_{\omega}\right|^2 I^2(\omega), \tag{3.3}$$

where $D^{(2)}$ is a factor that takes into account wavevector, light velocity, and electrical permittivity, β_i is the first-order hyperpolarizability of the i scatter, $\boldsymbol{e}_{2\omega}$ and $\boldsymbol{e}_{\omega}$ are polarizations versors in the direction of the harmonic scatter and in the field input, respectively.

If we consider a set of *N* non-interacting particles randomly distributed in the space, each particle is considered a scattering center.

Figure 9 – A set of *N* scatters randomly oriented. The red arrows indicated the dipole orientation.

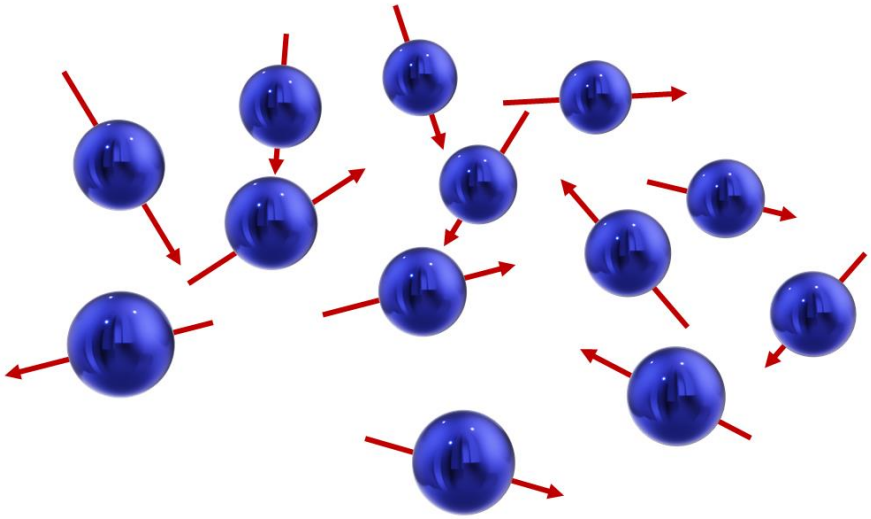

Source: The author (2021).

The intensity of the scatter harmonic is described by the equation (3.4) and writing how an average about all dipoles, we have:

$$I(2\omega) = D^{(2)} N \langle |\beta_i : \boldsymbol{e}_{2\omega} \boldsymbol{e}_{\omega} \boldsymbol{e}_{\omega}|^2 \rangle I^2(\omega), \tag{3.4}$$

where N is the number of molecules, $\boldsymbol{e}_{\omega}$ and $\boldsymbol{e}_{2\omega}$ are the versors of the input beam, and the generated harmonic. Solving the tensorial product between $\boldsymbol{e}_{2\omega}$ and $\boldsymbol{e}_{\omega}$ and the polarization versors of the frequencies ω and 2ω depend on the orientation of each molecule.

The equation (3.4) describes the scattering process in all directions. Considering a degenerate beam (where two beams with the same frequency are used to excite the sample), and z how the propagation direction, we can simplify this equation for a two-dimensional coordinate system (CYVIN, et al, 1965).

$$I(2\omega) = D^{(2)} N \langle {\beta_{izz}}^2 \rangle I^2(\omega), \tag{3.5}$$

where i is x *or* y. Writing β_{izz} in terms of components, we have

$$\langle {\beta_{xzz}}^2 \rangle = \frac{1}{7}\sum_i {\beta_{iii}}^2 + \frac{6}{35}\sum_{i\neq j} \beta_{iii}\beta_{ijj} + \frac{9}{35}\sum_{i\neq j} {\beta_{iij}}^2 + \frac{6}{35}\sum_{ijk,ciclic} \beta_{iij}\beta_{jkk} + \frac{12}{35}\sum_{i\neq j} {\beta_{ijk}}^2 , \tag{3.6a}$$

for x, and

$$\langle {\beta_{yzz}}^2 \rangle = \frac{1}{35}\sum_i {\beta_{iii}}^2 - \frac{2}{105}\sum_{i\neq j} \beta_{iii}\beta_{ijj} +$$

$$+ \frac{11}{105}\sum_{i\neq j} {\beta_{iij}}^2 - \frac{2}{105}\sum_{ijk,ciclic} \beta_{iij}\beta_{jkk} + \frac{8}{35}\sum_{i\neq j} {\beta_{ijk}}^2 . \tag{3.6b}$$

for y-direction.

When Kleisman's symmetry is satisfied, the permutation between the indices is null, leading to 10 different components. The polarization treatment is shown in the next section.

Generally, anyone technique to separate the components is used, and the average value for the hyperpolarizability is the sum of both contributions:

$$I(2\omega) = GN(\langle\beta_{XZZ}^2 + \beta_{YZZ}^2\rangle)I^2(\omega). \quad (3.7)$$

in the scope of the work, both cases are employed. HRS polarization-resolved measurements are made to understand the origin of nonlinearity in two samples. The description of polarization dependence is made in section 3.2.2.

3.2.2 Polarization dependence

The HRS technique can be used to identify the origin of nonlinearity. This is made by studying the polarization of the optical field associated with the HRS signal as a function of the polarization of the incident optical field. Figure 10 shows the geometry and polarization of the optical fields at ω and 2ω

Figure 10 – Vector electrical field $\vec{E}(\omega)$ in the *x* and *y*-axis and the transformation in your correspondents *X* and *Y* in $\vec{E}(2\omega)$.

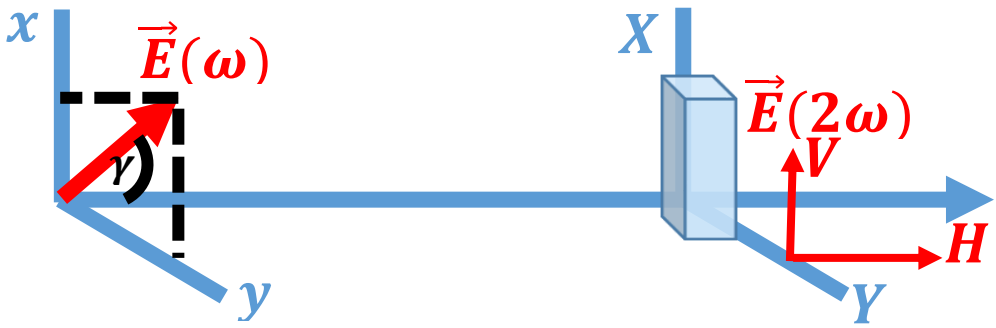

Source: The author (2021).

If we consider an input electrical field $\vec{E}(\omega)$ with components *x* and *y*, in the form:

$$\vec{E}(\omega) = \hat{x}Ecos(\gamma) + \hat{y}Esin(\gamma), \quad (3.8)$$

the electrical field at 2ω is proportional to $\vec{\beta}:\vec{E}(\omega)\vec{E}(\omega)$, where $\vec{\beta}$ is the first-order hyperpolarizability tensor.

Writing the HRS electrical field in terms of the components, we have:

$$E_X(2\omega) \propto \beta_{xxx}E_x(\omega)E_x(\omega) + \beta_{xxy}E_x(\omega)E_y(\omega) + \beta_{xyx}E_y(\omega)E_x(\omega) + \\ +\beta_{xyy}E_y(\omega)E_y(\omega), \quad (3.9a)$$

for the *x*-component, and

$$E_Z(2\omega) \propto \beta_{zxx}E_x(\omega)E_x(\omega) + \beta_{zxy}E_x(\omega)E_y(\omega) + \beta_{zyx}E_y(\omega)E_x(\omega) + \\ +\beta_{zyy}E_y(\omega)E_y(\omega). \quad (3.9b)$$

for the *y*-component.

Re-writing the equations 3.9a) and 3.9b), we have

$$E_X(2\omega) \propto E^2\{\beta_{xxx}cos^2(\gamma) + (\beta_{xxy}+\beta_{xyx})\cos(\gamma)\cdot\sin(\gamma) + \beta_{xyy}\, sin^2(\gamma)\}, \quad (3.10a)$$

$$E_Z(2\omega) \propto E^2\{\beta_{zxx}cos^2(\gamma) + (\beta_{zxy}+\beta_{zyx})\cos(\gamma)\cdot\sin(\gamma) + \beta_{zyy}\, sin^2(\gamma)\}, \quad (3.10b)$$

now, writing in terms of the intensity at 2ω, we have:

$$I_{SH}(2\omega) = E_x(2\omega)E_x^*(2\omega) + E_z(2\omega)E_z^*(2\omega). \quad (3.11)$$

Where $E_X^*(2\omega)$ and $E_Z^*(2\omega)$ are the conjugated complex of the electrical field in the *x* and *z* directions. For figure 10 we see that the detection of the polarization is made in the *x* component and therefore we now work with only this component:

$$I_{SH}^X(2\omega) = \{\beta_{xxx}cos^2(\gamma) + (\beta_{xxy}+\beta_{xyx})\cos(\gamma)\cdot\sin(\gamma) + \beta_{xyy}\, sin^2(\gamma)\} \times \{c.c\}. \quad (3.12)$$

Writing all the components and applying the permutation symmetry $\left(\chi_{xyz}^{(2)}(\omega_m + \omega_n, \omega_m, \omega_n)E_Y(\omega_m)E_Z(\omega_n)\right) = \left(\chi_{xyz}^{(2)}(\omega_n + \omega_m, \omega_m, \omega_n)E_z(\omega_n)E_y(\omega_m)\right)$, we have the following equation:

$$I_{SH}^X(2\omega) = |\beta_{xxx}|^2cos^4\gamma + (2\beta_{xyx}^*\beta_{xxx})cos^3\gamma sin\gamma + 2\beta_{xyx}\beta_{xxx}^*cos^3\gamma sin\gamma \cdot \\ (\beta_{xxx}\beta_{xyx}^* + 4\beta_{xyx}\beta_{xyx}^*)cos^2\gamma sin^2\gamma + \beta_{xyy}2\beta_{xyx}^*cos\gamma sin^3\gamma + \beta_{xyy}\beta_{xxx}^*cos^2\gamma sin^2\gamma + \\ |\beta_{xyy}|^2 sin^4\gamma + (2\beta_{xxy}\beta_{xxx}^*)\ \ cos\gamma sin^3\gamma, \quad (3.13)$$

defining the components of β of $a, b, c, d\ and\ e$, we have

$$I_{SH}^X(2\omega) = a\cdot cos^4\gamma + b\cdot sin^2\gamma\cdot cos^2\gamma + c\cdot sin^4\gamma + d\cdot cos^3\gamma\cdot sin\gamma + \\ +d\cdot sin^3\gamma\cdot cos\gamma, \quad (3.14)$$

and now, identifying the components

$$a = \beta_{xxx}^2, \tag{3.15a}$$

$$b = 2\beta_{xxx}\beta_{xyy} + 4\beta_{xyx}^2, \tag{3.15b}$$

$$c = \beta_{xyy}^2, \tag{3.15c}$$

$$d = \beta_{xxx}\beta_{xyx}, \tag{3.15d}$$

$$e = 4\beta_{xyy}\beta_{xyx}, \tag{3.15e}$$

If we perform a plot of the equation (3.15a)-e)) we can identify the components and the direction of oscillating dipoles, the quadrupole component, and the deviation associated to electromagnetic field retardation (NAPPA et al, 2005).

Figure 11 – Plot of the equation 3.15.

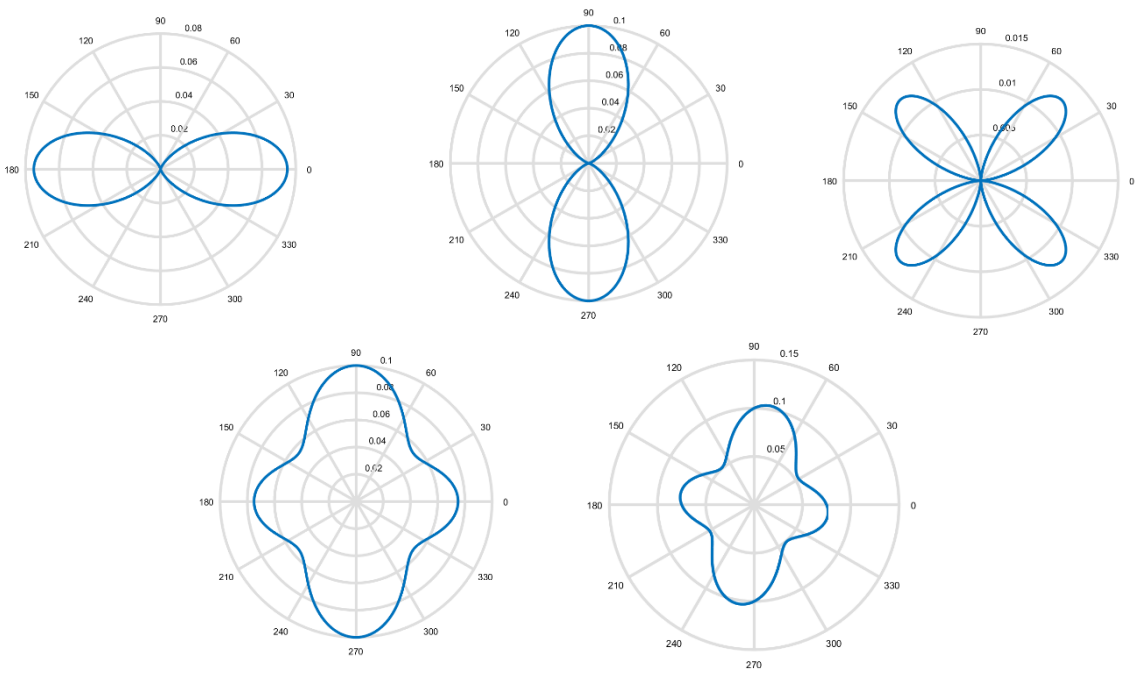

Source: The author (2021).

Figures 11a) and 11 b) represented the contribution of the terms *a* and *c*, respectively, and are attributed to dipole oscillation in perpendicular directions. Figure 11c) shown the contribution of quadrupole oscillation and is associated with term *b* in equation 3.15. The terms *d* and *e* has shown the retardation components in the intensity of the generated harmonics. To generate the Figures 11 a)-e) are used arbitrary parameters.

3.2.3 Hyper Rayleigh Scattering Technique

For characterization of the first hyperpolarizability, several techniques were developed (NALWA and MIYATA, 1996). For example, Electrical Field Induced Second Harmonic (EFISH) is a useful technique to characterize the first-order hyperpolarizability and is still used today. The problem of the EFISH technique is because it is necessary to know the second-order hyperpolarizability, γ_{ijkl}, to determine the first-order hyperpolarizability.

The Hyper–Rayleigh Scattering (HRS) technique was applied for the first time in 1977 (SCHIMID and SCHRÖTTER, 1977) and used for optimizing the detection of Hyper-Raman Scattering. The use of the HRS technique for the determination of nonlinear optical parameters occurred only in 1991 (CLAYS and PERSOONS, 1991) and a detailed description of the equations and experimental setup was made by CLAYS and PERSOONS, 1992.

In the present work, the technique was applied to study nanoparticles in a liquid suspension.

The total intensity of the SHS is:

$$I(2\omega) = g \sum_s N_s \langle \beta_s^2 \rangle I_0^2, \tag{3.16}$$

where g depends on the geometry of the scattering and contains the averages of the products of the direction cosines and the local field corrections at optical frequencies, N_s is the number of molecules $\langle ... \rangle$ indicates orientational averages of the molecules or nanoparticles in the liquid suspension, and I_0 is the input intensity.

For a dilute liquid system, we need to consider the contributions of the solvent and the contributions of the solute. Writing the equation (3.16) in terms of the collected signal, $S(2\omega)$.

$$S(2\omega) = GB^2 I_0^2 = G \sum_s N_s \langle \beta_s^2 \rangle I_0^2. \tag{3.17}$$

Where G includes the light collection efficiency and local field correction factors. Considering only one solute we may write $B^2 = N_{solvent}\langle \beta_{solvent}^2 \rangle + N_{solute}\langle \beta_{solute}^2 \rangle$. Therefore, if we know $\langle \beta_{solvent}^2 \rangle, N_{solvent}$ and N_{solute} we can calculate the value of $\langle \beta_{solute}^2 \rangle$.

The HRS technique has been particularly–useful for the determination of first-order hyperpolarizability of molecules and nanoparticles, but also for detection/identification of chemical species (DAS, 2006; SEGETS, et al, 2009).

3.2.4 The external reference method

In this work, we are interested in the determination of the first-order hyperpolarizability and for this proposal, it was used a method known as the external reference method. This method consists of using a reference sample with known hyperpolarizability to compare with the sample being investigated (SEGETS, et al, 2009). The intensity of a pair of solutions, or suspensions of samples measured here is.

$$I(2\omega) = K(N_{sol}\langle\beta_{sol}^2\rangle + N_{mol}\langle\beta_{mol}^2\rangle)I^2(\omega), \tag{3.18}$$

where K is a constant that contains information about the scattering geometry,

If the values of $\langle\beta_{solv}\rangle$ and $\langle\beta_{ref}\rangle$ are known, we can combine two of the equations (3.18) and find the hyperpolarizability of the molecule. The equation for two systems solvent-solute is.

$$\langle\beta^2(2\omega)\rangle = \frac{I_s(2\omega)}{I_{ref}(2\omega)}\left\{\frac{N_{ref}\langle\beta_{ref}^2\rangle + N_{solv-ref}\langle\beta_{solv-ref}^2\rangle}{N}\right\} - \frac{N_{solv}\langle\beta_{solv}^2\rangle}{N}. \tag{3.19}$$

where N is the sample's concentration, *ref* and *solv-ref* are related to the reference material and the solvent used in the dilution of the reference material, respectively.

This case match with molecules and nanomaterials where the refractive index of the species is close to the solvent. When this is not happening, we need to consider local field corrections. Taking a set of measurements as a function of the concentration of the reference sample and the samples of the materials, we have.

$$\begin{cases} \alpha_{ref} = KF_{ref}\beta_{ref}, \\ \alpha_{sample} = KT_{sample}\beta_{sample.} \end{cases} \tag{3.20}$$

where $F_{ref} = \left(\frac{3}{2+n_{ref}(\omega)}\right)^6$ is the Lorentz field factor correction of the reference sample and $T_{sample} = \left(\frac{3}{2+n_{sample}(\omega)}\right)^4\left(\frac{3}{2+n_{sample}(2\omega)}\right)^2$ is the internal field correction of the sample. By the combination of the two equations in (3.20) we have.

$$\langle\beta_{sample}\rangle = \sqrt{\frac{\alpha_{sample}}{\alpha_{ref}}\frac{F_{ref}}{T_{sample}}}\langle\beta_{ref}\rangle, \tag{3.21}$$

this equation is very useful for the evaluation of hyperpolarizability of nanocrystals, see for example (JOULAUD et al, 2013).

Figure 12 shows the experimental setup for the HRS technique used for the characterization of the samples in this work.

Figure 12 - Experimental setup used for the hyper-Rayleigh experiments. In the figure P is the Polarizer, BS is the Beam Splitter, RP is the Reference Photodetector, L1 is the focused lens, L2 and L3 are the collection lens, F2 is an interference filter, the AP is Analyzer Polarizer and PMT is the Photomultiplier Tube.

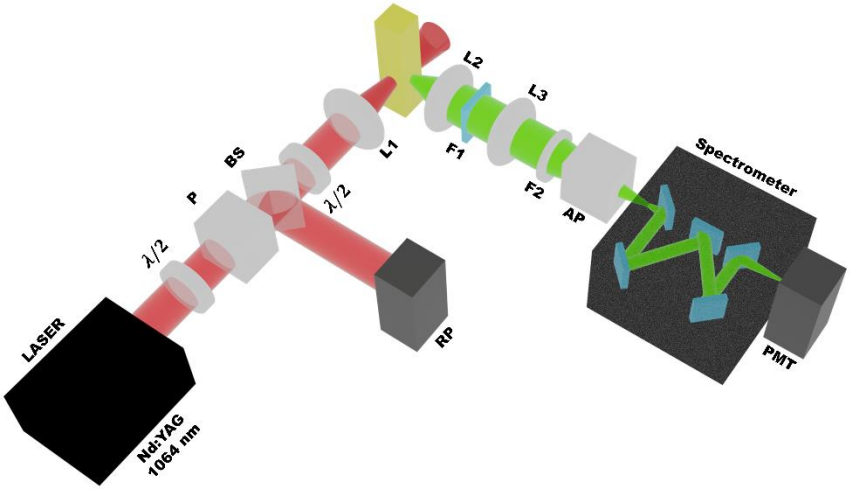

Source: The author (2021).

A bandpass filter (Filter 1) was used to avoid scattered light from the fundamental beam. A half-wave plate ($\lambda/2$), a polarizer, a beam splitter, and an infrared detector were employed to control the incident laser intensity on the sample. A 5 cm focal lens was used to focus the laser beam on the sample that was contained in a 1 cm long quartz cuvette. The HRS signal was collected perpendicularly to the laser beam direction by using two lenses (focal length: 5 cm) to focus the HRS signal in the photomultiplier (detector 2). Filter 2 was an interference filter centered at 532 nm with full width at half maximum (FWHM) of 8 nm. The photomultiplier was connected to an oscilloscope and a computer for data collection. For temporal analysis of the HRS signal, a fast photodetector (response time: 1 ns) was used. Para-nitroaniline (*p*-NA) dissolved in methanol was used as reference standard. For the polarization dependence measurements, a half-wave plate and a polarizer were inserted in the HRS experimental setup.

3.3 THE Z - SCAN TECHNIQUE

The Z - Scan technique was implemented by *Sheik-Bahae* and collaborators in 1990 (SHEIK-BAHAE et al, 1990), and has since been used for nonlinear optical characterization of various materials. This technique, based on the phase change of a Gaussian beam when it interacts with a nonlinear medium, can be used to characterize solid materials, liquids, solutions, and even gases (DONG et al, 2016; WANG et al, 2019; SHEIK-BAHAE et al, 1990; DOS SANTOS et al, 2019). This change in the beam phase can cause two interesting effects

called *self-focusing* (SF) and *self-defocusing* (SDF) and occur due to changes in the refractive index of the sample with intensity. These effects can be compared to a convergent or divergent lens, respectively.

Figure 13 – Self-focusing and self-defocusing of a beam when interacting with material.

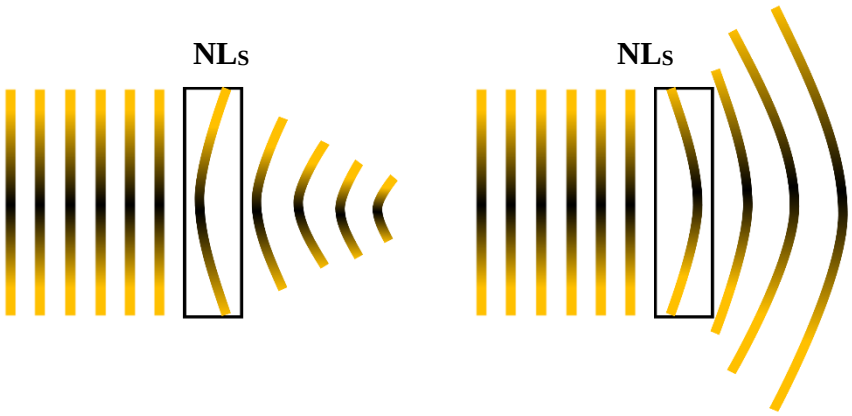

Source: The author (2021).

Figure 13 illustrates schematically the effect of self-focusing and self-defocusing when an optical field interacts with a nonlinear sample (**NL**s). The nonlinear refractive index and the nonlinear absorption coefficient are parameters related to SF and SDF, respectively, and can be measured using the Z-scan technique.

This technique uses a single beam (in some variations, two colors single beams are used (MA, et al, 1991)), and it is a relatively simple and fast technique for nonlinear optical characterization of materials.

Considering a Gaussian beam with amplitude *E*:

$$E(z,r,t) = E_0(t)\frac{w_0}{w(z)}exp\left[-\frac{r^2}{w^2(z)} - i\frac{kr^2}{2R(z)}\right]exp\left[-i\Phi(z,t)\right], \qquad (3.22)$$

In the equation (3.22), w_0 is the beam waist, $w(z) = w_0\sqrt{1+(z^2/z_0^2)}$ is the beam radius in position, z, $z_0 = kw_0^2/2$ is the diffraction length, $k = 2\pi/\lambda$ is the modulus of the wavevector, $E_0(t) = E_0\exp(-t^2/2\tau_0^2)$ the amplitude of the electric field when $z = 0\ e\ r = 0$, τ is the temporal width of the pulse. The last term of equation (3.22) is the dependence of the field phase due to the interaction with the material studied.

Figure 14 – Representation of a Gaussian beam and its parameters.

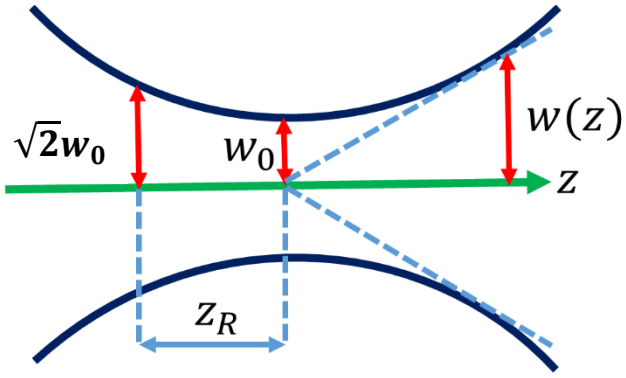

Source: The author (2021).

Figure 14 shows a representation of a Gaussian beam, and z_R is the Rayleigh length of the beam. In this case, both material and incident beam experience changes.

For a beam where the amplitude variation is small over length scales near to wavelength, the Slowing Variation Envelope Approximation (SVEA) can be applied, and the transverses coordinates of the field amplitude due to diffraction can be neglected, and therefore the equations can be separated and write as:

$$I(L) = \frac{I_0 e^{-\alpha L}}{1+\beta I_0 L_{eff}}, \tag{3.23}$$

for amplitude,

$$\Delta\Phi(L) = \frac{k\gamma}{\beta} ln\left[1 + \beta I_0 L_{eff}\right]. \tag{3.24}$$

for the phase variation.

In the equations (3.23) and (3.24) L is the thickness of the sample, α the linear absorption coefficient, and β the two-photon absorption coefficient. The term $L_{eff} = 1 - \exp(-\alpha L/\alpha)$ is the effective length of the sample, I_0 and $I(L)$ are the intensity in the entrance face of the sample and in the exit of the sample, respectively, and $\Delta\Phi(L)$ is the phase variation induced in the beam.

The Z-scan technique works correctly if does not occur diffraction and therefore, it is necessary to apply a thin sample approximation:

i) The thickness of the sample is enough thin, such that $L \ll n_0 z_0$;

ii) The thickness of the sample is enough thin, such that $L \ll n_0 z_0/\Delta\Phi_0$.

The condition i) tells us that the changes in the beam diameter due to the linear diffraction are negligible and the condition ii) that the beam diameter is not affected by the nonlinear diffraction.

The name of the Z-Scan technique is very suggestive to describe the technique: a sample is translated in the Z-axis of a focused Gaussian beam. Then, the intensity in the exit of the sample is different from each value of the propagation, *z*. Therefore, the equations (3.23) and (3.24) can be written as:

$$I_e(z,r,t) = \frac{I_0 e^{-\alpha L}}{1+\beta I_0 L_{eff}}, \tag{3.25}$$

for the intensity, and

$$\Delta\Phi_e(z,r,t) = \frac{k\gamma}{\beta} ln[1 + \beta I_0 L_{eff}]. \tag{3.26}$$

for the phase variation. The subscript e represents these two quantities at the exit of the sample. The beam is subject to variations in r, where beam phase information is stored. These variations are differents for differents positions, *z* and time, *t*.

After propagation, the beam has accumulated nonlinear phases described by:

$$E_e(z,r,t) = E(z,r,t)e^{-\alpha L/2}[1 + q(z,r,t)]^{(j\frac{k\gamma}{\beta}-1/2)}. \tag{3.27}$$

where $q(z,r,t) = \beta I_0 L_{eff}$.

3.3.1 Pure Nonlinear Refraction

In the *"closed aperture"* Z – Scan experiment, a small aperture is placed in front of a photodetector placed at the far-field. Then, the detector is sensitive to phase distortions. The scanning of the sample along the z-axis, starting far from the focus, produces an increase of the intensity on the sample, leading to a self-lensing effect. The signal of this self-lensing (positive/negative) before the focus will tend to broaden/narrow the beam aperture, which results in a decrease/increase of transmittance. For positions after the focus, occurs an intensity decrease, and the result is a reduction of the nonlinear effect.

Therefore, the closed aperture z-scan profile tells us about the signal of the nonlinearity (positive or negative): when the maximum of the transmittance is before the focus and the minimum is after the focus, we have a negative nonlinearity, and vice - versa.

The phase evolution through a sample exhibiting pure nonlinear refraction is described by:

$$\frac{d\Phi(z)}{dz} = \gamma k_0 I(z), \tag{3.28}$$

in the exit surface of the sample, the phase variation is:

$$\Delta\Phi_0(t) = k\Delta n_0(t) L_{eff}. \tag{3.29}$$

$\Delta n_0 = \gamma I$ i.e. a refractive index change that depends on the intensity.

Considering a sample thickness *L,* small enough that there is no big change in the diameter of the beam within the sample, this helps us simplify the problem. During the propagation in the sample, the phase variation will depend on the *z* point where the sample is and the intensity *I*, this can be described by the equation.

$$\Delta\Phi(z,r,t) = \frac{\Delta\Phi_0(t)}{1+z^2/z_0^2} exp\left[-\frac{2r^2}{w^2(z)}\right], \tag{3.30}$$

where $L_{eff} = (1 - e^{-\alpha_0 L})/\alpha_0$, being L the length of the sample and α_0 is the linear absorption coefficient.

The electric field in the exit of the sample contains information's about the phase distortion:

$$E_e(z,r,t) = E(z,r,t)e^{-\alpha L/2}e^{i\Delta\Phi(z,r,t)}. \tag{3.31}$$

Using the Gaussian decomposition method (WEAIRE, et al, 1979) we can propagate the $E_e(z,r,t)$ towards the aperture. This method works performing the decomposition of the complex electrical field in the exit plane in a summation of Gaussian beams through Taylor series expansion of the nonlinear phase term $e^{i\Delta\Phi(z,r,t)}$ in equation (3.30) (SHEIK-BAHAE et al, 1990). The expansion is made around $i\Delta\Phi(z,r,t)$ and is valid only if $|\Delta\Phi(z,r,t)| < 1$.

$$e^{i\Delta\Phi(z,r,t)} = \sum_{m=0}^{\infty} \frac{[i\Delta\Phi(z,t)]^m}{m!} e^{-2mr^2/w^2(z)}, \tag{3.32}$$

the beam is reconstructed in the aperture after the propagation of all beams. To find the transmitted power it needs to integrate into the radius of the aperture.

$$P_T(\Delta\Phi_0(t)) = c\varepsilon_0 n_0 \pi \int_0^{r_a} |E_a(r,t)|^2 r dr. \tag{3.33}$$

Performing temporal integration over the pulse duration we can find an expression for normalized transmittance:

$$T(z) = \frac{\int_{-\infty}^{\infty} P_T(\Delta\Phi_0(t))dt}{S\int_{-\infty}^{\infty} P_i(t)dt} \quad , \tag{3.34}$$

where $P_i(t) = \frac{\pi w_0^2 I_0(t)}{2}$ is the incident instantaneous power in the sample and *S* is the opening of the aperture and have a value of $S = 1 - \exp(-2r_a^2/w_a^2)$.

Figure 15 shows the standard Z-scan profiles for a closed aperture z-scan experiment in the case of positive (figure 15 a)) and negative (figure 15 b)) nonlinearity.

Figure 15 – Z – Scan pattern for a) positive nonlinearity and b) negative nonlinearity.

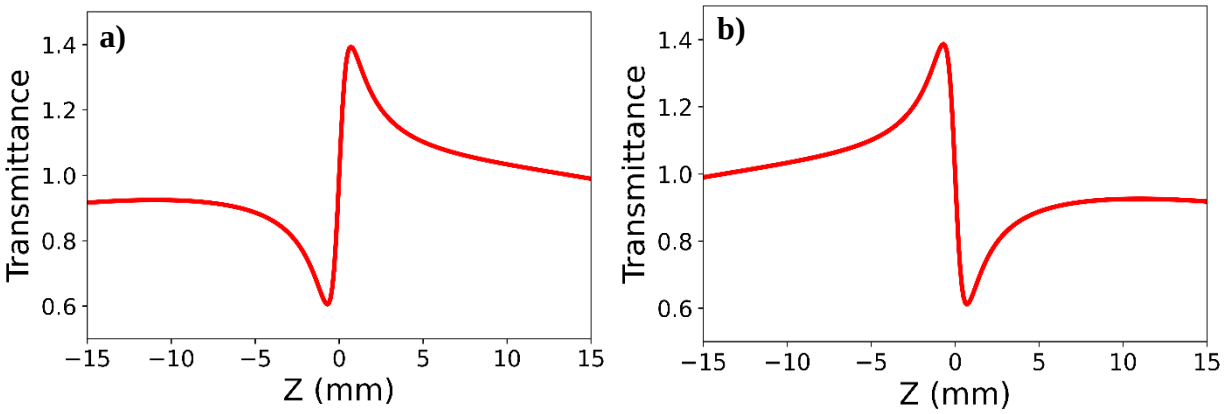

Source: The author (2021).

The distance between the focus and the peak and the focus to the valley is $0.86z_0$ (SHEIK-BAHAE et al, 1990). Therefore, the separation between the peak and the valley is $1.7z_0$.

3.3.2 Pure two-photon absorption (2PA)

From equation (3.24) if all light transmitted by the sample is detected, we lose all information about the phase variations, and consequently about the nonlinear refraction. Manipulating and integrating the equations (3.22) and (3.23), we have an expression for the power transmitted by the sample:

$$P(z,t) = P_0(t)e^{-\alpha L}\frac{\ln[1+q_0(z,t)]}{q_0(z,t)}, \tag{3.35}$$

in equation (3.35) $P_0(t) = I_0(t)\pi w_0^2/2$, $I_0(t)$ is the irradiance in the focus ($z = 0$), $q_0(z,t) = \beta I_0(t)L_{eff}/(1 + z^2/z_0^2)$.

Integrating (3.35) we can find the total energy detected at a distance z:

$$E(z) = \int_{-\infty}^{\infty} I_0(0)e^{-t^2/\tau_0^2}\frac{\pi w_0^2}{2}e^{-\alpha L}\frac{\ln\left[1+q_0(z,0)e^{-t^2/\tau_0^2}\right]}{q_0(z,0)e^{-t^2/\tau_0^2}}dt, \tag{3.36}$$

$$E(z) = \int_{-\infty}^{\infty} \frac{2E_0}{\pi^{3/2}w_0^2\tau_0}e^{-t^2/\tau_0^2}\frac{\pi w_0^2}{2}e^{-\alpha L}\frac{\ln\left[1+q_0(z,0)e^{-t^2/\tau_0^2}\right]}{q_0(z,0)e^{-t^2/\tau_0^2}}dt. \tag{3.37}$$

performing a changing of variables $t/\tau_0 \rightarrow t$, we have:

$$E(z) = E_0e^{-\alpha L}\int_{-\infty}^{\infty}\frac{\ln\left[1+q_0(z,0)e^{-t^2}\right]}{\sqrt{\pi}q_0(z,0)}dt, \tag{3.38}$$

so, the normalized transmittance is given by:

$$T(z) = \frac{1}{\sqrt{\pi}q_0(z,0)}\int_{-\infty}^{\infty}\ln\left[1+q_0(z,0)e^{-t^2}\right]dt. \tag{3.39}$$

A typical curve of an open aperture z-scan experiment is shown in figure 16.

Figure 16 – Z – Scan pattern for open aperture experiment.

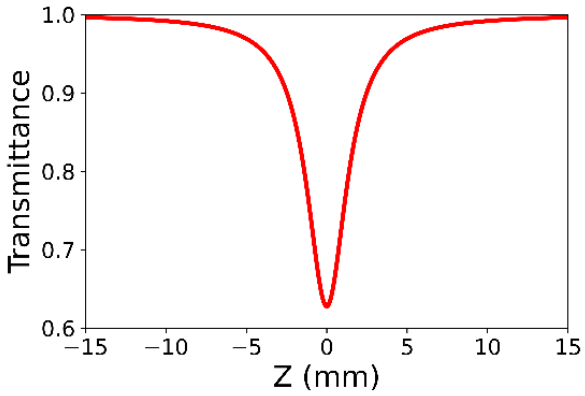

Source: The author (2021).

The name open aperture is because all the light transmitted by the sample is collected.

3.3.3 Simultaneous nonlinear refraction and absorption

When both, nonlinear refraction and absorption are present, the nonlinear phase in the equation (3.24) will be contributing to the Gaussian decomposition in equation (3.27) that relates to the field in the exit face of the sample. The term $[1+q(z,r,t)]^{(i\frac{k\gamma}{\beta}-1/2)}$ will be expanded in Taylor series around $q(z,r,t)$. Therefore, the field in the exit of the sample can be written as:

$$E_e(z,r,t) = E(z,r,t)e^{-\alpha L/2}\sum_{m=0}^{\infty}\frac{q(z,r,t)^m}{m!}\left[\prod_{n=0}\frac{ik\gamma}{\beta}-\frac{1}{2}-n+1\right], \quad (3.40)$$

For small phase variations, the Gaussian decomposition method is a useful tool to find analytical solutions for nonlinear refraction and absorption. However, when the product βIL is higher this method cannot be applied, and numerical solutions are needed. In some conditions, when $q_0(0,0) \leq 1$ and $\beta/2k\gamma \leq 1$ a division of the closed aperture signal by the open aperture signal can be performed, resulting in a pure nonlinear refraction signal.

Figure 17 shows the experimental setup for the Z-Scan measurements. Simultaneous measurements of the NLR and NLA were made, which were normalized to the shot-to-shot fluctuations of the excitation source.

Figure 17 - Z-Scan technique setup for simultaneous closed and open aperture measurements.

.

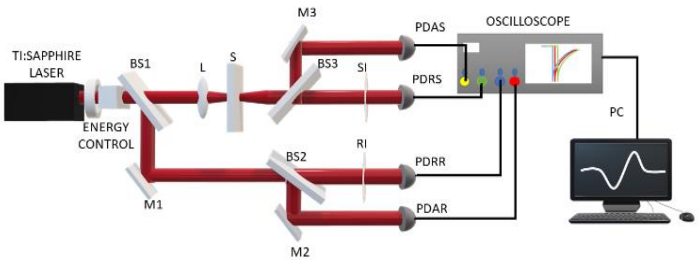

Source: The author (2021).

The laser beam passes through a half-wave plate and a polarizer for pulse energy control. BS1, BS2, and BS3 are beam splitters; M1, M2, and M3 are mirrors; L is the focusing lens; S is the sample; IS and IR are the closed aperture signal and reference irises, respectively; PDAS (PDRS) is the signal photodetector for the NL absorption (NL refraction) channel, while PDAR (PDRR) is its reference photodetector.

The light source was a Ti: Sapphire-based regenerative amplifier (800 nm) operating at 1 kHz and delivering 100 fs single pulses with maximum energy of 1 mJ. The beam was focused with a 15 cm focal length lens onto a 1 mm quartz cuvette. The peak intensity was varied up to I =140 GW/cm^2.

3.4 2PA INDUCED LUMINESCENCE

The technique of 2PA Induced Luminescence (2PAIL) is particularly useful to determine the 2PA cross-section. In this case, we may use a dye with a known absorption cross-section for comparison and determine the 2PA absorption cross-section of graphene quantum dots (GQDs). This method works correctly if the following hypothesis is satisfied:

- The solvents, reference dye, and GQDs do not present absorption on the excitation wavelength and do not emit in the wavelength of the luminescence;
- The emission wavelengths of the reference dye and GQDs are close.

The emitted intensity for the reference dye and GQDs for the same laser intensity is.

$$I_{GQD}(\lambda_{GQD}) = G\left[N_{GQD}\sigma^{(2)}_{GQD}(\lambda_{GQD})\right]I_L^2, \tag{3.41}$$

in the equation (3.41) $I_{GQD}(\lambda_{GQD})$ is the emission intensity in the maximum emission wavelength of GQDs, G is a parameter that depends on the collection geometry, N_{GQD} is the concentration of GQDs in the solution, $\sigma^{(2)}_{GQD}(\lambda_{GQD})$ is the 2PA cross-section in the wavelength emission of GQDs, and I_L is the incident intensity.

An analogous equation can be written to the reference dye, and by simple algebraic manipulation, we obtain the equation to calculate the 2PA cross-section for the GQDs.

$$\sigma^{(2)}_{GQD}(\lambda_{GQD}) = \frac{N_{DYE}}{N_{GQD}}\left[\frac{I_{GQD}(\lambda_{GQD})}{I_{DYE}(\lambda_{DYE})}\right]\sigma^{(2)}_{DYE}(\lambda_{DYE}). \tag{3.42}$$

here N_{DYE}, $I_{DYE}(\lambda_{DYE})$, and $\sigma^{(2)}_{DYE}(\lambda_{DYE})$ are the concentration of dye, the emission intensity of the dye in the wavelength λ, and the 2PA cross-section for the dye, respectively.

The experimental setup to perform the measurements is similar to the one used for the HRS experiments, with the difference that no polarization analysis was performed.

4 TRANSITION METAL DICHALCOGENIDES (TMD's)

Transition Metal Dichalcogenides (TMDs) have been studied for a long time but in their three-dimensional form. The optical, structural, electronic, and chemical properties are described by KOLOBOV A., and TOMINAGA J., 2016. MoS_2, also known as molybdenite, for example, is perhaps the best known of them and is used as a lubricant in bearings and gears. As mentioned in the introduction, interest in 2D materials increased dramatically after the isolation of a single sheet of graphene.

The electronic structure of Two-dimensional Transition Metal Dichalcogenides (2D – TMD's) with structural formula MX_2, where M is a transition metal and X a chalcogen, is being extensively studied both theoretically and experimentally in several works (YOU et al, 2018; ZHANG et al, 2019; WANG et al, 2010; DONG et al, 2016). The periodic table below shows the transition metals and chalcogens that are used in TMD's:

Figure 18 – Periodic table showing transition metals (in blue, red, green, and lilac) and chalcogens in orange.

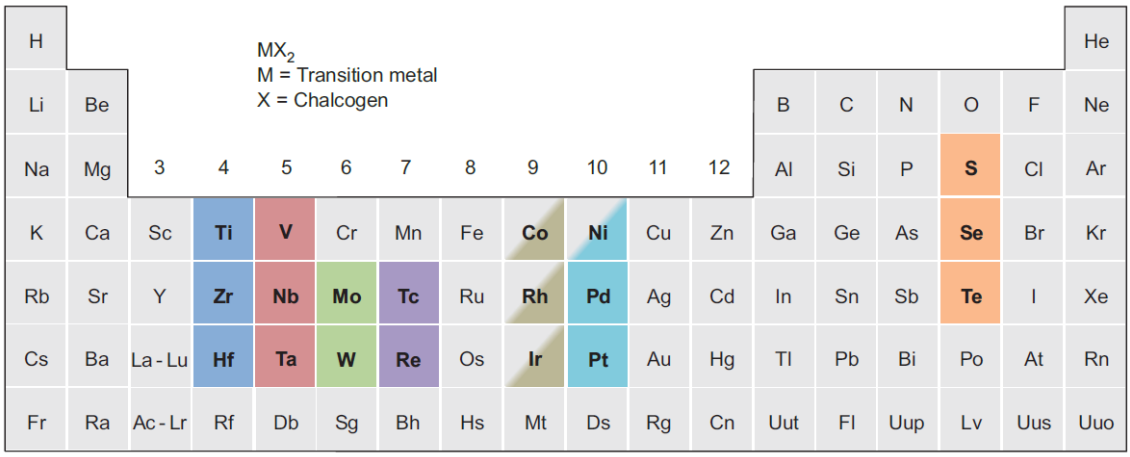

Source: Manish, et al (2013).

All transition metals of groups 4 – 7 crystallize in the form of layers, while the metals of groups 9 – 10 crystallize partially in the form of layers, an example is that NiS_2 has no layer structure, while $NiTe_2$ crystallizes in the form of layers. The chalcogens (S, Se, and Te), shown in orange in the periodic table, are used to prepare TMD's.

The color code in the periodic table is related to the electronic behavior of the material. The elements Ti, Hf, and Zr, in blue (group 4), form semiconductors TMD's with bandgap energy ranging from 0.2 – 2 eV, while the metals of group 5; V, Nb, and Ta, behave like metals, semiconductors, or superconductors, depending on coordination. Those in group 6; Mo and W,

have their electronic behavior dictated by the chalcogen linked to them; for example, when attached to S, Mo and W behave like semiconductor materials with bandgap ~ 1 eV; when they are attached to Te, these materials behave like semimetals. Tc and Re are small gap semiconductors (~1.5 eV). Finally, Pd and Pt, are semiconductors with bandgap ~ 0.4 eV when connected to S or Se and metallic when connected to the Te. Table 1 shows the electronic behavior for several TMD's.

Table 1 - Summary of TMDC materials and properties.

Group	**Metal (M)**	**Chalcogen (X)**	**Properties**
4	Ti, Hf, Zr	S, Se, Te	Semiconducting ($E_g = 0.2{\sim}2\ eV$)
5	V, Nb, Ta	S, Se, Te	Narrowband metals or semimetals. Superconducting, CDW, Paramagnetic, antiferromagnetic, or diamagnetic
6	Mo, W	S, Se, Te	Sulfides and selenides are semiconducting ($E_g{\sim}1\ eV$). Tellurides are semimetallics. Diamagnetic
7	Tc, Re	S, Se, Te	Small-gap semiconductors. Diamagnetic
10	Pd, Pt	S, Se, Te	Sulfides and selenides are semiconducting ($E_g = 0.4\ eV$) and diamagnetic. Tellurides are metallic and paramagnetic. $PdTe_2$ is superconducting

Source: Manish et al (2013).

The bonds between atoms are predominantly strong (covalent) bonds, while the bonds between layers are weak (van der Waals). The atoms of the metallic chemical elements provide four electrons to fill the bonds of the TMD's; thus, the oxidation states of the metals are +4 and the chalcogens, -2. The remaining electron pairs are on the surface of the chalcogens, and the absence of pending bonds makes these species stable against reactions with environmental species. The bonds between metals have a length ranging from 3.15Å to 4.03 Å.

The electronic structure of these materials depends heavily on the coordination in which the transition metal is bonded and the distribution of electrons in the *d* band. 2D TMD's can have coordination of type 1T (one atom per unit cell and trigonal coordination) and *2H/3R* (two atoms per unit cell and hexagonal coordination/three atoms per unit cell and rhombohedral coordination).

Figure 19 - Structures formed by TMD's.

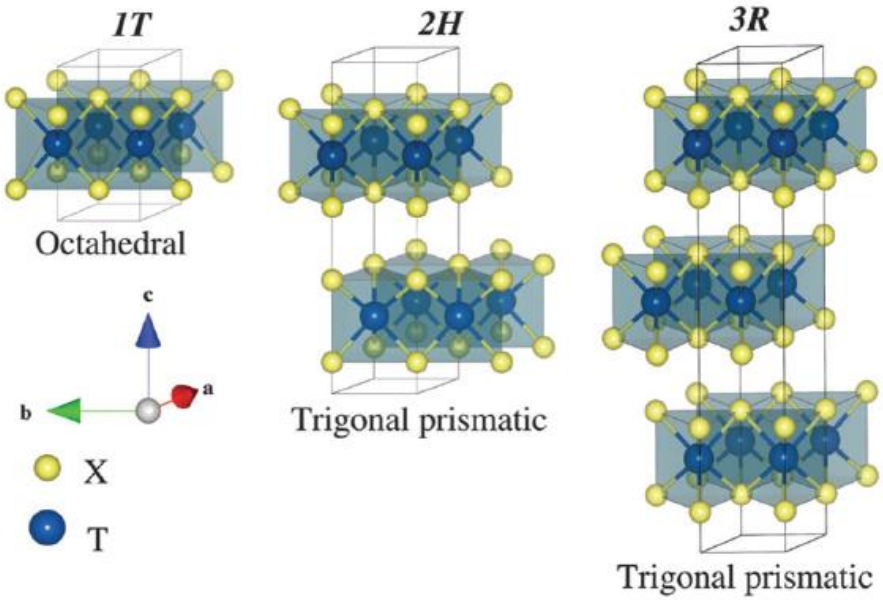

Source: Manish et al (2013).

In 1T and 2H phases, the unbound *d* bands of the TMD's are located within the range between the bound bands (σ) and unbound (σ*) of the M-X bonds, as illustrated in Figure 19. The centers of transition metals with octahedral coordination (D_{3d}) form degenerate orbitals d_{z^2}, $_{x^2 - y^2}$, and d_{yz}, $_{xz}$, $_{xy}$ (t_{2g}) which can accommodate together with the electrons *d* of TMD's (maximum 6, for TMD's of group 10). On the other hand, the orbitals *d* of transition metals with trigonal prismatic coordination (D_{3h}) are divided into three groups, d_{z^2}, $d_{x^2-y^2, xy,}$ and $d_{xz, yz}$, with a considerable difference (~1 eV) between the first two groups of orbitals. The various electronic properties of the TMD's arise from the progressive filling of the unbound *d* bands from group 4 to group 10. When the orbitals are partially filled, as in the case of 2H-$NbSe_2$ and 1T-ReS_2, the TMD's exhibit metallic conductivity.

The preferred phase for crystallization of TMD's depends strongly on the orbital *d* electrons of the transition metals. Group 4 TMD's with transition metal centers d^0 have an octahedral phase, while those in group 5 may have prismatic or octahedral trigonal phases (d^1) In group 6, the formed phase is trigonal prismatic (d^2) in group 7, a distorted octahedral structure (d^3) is available, and those in group 10 have an octahedral phase for all TMD's (d^6).

Figure 20 - Qualitative schematic illustration that shows the progressive filling of orbitals d that are located in the band range of the bonding (σ) and anti-binding (σ *) states in groups 4, 5, 6, 7 and 10. TMD's. D_{3h} and D_{3d} refer to the group of points associated with trigonal and octahedral prismatic coordination of transition metals.

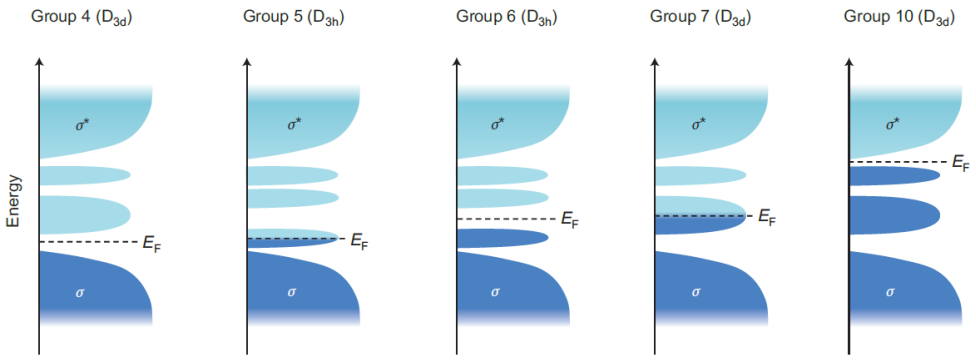

Source: Manish et al (2013).

The effect of chalcogen atoms on the electronic structure is small compared to that of metal atoms, but it is still possible to observe a trend: the enlargement of the *d*-bands and the corresponding decrease in the energy gap with the increase in the atomic number of chalcogen.

Figure 21 - Band structure showing the electronic transitions of MoS_2, $MoSe_2$, WS_2, and WSe_2. The lines dashed in blue and green the displacement of a state when the chalcogen is modified.

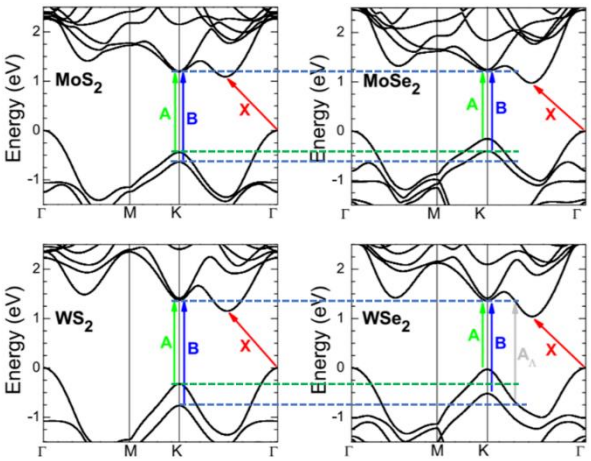

Source: Dybala et al (2016). (Modified)

For example, WILSON et al, 1969, show that the energy gaps of 2H-MoS_2, 2H-$MoSe_2$, and 2H-$MoTe_2$ gradually decrease from 1.3 to 1.0 eV.

Bulk TMD's are materials that have an indirect bandgap, but this indirect bandgap can be modified to direct, decreasing the number of layers of these materials from N layers to monolayer, where $N \geq 2$. TMDs of the group VI, as MoS_2 and WS_2, increase the energy of the gap by decreasing the number of layers, as can be seen in Figure 22.

Figure 22 – a) dependence of the gap energy as a function of the number of layers for MoS_2 samples, and b) Band structure showing the change from indirect bandgap to direct bandgap.

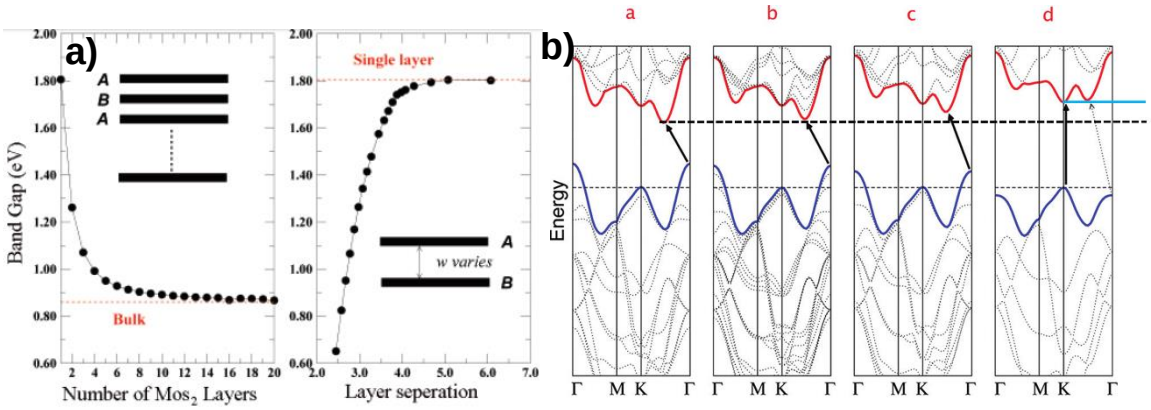

Source: Splendiani et al (2010). (Modified)

Figure 22 shows the dependence of gap energy as a function of the number of layers for MoS_2 flakes (SPLENDIANI et al, 2010). It is shown that with the decrease in the number of layers, the energy of the gap increases significantly. Figure 22 a) shows the energy of the gap as a function of the separation between the layers; in the monolayer regime, this separation is larger. Figure 22 b) shows the band structure for a sample of MoS_2, ranging from a bulk sample (a) to a monolayer (d). According to the decrease in the number of layers, the valence band, in dark blue, which for (a) is above the level of Fermi falls gradually, until it falls below the level of Fermi (d). The red curve represents the driving band; it is noticed that, with the decrease in the number of layers, the value of lower energy (which is between points K and Γ) increases to higher energy values, this behavior can be seen comparing the dashed black line and the continuous line, in blue. Now, the slightest energy difference between the valence band and the driving band is no longer the indirect transition, but rather a direct transition (K-K).

Since 2010 the interest in both linear and nonlinear optical properties of TMD's has increased. These materials have a transition from indirect bandgap to direct bandgap at the monolayer limit; these transitions have well-defined selection rules. In a semiconductor material, when absorption of a photon occurs, an electron is promoted to the conduction band, leaving a hole in the valence band. In 2D - TMD's, electrons and holes are strongly bound by Coulombic interaction, thus forming quasi-particles known as excitons, having binding energy of the order of 0.5 eV. The optical properties of these materials, at low temperature (~160 K) and room temperature, are determined by strong excitonic resonances.

Figure 23 – Diagram of excitons formation.

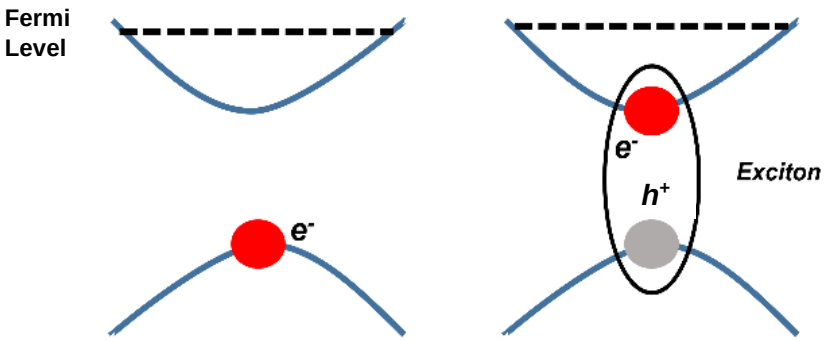

Source: The author (2021).

A diagram to illustrate the excitons formation is shown in Figure 23. An electron (e^-) undergoes a transition to the conduction band, leaving a hole (h^+) in the valence band. Due to the charges of opposite signs the electron and the hole are attracted by the Coulombic interaction.

The optical absorption spectrum of TMD's of group VI presents two excitonic resonances denoted as excitons A, B, and C. The origin of these resonances is mainly due to the strong spin coupling – orbit, increasing spin degeneration in the valence and conduction bands. The division of the valence band in these materials is relatively small, but much larger than for the conduction band, reaching values of the order of 200 meV for Molybdenum-based TMD's and 400 meV for tungsten-based TMD's (WANG et al, 2018).

Figure 24 shows the absorption spectra of the MoS_2 and WS_2 samples. Points A, B, and C show the excitonic transitions in these two materials. These are optical transitions from the valence band to the conduction band, leaving a hole in the valence band (Figure 24).

Figure 24 - Absorption spectrum of a) MoS_2 and b) WS_2.

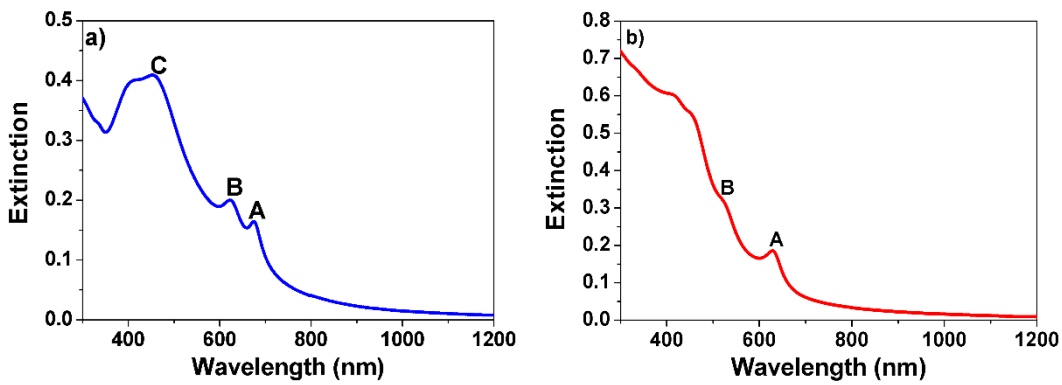

Source: The author (2021).

The optical bandgap of TMD's can be studied using the photoluminescence technique. We can use an equation to relate the optical absorption and energy of the bandgap, this equation is known as the Tauc plot and is given by the equation (TAUC et al, 1996).

$$\alpha h\nu = A(h\nu - E_g)^n \tag{4.1}$$

where α is the absorption coefficient, A is a constant, $h\nu$ is the photon energy, E_g is the energy of the bandgap and n is the type of transition involved and can assume values of $\frac{1}{3}, \frac{1}{2}, \frac{2}{3}\ e\ 2$.

The radiative recombination in 2D - TMD's, specifically the lifetime, is an important parameter for study in semiconductors. The control of the exciton dynamics of these materials can be very useful in optimizing the detector system. In this context, few studies have been conducted on the lifetime of radiative transitions. Some studies have shown that the lifetime of excitons in a monolayer of TMD's is in the range of picoseconds (1-10 ps) at low temperatures (0-4 K) and in the range of nanoseconds (0.1-10 ns) at room temperature (SLOBODENIUK and BASKO, 2016). It was also discovered that, in the TMD's studied, the lifetime in the bulk material and a few layers is slower than in the monolayer TMD's. For example, KUMAR et al., 2013, performed analyses of excitonic dynamics in $MoSe_2$ in bulk and monolayer forms, finding a decay rate of about 0.9 ns. These authors also noted that bulk materials have a lifetime about twice larger than in the monolayer format. PALUMMO et al, 2015, also studied the lifetime of the exciton for a monolayer of MoS_2, $MoSe_2$, WS_2, and WSe_2, as well bilayers and bulk samples of MoS_2 for excitation at low temperature and ambient temperature of the lowest peak energy absorption (exciton - A). They also noted that in MoS_2, when the number of layers increases from 1, 2, and bulk, the lifetime has increased to room temperature and 0 K. This adds another degree of freedom in the optoelectronic capabilities, as the dynamics of the exciton can be controlled and adjusted for various applications.

Many studies have used the absorption spectrum of direct and indirect transitions, as well as the Tauc plot to study the properties of bandgap in TMD's. Figure 25 shows the relation between the Tauc plot and the photon energy for MoS_2 and $MoTe_2$ samples. Extrapolating the linear part of indirect or direct transitions, it is possible to determine the optical bandgap of the material. WINCHESTER et al, 2014 performed liquid-phase exfoliation of bulk MoS_2, to obtain samples with few layers and monolayers. The authors found three peaks of excitation A, B, and C in the absorption spectra and find an $(\alpha E)^2$ dependence on the photon energy, *E*. The peaks A, B, and C were due to exciton transitions, corresponding to 680 nm, 620 nm, and 455 nm,

respectively. The linear extrapolation of the Tauc plot shows an optical bandgap estimate of 1.75 eV, which corresponds to flakes with about three to four layers.

Figure 25 - Tauc graph and linear extrapolation of a) MoS_2 using a direct transition and b) $MoTe_2$ using a direct and indirect transition, respectively.

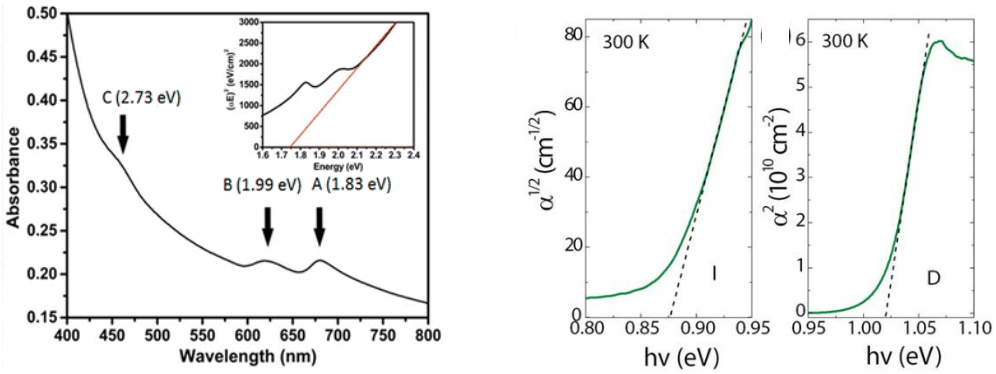

Source: a) Winchester et al (2014). b) Lezama et al (2014).

LEZAMA et al, 2014 performed absorption measurements in $MoTe_2$ films and use the Tauc plot to study the bandgap energy of direct and indirect transitions. The authors traced the indirect (*n=1/2*) and direct (*n=2*) transitions using Equation (4.1) and extrapolated the linear part of the curve. The group found indirect bandgap energy of about 0.875 eV and about 1.03 eV for the direct bandgap.

Tungsten-based TMD's, as WS_2 and WSe_2, exhibit optical properties close to molybdenum dichalcogenides, but with different transition energies for bulk, few layers, and monolayers. In this context, MORRISH et al. 2014, traced the Tauc's plot relationship to an indirect transition (n = 1/2) in the absorption spectra for WS_2 films, showing an indirect bandgap transition of about 1.4 eV. The results are shown in Figure 26 a). YU et al, 2015, performed optical absorption measurements in sheets of WSe_2 monolayer exfoliated in solution. From Figure 26 b), the authors extrapolated the linear part of the Tauc graph with an allowed direct transition (n = 2), showing a bandgap close to 1.75eV.

Figure 26 - Tauc graph and linear extrapolation of a) WS_2 using an indirect transition and b) WSe_2 using a direct transition.

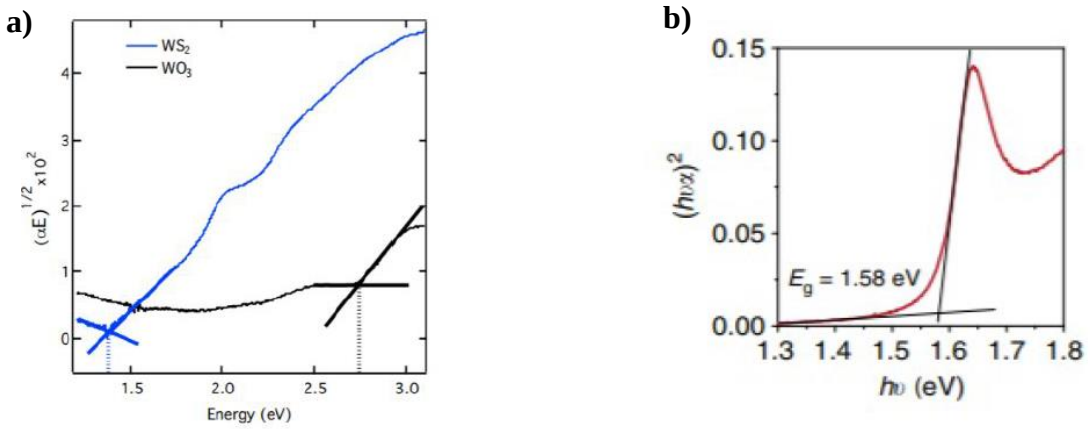

Source: a) Morrish et al (2014). b) Yu et al (2014).

The interaction of light with direct bandgap semiconductors is particularly important in optoelectronics. The absorption is proportional to the energy of the incident photons in the material and is commonly represented as a percentage of light not transmitted or reflected, therefore equal to $A = 1 - T - R$, where A, T, and R, are absorbance, transmittance, and reflectance, respectively.

However, in semiconductors, it is often useful to express absorption as a function of thickness, considered as the absorption coefficient. The absorption coefficient α, from the Beer-Lambert law, can be expressed as (FOX, 2001):

$$\alpha = \frac{2{,}303(\ln(1/T))}{t}, \tag{4.2}$$

where *t* is the thickness of the and *T* is the transmittance of the material. The numerator of the equation (4.2) refers to the logarithmic absorbance of light through a material, sometimes considered as "optical depth". Thus, it can be further simplified to $\alpha = A/t$.

Figure 27- Absorbance spectrum for $MoSe_2$, MoS_2, WS_2 and graphene and solar flow samples.

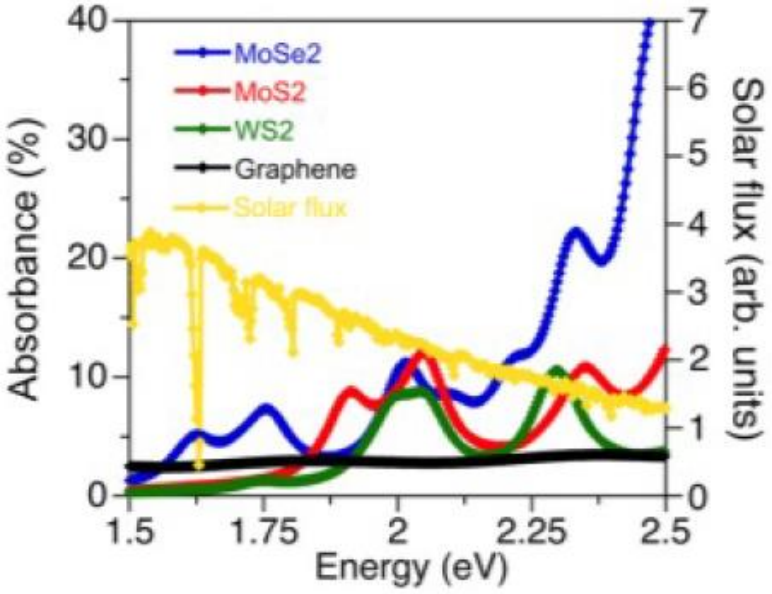

Source: Bernardi, et al (2013).

Another way to measure the absorption of light in thin-layered materials on a thick substrate can also be found from the reflected spectra acquired in a material. For a layered system, such as TMDs, for thicknesses $t<<\lambda$, the absorbance of the material is given by (MCINTYRE and ASPNES, 1971).

$$A = \frac{1}{4}(n_s^2 - 1)\frac{\Delta R}{R}, \tag{4.3}$$

where, n_s is the refractive index of the substrate, and ΔR/R is the contrast reflectance spectrum, given by:

$$\frac{\Delta R}{R} = \frac{R_{TMD+S} - R_S}{R_S}, \tag{4.4}$$

where R_{TMD+S} is the reflectance of TMD on the substrate and R_S is the reflectance of the substrate. To find and measure the exciton peak, only the contrast of the reflectance is necessary, since ΔR/R is proportional to the absorbance of light in the material.

Graphene showed absorbance of about 2.3% in the visible range and NIR. However, several monolayers of TMD's showed a much greater absorbance in the resonances of the bandgap, which usually is into the visible and NIR range. Absorbance >10% was observed in excitonic resonances, and even higher for some shorter wavelengths due to transitions between bands (EDA and MAYER, 2013). Figure 28 a), b), and c) shows the absorption for monolayers of three different TMD's (MoS_2, $MoSe_2$, and WS_2), compared to graphene for photon energy

of 1.5-2.5 eV (BERNARDI, et al, 2013). The spectra in Figure 29 show that all three TMD's has an absorbance of up to 10% in some parts of the visible spectrum, and absorbance larger than 30% for $MoSe_2$ in energies above 2.4 eV, although all samples are less than 1 nm thick. To compare with other common photovoltaic materials, some TMD's can absorb up to 10 times more sunlight incident than Si or GaAs (RUPPERT et al, 2014).

All monolayers of molybdenum dichalcogenides exhibit strong absorption in excitons-related peaks. Three separate studies were conducted to investigate the reflectance spectra using equation 4.2 in MoS_2 and $MoTe_2$, respectively (SPLENDIANI et al, 2010; RUPPERT et al, 2014; LY et al, 2014). SPLENDIANI et al, 2010 reported spectral data in the range of 500-900 nm (Figure 28) for ultrathin exfoliated MoS_2 on a 280 nm thick SiO_2 substrate.

Figure 28 – a) Reflectance of a monolayer of MoS_2 b) absorbance and transmittance to a sample of $MoTe_2$ and c) absorbance to a sample of $MoSe_2$ in free standing and on Silica.

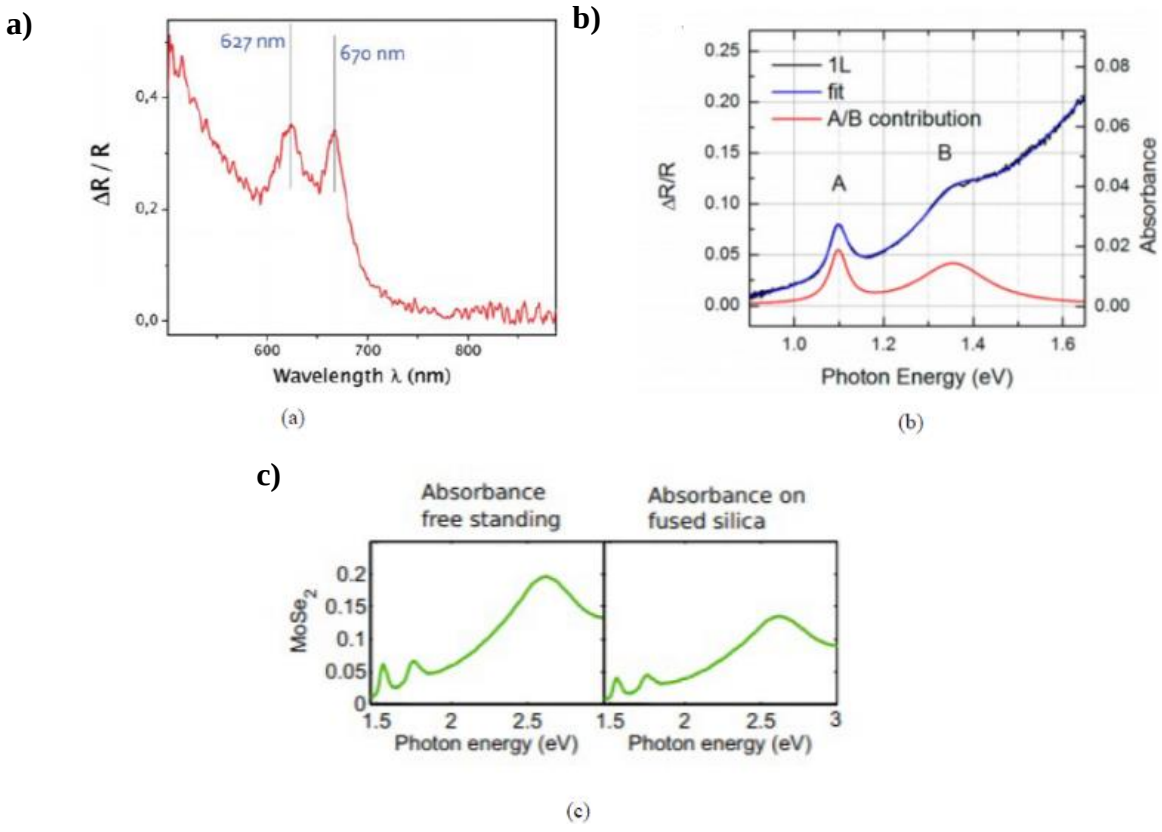

Source: a) Splendiani et al (2010). b) Ruppert et al (2014). c) Ly et al (2014).

The reflectance spectra for the MoS_2 monolayer showed two distinct absorption peaks located at 670 nm and 627 nm, corresponding to direct excitonic transitions at the K point of the Brillouin zone, known as excitons A_1 and B_1, respectively. RUPPERT et al, 2014 used mechanically exfoliated $MoTe_2$ monolayers deposited on SiO_2 substrates. The reflectance

spectra in Figure 28 b) show the excitonic peaks associated with the lowest direct optical transition at point K. The central point of the first position of the exciton (A) shows a direct bandgap of 1.095 ± 0.005 eV. This direct bandgap shows promising optical properties in the NIR region, with an absorbance of about 3% at peak A and 4% at peak B. LY et al, 2014 performed mechanical exfoliation of bulk TMD's in order to produce a few layers and measure optical absorbance in monolayers by means of a technique that measures the dielectric function, calculated from the reflectance spectra of the material. These authors show the absorbance of a liquid dispersion of $MoSe_2$ monolayer and on a transparent fused silica substrate. They also found that the dispersed monolayers exhibited strong absorption peaks of about 5%, 5%, and 18% at the exciton peaks A, B, and C, respectively, with a similar spectrum, but a lower value for $MoSe_2$ in the fused silica. For the dispersed sample, peaks A and B are centered on energies of 1.57 eV and 1.82 eV, respectively, that correspond to excitons A and B, which are the lowest direct transitions at K-points in the Brillouin zone (COEHOORN et al, 1987). At exciton C, the energies are spectrally broader, with a band located around 2.7 eV, to which the broadband is due to interband transitions close to the Γ point (QIU et al, 2013).

WX_2 monolayers, such as WS_2 and WSe_2, also showed high absorption along the visible spectrum. In this context, KOZAWA et al, 2014, performed reflectance measurements in mechanically exfoliated WS_2 monolayers on a quartz substrate using photon energies in the range 1.6 - 2.8 eV. The absorbance data were analyzed using the Lorentz model (FUJIWARA, 2007). The data show a strong absorbance of about 12% and 8% for the excitonic peaks A and B, respectively. Similarly, HE et al, 2014 performed linear and nonlinear optical absorption measurements in mechanically exfoliated WSe_2 monolayers. For the linear regime, reflectance spectra were performed in WSe_2 deposited on a fused quartz substrate, and the equation (4.4) was used to measure the absorption of the material. Figure 29 b) it is shown the calculated absorbance of the WSe_2 monolayer for photon energy 1.5 - 2.3 eV. Two exciton peaks A and B were found in 1.65 and 2.3 eV, respectively. The separation of energy between the states of exciton A and B is about 0.65 eV. This is due to strong spin-orbit interaction in WSe_2 and is very large compared to other TMD's (SPLENDIANI et al, 2010).

In MoX_2 and WX_2 compounds, the choice of transition metals and atoms of chalcogen may affect the absorption properties of the material. A redshift in the peaks of exciton A and B is present in the atoms of chalcogen heavier, thus showing that the absorption peaks of exciton occur in higher photon energies for molybdenum and tungsten sulfides compared to selenides. In addition, the exchange of Mo and W does not affect the position of the exciton A. However,

YU et al, 2015, reported that when the atom of Mo is replaced by W, the difference in photon energy between the peaks of exciton A and B increases.

Figure 29 – a) Absorbance spectrum of a sample of WS_2 and reference b) WSe_2.

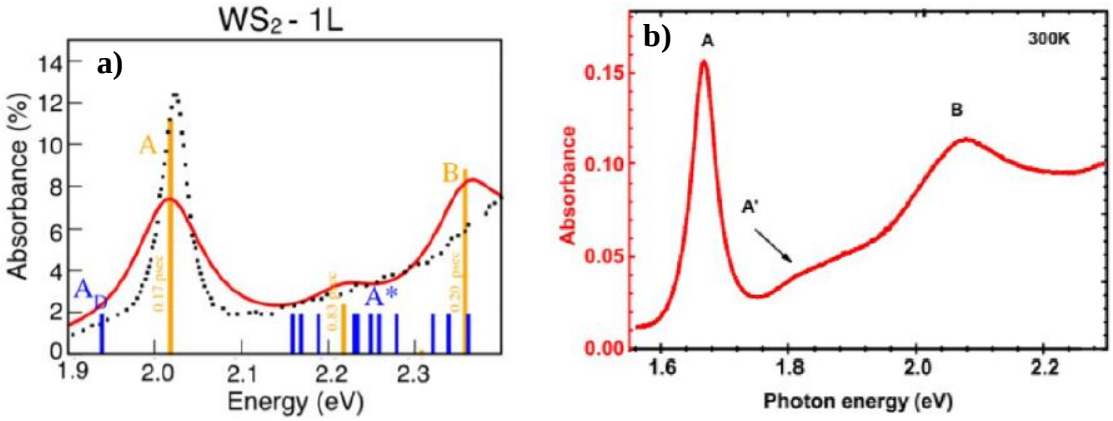

Source: a) Kozawa et al (2014). b) Bernardi et al (2017).

They found that by making this change, the MoX_2 monolayers have an energy difference of 150 meV and the WX_2 monolayers have an energy difference of about 450meV (YU et al, 2015). This is due to the larger spin-orbit coupling of tungsten atoms compared to molybdenum, which is intrinsic to the transition metal (LATZKY et al, 2015).

TMD's have shown unique properties of band structure and optical transitions as they change from bulk to a few monolayers (BHIMANAPATI et al, 2015). The bulk and few layers TMD's have an indirect bandgap, involving vibrations (phonons) in the lattice. However, TMD's monolayer exhibit a direct bandgap transition, showing greater absorption and requiring only an incident photon energy to perform this transition. Ellipsometry, micro-Raman, and photoluminescence (PL) are generally used to determine the thickness as well as the optical properties of TMD's. Interactions between layers cause transitions from indirect bandgap (bulk sample) to direct bandgap (in monolayer), which results in the reduction of the thickness of the TMD layer to monolayer due to quantum confinement, making it optically active.

The interactions between layers are attributed to Coulomb interactions between transition metal ions and chalcogens ions in adjacent layers, as shown in Raman spectroscopic studies (TONNDORF et al, 2013). The effects of surface relaxation in TMD's are also important, although the interactions between layers are weak. The transition from indirect to direct bandgap exists through all MX_2 compounds when the number of layers decreases from a few layers to a monolayer.

Molybdenum dichalcogenides, which include MoS_2, $MoSe_2$, and $MoTe_2$, show strong photoluminescence properties in the visible and NIR regions. The bandgap of these materials, in bulk form, is indirect and may range from about 0.9 to 1.3 eV (RUPPERT et al, 2014; MAK et al, 2010; TONNDORF et al, 2013). For monolayer forms of MoS_2, $MoSe_2$, and $MoTe_2$, all these materials exhibit a direct bandgap of 1-2 eV (RUPPERT et al, 2014; MAK et al, 2010). Monolayers also have high photoluminescence efficiency, up to more than 10^3 times greater than bulk forms (MAK et al, 2010). MoS_2 is the most widely studied TMD's, both in the form of a few layers and in the monolayer. The bulk MoS_2 has an indirect optical bandgap of about 1.29 eV (YU, et al, 2015), and the individual layers consist of hexagonal S and Mo atoms covalently bound in a trigonal prismatic organization. The photoluminescence spectra of the few-layer MoS_2 show-bandgap shifted as a function of the number of layers and is close to 0.6eV of the bulk material (MAK et al, 2010). The indirect bandgap changes as the number of layers of the material increases or decreases and becomes a direct bandgap of about 1.9 eV as a monolayer. In this context, MAK et al, 2010 they used mechanical exfoliation to create monocrystals and a few layers, consisting of 1 to 6 layers. The authors performed measurements of optical absorption, photoluminescence, and photoconductivity in the samples. For photoluminescence characteristics, there was an increase in quantum yield (QY) when the number of layers was reduced from the bulk material to a few layers. The MoS_2 monolayer shows a very large photoluminescence intensity, about 10^3 times that of the bulk material, due to the direct bandgap in the monolayer. Figure 30 b) shows the change in the bandgap as a function of the number of layers (1-6 layers), in Figure 30 a) shows the PL spectra for layers 2-6 layers. The bulk $MoSe_2$ has a crystalline structure similar to MoS_2, with an indirect bandgap, in the bulk form, in NIR with an energy of 1.09 eV. The Monolayer $MoSe_2$ shows a direct optical bandgap of 1.51 eV. Figure 30 c) shows the PL spectra for $MoSe_2$ of 1, 2, and 3 layers measured by TONNDORF et al, 2013.

$MoTe_2$ is the heaviest and largest molybdenum dichalcogenides, with an indirect bandgap, in its bulk form of about 1.0 eV, and a direct bandgap in the form of a monolayer of about 1.1eV (CONAN et al, 1979; BOKER, et al, 2001; RUPPERT et al, 2014). Figure 30 d) shows PL spectra of 1-5 layers of $MoTe_2$ reported by RUPPERT et al, 2014.

Figure 30 – a) Photoluminescence spectrum for 1-6 layers of MoS_2 b) photoluminescence peak signal as a function of the number of layers c) Photoluminescence spectrum for 1-3 layers of $MoSe_2$ and d) photoluminescence spectrum for 1-5 layers and bulk of $MoTe_2$.

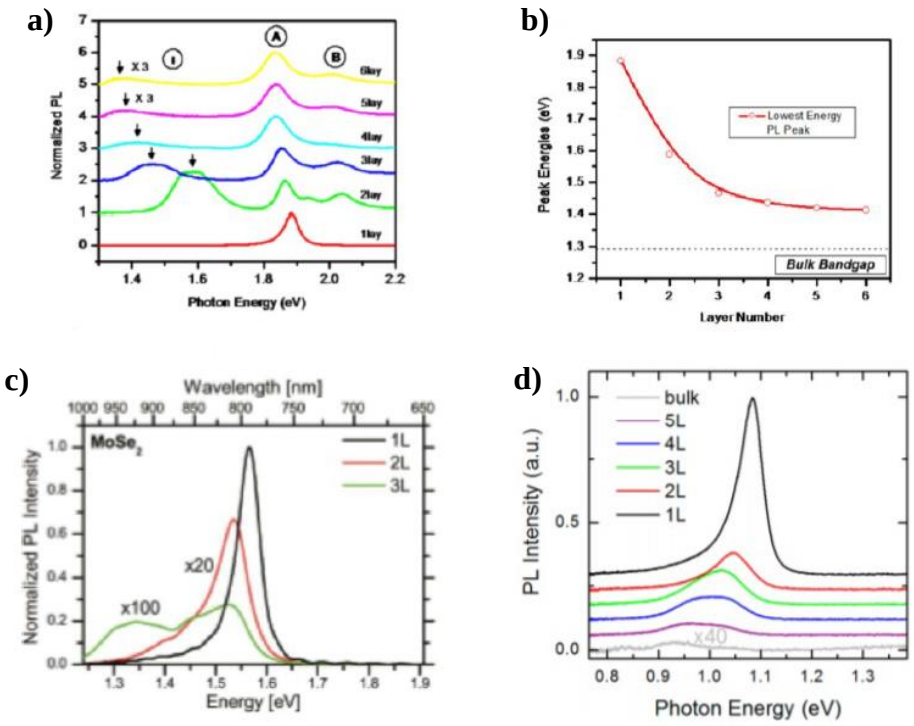

Source: a) and b) Mak, et al (2010). c) Tonndorf, et al (2013). d) Ruppert, et al (2014).

Like other TMD's, $MoTe_2$ monolayers show strong PL emissions, indicating a direct gap, while layers 2-5 showed weaker PL peaks tending multilayer or bulk emissions. Due to the small change in monolayer and the optical bandgap difference of $MoTe_2$, studies have found that the transition from indirect to direct bandgap can occur before the monolayer limit (BÖKER et al, 2001).

The tungsten-based dichalcogenides consisting of WS_2, WSe_2, and WTe_2 are other systems very much studied. WS_2 and WSe_2 are semiconductors, both in bulk and monolayer form. The indirect optical band gap of these materials is very similar, with a value of about 1.2-1.3 eV (RUPPERT, et al, 2014; TONNDORF, et al, 2013). However, their indirect bandgap changes dramatically when reduced to the form of a few layers. ZHAO et al, 2013 measured the PL profiles of WS_2 and WSe_2 for 1-5 layers. For WSe_2, there is a very small change between the energy peaks in indirect and direct bandgaps in the PL spectra, showing the largest difference in these energies to 5 layers of about 0.2 eV. However, WS_2 shows a large change in the indirect gap as the number of layers increases, with the largest difference being about 0.6 eV. Both the WS_2 as the WSe_2 exhibited a linear increase in emission as the number of layers decreased, with a single direct emission of energy of 2 eV and 1.65 eV, respectively.

WTe_2 is quite different from other WX_2 compounds. The stable form of its atomic structure is octahedral, as opposed to the trigonal prismatic form of the other tungsten and molybdenum dichalcogenides (TORUN et al, 2016).

Figure 31 – a) Photoluminescence spectrum for 1-5 layers of WS_2 and b) WSe_2.

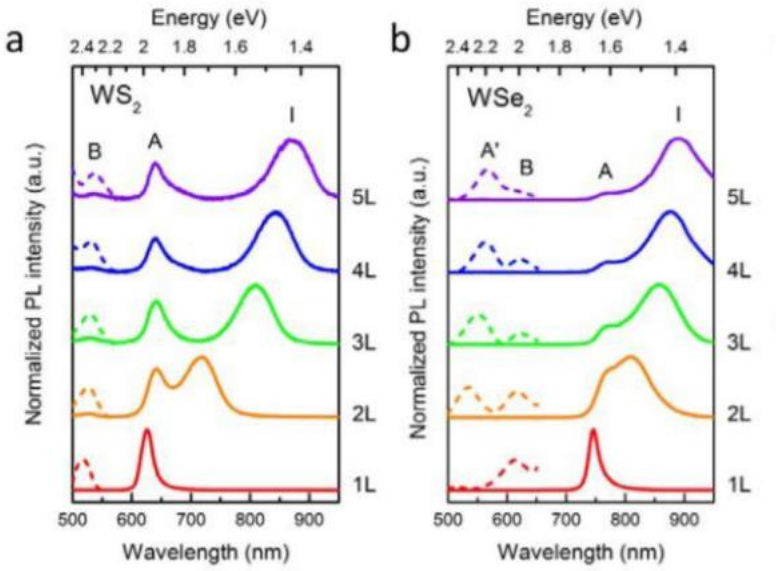

Source: Bernardi, et al (2015).

However, this form of the material acts as a semimetal, with a small overlap between the valence and driving bands. The hexagonal shape of the material has a bandgap of about 0.73 eV, much narrower than other TMD's (AMIN et al, 2014). The bandgap difference was determined theoretically, but no PL spectrum has been observed in this material.

4.1 NONLINEAR OPTICAL EXPERIMENT AND RESULTS

The nonlinear optical properties of several LTMD's are investigated in innumerable work having specially studied second and third-order nonlinearities. Due to the noncentrosymmetric behavior of 2H-MX_2 phases, second-order nonlinearity was applied to characterize MX_2 (M=Mo, W; X=S, Se, and Te) compounds. LIU et al, 2017, studied High Harmonic Generation (HHG) in MoS_2 samples. The authors explore a non-perturbative HHG in the sample showing even and odd harmonics extending to the 13th order. This property can be used for applications at attosecond physics, for example.

AUTERE et al, 2018 demonstrate second and third-order optical susceptibilities in MoS_2, $MoSe_2$, WS_2, and WSe_2 placing different samples at proximity to each other in a single substrate, finding a higher value for the optical susceptibilities. LI et al, 2016 performed studies of SHG, Four-Wave Mixing (FWM), and Sum Frequency Generation (SFG) in MoS_2 monolayers and their heterostructures using a nonlinear optical imaging technique. The authors show that the optical nonlinearities are sensitive to the number of layers, crystal orientation, and interlayer coupling. Nonlinear refraction and nonlinear absorption were studied in several works using many wavelengths, different temporal regimes, and repetitions rates. WANG et al, 2014 studied the nonlinear absorption of MoX_2 (X=S, Se, and Te) layers using pico and femtosecond lasers with different wavelengths.

The saturation of 2PA was studied by DONG et al, 2018 for MX_2 samples (M=Mo, W; X=S, Se). In this case, the excitation was at 1030 nm, exploiting the 2PA effect in the exciton's transitions at 2p states, the saturation of charge carries, and the depletion of the electron population in the ground state. The 2PA coefficients are highly dependent on the thickness (number of layers) in the samples. Four broadening models were used trying to fit the experimental data; the better fit was employed a homogeneous broadening. BIKORIMANA et al, 2016 investigate the nonlinear refraction and nonlinear absorption coefficients in MX_2 samples (M=Mo, W, M=$Mo_{0.5}W_{0.5}$; X=S, Se). The wavelength excitation used was 1064 nm, with 25 ps of temporal width and a repetition rate of 20 Hz. The authors show a transition from Reverse Saturated Absorption (RSA) to 2PA behavior in WS_2 layers with the increase of the intensity. Only saturated absorption was observed in MoS_2. In $Mo_{0.5}W_{0.5}S_2$ the 2PA was observed. In closed aperture Z-scan experiments, a self-defocusing effect was shown for all three

samples. A new structural phase, namely 1T'''-MoS_2 was characterized by the SHG technique. In this work, FANG et al, 2019, showed an interesting property not found for 1T'-MoS_2 and 1T-MoS_2, as noncentrosymmetric behavior, thus allowing the generation of even harmonics.

The nonlinear optical properties of 2D-TMD's were explored in several works for mode-lock and Q-switching of lasers. AHMED, et al, 2016 used MoS_2 layers in a fiber laser for mode-locking application. A MoS_2 thin film was used for mode-locking of an Er-doped fiber laser by KHAZAEIZHAD et al, 2014. LI et al, 2020 demonstrate the potential application of NbS_2 in a 2H-phase saturable absorber for an fs ultrafast fiber laser. A demonstration of 3R-NbS_2 as a saturable absorber was also performed by SUN et al, 2020 for a 1μm fiber laser.

4.2 $ZrTe_2$

$ZrTe_2$ is LTMD'S is a semimetal nonlinear optical properties were not studied before the work in this thesis. One of the initial works in $ZrTe_2$ was the investigation of the structural phases by Raman spectroscopy (HANGYO et al, 1983). In this work the authors characterized for the first time three MX_2 based TMD's, finding two characteristic peaks in the Raman spectra. Currently, a major part of investigations of $ZrTe_2$ samples is dedicated to study the structural properties of this TMD and their topological properties.

TSIPAS et al, 2018 studied mass-less Dirac fermions in $ZrTe_2$ monolayers deposited in InAs substrates using the Angle-Resolved Photoemission Spectroscopy (ARPES) technique. In this work, the authors suggested that the $ZrTe_2$ monolayers can be considered as an electronic analog of the graphene because the valence and conduction bands cross the Fermi level exhibiting abrupt linear dispersions.

WANG et al., used $ZrTe_2$ films synthesized by pulsed laser deposition, to study magnetotransport properties. A study about the point group of several TMD's was reported by RIBEIRO-SOARES et al, 2014, finding that $ZrTe_2$ monolayers are centrosymmetric with $\boldsymbol{P\bar{3}m1}$ point group.

4.2.1 Second-order nonlinearity in layered $ZrTe_2$

The experimental setup employed for the HRS measurements is shown in Figure 12. An Nd: YAG laser operating at 1064 nm, 10 Hz with pulses of 7 ns, was employed

as the light source. For these measurements, the layered $ZrTe_2$ nanoflakes were suspended in acetonitrile (ACN) at a concentration of $\mathbf{4.9 \times 10^{10}}$ particles/cm^3. To determine the first-hyperpolarizability, the external reference method was employed using para-nitroaniline (*p*-NA) as the reference standard.

Figure 32 shows the HRS spectrum for $ZrTe_2$ suspension, centered in 532 nm, as expected.

Figure 32 - HRS spectrum for the $ZrTe_2$ suspension.

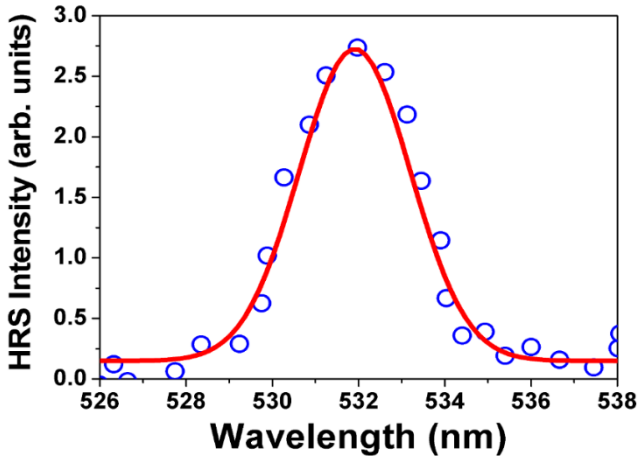

Source: The author (2021).

Figures 33 show the measured intensity dependence of the HRS signal versus the laser intensity. A quadratic intensity dependence is consistent with second harmonic generation.

Figure 33 - HRS spectrum for the $ZrTe_2$ suspension.

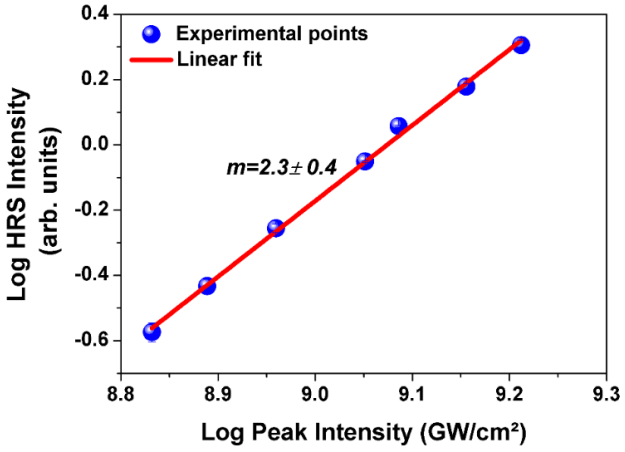

Source: The author (2021).

Figure 34a) shows the temporal profile of the HRS signal, which resembles the laser profile, with a 7ns duration, that is also consistent with the fast response of the second-order nonlinear process, also indicating that the signal does not come from luminescence processes.

Figure 34 – Temporal behavior for a) sample (blue circles) and Gaussian fit (red solid line), and b) sample (blue circles) and laser temporal profile (black solid line).

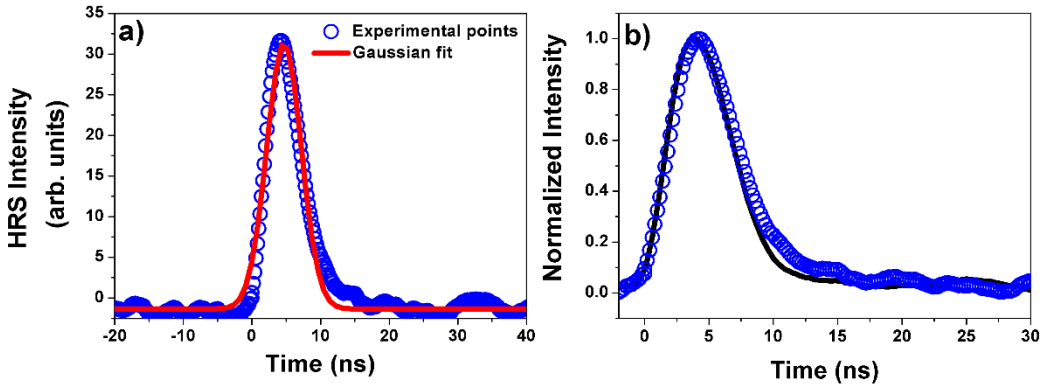

Source: The author (2021).

Figure 34b) is a plot of the HRS temporal behavior (blue circles) and the temporal profile of the excitation laser (black solid line). Both temporal behaviors match very well the expectations and confirm the HRS process.

Measurements of the HRS signal intensity versus the volume concentration of the $ZrTe_2$ nanoflakes were performed and can be seen in Figure 35.

Figure 35 – HRS intensity as a function of $ZrTe_2$ nanoflakes concentration. The linear behavior is indicative of no aggregation of the monolayers.

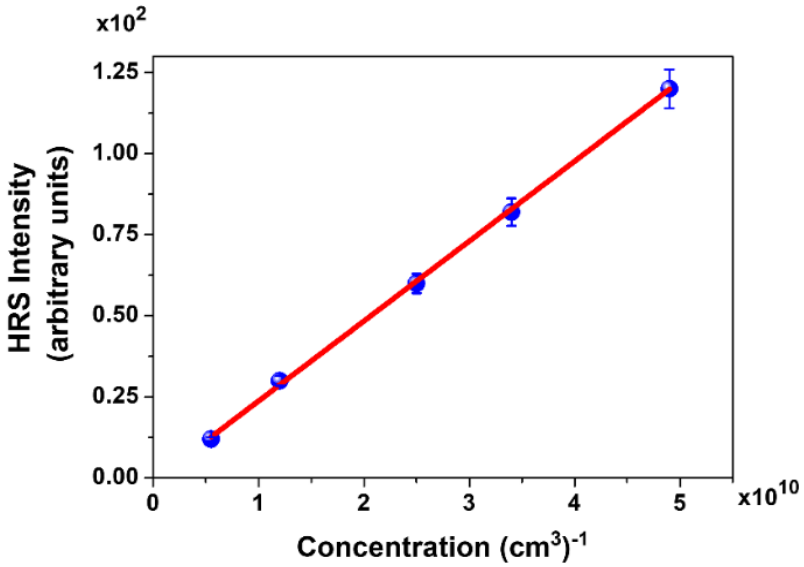

Source: The author (2021).

Linear behaviour is observed for nanoflakes concentrations of $\mathbf{0.5}, \mathbf{1.2}, \mathbf{2.5}, \mathbf{3.4}$, and $\mathbf{4.9}$ ($\times \mathbf{10^{10}\ cm^{-3}}$), indicating that the SH signal is due to individual nanoflakes and not due to aggregates. No saturation was observed in the range of the laser intensities used.

To further confirm the incoherent nature of the second harmonic generation, we performed an angular measurement of the emitted SH intensity at the highest available peak intensity ($\sim \mathbf{9.2}\ \boldsymbol{GW/cm^2}$). The experimental setup for this measurement, shown in Figure 36 a), was a modification of the original setup shown in Figure 12. All the excitation path was kept as in Figure 12, but the collection part, with the same components, was mounted on a base which could be rotated by $\pm 40^0$ (meaning a 50^0 to either side of the central point) around the 90° collection direction shown in Figure 12. The obtained results are shown in Figure 36b) where, within the experimental error of ±10% in the SH intensity, a constant second harmonic signal is measured, therefore showing that there is no enhancement at any preferential direction for the SH emission. SH signals in other directions (not shown), including backward, were also detected but with less intensity and a poorer signal-to-noise ratio. It confirms, therefore, that the SH signal is indeed incoherent in nature arising from HRS. For a literature comparison, CLAYS et al, 2001 studied angle-resolved HRS in specific chromophores, where coherent contributions to the incoherent SH were detected by angular measurements showing an enhanced signal at a particular angle. When the signal was completely incoherent, as is the case here, the SH signal was constant as a function of angle.

Figure 36 – a) Experimental setup for angular measurement of HRS signal; b) Measured HRS SH signal intensity as a function of angle for a fixed input intensity of $\sim \mathbf{9.2}\ \boldsymbol{GW/cm^2}$ for $ZrTe_2$ samples.

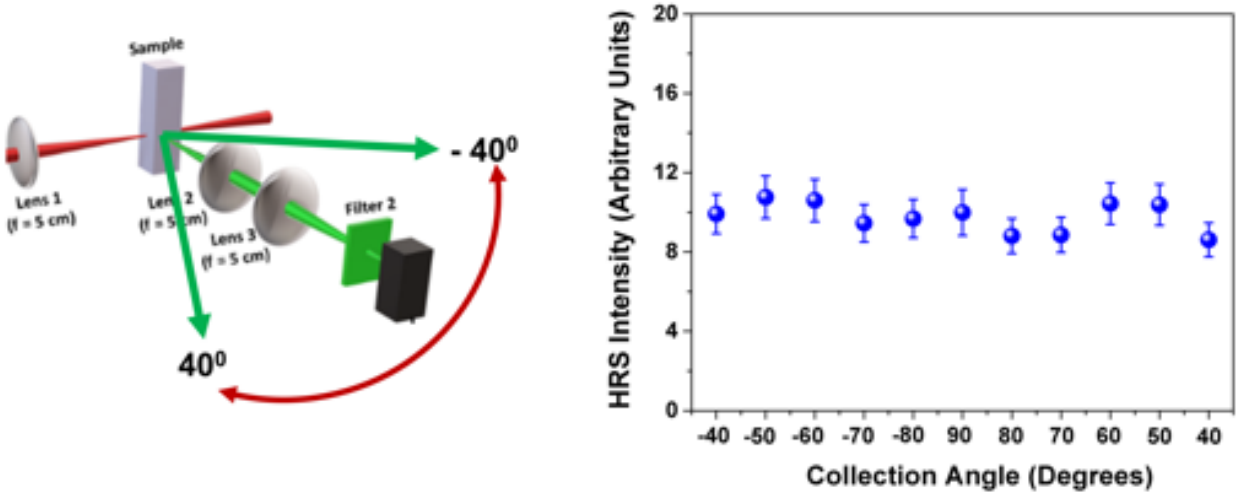

Source: The author (2021).

In order, to identify the origin of the SH light generated by the $ZrTe_2$ nanoflakes, polarization-resolved HRS experiments were performed. The experiments were carried out according to the usual procedure (NAPPA et al, 2005; BUTET et al, 2019). The incident laser beam was linearly polarized and the angle, $\boldsymbol{\gamma}$, between the optical field and the vertical direction was varied from 0 to $\mathbf{2\pi}$.

The intensity of the HRS signal along the direction perpendicular to the laser beam propagation was measured by placing an analyzer in front of a photomultiplier and measuring the HRS intensity either in the vertical or horizontal (i.e., parallel to the incident beam propagation axis) direction. Figure 37 is a polar plot of the input polarization angle dependence of the HRS intensity. As discussed in the next section, the obtained profiles indicate an electric dipole origin for the SH generation (BUTET et al, 2019). The non-circular shape of the curve for the analyzer in the horizontal orientation, Figure 37b), is expected when the shapes of the particles are not centrosymmetric.

Figure 37 - Polar plots of the HRS intensity generated by the $ZrTe_2$ nanoflakes in suspension versus the input laser polarization angle for detection along the direction perpendicular to the input beam propagation direction. Analyzer in the vertical a) and horizontal b) orientations.

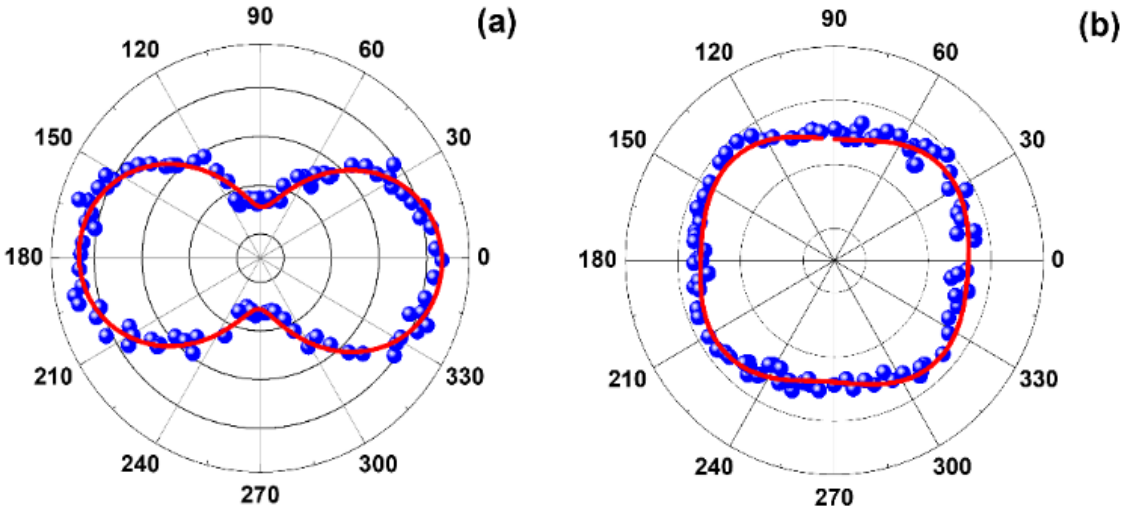

Source: The author (2021).

The theoretical treatment for the HRS data is described in section 3.2 as well as in (KLAYS and PERSONS, 1991; HUBBARD et al, 1996). The employed external reference method is well established, and we highlight the main equations used to fit the data. The SH scattered light intensity by a composite sample can be described as (KLAYS and PERSONS, 1991):

$$\boldsymbol{I}(\boldsymbol{2\omega}) = \boldsymbol{g}\{\sum_{\boldsymbol{c}} \boldsymbol{N_c F_c}\langle\boldsymbol{\beta_c^2}(\boldsymbol{2\omega})\rangle\}\, \boldsymbol{I^2}(\boldsymbol{\omega}), \tag{4.5}$$

where $\boldsymbol{N_c}$ is the nonlinear particle concentration, $\boldsymbol{I}(\boldsymbol{\omega})$ is the incident laser intensity, $\boldsymbol{\beta_c}(\boldsymbol{2\omega})$ is the effective first-hyperpolarizability and the sub-index represents the constituents of the suspension. The brackets in the factor $\langle\boldsymbol{\beta_c^2}(\boldsymbol{2\omega})\rangle$ indicate orientational average and $\boldsymbol{F_c}$ is a local field factor given by $\boldsymbol{F_c} = \{(\boldsymbol{n_{ACN}^2} + \boldsymbol{2})/\boldsymbol{3}\}$ (KLAYS and

PERSONS, 1991; HENDRICKX et al, 1998; JOULAUD et al, 2013), where $\boldsymbol{n_{ACN}}$ is the refractive index of ACN; the value calculated for this parameter is $\boldsymbol{F_c = 1.26}$. The factor *g* depends on the scattering geometry and contains information on the transformation of coordinates from the $ZrTe_2$ to the laboratory reference system (JOULAUD et al, 2013; BARBOSA-SILVA et al, 2020).

The HRS signal, $\boldsymbol{I(2\omega)}$, as a function of laser intensity for the two-component system studied can be written as

$$I(2\omega) = G(N_{sol}\langle\beta_{sol}^2\rangle + N_{solv}\langle\beta_{solv}^2\rangle)I^2(\omega), \tag{4.6}$$

where *sol* stands for solute ($ZrTe_2$), $\boldsymbol{solv}$ stands for solvent (acetonitrile-ACN) in our case, and $\boldsymbol{G}$ is a parameter that includes local field correction and light collection efficiency.

For determination of $\langle\boldsymbol{\beta_c^2(2\omega)}\rangle$ we used the external reference method (PAULEY et al, 1996) according to:

$$\langle\beta_{ZrTe_2}^2(2\omega)\rangle = \frac{I_{ZrTe_2}(2\omega)}{I_{p-NA}(2\omega)}\left\{\frac{N_{p-NA}\langle\beta_{p-NA}^2\rangle + N_{mOH}\langle\beta_{mOH}^2\rangle}{N_{ZrTe_2}}\right\} - \frac{N_{ACN}\langle\beta_{ACN}^2\rangle}{N_{ZrTe_2}} \tag{4.7}$$

where $mtOH$ refers to methanol. The results are given in Table 2.

Table 2 – Parameters used in equation (4.7)

	CH_3CN	$p-NA$	$mtOH$
$\beta(2\omega) \times 10^{-30} esu$	0.38	34	0.69
$Concentration\ (N)$ $(molecules/cm^3)$	1.3×10^{22}	1.0×10^{19}	1.5×10^{22}

Source: The author (2021).

The volume concentration of $ZrTe_2$ monolayers was $\boldsymbol{N_{ZrTe_2} = 4.9 \times 10^{10}\ particles/cm^3}$, allowing for determining $\boldsymbol{\beta\ (2\omega) = (7.0 \pm 0.3) \times 10^{-24}\ esu}$.

The fitting of the polarization data shown in Figure 4 was performed using the equation (3.14), with the values of $\boldsymbol{d = e = 0}$:

$$\boldsymbol{I_{HRS}^{\Gamma} = a^{\Gamma}cos^4\gamma + b^{\Gamma}cos^2\gamma sin^2\gamma + c^{\Gamma}sin^4\gamma} \tag{4.8}$$

where $\boldsymbol{I_{HRS}^{\Gamma}}$ is the HRS intensity and Γ corresponds to the H or V polarization. The coefficients $\boldsymbol{a^{\Gamma}}$, $\boldsymbol{b^{\Gamma}}$and $\boldsymbol{c^{\Gamma}}$ were obtained by theoretical fit. The depolarization ratio $\boldsymbol{\rho^{\Gamma} = c^{\Gamma}/a^{\Gamma}}$ and the multipolarity, determined by $\boldsymbol{\zeta^{\Gamma} = 1 - (a^{\Gamma} + c^{\Gamma}/b^{\Gamma})}$, were calculated. From the experimental data, the values of these parameters, as well as of the coefficients in Equation (4.8) are given in Table I. The good fitting obtained, as well as the fact that $\boldsymbol{2a_H \approx 2c_H \approx b_H}$ and $\boldsymbol{c_H \approx c_V}$, are in line with a pure dipole nature for the SH radiation (NAPPA et al, 2005).

Table 3 – Coefficients of Equation (4.8) determined from the polarization plots.

Coefficient	V polarization	H polarization
$\boldsymbol{a}$	0.89	0.33
$\boldsymbol{b}$	1.20	0.74
$\boldsymbol{c}$	0.27	0.25
$\boldsymbol{\rho}$	0.30	0.75
$\boldsymbol{\zeta}$	0.03	0.21

Source: The author (2021).

In order to compare the present results with the only previous report on HRS in TMDs (FORCHERIO et al, 2017; FORCHERIO et al, 2017), we recall that the authors obtained $\boldsymbol{\beta(2\omega) = 2.66 \times 10^{-25}}$ *esu* for WS_2 nanoflakes, which are semiconductors, measured at the same optical wavelength (1064 nm) with 1 ns pulses (FORCHERIO et al, 2017; FORCHERIO et al, 2017). The $\boldsymbol{\beta(2\omega)}$ value herein reported for the semi-metal $ZrTe_2$ is larger by a factor of 26.3 with respect to the WS_2 nanoflakes. RIBEIRO-SOARES et al, 2014 showed that $ZrTe_2$ in the 1T phase is centrosymmetric (from bulk all the way down to the monolayer), meaning that the observed second-order nonlinearity is of a surface/edge nature, as with metallic nanoparticles (BUTET et al, 2019).

The fact that the nonlinear scattering profile has a dipolar character indicates that it arises from the non-centrosymmetric shape of the nanoflakes with important contributions from the nanoflakes edges.

Also, the higher hyperpolarizability value obtained here relative to that obtained for the WS_2 by FORCHERIO et al, 2017; FORCHERIO et al, 2017 is probably due to two further reasons: first, the number of $ZrTe_2$ atoms, because the nanoflakes have a

higher average volume [Vol (WS_2) = 1500 nm³ vs Vol ($ZrTe_2$) = 21443 nm^3]. Besides, as another reason, one should recall that the unit cell of $ZrTe_2$ has 144 electrons, which is more than the 106 electrons in the unit cell of WS_2. Thus, the nonlinear response of $ZrTe_2$ would be higher.

4.2.2 Real Third–Order Nonlinearity in $ZrTe_2$

The NLO characterization used the well-established Z-scan method and was described in section 3.3. The light source was a Ti: Sapphire-based regenerative amplifier (800 nm) operating at 1 kHz and delivering 100 fs single pulses with maximum energy of 1mJ. The beam was focused with 15 cm focal length lens onto a 1 mm quartz cuvette. The peak intensity was varied up to $I = 140\ GW/cm^2$ for the present experiment. The NL refractive index (n_{NL}) and NL absorption coefficient (α_{NL}) were measured, from which the values of Re$\chi^{(3)}$ and Im $\chi^{(3)}$ could be inferred.

As a control experiment, Z-Scan measurements were initially performed for the solvent, pure ACN, as shown in Figure 38(a,b,c). Notice that the Z-Scan curves showed a positive (self-focusing) NLR with the value of $n_2 = 1.9 \times 10^{-17}\ cm^2/W$, consistent with the literature (ILIOPOULOS, et al, 2015). The intensity used was $25\ GW/cm^2$, $60\ GW/cm^2$, and $105\ GW/cm^2$, respectively.

Figure 38 – CA Z-scan curve for ACN at a) 25 GW/cm^2; (b) 60 GW/cm^2; c) 105 GW/cm^2. d) Intensity dependence of n_2.

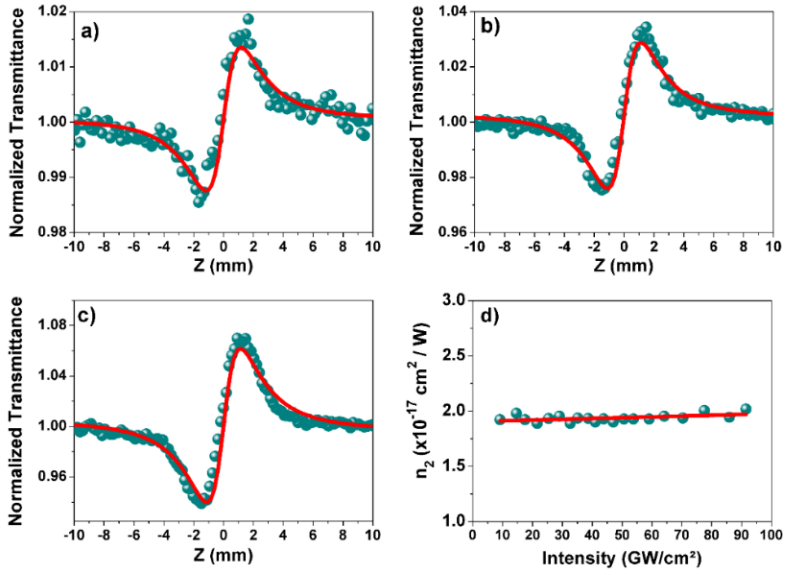

Source: The author (2021).

The $n_2 \times I$ curve shown in Figure 38 d) was a constant, indicating that third-order NLR was the dominant mechanism at such excitation conditions. Open aperture measurements did not show any results for the range of intensities employed, and therefore NLA was negligible.

Figure 39 a), b), c) show the NLR result for $ZrTe_2$, which behaved qualitatively similar to the solvent, with the same positive sign for the NLR. Similar to the solvent, NLA was not observed in the range of intensities employed for the 2D exfoliated $ZrTe_2$ suspension.

NLA can arise, for instance, from one- or two-photon absorption, saturated absorption, or reverse saturated absorption, among others. All these phenomena have been identified in MoS_2 and WS_2 at intensities higher than $200\ GW/cm^2$, and using appropriate excitation photon energies compared to the bandgap of the material studied, including the equivalent wavelength of $800\ nm$ (BIKORIMANA et al, 2016; ZHENG et al, 2015; WANG et al, 2014).

We note that although we did not observe NLA in intensity ($< 140\ GW/cm^2$) regime, for intensities higher than $400\ GW/cm^2$, NLA well above the noise (which made the data unreliable between $140\ GW/cm^2$ and $400\ GW/cm^2$) was observed in the $ZrTe_2$ sample in ACN suspension, but it was also observed, with similar signal intensity, in ACN alone, and therefore it could not be unambiguously separated.

Figure 39 – Closed aperture Z-scan curves for $ZrTe_2$ layers for a) I=20 GW/cm², b) 50 GW/cm², and c) 120 GW/cm². d) n_2 x I curve show a linear behavior.

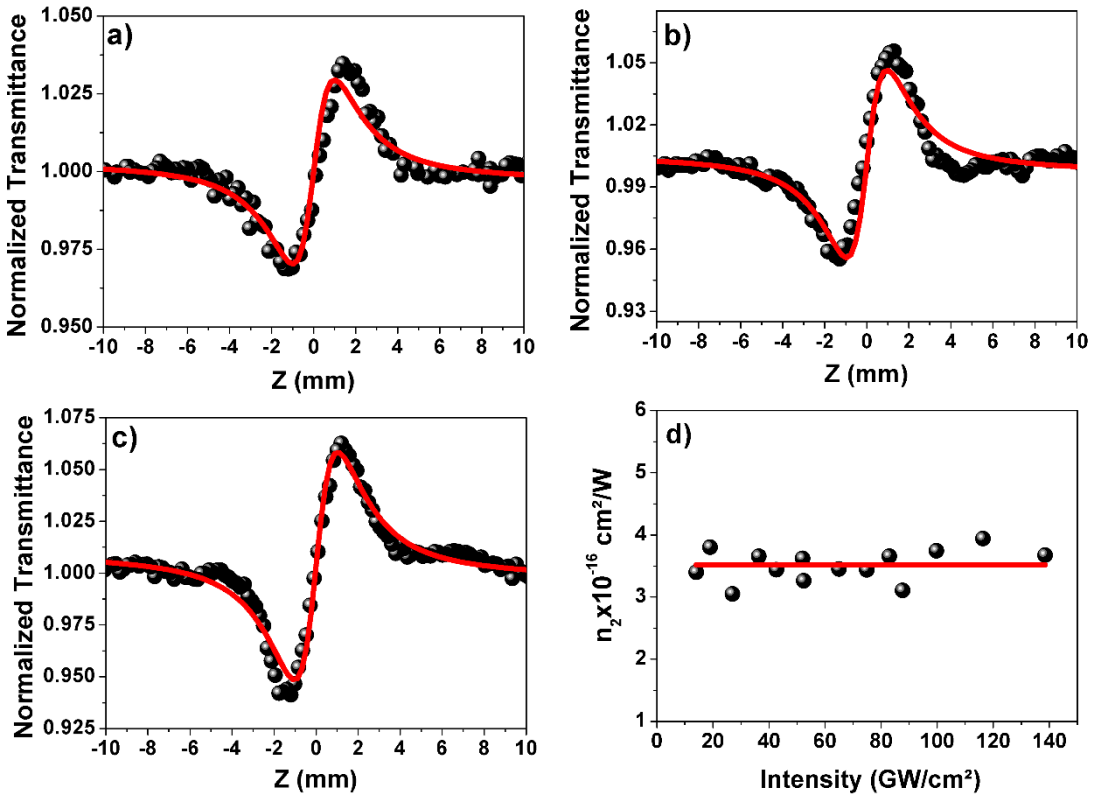

Source: The author (2021).

Therefore, our NLR data analysis was restricted to the range indicated above (maximum 140 GW/cm^2).

To determine the NLR coefficient, we employed the known equation for the closed aperture Z-Scan, as shown in chapter 3, section 3.3:

$$T = 1 + \frac{4\Delta\Phi^{(3)}a}{(a^2+1)(a^2+9)} \tag{4.9}$$

where $\Delta\Phi^{(3)} = kn_2 I\left(\frac{1-\exp(-\alpha_0 L)}{\alpha_0}\right)$, k is the wavevector, n_2 is the third-order NL refractive index, α_0 is the linear absorption coefficient, L the sample thickness and $a = z/z_0$, where z is the sample position and z_0 the Rayleigh parameter. The value of n_{NL}=+(4.2±0.3)×10^{-16} cm²/W was calculated using the equation (4.9).

To qualitatively explain the origin of the NLR in the 2D exfoliated $ZrTe_2$ monolayer suspension, its band structure was calculated using DFT, as shown in Figure 40. The DFT calculations are performed by the Mackgraphe collaborator group.

To summarize, Leandro Seixas, from the Mackgraphe collaborator group used *ab initio* methods based on Density Functional Theory (DFT), as implemented in SIESTA code (SOLER et al, 2002). He used exchange-correlation functional with nonlocal van der Waals (vdW) correction (VYDROV et al, 2010), energy mesh cutoff of 400 Ry, energy shift of 0.03 eV, and Monkhorst-Pack grid of 20x20x1 for Brillouin zone k-point sampling (MONKHORSTAND and PACK, 1976).

Figure 40 – Calculated band structure and projected density of states (PDOS) for $ZrTe_2$ using the DFT method. VHS indicates a van Hove singularity.

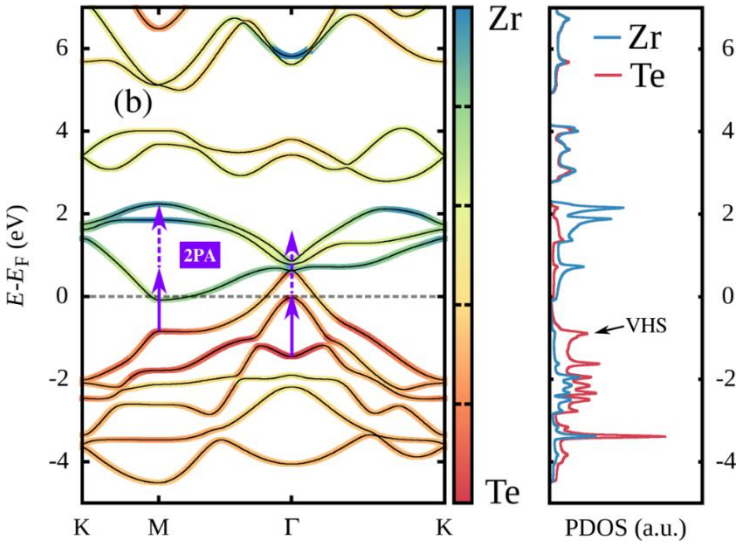

Source: Mackgraphe (São Paulo).

In the analysis of Figure 40, the length of the arrow corresponds to the excitation wavelength (800nm) energy of 1.55eV. They are placed in two possible positions in K-space, where the transition probability is higher compared to other positions. The one-photon transitions corresponding to 1.55eV are indicated by the heavy lines, whereas the dashed arrows indicate the additional 1.55eV for a two-photon process. From the DFT calculations, it can be seen that there is no one-photon transition from the valence to the conduction band, neither any two-photon transitions allowed by the selection rule. This explains that, in this experimental regime, there is none (or negligible) absorption that can lead to no nonlinear absorptive effects.

Also, because the incident photon energy is below the absorption gap, only virtual transitions occur, and the self-focusing nonlinear refraction measured is also explained by the band structure calculation. It should also be pointed out that the transition near point M of the band structure diagram is more likely since it also corresponds to a van Hove singularity, which indicates a higher oscillator strength.

4.2.3 $ZrTe_2$ as scatterers for Random Laser

Two random laser devices employing scatters with different dimensionality were prepared using Rhodamine 6G (Rh6G 10^{-4} M) in a solution of ACN. First, traditional 3D scatters consisting of bulk $ZrTe_2$ powders were suspended in ACN under vigorous stirring in a concentration of 35 μg/ml. On the other hand, 2D nanoscatters consisting of redox exfoliated monolayers of $ZrTe_2$ were suspended in ACN at 5 μg/mL. Anhydrous conditions during preparation and storage were maintained to minimize any solution instability or photo-hydrolytic degradation processes. The suspension was placed in a 1cm x 1cm cuvette and excited by the second harmonic of a pulsed (532nm, 5Hz, 5ns) Nd: YAG laser. The excitation beam was incident on the cell at ~45 degrees angle of incidence (concerning the cell front wall) and the emission was collected perpendicularly to the cell front wall. Reflections from the cuvette walls were avoided. The collected emission was directed to a spectrometer (Ocean Optics HR 4000), and the emitted intensity and bandwidth variation as a function of pump energy was obtained.

The typical characterization of random laser operation is shown in Figure 41, where the intensity emission and bandwidth reduction as a function of excitation energy are clearly seen for both bulk 3D $ZrTe_2$ particles (Figure 41 (a), and (b)) and 2D exfoliated $ZrTe_2$ monolayers (41 (c), (d). Figure 42(a) shows the emission spectrum for a pulse excitation energy below the threshold (0.33 mJ) and another above the threshold (4.3 mJ) for which the narrowing of the

full width at half maximum (FWHM) is observed. Figure 41(b) presents the bandwidth narrowing, characterized by the FWHM and the peak intensity as a function of the excitation pulse energy. For the 3D $ZrTe_2$ sample, the RL threshold can be determined from the emitted intensity slope, being approximately 1.8 mJ.

Figures 41(c) and 42(d) show the same phenomenon described above, but for the 2D $ZrTe_2$ sample. It is also evident the decrease in the FWHM of the emission spectrum, although the narrowing reaches approximately 15 nm, instead of ~5nm observed for the powder case. The threshold, in this case, is approximately 1 mJ, which shows that the two-dimensional sample is somewhat more efficient than in the 3D case.

One important issue in RLs, particularly organic-based RLs, is the useful lifetime, meaning the RL lifetime under pumping conditions above the threshold. It has been reported in many publications that, due to chemical incompatibility between the organic dye and the scatterer. For instance, semiconductor nanoscatters, such as TiO_2, degrade organics via photocatalytic production of reactive oxygen species under hydrous conditions (PAVAR, et al, 2018). This photodegradation limits RL lifetime. to just a few minutes under 5-10Hz repetition rate. PINCHEIRA et al, 2016 use the management of scatter. CAO, 2005 and GOMES et al, 2016 use a different gain-scatter combination. For example, semi-metals, such as $ZrTe_2$, do not photogenerated electron-hole pairs aligned with water's redox potential. Thus, photodegradation of the organic fluorophore (Rh6G) in the anhydrous $ZrTe_2$ suspensions will be suppressed, increasing the relative RL lifetime.

Figure 41 – (a) In blue is shown the spontaneous emission spectrum of Rh6G and in red the stimulated emission. (b) Output intensity as a function of the Input energy, in blue and in red the decrease of linewidth for the bulk powder. (c) in blue is shown the spontaneous emission spectrum of Rh6G and in red the stimulated emission, and (d) Output intensity in function Input energy, in blue and in red the decrease of linewidth for the layered $ZrTe_2$.

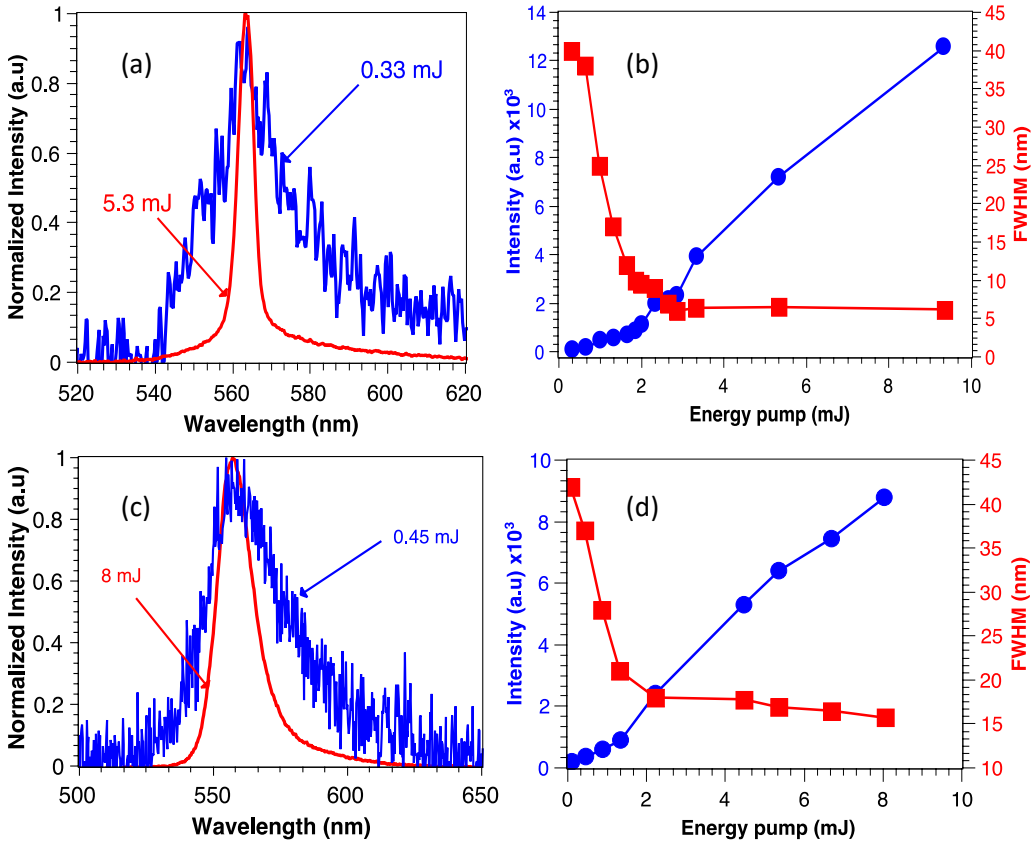

Source: The author (2021).

Figure 42 shows the results of the $ZrTe_2$ for both the 3D particles powder-based RL (Figure 42(a) and the 2D exfoliated monolayer-based RL (Figure 42(b)), showing no photodegradation for over 90 min of continuous operation.

Figure 42 - Intensity behavior of the RL as a function of the time in seconds. The range of energy to which the 2D ((b) and 3D ((a) samples were exposed ranges from 300 ***μJ*** to 10 mJ. No photodegradation was observed.

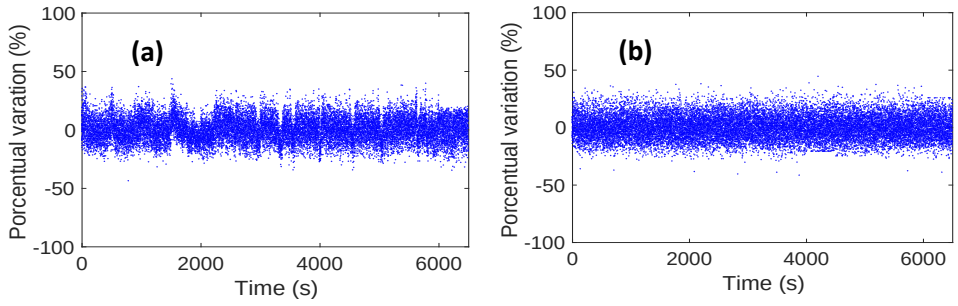

Source: The author (2021).

Due to its long-term (several hours) lifetime and good shot-to-shot stability, we tested both $ZrTe_2$-based RL systems for observation of photonic paramagnetic-to-photonic spin-glass transition, similar to the work reported by PINCHEIRA et al, 2016, which followed the pioneering work of GHOFRANIHA et al, 2014. This is a phenomenon very characteristic of RL, and as mentioned before arises from a combination of scattering, multimode emission, and gain, already observed in different RLs, besides the already referenced work (GOMES et al, 2016; TOMASI et al, 2016; SARKAR et al, 2017; XIA et al, 2019). Although this subject has been treated theoretically in early works, we summarize the main points here (GHOFRANIHA et al, 2015; GOMES et al, 2016; MÉZARD et al, 1987). In the laser physics context, each laser shot corresponds to one replica, which is a copy of the random laser emission under very identical experimental conditions, provided the configurational disorder set by the random positions of the scatters does not change much during the N_s laser shots. It can be shown that P(q), the probability density function (PDF), analogous to the Parisi order parameter in the RSB spin-glass theory by MÉZARD et al, 1987, describes the distribution of replicas overlaps $\boldsymbol{q} = \boldsymbol{q_{\gamma\beta}}$, therefore indicating a photonic paramagnetic or a RSB spin-glass phase, whether it peaks solely at $\boldsymbol{q} = \mathbf{0}$ (no RSB) or at values $|\boldsymbol{q}| \neq \mathbf{0}$ (RSB), respectively.

To characterize the transition from the fluorescent paramagnetic to the RL glassy behavior, an evaluation of the two-point correlation function that measures pulse-to-pulse fluctuations in the spectral intensity averaged over N_s laser shots at each pump energy is given by (GHOFRANIHA et al, 2015; PINCHEIRA et al, 2016):

$$q_{\gamma\beta} = \frac{\sum_k \Delta_\gamma(k)\Delta_\beta(k)}{\sqrt{\left[\sum_k \Delta_\gamma^2(k)\right]\left[\sum_k \Delta_\beta^2(k)\right]}}, \tag{4.10}$$

where $\gamma, \beta = 1,2,\dots,N_s$. The average intensity at the mode wavelength indexed by k reads $\bar{I}(k) = \sum_{\gamma=1}^{N_s} I_\gamma(k)/N_s$, and the intensity fluctuation is measured by $\Delta_\gamma(k) = I_\gamma(k) - \bar{I}(k)$.

Figure 43 - Figures 43)–43 c) and 43e)-43 g) display the PDF P (q) of the system for Ns = 2000 shots bulk powder 3D $ZrTe_2$ particles and 2D exfoliated $ZrTe_2$ monolayers RL respectively. Energies 330 μJ, 1.67 mJ, and 9.3 mJ were chosen under, near, and above the threshold to sample 3D. In the case 2D, the energies shown are 90 μJ, 450 $\mu J$and 4.4 mJ. Figure 43(d) and 43 (h) shows q_{max} corresponding to the position of the maximum of P(|q|) versus pumping to 3D and 2D sample respectively

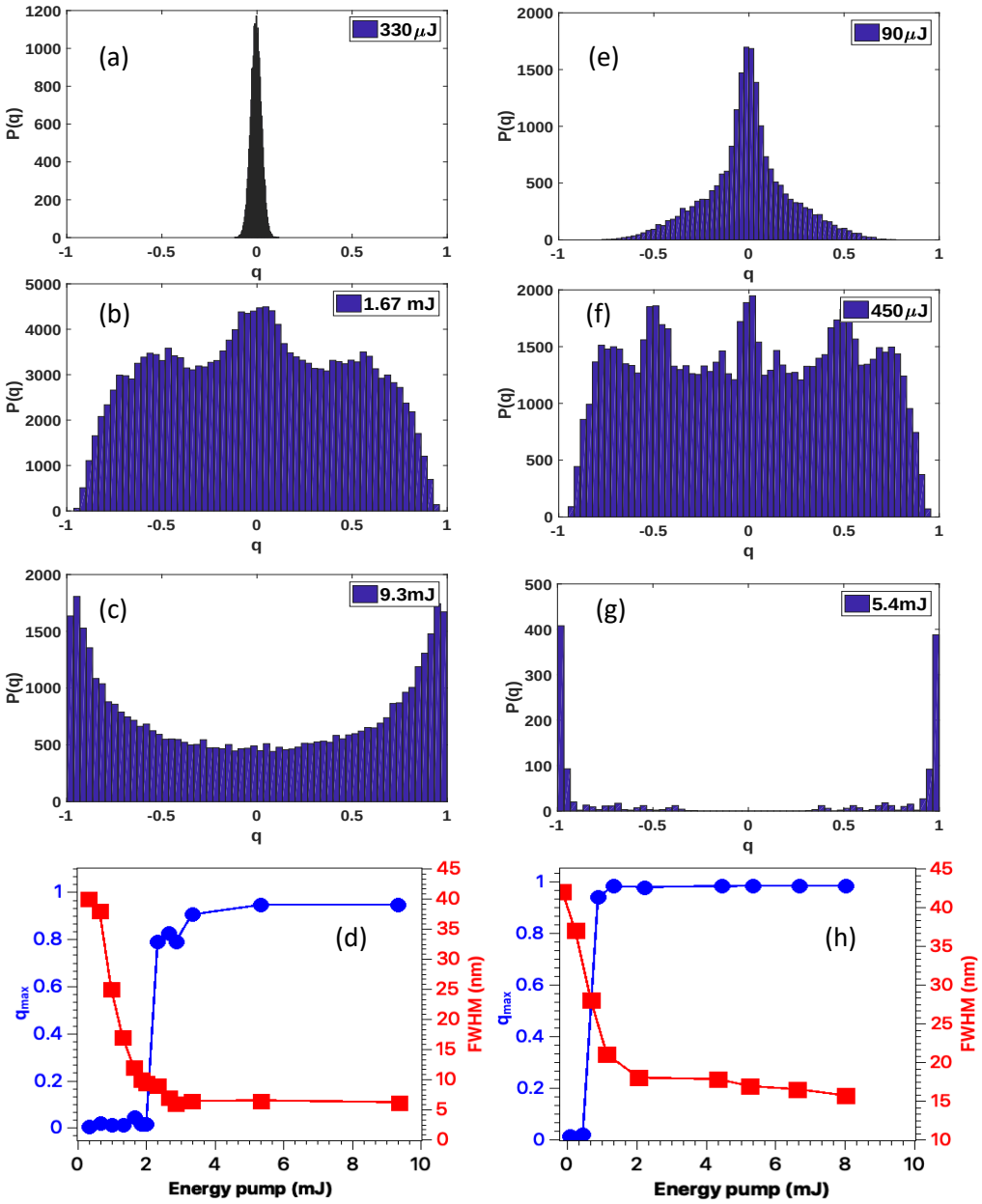

Source: The author (2021).

Considering that neither the nanoflakes or the powder in the ACN solution did not degrade or precipitate during the experiment (~2 hours), one can consider the system conditions appropriate for the existence of replicas. Figure 43 shows the PDF $P(q)$ of both RL systems

studied here, for N_s = 2000 shots. The characteristic signature of both phases below and above the threshold are seen in both 3D and 2D configurations (Figures 43a-c) and e-g) respectively), and the calculated q_{max} in both cases show the phase-transition at the threshold values corresponding to the estimated before from Figure 41. The phase transition is very distinct and the threshold values are quantitatively much better determined.

4.3 NbS_2

NbS_2 is a metallic LTMD'S, having superconductivity and Charge Density Wave (CDW) properties at low temperatures. NbS_2 layers can have 1T, 2H, or 3R phases (see Figure 19). One of the first works of NbS_2 monolayers was interested in investigating the electric transport properties (NAITO and TANAKA, 1982). The Raman spectrum was studied by NASHAMIRA et al, 1982 that identify the vibrational modes E_{2g}^1 and A_{1g}.

The majority of the works is concentrated on the investigation of superconductivity of NbS_2 layers. GUILLAMÓN et al, 2008 investigate the superconductivity in 2H-NbS_2 using Scanning tunneling microscopy and spectroscopic measurements. The superconductivity properties of NbS_2 flakes under pressure were investigated by TISSEN et al, 2013. In this paper, the authors showed an increase in the critical temperature when pressure is applied to the flakes. CDW was studied by LEROUX et al, 2018. In this work, the authors showed traces of CDW a technique of diffusive X – ray scattering.

UV-VIS-NIR Spectroscopy:

Absorption spectroscopy was performed to understand possible optical transitions in metallic 2H-NbS_2. The absorption spectrum measurements were performed using a sample concentration of $5\mu g/ml$. A cell with an optical path length of 2mm was employed to perform the measurements.

Figure 44 shows the extinction spectra of NbS_2 layers. Due to the metallic character, the extinction spectrum is characterized by no excitons peaks as occur for semiconductors. A small absorption band is shown close to 500 nm and can be related to plasmon resonance.

Figure 44 – Extinction spectrum for NbS_2 layers.

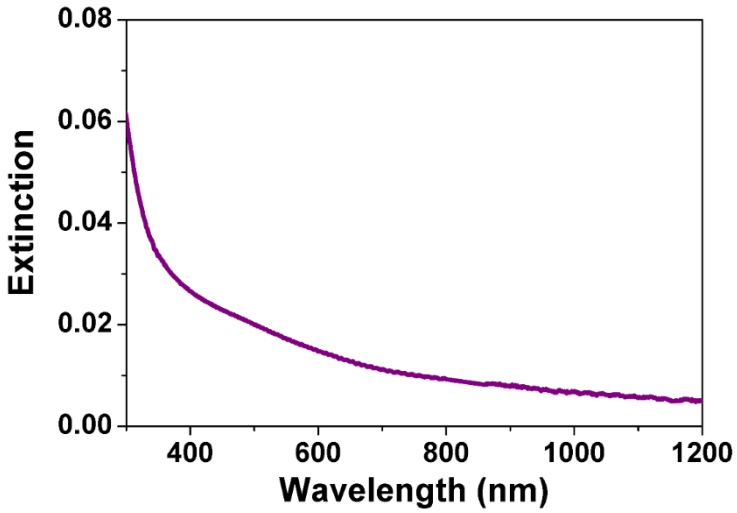

Source: The author (2021).

4.3.1 Nonlinear Refraction in NbS_2 layers

The exfoliated metallic NbS_2 showed a quite interesting behavior for the NLR, as shown in Figure 45. An inversion in the sign of the NLR as the intensity increased was observed, changing from negative (self-defocusing) for intensities below ~22 GW/cm^2 to positive (self-focusing) above this critical intensity. This is clearly seen in the Z-scan profiles shown in Figures 45(a) and 45(b), and in the $n_2 \times I$ plot in Figure 45c). The calculated value of n_2, for intensities above the critical value of ~22 GW/cm^2 is 3.0±0.2 x10^{-16} cm^2/W, as shown in Table 4

Figure 45 - Closed aperture measurements for NbS_2 (a) below the critical intensity of ~22 GW/cm^2 , (b) above the critical intensity.

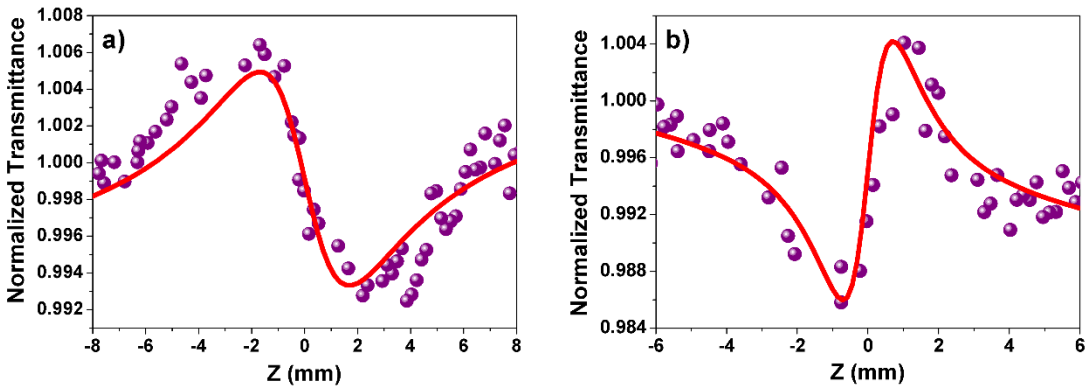

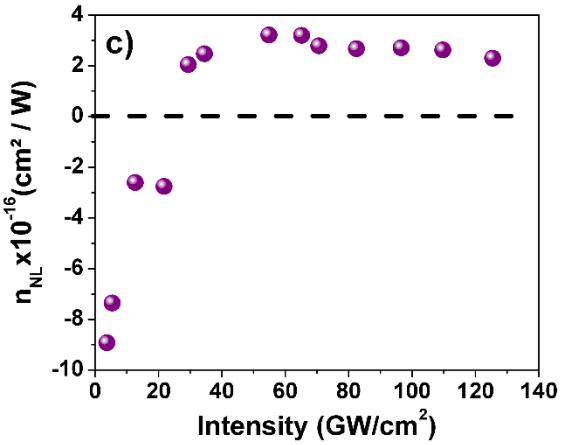

Source: The author (2021).

ZHAN et al, 2001, have shown a change in the nonlinear refractive index from positive to negative in an azo-perydinum based molecule and attributed this change to Excited-State Absorption (ESA). LAWRENCE et al, 1994 showed the same behavior for a single crystal of *p*-toluene sulfonate excited on 1064 nm; a dependence with the square of the intensity was found. GARCIA, 2012 investigated a molecule that shows a behavior close to Figure 45 c). A dynamic model was developed to understand the behavior of the absorption process. A competition between the SA, ESA, and 2PA is responsible for the change in the nonlinear refractive index signal.

4.3.2 Nonlinear Absorption Measurements

The open aperture Z-Scan allows the measurement of the NLA coefficient, which was observed in the NbS_2 sample, as shown in Figure 46. The NLA profile varies as a function of intensity, changing from a 2PA to two-photon saturated absorption (TPSA) at the intensity of ≈ 64.2 GW/cm^2. This behavior is probably associated with the change in NLR, since after saturation is reached, the nonlinear refractive index changes accordingly to the nonlinear Krammers-Kronig relation. The solid curves on the data were obtained as described in the section below.

Figure 46 – NLA measurements for sample NbS_2 for a) I = 12.7 GW/cm² b) I = 64.2 GW/cm² c) I = 96.5 GW/cm² and (d) 124.6 GW/cm².

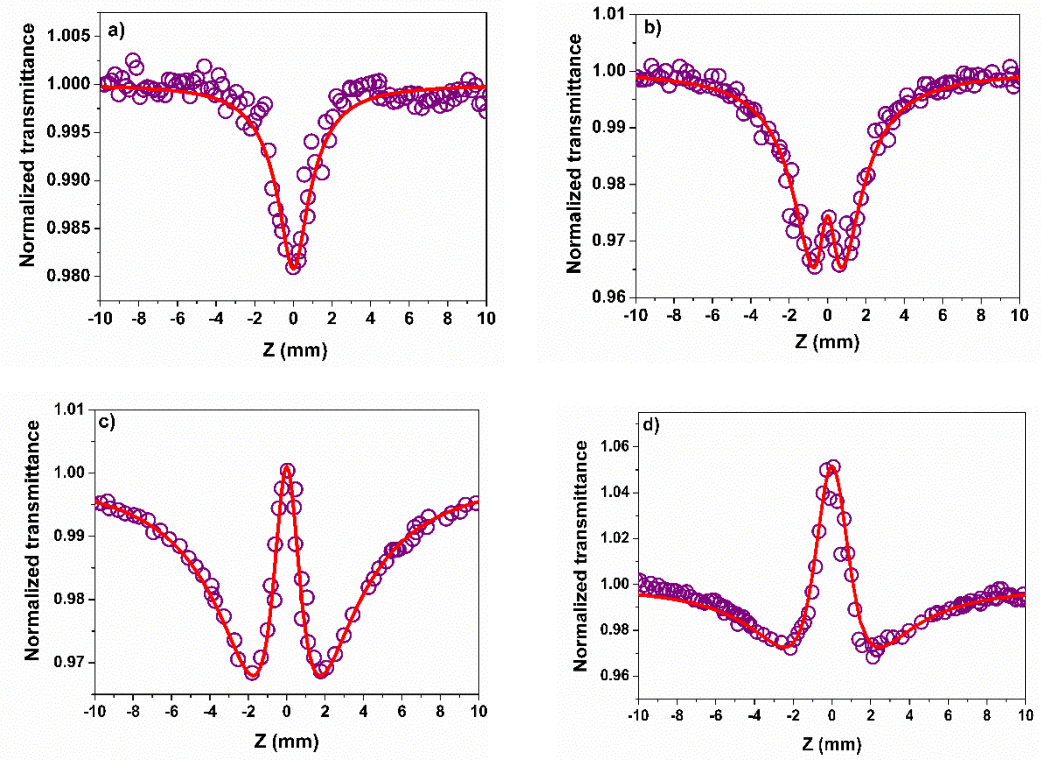

Source: The author (2021).

4.3.3 Atomistic simulations

Before discussing the above results, we describe here the first-principles calculations method, based on density functional theory (DFT) (HOHENBERG AND KOHN, 1964; KOHN and SHAM, 1965) as implemented in SIESTA code (SOLER et al, 2002) to calculate the electronic properties of NbS_2. Leandro Seixas, from the Mackgraphe collaborator group, used a localized double-ζ basis (DZP), with an energy shift of 0.03 eV, and a mesh cutoff of 400 Ry. He used norm-conserved pseudopotentials with Troullier-Martins parameterization (HOHENBERG AND KOHN, 1964). For the exchange-correlation functional, the Vydrov-van Voorhis functional (VV10) (KOHN and SHAM, 1965), which includes non-local terms for the correction of van der Waals forces. The Brillouin zone sampling was based on Monkhorst-Pack method (SOLER et al, 2002), with 20x20x1 grid for monolayers, and 20x20x7 grid for bulks. For the density of states calculations, we use thinner grids of 200x200x1 for monolayer and 80x80x40 for bulk. All geometries were completely relaxed until forces less than 0.001 eV/Å.

To determine the NLO coefficients, we employed the known equations for the closed and open aperture Z-Scan, as described in Chapter 3, section 3.3:

$$T = 1 + \frac{4\Delta\Phi^{(3)}a}{(a^2+1)(a^2+9)} \tag{4.11}$$

where $\Delta\Phi^{(3)} = kn_2I\left(\frac{1-\exp(-\alpha_0 L)}{\alpha_0}\right)$, k is the wavevector, n_2 is the third-order nonlinear refractive index, α_0 is the linear absorption coefficient, L is the sample length, $a = z/z_0$, where z is the sample position and z_0 the Rayleigh parameter.

Figure 47 - Theoretical curves from different nonlinear absorption contributions. The intensities are a) 12.7 GW/cm², b) 64.2 GW/cm², c) 96.5 GW/cm² and d) 124.6 GW/cm².

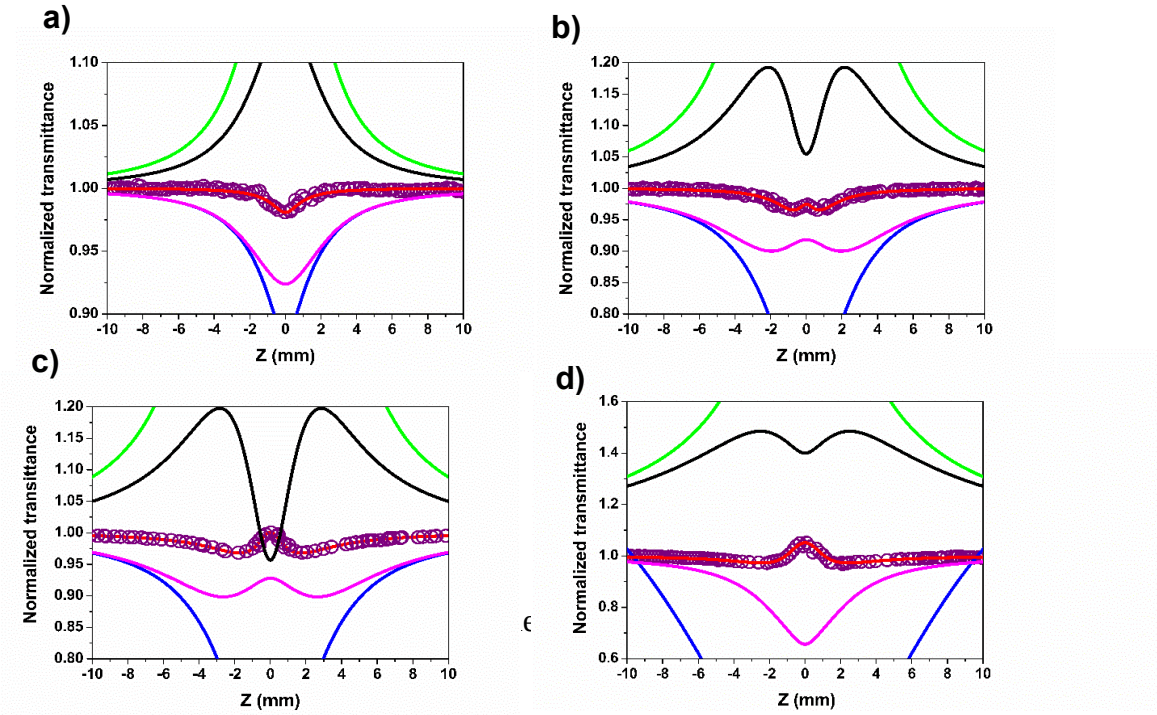

Source: The author (2021).

In order to identify the physical mechanisms contributing to the nonlinear absorption profiles we tried to fit the data in Figure 47 considering the following contributions: (1) saturated one-photon absorption (1PA) only - green lines; (2) simultaneous saturation of 1PA and two-photon absorption (2PA) - black lines; (3) 1PA plus 2PA (no saturation effects) – blue lines; (4) 1PA (no saturation) and saturated 2PA –magenta lines; (5) 1PA (no saturation), saturated 2PA saturation and nonlinear scattering – red lines.

We considered the 1PA (2PA) saturation intensity equal to 10 GW/cm² (52 GW/cm²); the 2PA coefficient (α_2) was 0.21 cm/GW and the nonlinear scattering coefficient (η_2) was -0.19 cm/GW. The 1 PA and 2PA saturation intensity used was 10 GW/cm² and 52 GW/cm², the 2PA coefficient (α_2) was 0.21 cm/GW and the nonlinear scattering (η_2) was -0.19 cm/GW.

Different 2PA broadening processes were tested to fit the saturation of two-photon absorption:

hyperbolic model:

$$\alpha(I) = \frac{\alpha_2(I)}{1+I/I_S}, \tag{4.12}$$

homogeneous model:

$$\alpha(I) = \frac{\alpha_2(I)}{1+I^2/I_S^2}, \tag{4.13}$$

inhomogeneous model:

$$\alpha(I) = \frac{\alpha_2(I)}{\sqrt{1+I^2/I_S^2}}, \tag{4.14}$$

Figure 48 shows the theoretical fits of the nonlinear absorption curves for the three models. The experimental data is the same as in Figure 47, but the scales are different to show the details.

The green curve was obtained considering the hyperbolic model; the blue curve with the homogeneous model and the red curve with the inhomogeneous broadening model. All curves were plotted considering the equations (4.12), (4.13), and (4.14) plus the nonlinear scattering contribution in all cases. The nonlinear coefficients were: $\alpha_2 = 0.21\, cm/GW$ and $\eta_2 = -0.19\, cm/GW$. The 2PA saturation intensity was 52 GW/cm².

The open aperture Z-scan scheme gives information on the NLA, which can be due to two-photon absorption (TPA) or multi-photon absorption (MPA), saturated absorption (SA), reverse saturation absorption (RSA), or two-photon saturated absorption (TPSA). These phenomena were identified in MoS_2 and WS_2 at intensities higher than 200 GW/cm^2 and using appropriate excitation photon energies compared to the bandgap of the material studied (DONG et al, 2015; VARMA et al, 2017; THOMAS et al, 2014; ZHENG et al, 2015; BIKORIMANA et al, 2016). The equations used to fit the experimental data depend upon the model employed, which can include nonsaturable or saturable TPA due to hyperbolic homogeneously or inhomogeneously broadening models (ZHANG et al, 2018). To fit our experimental results in NbS_2, we investigated contributions for the open aperture Z-scan profile due to saturation of the linear absorption coefficient, TPA saturation, and nonlinear light scattering (NLS) as illustrated in Figure 49.

Figure 48 – Theoretical fits of three models of nonlinear absorption saturation. The intensities are a) 12.7 GW/cm², b) 64.2 GW/cm², c) 96.5 GW/cm² and d) 124.6 GW/cm².

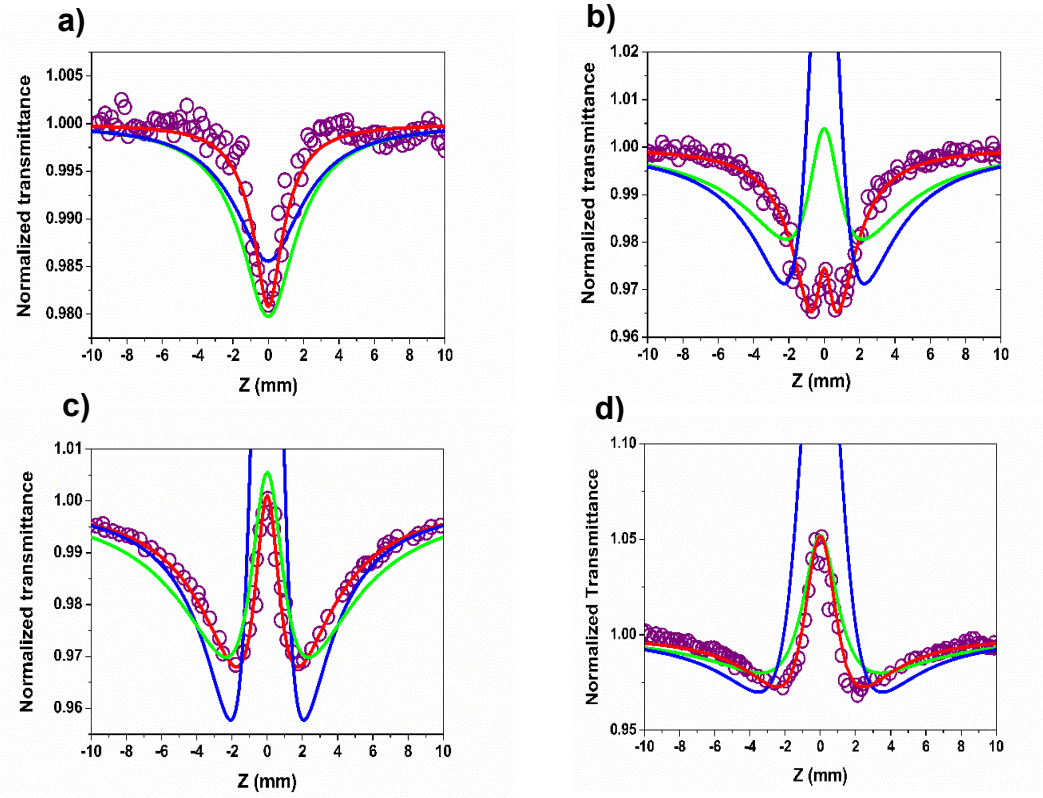

Source: The author (2021).

The best-fitting corresponding to the solid curves of Figure 47 was obtained considering the saturation of TPA and contribution of NLS which is relevant for intensities larger than 60 GW/cm^2, accordingly to Equation (4.15):

$$\alpha(I) = \alpha_0 + \frac{\alpha_2 I}{\sqrt{1+I^2/I_S^2}} + \eta_2 I \qquad (4.15)$$

where α_0 is the linear absorption coefficient, α_2 is the TPA coefficient, I_S is the TPA saturation intensity, and η_2 is the nonlinear scattering coefficient.

The solid lines shown in Figure 48 were fitted considering the effect of inhomogeneous broadening. Other mechanisms were evaluated as discussed in Figure 48 but they could not reproduce the Z-scan profiles. The saturation intensities obtained, as well as the coefficients α_2 and η_2, are shown in Table 4 (with α_0 = 8.2 cm^{-1} at 800 nm), together with literature values for other LTMD's.

Also shown in Table 4 is the value of n_2 for MoS_2 in ACN, which is of the same order as for NbS_2 (for intensities above I_S) but does not present inversion of sign in the whole range of intensities used.

We also investigated the nonlinear light scattering (NLS) properties of the NbS_2 suspension by measuring the scattered intensity as a function of input intensity, and the results are shown in Figure 49. Notice that the scattered intensity starts to deviate from a linear response at around 75 GW/cm^2.

DE OLIVEIRA, et al, 2019 showed that NLS can play a role in the optical nonlinearity of nanoparticles, leading to, e.g., an optical limiting behavior in LTMD's (DONG et al, 2015).

Figure 49 – Scattered light intensity behavior versus the input laser intensity in the NbS_2 suspension.

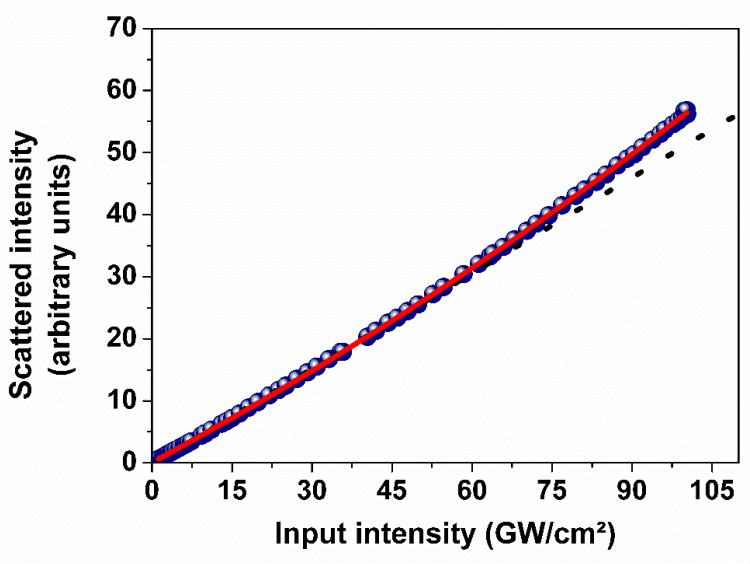

Source: The author (2021).

Table 4 – Experimentally determined values of the NLR and NLA coefficients for the NbS_2 suspension and related literature values for other LTMD'Ss in the same spectro-temporal regime (800nm, ~100fs)

Sample	Solvent/ Substrate	n_2 x10^{-16} cm²/W	α_2, η_2 (cm/GW)	I_s (GW/cm^2)	Ref.
NbS_2	ACN	+(3.0±0.2) (I > I_c)	$\alpha_2 = 2.1 \times 10^{-1}$ $\eta_2 = 1.1 \times 10^{-1}$	52	This work
MoS_2	ACN	+(4.5±0.3)	----------	--------	This work
MoS_2	NMP	NA	α_2= 4.6 x 10^{-3}	413±24	WANG et al, 2013

MoS_2	CHP	NA	α_2 = -2.4 x 10^{-2}	381±346	WANG et al, 2014
WS_2	Sapphire	+1.2	α_2 = -3.7 x 10^{-5}	NA	ZHENG et al, 2015

Source: The author (2021).

To understand qualitatively the origin of the nonlinearity in NbS_2 was calculated the electronic band structure of 2H-NbS_2 monolayer and bulk with first-principles methods based on density functional theory as described before, whose results are shown in Figure 50. For the monolayer, indicate possible electronic transitions for one-photon and two-photon absorption for incident laser photons with energy of 1.55 eV (~800 nm). In principle, to conserve angular momentum, one-photon transitions must occur from bands with major S compositions (p orbitals) to bands with primary Nb composition (d orbitals), while two-photon transitions may occur between two bands with major Nb composition, or from a band with major S composition to a band with mixed composition. If the material is doped with electrons, it can make electronic transitions for two-photon absorption in a van Hove singularity at K point. For this van Hove singularity, there is a peak in the density of states that can increase the optical absorption. VAN LOON, et al 2018 found similar results for the monolayer band structure.

Figure 50 – Electronic band structure and projected density of states (PDOS) of 2H-NbS_2: (a) monolayer; (b) bulk. Projections on the Nb orbitals are represented in blue, while projections on the S orbitals are represented in red. One photon absorption (1PA) and two-photon absorption (2PA) are depicted in blue and black, respectively.

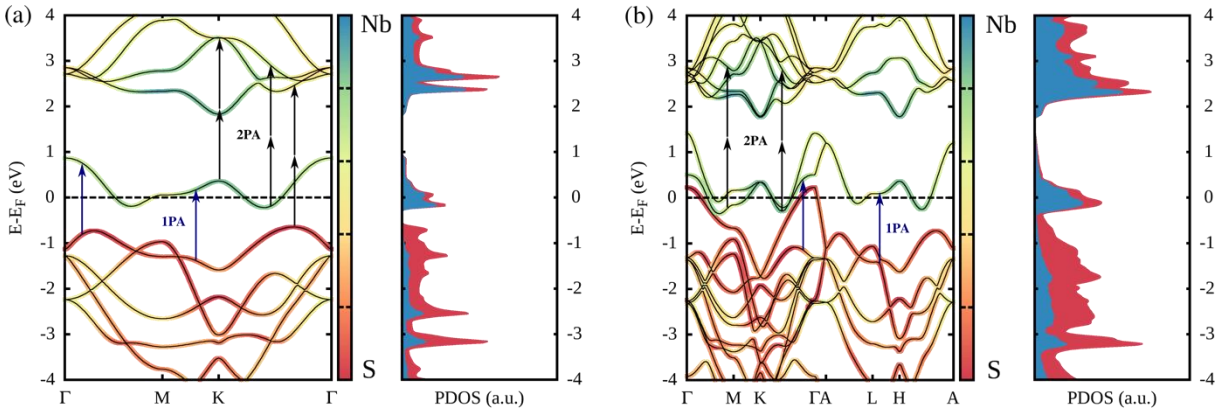

Source: Mackgraphe (São Paulo)

A qualitative analysis of Figure 51 shows that both one-photon and two-photon absorption are allowed. In particular, for doped NbS_2, the two-photon process may involve a van Hove singularity, which would greatly enhance the NLA. Further increase in input pump

intensity leads to TPA saturation, as observed in our experiments. The negative n_2 sign for intensities below the critical intensity to induce the NLR sign change is consistent with this behavior. As we mentioned before, the change in sign of n_2 may follow from the change in sign in the NLA since n_2 and α_2 are related via the nonlinear Krammers –Kronig relation. However, a quantitative description of the entire phenomenon is beyond the scope of this work.

4.4 MoS_2

Molybdenum disulfide (MoS_2) is one of the more investigated LTMD'S. The literature revision in section 4.1 is almost entirely dedicated to MoS_2 studies, due to the great number of works in the literature (SPLENDIANI et al, 2010; LI et al, 2012; WINCHESTER, et al 2014). Several authors studied optical nonlinearities in MoS_2 in both multilayers (BIKORIMANA et al, 2016; ZHANG et al, 2018) and monolayer regimes (YIN et al, 2014), in suspension (DHASMANA et al, 2016) or films (ZHANG et al, 2014), and different ranges of intensity (WANG et al, 2015; ZHANG et al, 2014). However, the fifth-order nonlinearity never was exploited in this sample (or in any LTMD'S).

Absorption Spectroscopy: Absorbance spectroscopy was performed to characterize the optical transitions in LTMD's. Figure 51 shows the absorption spectrum from MoS_2.

Figure 51 – Extinction spectrum for MoS_2 flakes suspended in ACN.

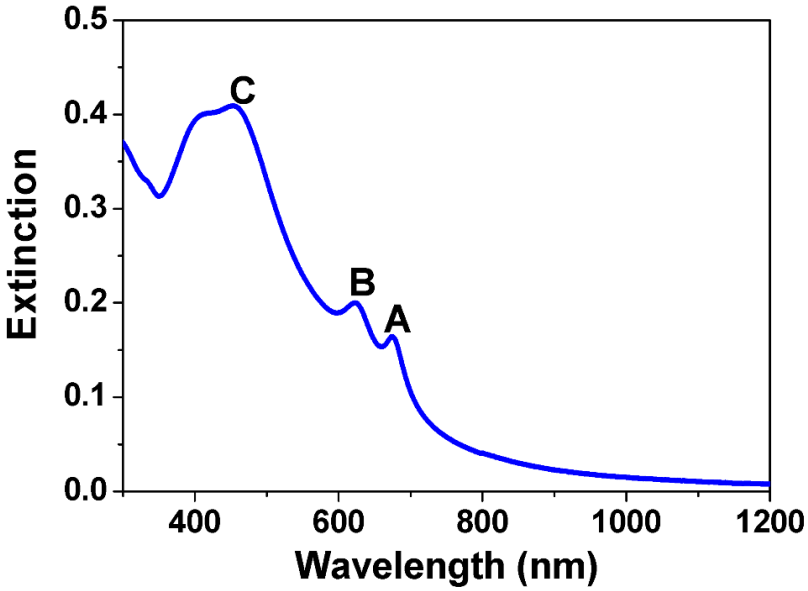

Source: The author (2021).

In semiconductor MoS_2, the absorption spectrum is characterized by three excitonic transitions in the visible range: 675 nm (1.83 eV) 623 nm (1.99 eV), and 454 nm (2.73 eV) and are named excitons A, B, and C, respectively.

4.4.1 Real third- and fifth-order nonlinearity in MoS_2

For the MoS_2 suspension, a different behavior was found as the intensity was raised. Figure 52(a, i) and their respective insets show representative closed aperture Z-scan curves, with a positive sign for the effective nonlinear susceptibility at the measured intensities. For intensities up to ~ 60 GW/cm^2, the curve was symmetric and fitted well a third-order nonlinearity contribution.

Figure 52 a)-i) Z-scan profiles for MoS_2 flakes for different intensities.

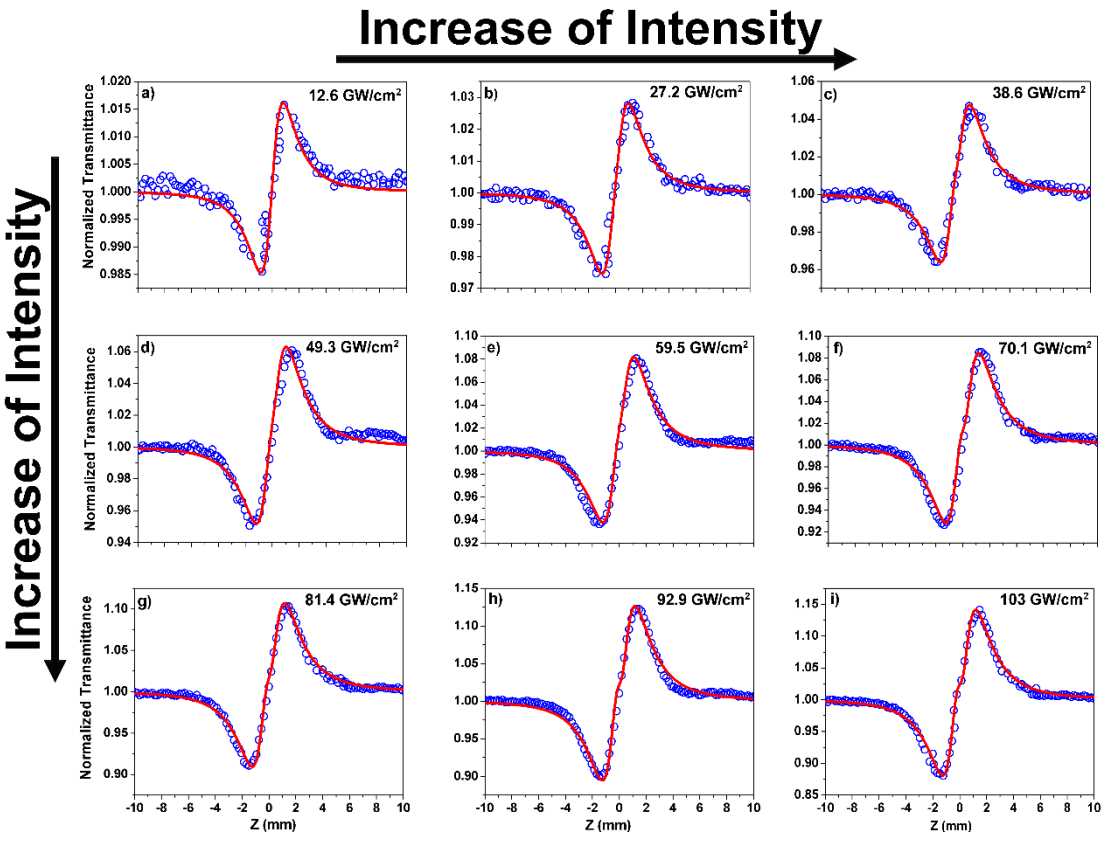

Source: The author (2021).

However, above this value an asymmetry (Figure 53b) and inset) was seen in the Z-scan curve, compatible with the influence of a higher-order nonlinearity as described by the equations. For better visualization of the curves in Figure 53, it is needed a zoom in the figure. Two intensities, one low and a higher intensity are the choices to see this behavior.

Further confirmation of the presence of a higher-order nonlinearity can be seen in Figure 54 where the closed aperture curves for MoS_2 (Figure 54a) and WS_2 (Figure 54b) are shown, for a relatively high intensity ~70-75 GW/cm^2.

Figure 53 – Closed aperture Z-scan curves for MoS_2 at intensities of (a) 38.6 GW/cm^2 and (b) 103 GW/cm^2. The inset shows a zoom at the symmetric (a) and asymmetric characteristic of the influence of higher-order effects in (b). The dots are the experimental results and the solid lines the theoretical fit.

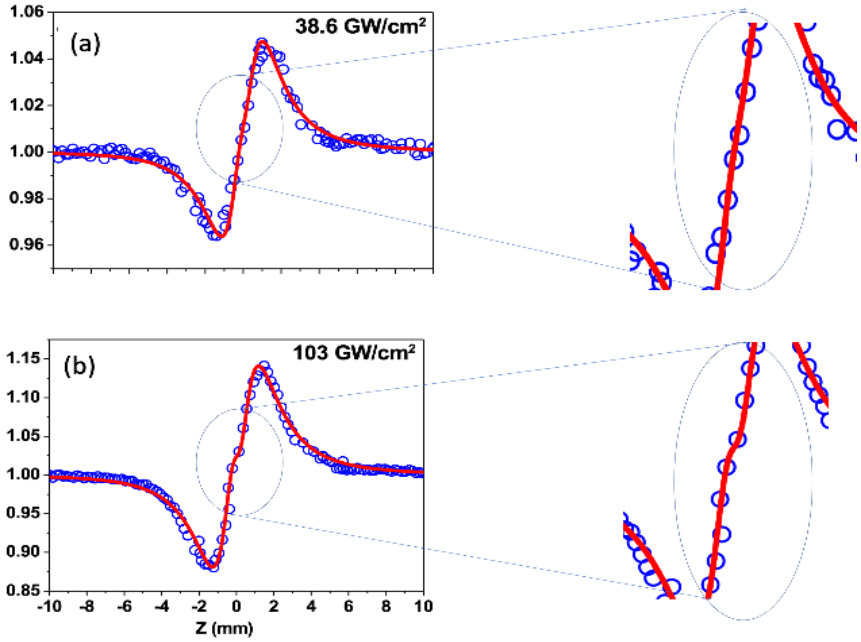

Source: The author (2021).

In both figures, the dots are the experimental data and the solid lines are the calculations, as indicated, using the appropriate equations (see below).

Figure 54 – (a) Closed aperture Z-scan profile for MoS_2; The double arrow indicates the peak-to-valley Z-distance, showing that it is larger for the fifth-order curve (red arrow) than for the third-order one (blue arrow). (b) Same, for WS_2. ($|\Delta T|/I$) dependence on I for (c) MoS_2 and (d) WS_2.

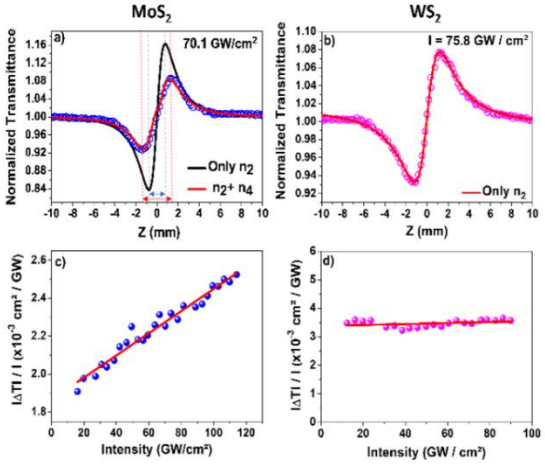

Source: The author (2021).

First, we note that the peak-to-valley distance in the Z-direction is larger for the fifth-order closed aperture Z-scan curve than for the third-order, as pointed by KONG et al, 2009. In both figures, the dots are the experimental data and the solid lines are the calculations, as indicated, using the appropriate equations (see below).

We verified this behavior in our case and confirmed such variation. Second, and perhaps most important as an indicator of high order contributions to the nonlinearity, the (|ΔT|/I) versus I functional behavior for MoS_2 shows a linear dependence, characteristic of fifth-order nonlinear contribution (GU et al, 2005), whereas for WS_2 it shows a constant behavior, which signalizes the sole contribution of third-order effect.

Figure 55 - $\frac{\Delta T_{p-v}}{Z_0} \times I$ plot. For write, part is pure third-order nonlinearity and the green part is third-and fifth-order contribution.

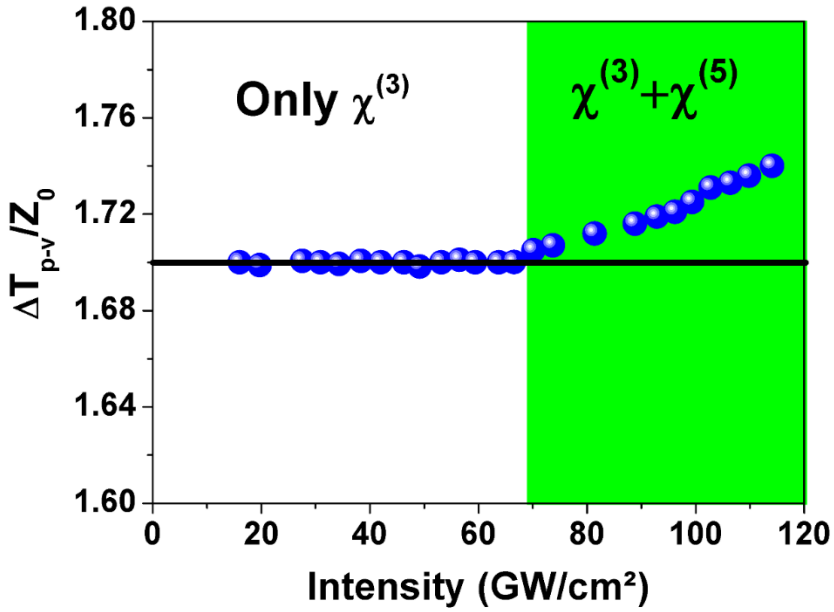

Source: The author (2021).

These findings can be understood by considering the extinction spectra shown in Figure 55 and the respective nanoflake concentrations: 70 μg/ml for MoS_2 and 40 μg/ml for WS_2. Considering the atomic weights of MoS_2 (160 Da) and WS_2 (248 Da), one concludes that the studied samples had 2.7 times more MoS_2 than WS_2 nanoflakes. Also, the nanoflakes' average lateral extension is 84 nm for MoS_2 and 325 nm for WS_2. Therefore, the ratio between the nanoflakes areas is 15 times and since the extinction coefficient is proportional to the scattering and absorption cross-sections, is reasonable to assume that the larger geometric cross-section of the WS_2 nanoflakes originates the major contribution for the nonlinear transmittance detected in the closed aperture Z-scan experiment because owing to the large scattering, less light is transmitted by the sample and this reflects in the larger $|\Delta T|$ measured. On the other hand, with

the basis on the nanoflakes' concentrations and the materials' atomic weights, one concludes that the samples had 2.7×15≈40 more MoS_2 nanoflakes than WS_2. This explains why $|\Delta T|/I$ is independent if I for WS_2; the expected signal due to $\chi_{eff}^{(5)}$ in the Z-scan experiment with WS_2 should be much smaller than for MoS_2 and the small concentration of WS_2 justifies the absence of a contribution from $n_{4,eff}$.to the Z-scan traces, within the apparatus sensitivity.

The experimental results were analyzed by following the procedure of (GU et al, 2005). Accordingly, for low intensities such that the only relevant nonlinearity is the third-order, the experimental results for the samples' transmittance can be fit by using the expression:

$$T(a) = 1 + \frac{4\Delta\Phi_0^{(3)} a}{(a^2+1)(a^2+9)} \tag{4.16}$$

where $\Delta\Phi^{(3)} = kn_2 I(1 - \exp(-\alpha_0 L)/\alpha_0)$, k is the wavevector, n_2 is the nonlinear refractive index associated with the third-order nonlinear response, α_0 is the linear absorption coefficient, L is the sample length, $a = z/z_0$, where z is the sample position with respect to the focal point and z_0 is the Rayleigh length.

For intensities larger than ~70GW/cm² the normalized transmittance profile changes in the focal region and the expression for $T(a)$, based on the Gaussian decomposition method was used for the theoretical fit (GU et al, 2005).

$$T(a) = \sum_{m,m'}^{N_{opt}} f_{mv} f^*_{m'v'} \frac{a^2+1}{[a + i(2B_{mv}+1)][a - i(2B_{m'v'}+1]}, \tag{4.17}$$

In eq. (2), $f_{mv} = \sum_{v=0}^{m} \frac{(i\Delta\Phi_0^{(3)})^v (i\Delta\Phi_0^{(5)})^{m-v}}{v!(m-v)!} \frac{1}{[1+a^2]^{B_{mv}}}$, $B_{mv} = 2m - v$, $\Delta\Phi^{(5)} = kn_4 I^2(1 - \exp(-2\alpha_0 L)/2\alpha_0)$ and n_4 is the nonlinear refractive index associated with the effective fifth-order nonlinear response of the sample. For a high accuracy fit it is necessary that the condition $\left|\sum_{v=0}^{m} \frac{1}{v!(N_{opt}-v)!} [i\Delta\Phi_0^{(3)^v}][i\Delta\Phi_0^{(5)}]^{N_{opt}-v}\right| = 0.5$ is fulfilled (GU et al, 2005).

Therefore, using Equation (4.16) and (4.17), the values of the third and fifth order effective nonlinear refractive indices for the MoS_2 nanoflakes suspension were measured to be $n_{2,eff}$ = +(4.8±0,5)×10^{-16} cm²/W and $n_{4,eff}$ = –(7.6±0.5) ×10^{-26} cm^4/W². For WS_2 we obtained $n_{2,eff}$ = +3.4×10^{-16} cm²/W, solely due to the third-order nonlinearity, in the excitation intensity range investigated.

4.5 PARTIAL CONCLUSIONS

The different nonlinear optical properties of 2D – TMD's are investigated using different techniques and one application is demonstrated. Second- and third-order optical

nonlinearities are demonstrated in $ZrTe_2$ flakes using the techniques of HRS and Z-Scan. A large first-order hyperpolarizability is found for $ZrTe_2$ flakes (~10^{-24} esu) and is larger when compared with WS_2 flakes. This large hyperpolarizability can be attributed to the volume of the sample when compared to WS_2, and also to atomic number of atoms that is bigger than the W, giving a bigger contribution to the first-order hyperpolarizability. Polarization resolved HRS is performed to understand the origin of nonlinearity, and a dipolar behavior is shown, indicating a large contribution of edges when compared to volume.

Real third-order nonlinearity is shown in $ZrTe_2$ semi-metallic flakes. A positive n_2 is shown and any NLA absorption is found. DFT calculations are performed to support the experimental results and have a good agreement.

An application of $ZrTe_2$ as scatters for RL in both 3D and 2D forms is demonstrated using Rh6G as the gain medium. A standard characterization of RL is performed, the curves of threshold and linewidth reduction are demonstrate, and the 2D flakes exhibited a small threshold when compared with 3D form. In order to find the right value of the threshold, a statistical analysis is performed using the RSB method. A transition from a paramagnetic photonic to a photonic spin glass is shown. The stability of RL is also investigated and good results are shown.

The second LTMD'S investigated was NbS_2. These flakes have a metallic behavior and interesting results are found using the Z-Scan technique. First, a change from 2PA to SA is shown. Different models are employed to fit the NLA curves, and the better model is an inhomogeneous broadening model, an expected result. DFT calculations were performed by Leandro Seixas, from Mackgraphe collaborator group used and have a good agreement with the experimental results. The nonlinear refractive index also showed an unusual behavior, a change from negative to positive in the signal of the nonlinear refractive index.

The last LTMD'S investigated was MoS_2. MoS_2 is a semiconductor LTMD'S, with interesting exciton transitions. Simultaneous real third and fifth-order nonlinearity are demonstrated for intensities relatively higher. A comparison with WS_2 flakes was performed, and the fifth-order nonlinearity was observed for a high concentration of MoS_2 flakes when compared to WS_2 flakes.

5 GOLD CLUSTERS

Synthesis and characterization performed at Indian Association for the cultivation of science - India

Noble metal nanoclusters (MNCs) are a new class of nanomaterials that are receiving notable interest. Due to the small size, MNCs are considered *molecular-like* materials, in other words, the MNCs have properties between the molecules and the *bulk* plasmonic nanoparticles. MNCs can be constituted by a few to several hundred atoms of only one noble metal, like Ag, Au, Cu, or Pt or alloys of these elements (BAIN et al, 2019).

Figure 56 - a) Density of States (DOS) of MNCs and NPs b) in the top, number of atoms of a MNC and the limit between a MNC and a nanoparticle, in bottom, the energy levels for MNCs and bulk-like plasmonic nanoparticles.

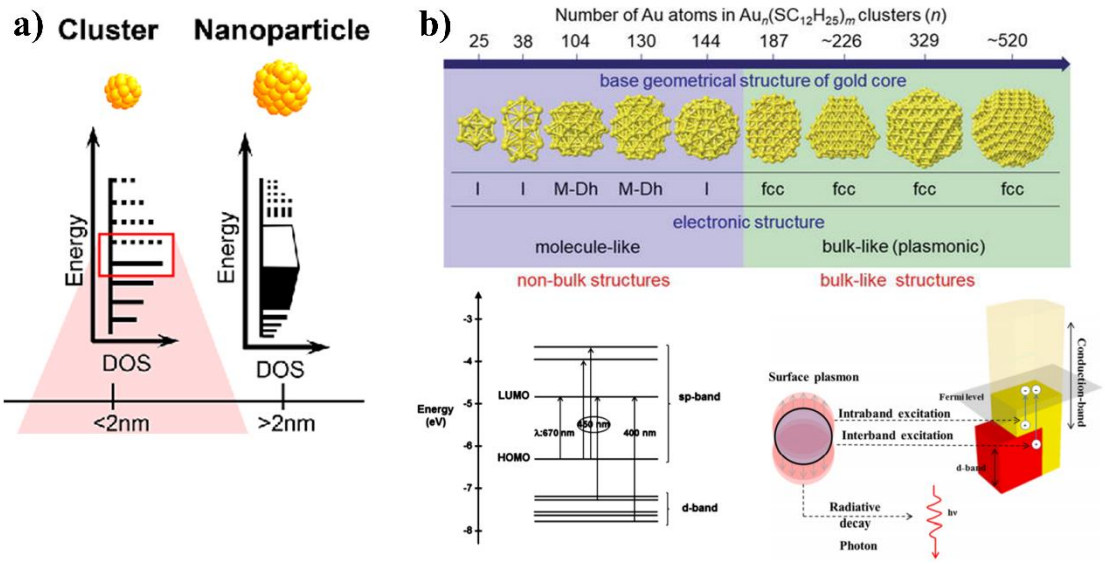

Source: a) Negishi, et al (2015). b) Philip, et al (2012)

The energy levels in Figure 56 a) indicate the Density of States (DOS) for MNCs and *bulk* like plasmonic nanoparticles. The MNCs are characterized by discrete energy states, as in molecules, having the *gap* characterized by HOMO-LUMO transitions, as shown in the left part of the bottom in Figure 56 b). The right part of Figure 56 b) it is shown the DOS for plasmonic nanoparticles, characterized by a continuum of energy, showing band structures. At the top of Figure 56 b) it is shown the limit between MNCs and plasmonic nanoparticles; the limit is close to 160 atoms.

The fluorescent properties of the MNCs are tuned by the number of atoms and ligands. Figure 57 a) shows the fluorescence spectra of MNCs with a different number of atoms. The dashed lines represent the excitation spectra, and the solid lines the emission spectrum for Au clusters with 5 (emitting in UV), 8 (emitting in blue), 13 (emitting in red), and 15 (emitting in

NIR). A theoretical model that correlates the MNCs sizes with the emission energy is presented in (ZHENG et al, 2005). A behavior type $E_F/N^{1/2}$ is find, where E_F is the Fermi energy, and N the number of atoms in the cluster. The emission energy as a function of the number of atoms is shown in Figure 57 b).

Figure 57 – a) Excitation (dashed lines) and emission (solid lines) energies for clusters with a different number of atoms. b) Theoretical model fitting the experimental data of emission energy as a function of the number of atoms.

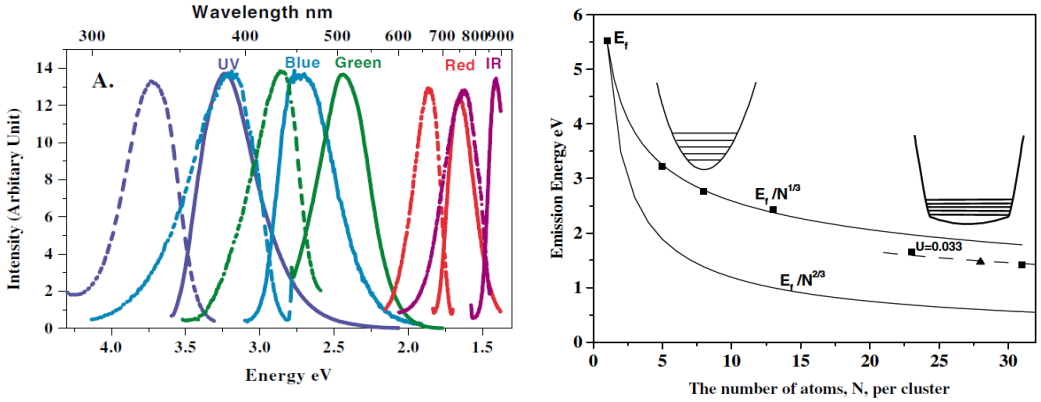

Source: Zheng, et al (2005)

MNCs are not stable if they do not have molecules around the atoms. The presence of these molecules changes the photoluminescence spectrum. Some examples are shown in Figure 58, where it is shown metal nanoclusters using the template-based synthesis (i.e. dendrimer (PAMAM), oligonucleotide (DNA), proteins (BSA), polyelectrolyte, polymer (PMAA), monolayer-protected nanoclusters (MPCs) synthesis (i.e. dihydrogen lipoic acid (DHLA), and mercaptoundecanoic acid (MUA).

Figure 58 - Representative fluorescent noble-metal nanoclusters scaled as a function of their emission wavelength superimposed over the spectrum. Fluorescent metallic nanoclusters can be protected by ether template (AAuNC's@DNA, AuNC@BSA, AuNC@PAMAM , AAuNC's@PMAA) or monolayer ligands (AuNC@DHLA, AuNC@MUA).

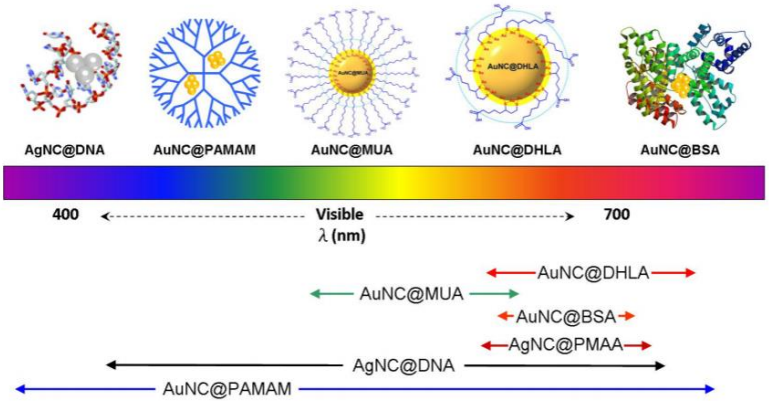

Source: Zhu, et al (2010)

Another important characteristic of MNCs is the correlation between the electronic, optical, and catalytic properties with the spatial arrangements of atoms or molecules. For these correlations to occur, it is necessary a deep understanding of the structural aspect of the nanoclusters. Photoluminescence (PL) of MNCs arises due to different electronic transitions through their HOMO-LUMO bandgap. KANG and ZHU, 2019 performed a literature review to show the engineering used to change the bandgaps of MNCs. HUANG, et al, study the mechanisms contributing to the PL process, with an emphasis on size, valence states, ligands, and crystallinity. In the paper, the authors summarize the emission mechanisms in MNCs.

The PL quantum yield (QY) of metal nanoparticles (size 2-3 nm) is very low (around 10^{-5}) when compared with ultrasmall NCs (size < 2 nm) (MUHAMMED et al, 2009). The QYs in Au NCs enhance tremendously around 10^5 fold compared to metal NPs, as the energy states in Au NCs are completely discrete.

Figure 59 – (A) Kohn-Sham orbital energy levels diagram for a model compound $[Au_{25}(SH)_{18}]$-. The energies are in units of eV. (B) The theoretical absorption spectrum of Au25(SH)18-. Peak assignments: peak a corresponds to 1.8 eV(observed), peak b corresponds to 2.75 eV (observed), and peak c corresponds to 3.1 eV (observed).

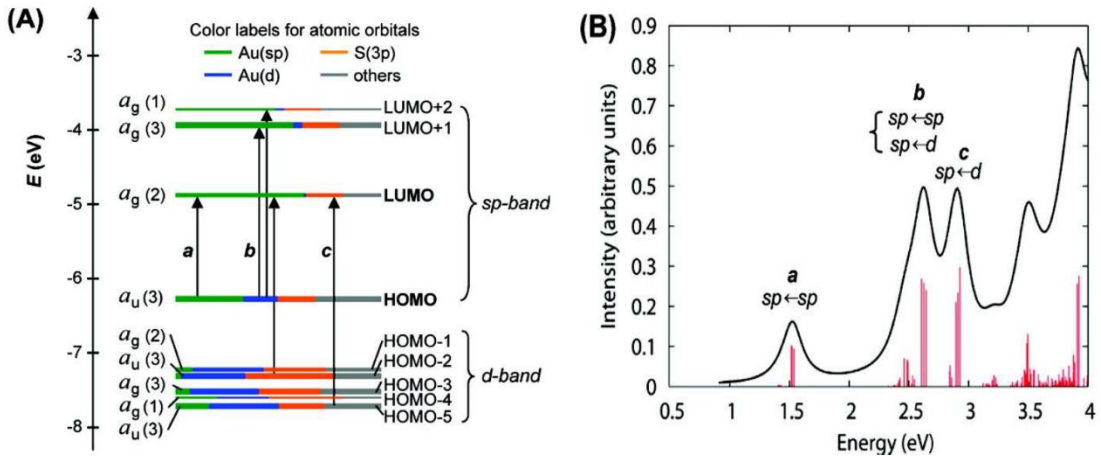

Source: Zhu, et al (2008)

ZHU et al, 2008 reported the different possible electronic transitions in Au NCs and correlated them with experimental results (Figure 59a)). In Figure 59b), the absorption band at 670 nm (1.85 eV) is due to the intra-band transition (sp to sp transition), and the other absorption band around 560 nm (2.21 eV) is ascribed to d to sp inter-band transition.

Beyond the linear optical properties of MNCs, several works have investigated the nonlinear optical properties of these nanomaterials. The nonlinear optical properties of MNCs, especially those based on Ag and Au are investigated using known techniques as HRS, to measure the second-order nonlinearity (RUSSIER-ANTONIE, et al, 2014), Two-Photon

Luminescence (WANG, Y. et al, 2013), and Z-scan in the open aperture configuration to determine the 2PA cross-section (REYNA et al, 2018), and Z-scan, in the closed aperture configuration to measure the nonlinear refractive index (REYNA et al, 2018).

In the case of second-order nonlinearity, the first–order hyperpolarizability was measured in MNCs with a different number of atoms and different ligands. The effect of ligands on the value of the first-order hyperpolarizability is sufficiently small and can be despised as described by DUBOISSET et al, 2013. When compared clusters with the same number of atoms but different ligands, the value is close, suggesting again that the ligands do not contribute much in the first-order hyperpolarizability.

Figure 60 - β/atom as a function of the number of gold atoms, obtained with 802 nm excitation.

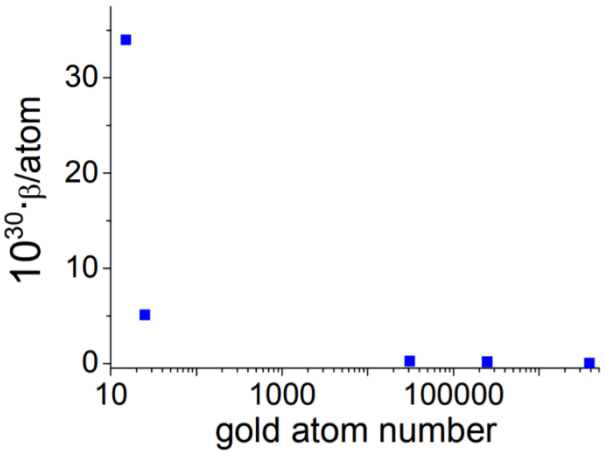

Source: Russier-Antoine et al, (2014)

An interesting effect shown by RUSSIER-ANTOINE et al, 2014 is the increase in the value of hyperpolarizability/atom when the number of atoms in the cluster decreases, as shown in Figure 63. The values found are two orders of magnitude large in comparison with nanoparticles. The smallest value for the hyperpolarizability of Au NPs, when compared with Au NC's, occurs due to the transition of the cluster behavior to a gold nanoparticle behavior possessing strong surface plasmon absorption.

Figure 61 shows the nonlinear optical behavior of plasmonic nanoparticles in comparison with clusters for the same excitation conditions. While strong two-photon absorption (2PA) is observed for plasmonic NPs, clear saturation of the linear absorption has been demonstrated as well as reverse saturated absorption (RSA). However, for Au NCs with less than 150 atoms, a non-saturated 2PA was observed for excitation wavelength at 532 nm (PHILIP, et al, 2012). In such case, the saturation intensity of the NL absorption is typically beyond 10^8 W/cm^2.

Figure 61 - Open-aperture z-scans measured in the Au clusters and nanocrystals. (a) Au25, (b) Au38, (c) Au144, and (d) Au nanocrystals (~4 nm). Samples are excited using 5 ns laser pulses at 532 nm

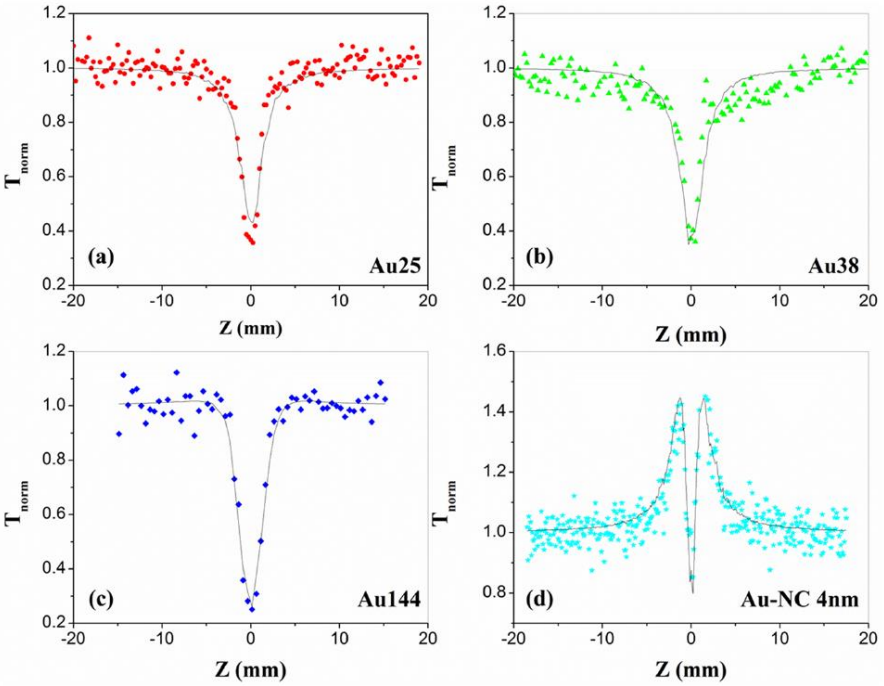

Source: Philip, et al (2012)

For example, Au_{144} NCs (Figure 61 c)), standing at the frontier between the molecular to the plasmonic transition, present saturation intensity of 1.5×10^8 W/cm^2 and 2PA coefficient $\alpha_2 = 7.5 \times 10^{-10}$ m/W at 532 nm.

For the $Au_{25}Capt_{18}$ nanoclusters, where Capt stands for Captopril, σ_2 reaches 2.4×10^4GM ($1\text{GM} = 10^{-50}\ cm^4 \cdot s$) for excitation at 830 nm (OLESIAK-BANSKA et al, 2016). The 2PA cross-section for $Au_{15}SG_{13}$ is 5.5×10^4 GM at 800 nm whereas it can reach values beyond 10^6 GM for gold NPs with thousand atoms (PHILIP, et al, 2012; RAMAKRISHNA et al, 2008). The value of σ_2 is related to the 2PA coefficient by $\sigma_2 = \alpha_2(\omega)\hbar\omega/N$ where N is the density of NL absorbers and $\hbar\omega$ is the incident photon energy. NL optical properties of Au NCs stabilized by glutathione containing 15 and 25 gold atoms, Au_{15} and Au_{25}, respectively, were reported where the SH generation and 2PA were studied (RUSSIER-ANTOINE, et al, 2014). The authors observed an increase of $\beta(-2\omega;\ \omega, \omega)$ per atom for the smaller cluster (Au_{15}) with respect to the Au_{25}; moreover, $\beta(-2\omega;\ \omega, \omega)$ per atom was two orders of magnitude larger than the values reported for gold NPs with diameters in the 10-50 nm range.

5.2 ABSORPTION SPECTROSCOPY

The absorbance spectrum (from 300 to 1200 nm) of the Au NCs in water shows strong absorption bands in the blue region tailed by a transmittance window in the red-to-infrared region. The band in the blue-UV spectrum is originated owing to distinctive electronic transition (ZHENG et al, 2004; ZHU et al, 2008). The absence of an LSP resonance band at 520 nm indicates the formation of Au NCs having an average size smaller than 2 nm, in accordance with the TEM data (See Figure 105a).

Figure 62 - Linear absorbance spectrum of $Au_6(GSH)_2(MPA)_2$ suspended in water (concentration of 2.1×10^{16} nanoclusters/mL). Cell thickness: 1 mm.

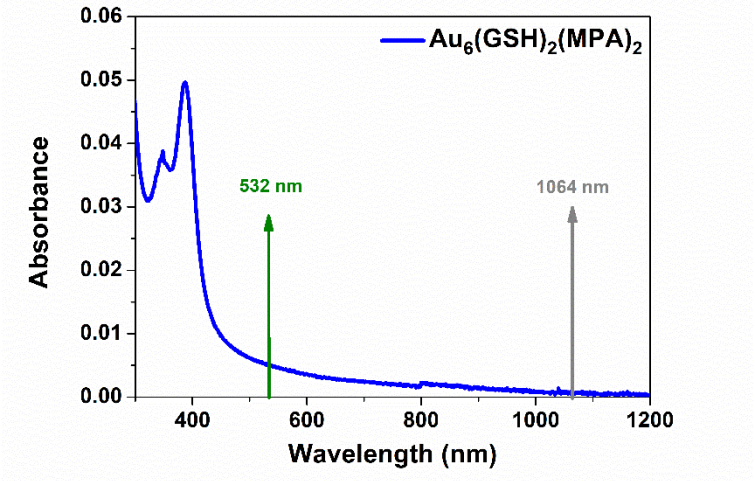

Source: The author (2021).

5.3 HYPER-RAYLEIGH SCATTERING EXPERIMENTS.

In order to perform the NL optical experiments, the Au NCs were dispersed in water with concentrations in the range of 0.8×10^{16} to 2.1×10^{16} clusters/mL. The excitation source was a Q-switched Nd: YAG laser ($1064\ \text{nm}, \approx 7\ \text{ns}, 10\ \text{Hz}$). The experimental setup is the same shown and described in section 3.1. Para-nitroaniline (*p*-NA) dissolved in methanol, with concentrations between 1.3 x 10^{18} and 1.0 x 10^{19} molecules per cm^3, was used as a reference standard for measurements of $\beta(-2\omega;\ \omega, \omega)$.

The HRS technique (KLAYS and PERSOONS, 1991; HENDRICK et al, 1998; JOULAND et al, 2013) was employed to determine the $\beta(-2\omega;\ \omega, \omega)$ value of the Au NCs, $\beta_{Au\ NCs}(2\omega)$. The laser wavelength was chosen at 1064 nm because, as can be seen from Figure 62, a shorter wavelength would generate two-photon induced PL overlapping with the HRS signal. The HRS technique has been largely applied for measurements of molecules, NPs (in

solutions or suspensions) (KLAYS and PERSOONS, 1991; HENDRICK et al, 1998), and powders (RODRIGUEZ, E. V. et al; JOULAND et al, 2013) for citing some examples.

The SH light intensity generated in a composite sample with various constituents is described by $I(2\omega) = g\ \sum_c N_c \langle \beta_c^2(2\omega) \rangle I^2(\omega)$, where $I(\omega)$ is the laser intensity and $\langle \beta_c^2(2\omega) \rangle = \langle \beta_c^2(-2\omega;\ \omega, \omega) \rangle$ is the orientational average of the first-hyperpolarizability associated to the constituent labeled by c. The factor g depends on the scattering geometry, local field corrections, and coordinates of the molecule (or particle) concerning the laboratory coordinates.

Figure 63 - shows the scattered SH signal for laser intensity of 2 GW/cm^2. Notice that only the SH at 532 nm was present and the signal linewidth of $\approx 0.8\, nm$ was limited by the monochromator resolution. The narrow linewidth observed is an indication that the signal at 532 nm is due to the parametric process and not due to PL induced by 2PA. Indeed, the two-photon quantum yield is about two orders of magnitude smaller for Au NCs than for Ag NCs (RUSSIER ANTOINE et al, 2016), and therefore, the dominance of the HRS signal in the present experiment was already expected.

Figure 63 - Spectrum of the scattered light (for excitation at 1064 nm) showing the HRS signal centered at 532 nm. The experimental data are represented by the open circles and the solid line is a Gaussian fit.

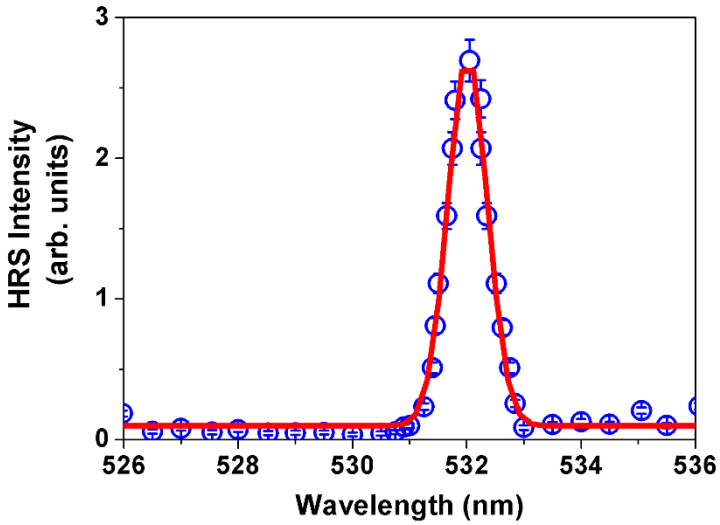

Source: The author (2021).

The straight line in Figure 64 shows the dependence of $I(2\omega)$ versus the incident laser intensity, $I(\omega)$. The relation $I(2\omega) \propto I^m(\omega)$, with $m = 1.9 \pm 0.2$, indicates the expected quadratic dependence.

Figure 64 - HRS intensity as a function of laser intensity 1.9 ± 0.2 is the slope of the straight line.

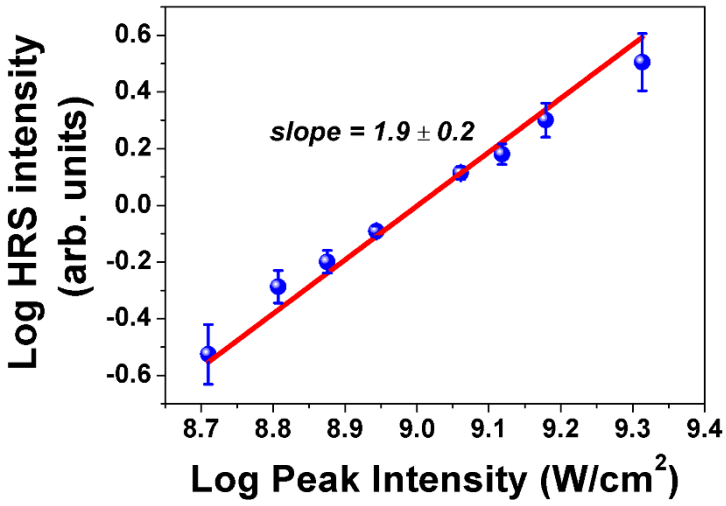

Source: The author (2021).

Figure 65a) and Figure 65b) show the HRS intensity as a function of the $Au_6(GSH)_2(MPA)_2$ and *p*-NA concentrations, respectively. The linear dependence indicates that NCs agglomeration is negligible in the samples.

Figure 65 - a) HRS intensity versus the nanoclusters concentration. b) HRS intensity of *p*-NA as a function of concentration.

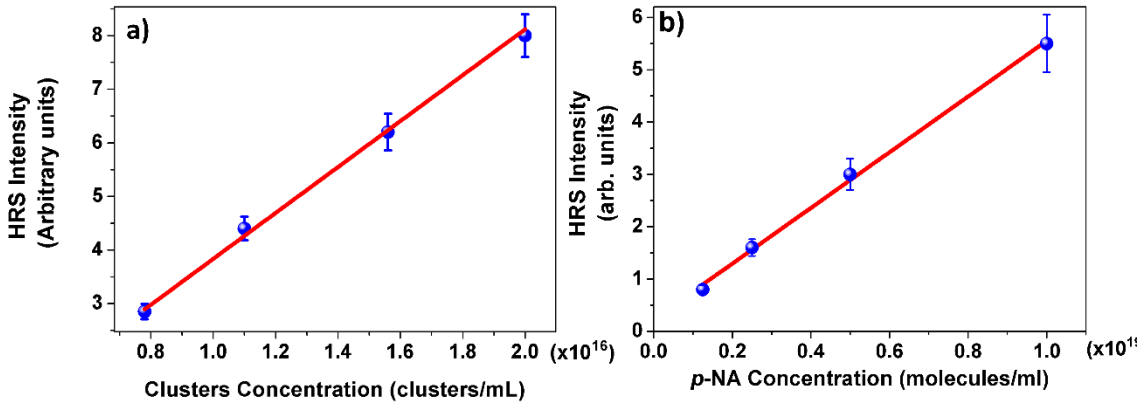

Source: The author (2021).

In order to get further evidence that the SH signal at 532 nm is due to the HRS process and it is not contributed by 2PA induced PL, the temporal evolution of the SH signal was recorded and compared with the laser temporal profile; since the HRS is a parametric process its temporal evolution should follow the laser pulse. Figures 66a) and 66b) show the temporal profile of the laser pulse and SH signal that are similar (within the temporal resolution) corroborating the interpretation of the SH signal as due to the pure HRS process.

Figure 66 - a) Laser pulse temporal profile. b) Temporal profile of the signal at 532 nm. The red lines represent Gaussian fits to the data. The laser peak intensity was 2 GW/cm^2.

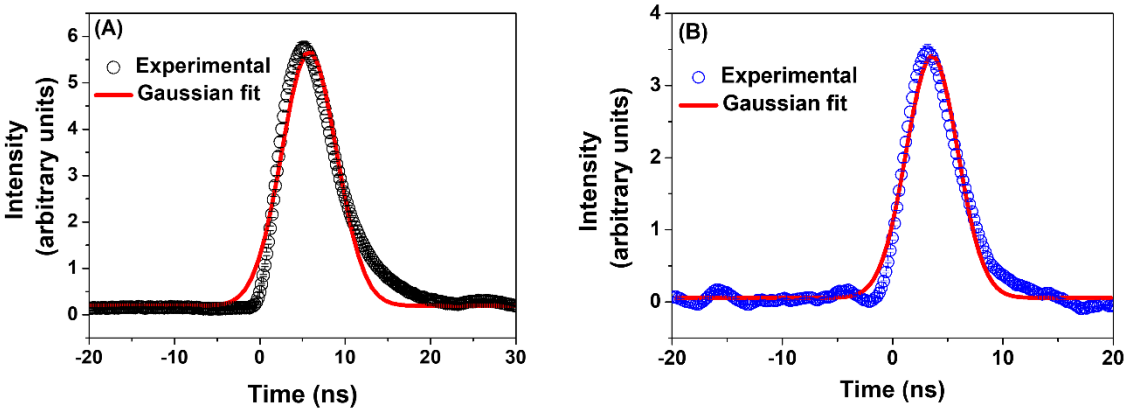

Source: The author (2021).

The HRS signal, $S(2\omega)$, as a function of laser intensity for the two-component system studied is given by $S(2\omega) = G(N_{sol}\langle\beta_{sol}^2\rangle + N_{solv}\langle\beta_{solv}^2\rangle)I^2(\omega)$, where sol stands for solute (Au NCs), $solv$ stands for solvent (water) and G is a parameter that includes local field correction and light collection efficiency.

The value of $\beta_{Au\,NCs}(2\omega)$ was determined by using the *external reference method* (HENDRICK et al, 1998) with a *p*-NA solution (10^{19} molecules/mL) dissolved in methanol as reference.

Therefore, $\langle\beta_{Au\,NCs}^2(2\omega)\rangle$ was determined using the expression:

$$\langle\beta_{Au\,NCs}^2(2\omega)\rangle = \frac{S(2\omega)}{S_{ref}(2\omega)}\left\{\frac{N_{ref}\langle\beta_{ref}^2\rangle + N_{solv-ref}\langle\beta_{solv-ref}^2\rangle}{N}\right\}$$

$$-\frac{N_{solv}\langle\beta_{solv}^2\rangle}{N}, \qquad (5.1)$$

where *N* is the Au NCs concentration, *ref* and *solv-ref* are related to the reference material (*p*-NA) and the solvent used in the dilution of the reference material (methanol), respectively.

The first-hyperpolarizability value considered for *p*-NA was $\beta_{pNA}(-2\omega;\,\omega,\omega) = 34 \times 10^{-30}\,esu$ (KLAYS and PERSOONS, et al, 1991) and the value of $\langle\beta_{Au\,NCs}(2\omega)\rangle$ obtained from Eq. (5.1) was $760 \times 10^{-30}\,esu$. With basis on this result we estimate the static first-hyperpolarizability, $\beta(0)$, applying a two-level model approximation (MARDER, et al, 1991; CHEMLA, 1987) according to Eq. (5.2):

$$\beta(0) = \left[1 - 5\left(\frac{\omega}{\omega_{eg}}\right)^2 + 4\left(\frac{\omega}{\omega_{eg}}\right)^4\right]\langle\beta_{Au\,NCs}(2\omega)\rangle, \qquad (5.2)$$

where ω is the laser frequency and ω_{eg} is the frequency corresponding to the HOMO-LUMO energy gap (3.22 eV), determined considering the blue-UV absorption band in Figure 62. The value of $\beta(0)$ obtained from Equation (5.2) was $300 \times 10^{-30} esu$.

Table 5 - First-hyperpolarizability of the gold nanoclusters. The present measurements of $\langle \beta_{Au\ NCs}(2\omega) \rangle = \beta(2\omega)$ have an uncertainty of ±10%. $\beta(0)$ is the static hyperpolarizability calculated using the experimental value of $\beta(2\omega)$ in the two-level system model.

Gold nanocluster	Wavelength (nm)	$10^{+30}\,\beta(2\omega)$ (esu)	$10^{+30}\,\beta(0)$ (esu)	Reference
Au_6	1064	760	300	This work
Au_{15}	802	509	*	RUSSIER-ANTOINE, et al, 2014
Au_{25}	802	128	*	RUSSIER- ANTOINE , et al, 2014

Source: The author (2021).

* value not provided in reference RUSSIER- ANTOINE, et al, 2014.

The values of $\langle \beta_{Au\ NCs}(2\omega) \rangle = \beta(2\omega)$ and $\beta(0)$ are given in Table 5 together with results from previous experiments with gold NCs of different sizes. Notice that the present results are larger than the ones for NCs with 15 and 25 gold atoms stabilized by glutathione (RUSSIER- ANTOINE, et al, 2014). Indeed, both Au_{15} and Au_{25} NCs are expected to have symmetric core structures that prevent large SH generation efficiency. On the other hand, in the present case, the surface capping ligands (GSH and MPA) produce a large change in the cluster geometry which contributes to large SH generation efficiency as discussed in the next section.

5.4 PARTIAL CONCLUSIONS

The first-order hyperpolarizability of one gold cluster with 6 atoms and supported by glutathione and mercaptopropitic acid ($Au_6(GSH)_2(MPA)_2$) was measured. A value of $760 \times 10^{-30}\ esu$ was calculated for the hyperpolarizability and $34 \times 10^{-30}\ esu$ for static hyperpolarizability. A comparison with the literature showed that the calculated value is higher when compared with Au NCs with a larger number of atoms. The value found to confirm that the hyperpolarizability per atom increases when the number of atoms is decreased. In addition, quantum mechanics calculations were performed (by collaborators) to support the experiments but this is not the objective of this thesis.

6 GRAPHENE QUANTUM DOTS

Commercial samples

6.1 GRAPHENE

Carbon-based systems offer a variety of structures, also offering several interesting physical properties. The physical properties are mainly related to the dimensionality of these structures. One of these structures, called carbon allotropes, is known as graphene. Graphene has a "honeycomb" structure, and atoms are ordered hexagonally.

Figure 67 – Comparison between a) structure of a honeycomb and b) hexagonal structure of graphene.

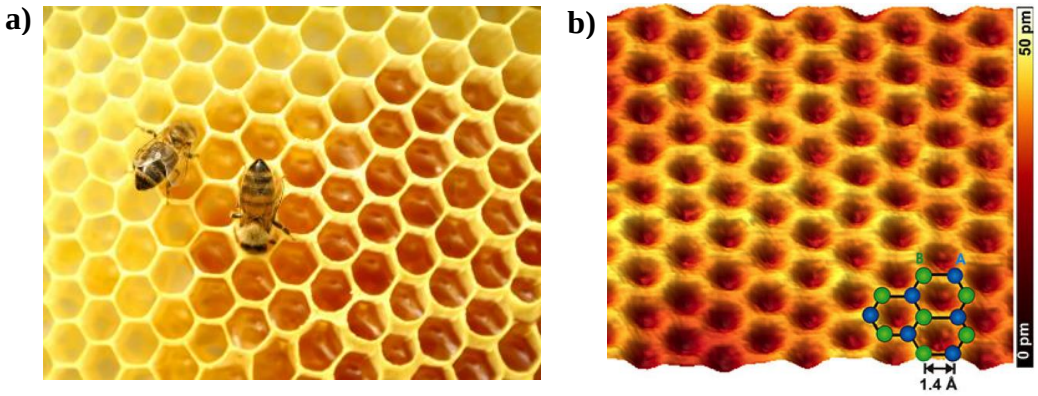

Source: a) Rural News, (2019) b) Nanoscience, (2012)

Figure 67a) shows the structure of a honeycomb, and Figure 67b) shows a tunneling microscopy image with scanning of a graphene sheet (NANOSCIENCE, 2012). The arrangement of carbon atoms can be thought of as benzene ring compounds removing their hydrogen atoms.

The material precursor of graphene is graphite, which consists of the stacking of several sheets of graphene, linked by van der Walls interaction (weak interaction), thus forming a three-dimensional arrangement of the material. The van der Wall's interaction in graphite facilitates the preparation of graphene by mechanical means. In 2010, the Nobel Prize in Physics was awarded for Andre Geim and Konstantin Novoselov, researchers at the University of Manchester (UK), responsible for isolating, for the first time, a single sheet of graphene, in 2004, using an adhesive tape to exfoliate graphite (KONSTANTIN et al, 2004).

To understand the electronic structure of graphene it is necessary to understand how the hybridization of orbitals occurs sp^2, with the formation of three orbitals: an orbital *s* and two orbitals *p*. This hybridization leads orbitals to organize themselves into a trigonal prismatic

structure, leading to the formation of σ orbital between carbon atoms, which are separated by the distance a = 1.42 Å. The orbitals σ is responsible for the robustness of the lattice structure in all allotropes. The orbitals π are perpendicular to the surface of the sheet.

Figure 68 – a) arrangement of carbon atoms forming a graphene sheet, b) Hybridization of the *sp²* orbitals of carbon.

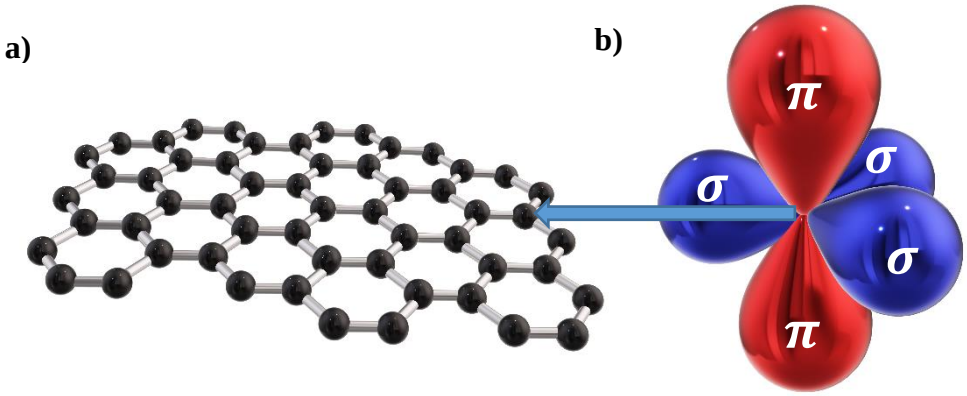

Source: The author (2021).

Figure 68 a) represents an arrangement of carbon atoms forming a hexagonal structure. Figure 68 b) represents the hybridization of the orbitals of carbon atoms. Due to Pauli's exclusion principle, the σ orbitals have a filled part and therefore form a deep valence band. The orbital p is not affected, because it is perpendicular to the flat structure. It can bind covalently to the neighboring carbon atoms, leading to the formation of a π orbital. Because each *p-orbital* has an extra electron, this causes the band π that half full.

The electronic structure of graphene can be explained using a *tight-binding* Hamiltonian, leading to analytical solutions for its energy dispersion and related states (NETO et al, 2009). Because the σ bands are well separated in energy (> 12 eV at Γ point), they are often neglected in semi-empirical calculations, as they are too far from Fermi's level to play some role in electronic transitions in graphene. Thus, only the π orbitals are used to describe the bands' structure of the material (SIMON et al, 2009). This carbon ligand (π) and anti-ligand (π*) orbitals form electronic valence and conduction bands crossing the Fermi level at symmetrical points of the graphene Brillouin zone.

The Bravais lattice of graphene has a triangular shape and consists of two atoms per unit cell, as indicated by the arrows in Figure 69a), with lattice vectors $a_1 = (a/2)(3, \sqrt{3})$ and $a_2 = (a/2)(3, -\sqrt{3})$. The reciprocal lattice of graphene is also triangular with lattice vectors $b_1 = (2\pi/3a)(1, \sqrt{3})$ and $b_2 = (2\pi/3a)(1, -\sqrt{3})$. The first Brillouin Zone (BZ) of the

reciprocal lattice have also a honeycomb shape but is rotated by an angle of $\pi/2$ about the lattice of real space. The six corners of the first BZ consist of two sets of non-equivalent points, **K** and **K',** which are known as Dirac points. In the band structure of graphene, the σ states form occupied and unoccupied states with a bandgap, while π states form a single band with cone-shaped intersection points at K points (and similarly at K′ points).

Figure 69 - a) Lattice structure of Graphene. The unit cell consists of carbon atoms represented by A and B, a1 and a2 are the lattice vectors. (b) The corresponding BZ, showing the points of high symmetry.

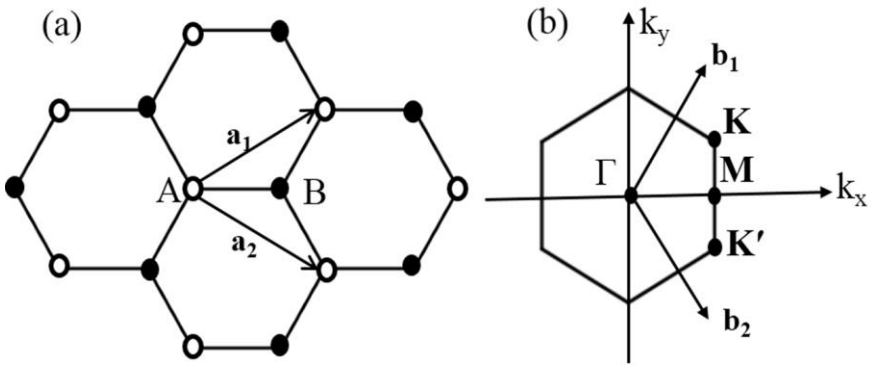

Source: Neto, et al (2009).

The electronic structure of energy bands and the Brillouin zone are developed using the approximation of tight-biding, considering the electron transitions in the plane of the structure (WALLACE, 1947). The band energy derived from the strong-binding Hamiltonian is given by Equation (6.1) (KAVITTA et al, 2016):

$$E_{\pm}(k) = \pm t\sqrt{3 + f(\boldsymbol{k})} - t'f(\boldsymbol{k}) \tag{6.1}$$

where $f(\boldsymbol{k}) = 2\cos\left(\sqrt{3}k_y a\right) + 4\cos\left(\frac{\sqrt{3}}{2}k_y a\right)\cos\left(\frac{3}{2}k_y a\right)$ and is related to lattice vectors of the structure.

Figure 70 a) shows the complete band structure of graphene. The transition energy for the nearest neighbors decreases with the distance in the lattice and the energy dispersion spectrum is symmetrical around the Dirac cone. Fermi's level coincides with the Dirac cone, where the filled valence band and the empty conduction band meet with a range of energy equal to zero. Figure 70 b) clearly illustrates that the energy bands near the Dirac points are linear and also reveals that graphene is a semimetal, that is, a semiconductor with zero band interval. In the vicinity of the Dirac point, the energy dispersion ratio is isotropic and forms a Dirac cone. Moving away from the Dirac cone, the trigonal structure initially modifies the contours of

energy; in addition, there is a saddle point (Point M) in the energy bands, and at this point, the energy bands are largely separated.

Figure 70 – a) Electronic dispersion of graphene. b) Bands structure near to Dirac point.

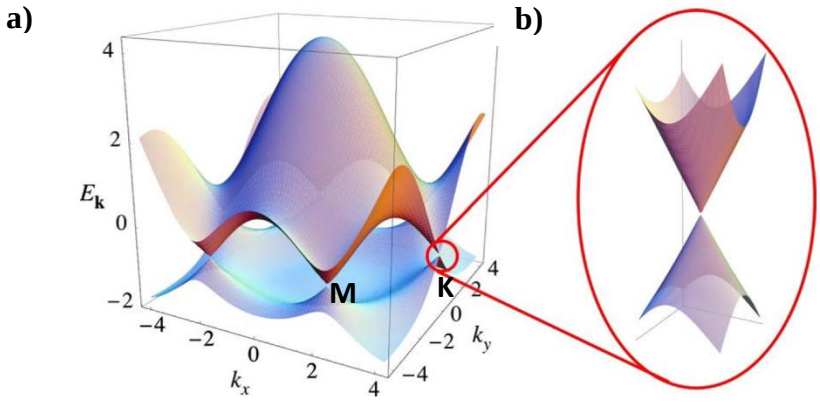

Source: NETO, et al (2009).

The electronic dispersion near the Dirac points in the hexagonal BZ is $E = \pm\hbar v_F|\boldsymbol{q}|$, where v_F is the Fermi velocity of the charge carriers and has a value of ~ 10^6 m/s and $\boldsymbol{q}$ is the vector k measured about **K** point.

The optical properties of graphene are unique due to the linear structure of the band, bandgap zero, and strong interaction of Dirac fermions with electromagnetic radiation. Graphene absorbs in a wide spectral range, due to interband and intraband optical transitions. Graphene absorption from visible to near-infrared is modeled by transitions between bands and is frequency-independent (NAIR et al, 2008; MAK et al, 2008). The optical response in the far-infrared region is due to interband transitions and/or absorption of free carriers (GIERZ et al, 2013). Direct absorption of photons is not possible by intraband transitions due to the condition of momentum conservation. To preserve the momentum is necessary the participation of phonons, followed by a population inversion of free carriers near to K-point. The conductivity associated with absorption of free carriers shows a frequency dependence that can be explained by the Drude model (HORNG et al, 2011). The response in the far-infrared can be adjusted to the terahertz band by plasmonic excitation (JU et al, 2011). Plasmon-assisted light absorption is not allowed in graphene due to the large moment difference between photons and plasmons (MAK et al, 2012). However, plasmonic excitation can be activated by electrostatic coupling using an electrical voltage, as well as engineering graphene nanostructures (KIM et al, 2012).

Therefore, Graphene is a material with zero bandgap and linear energy dispersion; the valence and conduction bands touch the Dirac point, as shown in Figure 70. The dispersion of

energy near the Dirac point is linear, that is, the behavior of electrons and holes at the bottom of a lattice of the structure mimics relativistic particles that are described by the relativistic equation of Dirac. Graphene exhibits a particularly unique but simple optical absorption spectrum. In the spectral range from infrared to visible, its absorbance was calculated independently not only of the frequency of electromagnetic radiation but also independent of any material properties of the absorber. The absorbance of graphene in suspended monolayers is defined by the constant of thin structure, $\pi\alpha$, where $\alpha = e^2/\hbar c$. The fine structure constant is a dimensionless number, with a value of 1/137 The origin of the optical properties defined by the fine structure lies in the two-dimensional relativistic nature of the load carriers in graphene, as discussed below.

The excitation close to the Dirac point is governed by linear dispersion energy dependent on the wave vector*(k)*, $E_k = v_F f |k|$, where $v_F = 10^6\ m/s$, is the Fermi velocity. When a light wave with electrical field component (E) and frequency (ω) is incident perpendicular to a graphene sheet, the incident energy density can be estimated as, $W_i = (c/4\pi) |E|^2$. The absorption can be estimated using time-dependent perturbation theory. The interaction between electromagnetic radiation and the charge carriers in graphene is described by the Hamiltonians, $\widehat{H} = v_F \boldsymbol{\sigma} \left(\hat{p} - \frac{e}{c}\boldsymbol{A}\right) = \widehat{H} + \widehat{H}_{int}$ where the first term is the standard Hamiltonian for graphene quasiparticles and the second term describes its interaction with the electromagnetic field (NAIR et al, 2008). According to Fermi's golden rule, the absorbed energy, W_a is given by Equation (6.2).

$$W_a = \frac{2\pi}{\hbar} |M|^2 D(E_k - E_i), \tag{6.2}$$

where *D* is the Density of States (DOS) with half the energy of the incident radiation. For 2D Dirac fermions in graphene, $D(\hbar\omega/2) = \omega\hbar/\pi\hbar^2 v_F^2$. M is the matrix element for the interaction of Dirac fermions in graphene with the electrical field component and is given by Equation (6.2) (KITTEL, C. 1986).

$$|M|^2 = \left|\left\langle f \left| v_F \boldsymbol{\sigma} \frac{e}{i\omega} \boldsymbol{E} \right| i \right\rangle\right|^2 = \frac{1}{8} e^2 v_F^2 \frac{|E|^2}{\omega^2}. \tag{6.3}$$

The percentage of absorbed energy is given as $W_a/W_i = \pi\ (e^2\ /\ \hbar c) = \pi\alpha = 2.3\%$. Therefore, the optical absorption is independent of the incident frequency and the materials' parameters. The amount of light passing through graphene can therefore be used as a simple means to estimate the fine structure constant or Planck constant. Figure 71 a) shows the optical

image of an opening partially covered by monolayer and bilayer graphene and Figure 74b) represents the light-measured transmittance (NAIR et al, 2008). When graphene is illuminated with white light, the monolayer region absorbs 2.3%, with negligible reflectance <0.01%. It was found that the absorption increases with the thickness of graphene so that each layer adds another 2.3% to the amount of absorbed radiation.

Figure 71 - Photograph of a 50 μm opening covered by graphene and its bilayer. Inserted image: A 20 μm thick metal support structure with multiple openings of 20, 30, and 50 μm in diameter with graphene crystals placed on them. (b) The transmittance of a graphene monolayer. Transmission of white light depending on the number of graphene layers.

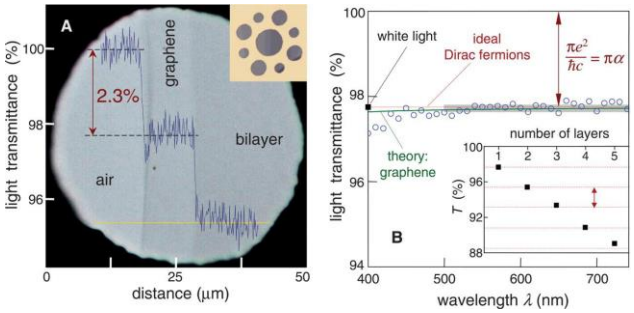

Source: Kavitha, et al (2016).

There is an interesting analogy of this result with the phenomenon of planetary motion, as described in Newtonian mechanics. Kepler's third law of planetary motion states that R^3/T^2 is a constant for the planet orbiting the sun, where R is the natural length scale and T is the natural time scale of the problem. This constant value becomes independent of the initial conditions of the problem because the angular momentum is canceled in the reason. On the same line, Heinz et al. explained purely based on dimensional analysis, that graphene Hamiltonian describing linear band structures does not have an intrinsic energy scale with which photon energy can be compared (MAK et al, 2012). It follows that Fermi's velocity and frequency do not appear in the expression for optical graphene transmission. The “relativistic” nature of graphene carriers is therefore at the center of the explanation of why optical transmission is simply given by π times the constant of the thin structure. The electronic properties of graphene can be significantly modulated with lattice deformation (SHAINA and JAISWAL, 2014; NI et al, 2014; SEKIMOTO et al, 2017). The polarization-dependent graphene optical response also contains signatures of changes induced by deformations in the band structure, which can be monitored directly in a transmission experiment (YANKOWITZ et al, 2018).

6.1.1 – Graphene Quantum Dots

From several forms to open the bandgap of graphene, the reduction of the dimensionality from 2D to a 0D character is one of the most used. The increase in the quantum confinement due to the size reduction leads to new effects not found in 2D shapes, having more possible applications. The electronic properties change drastically in this size regime, leading from the continuum energy bands in the conventional 2D form to discrete states in the quantum dot form, and the transitions occur now in the HOMO-LUMO levels.

Figure 72 – a) Modulation of the bandgap for GQDs via size variation; b) The energy gap as a function of a total number of conjugated carbon atoms(N) for type-1 GQD (dash line with black circle), type-2 GQD (dash line with red square), type-3 GQD (dash line with a green triangle) and type-4 (dash line with blue star).

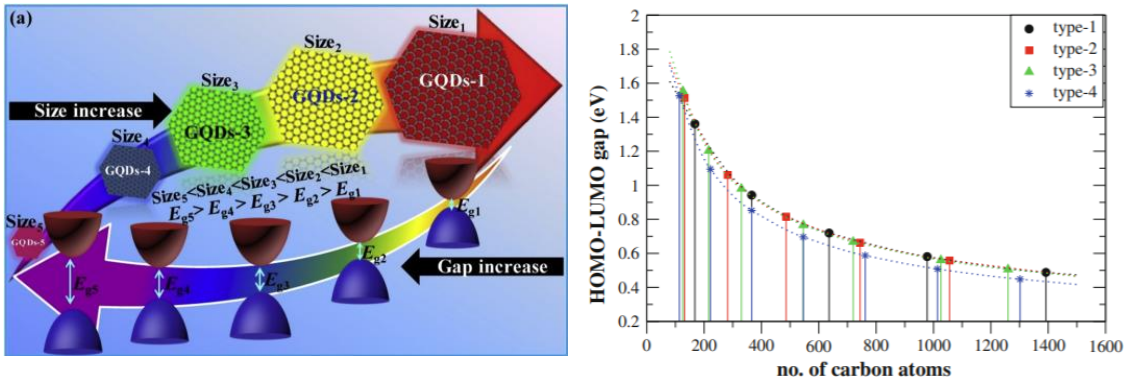

Source: Tian, et al (2018).

Figure 72 shows the bandgap value as a function of the quantum dots size, as is expected. The bandgap is large for small GQDs, and the optical properties can be tuned from NIR to UV with the decrease of dimensions. Figure 72 b) shows the calculated number of atoms versus the HOMO-LUMO energy transition; the behavior is close to the behavior shown by gold clusters.

Beyond the size-tunable bandgap, functionalization plays an important role in tunning of the HOMO-LUMO transition in GQDs. The surface modification of GQDs changes the electronic, optical, and chemical properties of these nanomaterials. The GQDs can be functionalized with different atoms, like B, N, O, and others. FAN et al, 2014 showed an increase in the photoluminescence of B-GQDs, obtaining a Quantum Yield (QY) of 95% when compared with no-doped GQDs. N-GQDs exhibit a large 2PA Cross Section (2PACS), as demonstrated by LIU et al, 2013.

Due to the interesting properties of GQDs, these nanomaterials have several applications. FACURE et al, 2020 showed the synthesis methods of GQDs – nanocomposites and their possible applications in the environment and agriculture. SUN et al, 2018

demonstrated the application of GQDs in photodynamic therapy exploiting the high 2PACS enhancement in N-GQDs. WANG et al, 2016 exploit the non-toxicity of GQDs as useful material for biological applications.

The unique properties of GQDs nanocomposites are suitable for designing devices employed in filtration membranes and adsorbent materials for contaminants removal, optical devices, and sensors with different transduction modes for detecting hazardous analytes including pesticides, heavy metals, antibiotics, food contaminants, and novel catalysts systems for degrading pollutants.

6.2 – STANDARD CHARACTERIZATION

6.2.1 – Absorption Spectroscopy

Optical absorption spectroscopy was performed using a two-arms CARY 5000 – UV – VIS-NIR spectrometer (Agilent technologies) in a range from 200 – 1200 nm, to identify optical transitions of commercial GQDs. Figure 73 shows the absorption spectra for both Acqua Cyan and Acqua Green GQDs.

Figure 73 – Absorption spectra for a) Acqua – Cyan GQDs and b) Acqua – Green GQDs.

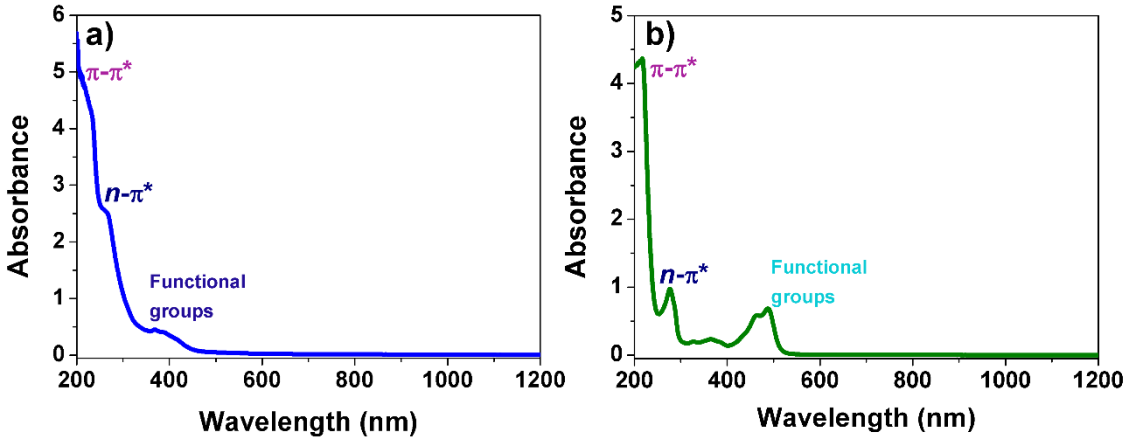

Source: The author (2021).

The optical transitions are indicated in the absorption spectra, the $\pi \rightarrow \pi^*$ excitation of the π bonds of aromatic C=C and a weaker peak at $\approx 300\,nm$ due to $n \rightarrow \pi^*$ transitions of C=O bonds (TANG, et al, 2012; LUO, et al, 2009). These transitions are present in both spectra, for Acqua - Cyan and Acqua - Green GQDs in Figures 73 a) and 73 b). The introduction of functional groups in the GQDs may lead to new absorption features and may change the GQD's optical properties (BACON et al, 2014; CHEN et al, 2018). The Acqua – Green GQDs presented another band of absorption, due to functional groups on the surface of the GQD.

6.2.2 – Photoluminescence Spectroscopy

Photoluminescence spectroscopy was performed using a commercial Spectrofluorimeter (Fluoromax - HORIBA) in the range between 425 – 700 nm. The excitation wavelengths are 385 nm for Acqua – Cyan GQDs and 485 nm for Acqua Green GQDs. In these wavelengths, the functional groups are responsible for the absorption bands. Zhou, S. et al. argues that high density of defects, functional groups, and oxygen groups are usually present on the surface of GQDs.

Figure 74 – PL for a) Acqua – Cyan GQDs and b) Acqua – Green GQDs.

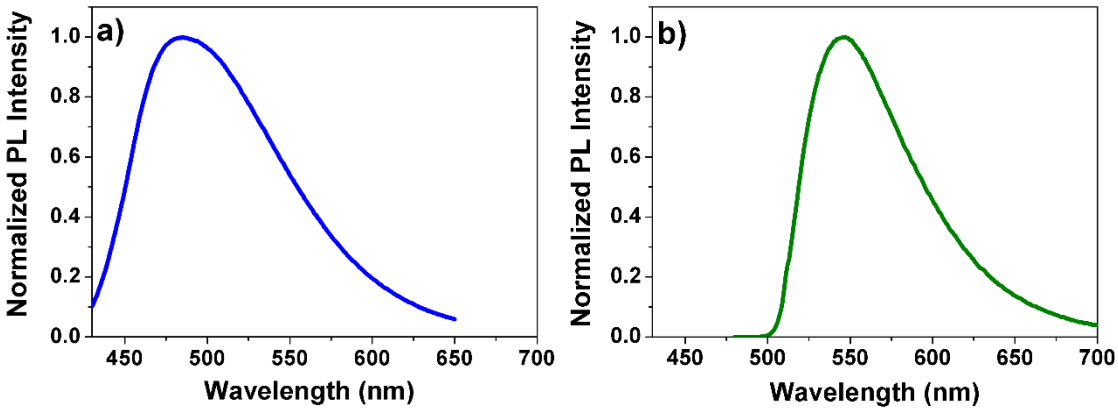

Source: The author (2021).

6.2.3 AFM

The GQDs dimensions were measured by Atomic Force Microscope (AFM) measurements. Figure 75 shows the AFM image for Acqua-Cyan and Acqua-Green GQDs.

Figure 75 – AFM images: (a) Acqua-Cyan GQDs; (b) Acqua-Green GQDs. The scale is 500 nm for both images. The scale bar is 500 nm for both images.

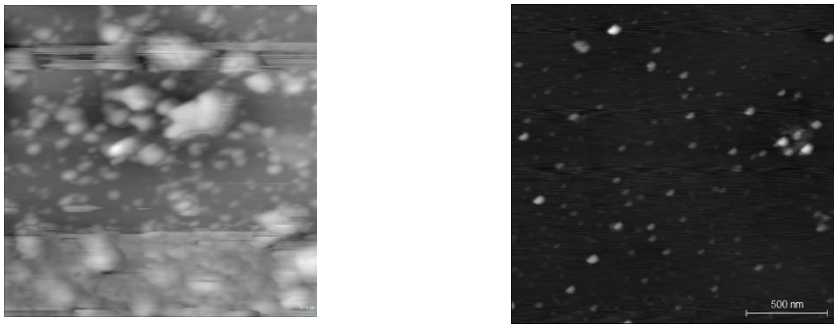

Source: The author (2021).

From the AFM images, it was possible to make a histogram of diameters and heights of the GQDs, as shown below. From the AFM images is possible to observe that the GQDs have

a rod-like shape. Figure 76 shows the histogram for diameters and heights of Acqua-Cyan and Acqua-Green GQDs. The log-normal fit indicates a maximum distribution for the diameter of 4 nm and a height of 52 nm for Acqua-Cyan GQDs. For the Acqua-Green GQDs, the size distribution is peaked for the diameter of 3.9 nm and the height of 46 nm.

Figure 76 – (a) Diameter and (b) lateral size for Acqua-Cyan GQDs; (c) Diameter and (d) height for Acqua-Green GQDs.

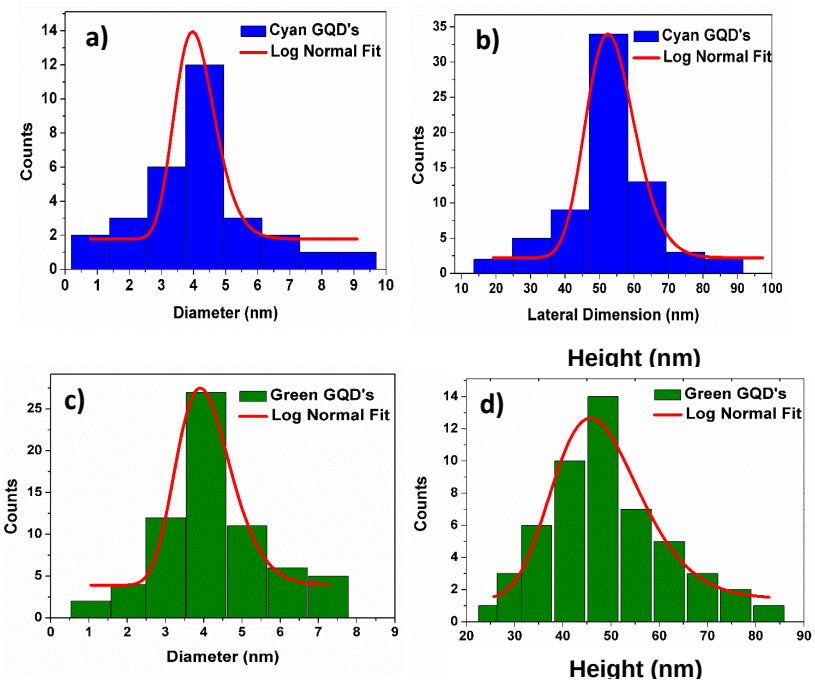

Source: The author (2021).

Using the size distribution, we could calculate the concentration of GQDs per cm³. The value obtained was $0.9 \times 10^{15}\ GQDs/cm^3$ for Acqua-Cyan and $1 \times 10^{15}\ GQDs/cm^3$ than Acqua-Green.

6.3 OPTICAL NONLINEARITIES IN GQD's

Optical nonlinearities have been investigated, both theoretically and experimentally in GQDs. Deb et al. investigated second-order nonlinearities using Density Functional Theory (DFT) for GQD's with a different number of atoms and shapes in two different regimes. They demonstrate a tunable nonlinearity and strong nonlinear optical response. YAMIJALA et al, 2015 performed computational studies of linear and nonlinear optical properties of ~400 different systems of GQDs, changing shape, number of atoms, and ligands. LI et al, 2019 employ theoretical calculations using the EFISH technique was used to characterize the first-order hyperpolarizability of GQDs.

Experimentally, some techniques have been employed to characterize nonlinear optical coefficients of GQDs. For example, 2PA induced luminescence is used to characterize the 2PACS doped and no-doped GQDs. QI, et al, 2019 used SHG to characterize B-GQDs introduced in cells to use as a probe for biological microscopy. The third-order nonlinear optical process has been also characterized. KUMARA et al, 2018 characterize thermal nonlinearities in GQDs using the Z-scan technique in 532 nm. The authors report closed and open aperture experiments using a continuous wave (CW) laser. WANG et al, 2019 showed a nonlinear refractive index and nonlinear absorption in the UV-VIS-NIR range using a variation of Z-Scan technique.

6.3.1 Second-order Nonlinearity in GQDs

The HRS technique was employed to characterize the first-order hyperpolarizability. The experimental setup is described in section 2 of chapter 3. Polarization resolved HRS was used to understand the origin of nonlinearity in GQDs. As shown in Figure 77, the laser frequency and its second harmonic are off-resonance with the absorption bands of both samples; therefore, we do not expect a luminescence signal superimposed on the HRS signal.

Figure 77 shows the HRS spectra for a) Acqua – Cyan GQDs and b) Acqua – Green GQDs. Notice that the spectra are centered at 532 nm, the second harmonic of the incident laser beam, with the linewidth limited by the spectrometer resolution.

Figure 77 – HRS spectra for a) Acqua – Cyan and b) Acqua Green GQDs.

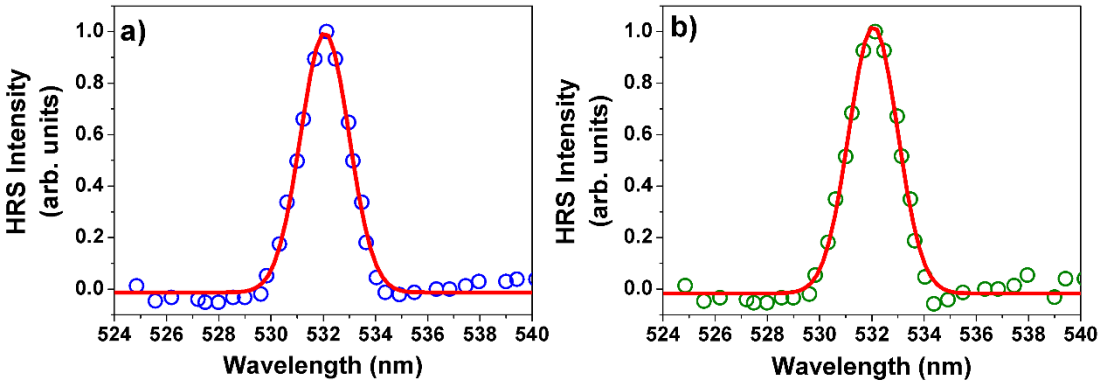

Source: The author (2021).

The blue and green open circles represent the experimental points for Acqua – Cyan and Acqua – Green GQDs, respectively and the red line represent a Gaussian fit performed for the experimental points. For the theoretical fit, the FWHM was obtained and has a value of ~2.2 nm.

The temporal evolution of the HRS signal follows the laser pulse corroborating the above statement that no long-lived luminescence is overlapping with the HRS signal. These measurements were performed with a laser peak intensity of $12\ \mathrm{GW/cm^2}$, and the minimum intensity to detect the HRS was $8.0\ \mathrm{GW/cm^2}$.

Figure 78 - Temporal evolution of the HRS signal (single laser shot) for (a) Acqua – Cyan GQDs, in blue and b) Acqua – Grenn GQDs in green. c) Superposition of temporal behavior (continuo black lines) of laser and Acqua – Cyan GQDs and Acqua – Green GQDs.

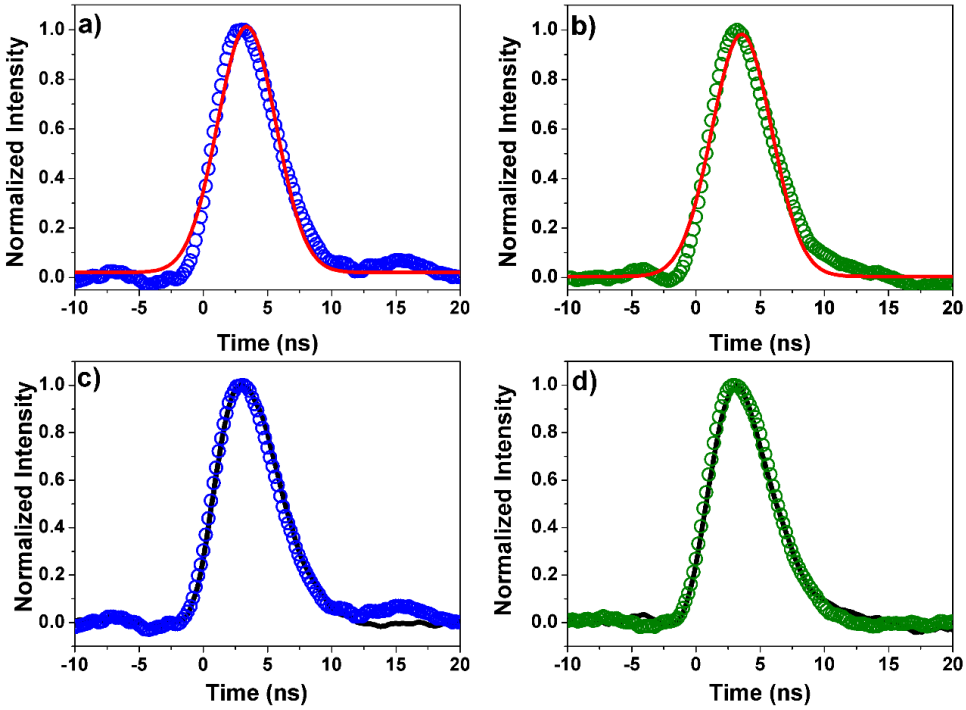

Source: The author (2021).

Figure 78 shows the temporal dependence of HRS for a) Acqua – Cyan and b) Acqua – Green GQDs. Figure 78 c) and d) show that the HRS signal follows the temporal evolution of the laser pulses for c) Acqua – Cyan GQDs and d) Acqua – Green GQDs. The black solid lines represent the laser profile.

The HRS signal is due to the nonlinear scattering by the randomly oriented GQDs and water molecules. The scattered intensity, at the second harmonic frequency of the incident laser beam, is described by $I\ (2\omega) = g\ \{\sum_c N_c \langle \beta_c^2 (2\omega) \rangle\}\ I^2(\omega)$, where $I(\omega)$ is the laser intensity, $\beta_c\ (2\omega)$ is the first hyperpolarizability and the sub-index represents the constituents of the suspension. The symbol $\langle \ldots \rangle$ indicates orientational average. The factor g depends on the scattering geometry and contains information on the transformation of coordinates from the GQD to the laboratory reference system (JOULAUD et al, 2013; BARBOSA-SILVA et al, 2020).

Figure 79 (a) shows plots of the HRS signal, $S(2\omega) \propto I\ (2\omega)$, versus the incident laser intensity were a quadratic dependence with $I\ (\omega)$ was verified.

Figure 79 - HRS intensity signal, $S(2\omega) \propto I\ (2\omega)$, versus the laser intensity for a) Acqua – Cyan GQDs and b) Acqua – Green GQDs.

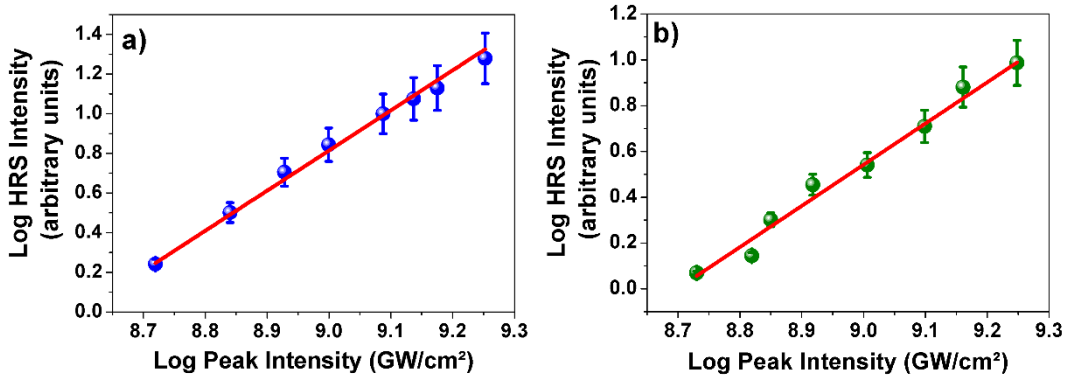

Source: The author (2021).

The slopes are 1.9 ± 0.1, and 1.8 ± 0.2 for Acqua – Cyan and Acqua – Green GQDs, respectively. These results are as expected and represent the participation of two photons in the measured process.

Figure 80 shows linear dependence of the HRS signal with the GQDs concentration and indicates that no agglomeration of GQDs is contributing to the HRS signal.

Figure 80 – Concentration dependence of $S(2\omega)$ with the concentration of GQDs per ml for a) Acqua – Cyan GQDs and b) Acqua – Green GQDs.

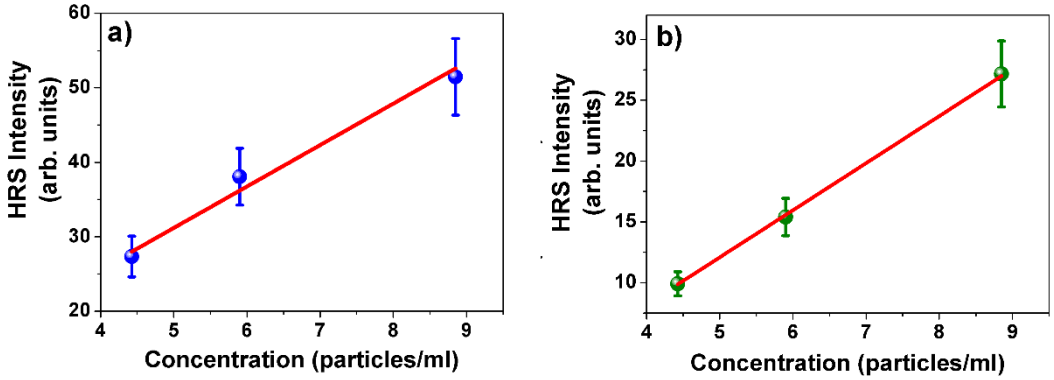

Source: The author (2021).

Figure 80 a) and b) shows a linear dependence of $S(2\omega)$ versus the GQDs concentration, for Acqua – Cyan and Acqua – Green GQDs. The x – axis is divided by a 10^{13} factor.

Since the samples consist of GQDs with different dimensions, the experiments provided effective values for the GQD hyperpolarizability, $\langle\beta(2\omega)\rangle_{eff}$. The external reference method (PAULEY, et al, 1996) using p-NA dissolved in methanol as the reference was applied to measure $\langle\beta(2\omega)\rangle_{eff}$ and the numerical values were obtained from

$$\langle\beta(2\omega)\rangle_{eff} = \left[\frac{S_{GQD}(2\omega)}{S_{pNA}(2\omega)}\left\{\frac{N_{pNA}\langle\beta^2_{pNA}\rangle + N_{mtOH}\langle\beta^2_{mtOH}\rangle}{N_{GQD}}\right\} - \frac{N_{water}\langle\beta^2_{water}\rangle}{N_{GQD}}\right]^{1/2}, \quad (6.4)$$

where $mtOH$ refers to methanol. The values obtained are given in Table 6.

Table 6 – Coefficients for equation 6.4.

	$water$	$p-NA$	$mtOH$
$\beta(2\omega) \times 10^{-30} esu$	0.087	30	0.69
$Concentration\ (N)$ $(molecules/cm^3)$	5.0×10^{22}	1.0×10^{19}	1.5×10^{22}

Source: The author (2021).

The concentration of GQDs, N_{GQD} , was $0.94 \times 10^{15}\ particles/cm^3$ for Acqua-Cyan GQDs and $1.0 \times 10^{15}\ particles/cm^3$ for Acqua-Green GQDs; both samples were suspended in water.

The quantity $\langle\beta(2\omega)\rangle_{eff}$ is an effective value contributed by GQDs with a different number of nanosheets. Consequently, we considered the following approach to estimate the hyperpolarizability per nanosheet, $\langle\beta(2\omega)\rangle_{NS}$. First, we considered the distribution of GQDs sizes; then, assuming nanosheet thickness of 1.5 nm, and a Gaussian distribution of GQDs sizes represented by $P(n) \propto \exp\left(-\frac{n^2}{n_{av}^2}\right)$, where n is the number of nanosheets in a GQD, we obtained $10 \leq n \leq 60$ for Acqua-Cyan and $15 \leq n \leq 57$ for Acqua Green. The value of n_{av} is obtained from the AFM measurements given in Figure 79. The value of $\langle\beta(2\omega)\rangle_{NS}$ is determined from $\langle\beta(2\omega)\rangle_{eff} = \langle\beta(2\omega)\rangle_{NS}\{\sum_1^n n\,P(n) / \sum_1^n P(n)\}^{1/2}$. Therefore, considering $n_{av} = 35$ for the Acqua-Cyan GQDs, we obtain $\langle\beta(2\omega)\rangle_{eff} = 5.0 \times \langle\beta(2\omega)\rangle_{NS}$, while for Acqua – Green GQDs, considering $n_{av} = 31$, we determined $\langle\beta(2\omega)\rangle_{eff} = 5.2 \times \langle\beta(2\omega)\rangle_{NS}$. These results allow quoting the hyperpolarizability per nanosheet as $\langle\beta(2\omega)\rangle_{NS} = 6.2 \times 10^{-27}$ esu (Acqua-Cyan) and $\langle\beta(2\omega)\rangle_{NS} = 4.6 \times 10^{-27}$ esu (Acqua-Green).

The two-level model (MARDER et al, 1991; CHEMLA et al, 1987) was used to relate $\langle\beta(2\omega)\rangle_{NS}$ with the static hyperpolarizability, $\beta_{NS}(0)$, by considering the laser frequency detuning with respect to the lowest energy band in the absorption spectrum that corresponds to the frequency ω_{eg}. The following equation was used:

$$\beta_{NS}(0) = \left(1 - 4\frac{\omega^2}{\omega_{eg}^2}\right)\left(1 - \frac{\omega^2}{\omega_{eg}^2}\right)\langle\beta(2\omega)\rangle_{NS}, \quad (6.5)$$

where ω_{eg} = 22222 cm^{-1} (Acqua-Cyan) and ω_{eg} = 19608 cm^{-1} (Acqua-Green).

The values for $\beta_{NS}(0)$ determined from Eq.(6.5) are $1.42 \times 10^{-27}\ esu$ (Acqua-Cyan) and $0.28 \times 10^{-27}\ esu$ (Acqua-Green).

Notice that the value of $\langle\beta(2\omega)\rangle_{NS}$ is approximately equal for both samples but the values of $\beta_{NS}(0)$ are different by $\approx 400\ \%$ because of the different laser frequency detuning with respect to the first excited resonance frequency ω_{eg}.

Although other materials, such as inorganic semiconductor quantum dots and perovskite alkaline niobates, may exhibit equal or even larger hyperpolarizabilities than the GQDs studied here, they present toxicity to living cells, unlike the GQDs. We recall that imaging measurements have been performed using GQDs exploiting their large PL, but HRS experiments present an important advantage concerning PL experiments because lasers operating in a large infrared wavelength range can be used since no resonance with excited states is required. This is a benefit because one may select the laser wavelength according to the transparency window of the biological system of interest.

To characterize the origin of the HRS signal, polarization-resolved experiments were performed following the usual procedure (HARFOUCH et al, 2013; RUSSIER-ANTOINE, et al, 2018; KHEBBACHE et al, 2017). The laser beam was linearly polarized and the angle γ, between the optical field and the vertical direction, was varied from 0 to 2π. The polarization of the HRS signal either in the vertical direction or parallel to the beam propagation axis was measured. The results are shown in Figure 81 and to fit the data it was used the expression:

$$I_{HRS}^{\Gamma} = a^{\Gamma}cos^4\gamma + b^{\Gamma}cos^2\gamma sen^2\gamma + c^{\Gamma}sin^4\gamma + d^{\Gamma}cos^3\gamma sin\gamma + e^{\Gamma}cos\gamma sin^3\gamma\,. \quad (6.6)$$

where I_{HRS}^{Γ} is the hyper–Rayleigh scattering intensity and Γ refers to the horizontal (H) or vertical (V) polarization. The coefficients a, b, c, d, e, were obtained from the fit. The depolarization coefficient, $\rho^{\Gamma} = c^{\Gamma}/a^{\Gamma}$, and the coefficient of multipolarity, $\varsigma^{\Gamma} = 1 - (a^{\Gamma}+c^{\Gamma}/b^{\Gamma})$, were also determined and their values are indicated in Table 7.

Table 7 – Depolarization and multipolarity parameters for both GQDs samples.

Sample Parameters	Cyan GQD V polarization	Cyan GQD H polarization	Green GQD V polarization	Green GQD H polarization
a	0.37	0.039	0.35	0.0031
b	0.85	0.16	0.8	0.12
c	0.34	0.037	0.31	0.0030
d	0.0020	0.00023	0.0018	0.00018
e	-0.015	0.00023	-0.011	0.00018
ρ	0.91	0.95	0.88	0.96
ς	0.16	0.52	0.18	0.49

Source: The author (2021).

Figure 81 is a polar plot of the laser polarization angle dependence of the HRS signal for both GQDs samples. The profiles obtained indicate electric quadrupole origin for the incoherent second harmonic observed that indicate a dominant GQDs volume contribution for the HRS signal.

Figure 81 – (a) Vertical polarization from Acqua-Cyan GQDs. (b) Horizontal polarization from Acqua-Cyan GQDs. (c) Vertical polarization from Acqua-Green GQDs. (d) Horizontal polarization from Acqua-Green GQDs.

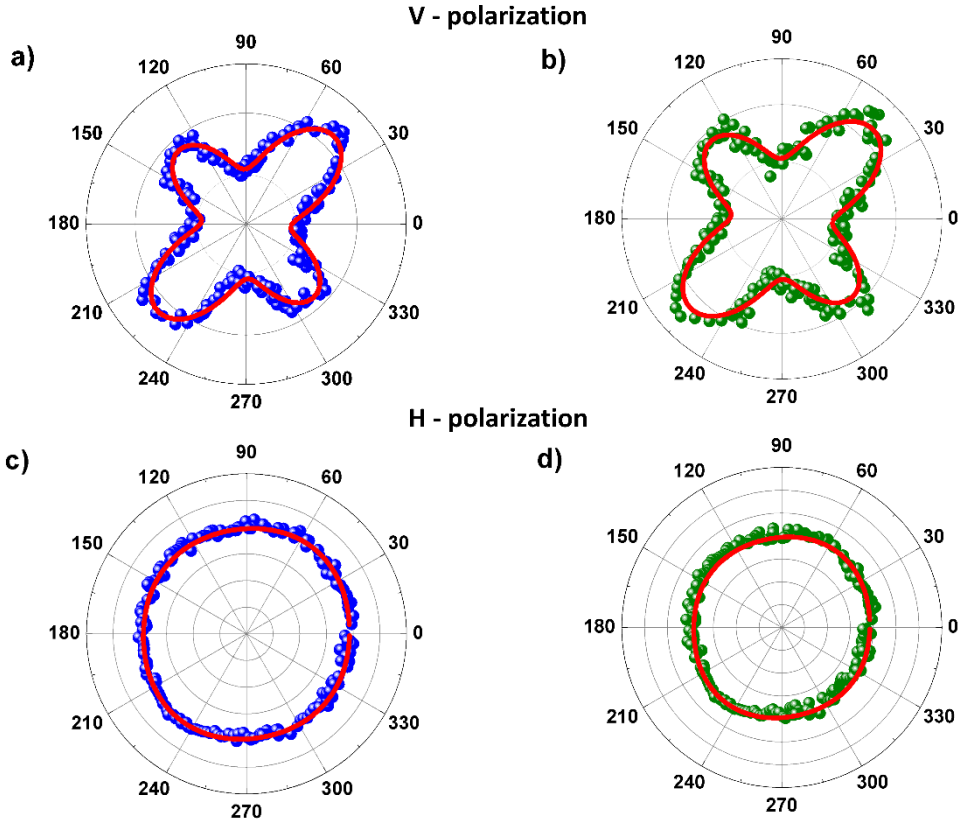

Source: The author (2021).

The same behavior was found in metallic nanoparticles and reported by Nappa and co-workers. Considering the dimensions of both GQDs, we already expected that retardation effects play an important role in the origin of nonlinearities.

6.4 2PA CROSS-SECTION OF GQD's MEASURED BY TWO – PHOTON ABSORPTION INDUCED LUMINESCENCE.

Two-photon induced luminescence is a useful technique for microscopy of biological samples. Two-photon microscopy with advantages such as a larger penetration depth minimized tissue autofluorescence background, and reduced photodamage in bio tissues has received much attention for its promising applications in both basic biological research and clinical diagnostics. In this sense, several types of quantum dots (QD) have been applied in

spectroscopy and imaging techniques in biological systems (MAESTRO et al, 2010). However, the toxicity of heavy metal-based QD is a problem for applications while GQDs present low toxicity.

In this section, it is shown the characterization of two-photon absorption induced luminescence (2PL) with excitation at 850 nm performed for both GQDs. Figures 82 a) and 82 b) show the 1PL (red line) and 2PL (dots) spectra for both samples.

Figure 82 – Normalized 1PL and 2PL Intensity a) Acqua-Cyan GQDs and b) Acqua Green GQDs. 2PL time behavior for c) Acqua-Cyan GQDs and Acqua – Green GQDs.

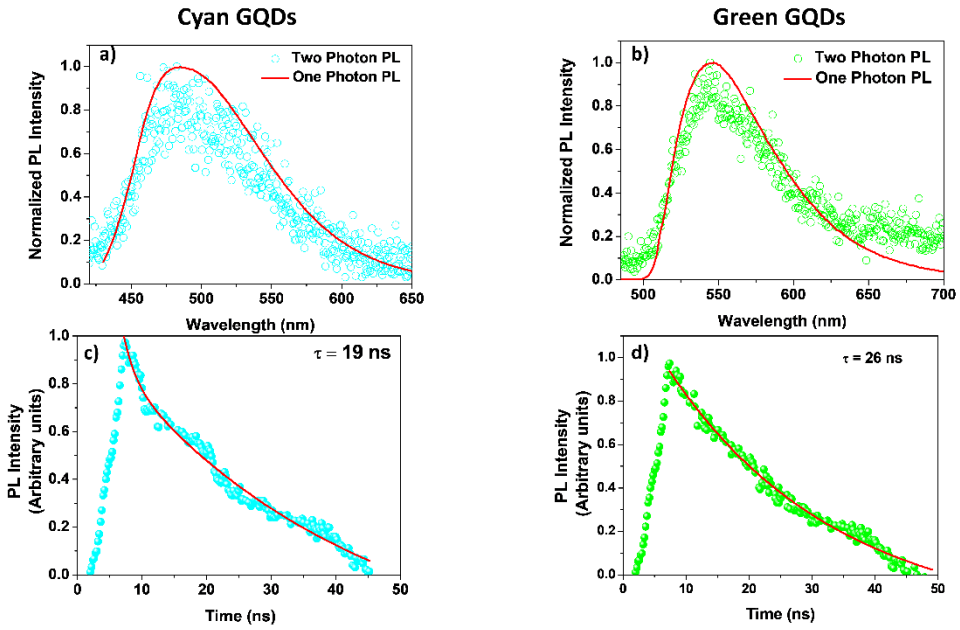

Source: The author (2021).

From Figures 82a) and 82b) it is possible to see the superposition of spectra for 1PL and 2PL, as expected.

The knowledge of the fluorescence lifetime decay of excited states for any material is significant to understand optical properties and open new possibilities to application. In Figures 82 c) and 82 d) we show the temporal behavior of 2PL, with a fluorescence lifetime of 19 ns for Acqua-Cyan GQDs and 26 ns for Green GQDs. These results are compatible with previous studies reported (RODING et al, 2014).

In order, to show that the fluorescence detected is due to the absorption of two photons, measurements of output intensity in the function of input intensity were performed and a log x log plot is presented.

Figure 83 – $Log(I_{out}) \times Log(I_{in})$ for a) Acqua – Cyan GQDs and b) Acqua – Green GQDs.

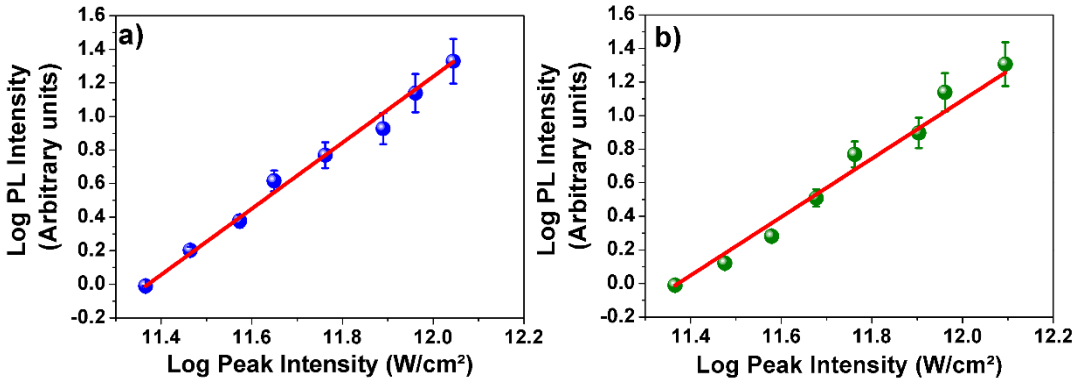

Source: The author (2021).

Figure 83a) and 83b) shows the $Log(I_{out}) \times Log(I_{in})$ plots for Acqua – Cyan and Acqua-Green GQDs, respectively. The experimental points are represented by the blue and green circles, and the red line is the linear fit. From the linear fit was possible to determine the slopes of the straight lines for both samples: 1.9 ± 0.2 for Acqua Cyan and 1.7 ± 0.3 for Acqua green GQDs.

To calculate the 2PA cross-section (2PACS) it was used the procedure described in Chapter 3, section 3.3. A dye with a known 2PACS and emission close to GQDs is used. For this, the dye Coumarin 540 A (Exciton) is employed. The value of 32 GM is used for dye, calculated by MAKAROV et al, 2008. Using the equation (3.42) we find the values of $\sigma^{(2)} = 975\ GM$ for Acqua Cyan GQDs and $\sigma^{(2)} = 655\ GM$ for Acqua Green GQDs. The difference in 2PACS is due to the higher concentration of Acqua – Green GQDs when compared with Acqua – Cyan. The values found are one order of magnitude large when compared with synthetic dyes (MAKAROV et al, 2008).

These values are small when compared with Nitrogen (N) doped GQDs that have values of 48000 GM, as shown by LIU et al, 2013. Nitrogen doping enhances the cross-section. The enhancement effect may be due to the change in the density of electronic states induced by the N atoms. In their samples, the authors report N-GQDs as quasi-round nanosheets (diameters =3 nm), with heights between 0.5 and 1 nm (monolayers). For our samples, the heights are about 60 nm. Probably quantum confinement effects are smaller in our samples because of their large thicknesses.

6.5 PARTIAL CONCLUSIONS

The first-order hyperpolarizability and the 2PACS of two different GQDs in aqueous solution by using the techniques of hyper-Rayleigh scattering and Two-photon absorption

induced luminescence, respectively. The first-order hyperpolarizability measurements indicate $\langle\beta(2\omega)\rangle_{NS}\sim 10^{-27}\ esu$ per nanosheet. The spectra of the scattered light (centered at the second harmonic frequency), as well as their fast temporal behavior, prove that the signals detected are due to the second harmonic generation and not due to luminescence induced by two-photon absorption. Using the two-level model, we could determine the static hyperpolarizability from the hyper-Rayleigh scattering data.

Two Photons Absorption Cross Section was calculated using a reference method. The values found are larger than the 2PACS of several organics dyes but smaller than N-doped GQDs. The large size and the absence of defects in the sample can be contributed to the small value of 2PACS.

The values of the GQDs hyperpolarizabilities indicate that the two samples studied are useful for imaging in microscopy of biological systems especially because of nontoxicity to living cells. Moreover, we observe that the use of hyper-Rayleigh scattering for imaging is advantageous because lasers in a large wavelength range can be used according to the transparency window of the system being investigated.

7 $NaNbO_3$ SUBMICRO-CRYSTALS

Synthesis and characterization performed at Universidade Federal of Alagoas

Sodium Niobate ($NaNbO_3$) are inorganic perovskites that have interesting physical and chemical properties. The $NaNbO_3$ can be present in two different phases: cubic and orthorhombic. Depending on the phase, different properties can be found. For example, LI et al, studied the dependence of the electronic and photocatalytic properties with the crystallographic symmetry. He showed a reduction of the bandgap when the cubic phase is synthetized (3.29 eV) versus 3.45 eV for the orthorhombic phase. The photocatalytic H_2 evolution activity over cubic $NaNbO_3$ was approximately twice that of the orthorhombic $NaNbO_3$.

Figure 84 – a) Schematic crystal structures of cubic and orthorhombic $NaNbO_3$ b) Absorption spectra for cubic phase (in red) and orthorhombic phase (in black). The inset shows the Tauc plot for both samples. c) Photocatalytic H_2 evolution from the aqueous methanol solution over c-$NaNbO_3$ and o-$NaNbO_3$ samples with loading of 0.5 wt % Pt.

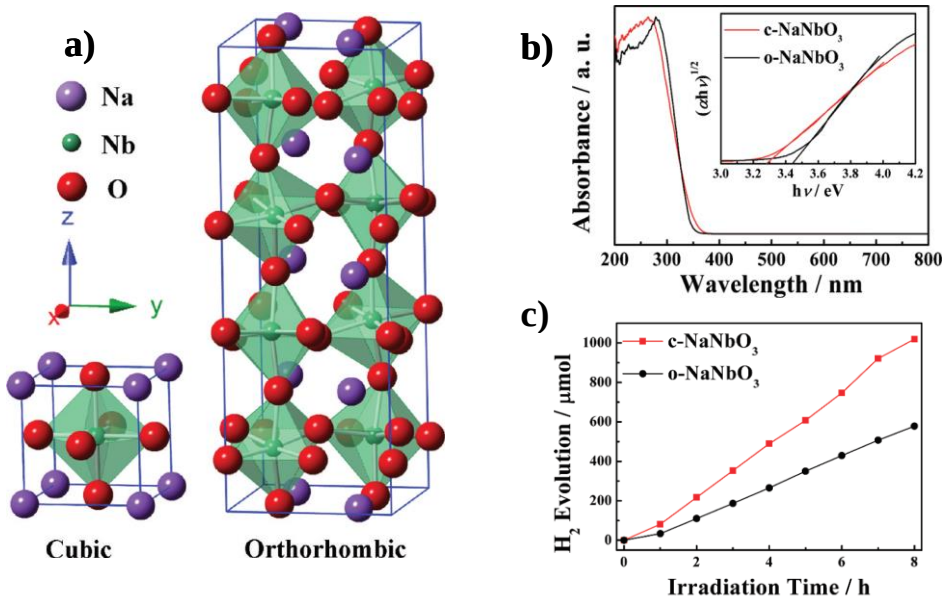

Source: Li, et al (2012).

Figure 84a) shows the schematic representation of the crystalline structures of $NaNbO_3$. An important aspect is that the cubic phase is not stable at room temperature, but only for temperatures >913K. When the temperature is reduced, the material presents a transition to rhombohedral phase, and after, at room temperature, a stable antiferroelectric orthorhombic phase, with *Pbcm* space group, and lattices constants with values of $a = 5.506$ Å, $b = 5.566$ Å, and $c = 15.52$ Å. Figure 84b) shows the absorption spectra for a cubic phase in red, and an

orthorhombic phase in black; the inset of the figure shows the Tauc plot for both phases, with indirect bandgap, and a small change in the bandgap energy for the different phases. Figure 84c) shows the behavior of H_2 evolution for both samples. The authors attribute the difference in the photocatalytic properties to the difference in the electronic structure of the phases.

Another important property of $NaNbO_3$ is piezoelectricity. XHANG et al, 2013 study the piezo and dielectric properties of $NaNbO_3$ ceramics using different techniques. The structural properties of $NaNbO_3$ samples were characterized several times, using techniques of X-Ray Diffraction (XRD) and Raman spectroscopy, for example. Polymorphism from micro to nanocrystals of $NaNbO_3$ are identified by using the techniques of XRD and Raman spectroscopy (SHIRATORI et al, 2005). The polymorphism is induced by the different sizes. Successive phase transitions were identified by SHIRATORI et al, 2007 in a range between -150°C and 400°C by using XRD technique. The authors also showed characteristic Raman actives modes and their dependence on the temperature. The contribution to the Raman spectra is due to translational, librational, and internal vibrations.

7.1 HRS EXPERIMENTS

The experimental setup for the HRS experiments is the same used in previous experiments and is described in section 3.2. Shortly, the excitation source was a Q-switched Nd: YAG laser (1064 nm, 10 Hz, 7ns). The excitation intensity on the samples was controlled by a half-wave plate and a polarizer. A 5 cm lens was used to focus the laser beam on the samples and the HRS signal (wavelength: 532 nm) was collected perpendicularly to the laser propagation direction. A pair of lenses was applied to collect the HRS signal and focus on a spectrometer fitted with a photomultiplier or a fast detector (rise time: 1ns). In this setup, the use of filters is pivotal to collect the HRS signal. Thereby, a filter was used in the laser output to avoid scattered light from the flashlamp to reach the samples. Also, an interference filter, centered at 532 nm (FWHM: 1nm), was placed between the two lenses that collect the HRS signal to prevent the scattered infrared at 1064 nm to reach the detector.

Figure 85 - Log-log plot of the HRS signal intensity versus the laser intensity for samples: A (black), B (purple), C (Green), D (Blue), and E (magenta). The nanocrystals were suspended in methanol. The parameter *m* is the slope of the straight lines. The values of about 2 indicate the number of laser photons for the generation of the HRS signal.

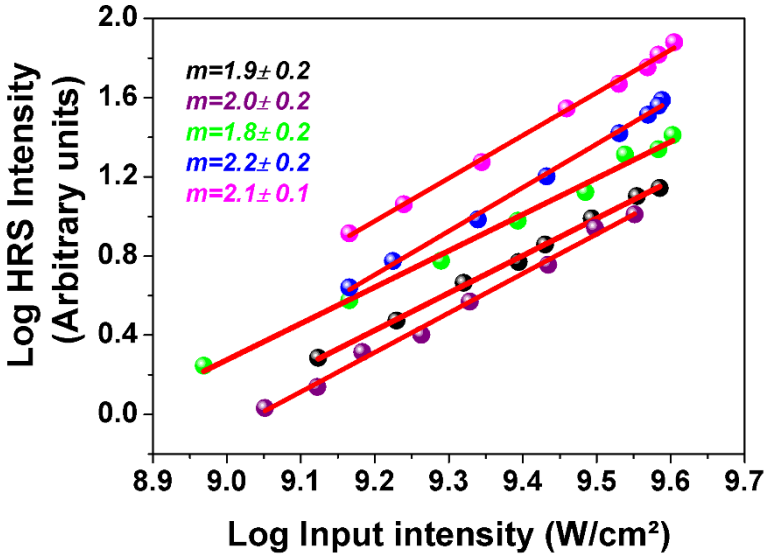

Source: The author (2021).

The hyper-Rayleigh spectra for all samples are shown in Figure 86. The signals, centered in the second harmonic of the incident laser wavelength, had their amplitudes normalized with respect to the signal of the normalization factors are indicated beside the curves.

Figure 86 - HRS spectra. Samples: A (black), B (purple), C (Green), D (Blue), and E (magenta). The curves were shifted in the vertical axis to prevent overlap between them.

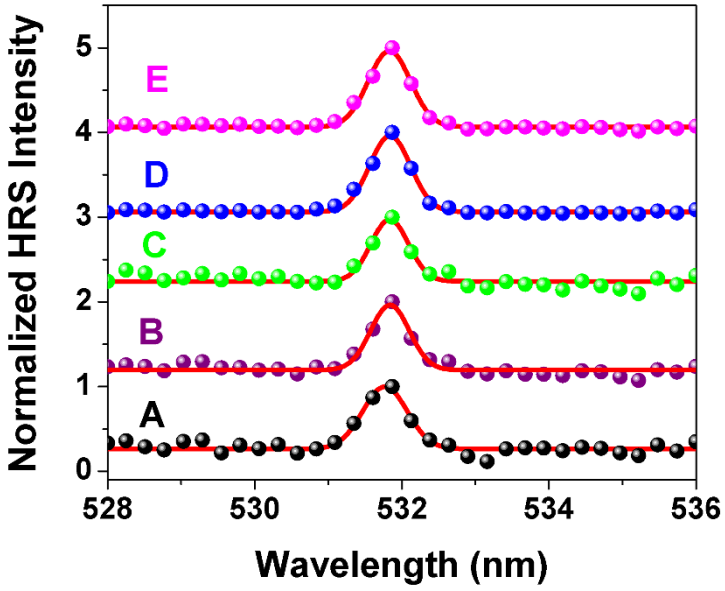

Source: The author (2021).

The intensity of the HRS signal $I(2\omega)$ and the intensity of excitation source $I(\omega)$ is given by JOULAUD et al, 2013:

$$I(2\omega) = G(N_m F_m \langle \beta_m^2 \rangle + (N_{nc} T_{nc} \langle \beta_{nc}^2 \rangle) I^2(\omega), \quad (7.1)$$

where N, F, T and $\beta_{m,nc} = \beta_{m,nc}(2\omega)$ are the concentration, local field factor, internal field factor, and the effective first hyperpolarizability of the host medium and the nanocrystals, respectively. G is a parameter that includes the light collection efficiency. The subscripts *m* and *nc* refer to the host medium (methanol) and nanocrystals. The symbol $\langle \dots \rangle$ indicates the orientational average. The local field factors and the internal field factor are given by JOULAUD et al, 2013 $F_m = \left(\frac{n_m^2+2}{3}\right)^6$ and $T_{nc} = \left(\frac{3n_m^2}{2n_m^2+n_{nc}^2}\right)^6$, where $n_m = 1.32$, and $n_{nc} = 2.12$ the linear refractive indices.

As shown in equation (7.1), there is a quadratic dependence between $I(2\omega)$ and $I(\omega)$ as confirmed in Figure 85. The maximum laser peak intensity was ≈2 GW/cm^2. Another feature to point out in the HRS signal is the narrow linewidth of spectra, shown in Figure 90, obtained by using a spectrometer.

The method applied to determine the first hyperpolarizability of the samples was the *external reference method* (ERM). Accordingly, the evaluation of $\beta(2\omega)$ is performed by comparison with a standard reference sample: a solution of *para*-nitroaniline (*p*-NA) in methanol with hyperpolarizability of 34×10^{-30}. Experiments to measure the HRS signal as a function of concentration was performed for all samples (including the reference sample) and the values of $\beta(2\omega)$ can be calculated using the equation $\langle \beta_{nc} \rangle = \sqrt{\frac{\alpha_{nc} F_{p-NA}}{\alpha_{p-NA} T_{nc}}} \langle \beta_{p-NA} \rangle$ where, α_{nc} and α_{p-NA} are the slopes of the straight lines and $F_{p-NA} = F_m$ (JOULAUD et al, 2013).

Plots of $I(2\omega)$ versus concentration for the nanocrystals and reference solutions are shown in Figure 87. The values of $\langle \beta_{nc} \rangle$ are determined from the slopes of the straight lines in Figure 87 and the above relation between $\langle \beta_{nc} \rangle$ and $\langle \beta_{p-NA} \rangle$. Note that $\langle \beta_{nc} \rangle$ scales with the average diameter of the nanocrystals as predicted for NPs made of non-centrosymmetric materials (BREVET et al, 2013). In this case, most of the nonlinear effect is due to the entire volume of the NP. However, since samples C, D, and E are not composed of 100% of $NaNbO_3$, corrections for the values of the first hyperpolarizabilities were performed. The results are summarized in Table 8.

Figure 87 - HRS signal as a function of concentration in units of NC's/cm^3 (nanocrystals per cm^3): a) sample A, b) sample B, c) sample C, d) sample D, e) sample E, and f) *p*-NA.

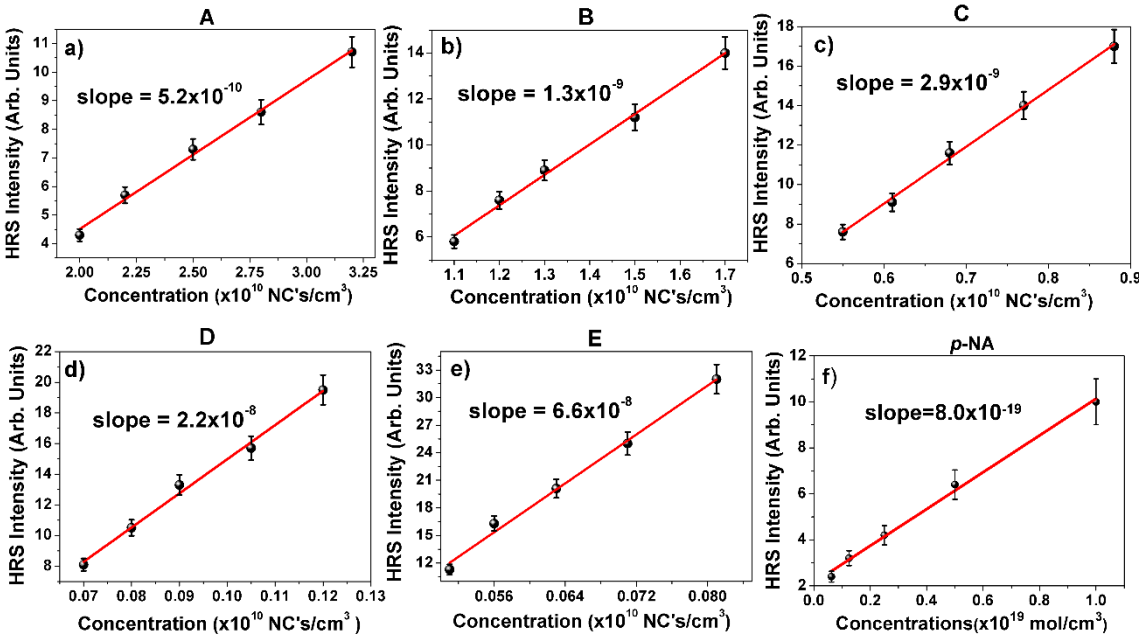

Source: The author (2021).

Table 8 - First hyperpolarizabilities of the samples. The uncertainty for $\langle \beta_{nc} \rangle$ is ±10% .

PARAMETERS / SAMPLES	$\langle \beta_{nc} \rangle$ (esu) $(x10^{-24})$	$\langle \beta_{nc} \rangle^*$ (esu) $(x10^{-24})$	$\langle \beta_{nc} \rangle^* / V$ (esu/nm^3) $(x10^{-29})$	$\langle \beta_{nc} \rangle^* / unit\ cell$ (esu) (10^{-28})
A	5.98	5.98	4.95	118.2
B	9.46	9.46	3.67	87.5
C	14.13	13.20	2.57	57.2
D	38.91	36.38	0.41	9.2
E	67.40	58.37	0.06	1.3

Source: The Author (2021).

*Corrected for the relative concentration of $NaNbO_3$ (according to the Rietveld refinement).

Values of $\langle \beta_{nc} \rangle / V$ were reported for various nanocrystals by JOULAUD et al, 2013. For example, the values reported for $LiNbO_3$ and $KNbO_3$ nanocrystals (with average diameter ≈

126 nm) were 1.6 $x10^{-29}$ esu and 1.98 $x10^{-29}$ esu, respectively. As one can see in Table 8 of this report, the values obtained for $NaNbO_3$ have the same order of magnitude, and the values achieved are understood considering its crystalline structure and shape. Differently of bulk $NaNbO_3$ (a known antiferroelectric material), the nanocrystals studied here are ferroelectric as supported by the XRPD and Rietveld refinement results and by previous reports (SHIRATORI et al, 2005; SHIRATORI et al, 2007; KORUZA et al, 2007).

Also presented in Table 8 are the results for the first hyperpolarizability considering the presence of impurities, $\langle\beta_{nc}\rangle^*$, as indicated in Table 8. Notice that $\langle\beta_{nc}\rangle^*/V$ increases as the nanocrystal's average size decrease. This behavior suggests the possibility of surface effects contributing to the effective first hyperpolarizabilities of the samples. Although the surface contribution is expected to be more important for small nanoparticles (diameter $\approx$ 10 nm), the size contribution is observed in this report being attributed to the asymmetric shapes and defects in the surfaces of the nanoparticles.

7.3 PARTIAL CONCLUSIONS

We measured the first-order hyperpolarizability of $NaNbO_3$ nano and submicron crystals synthesized in different temperatures (600 °C, 700 °C, 800 °C, 900 °C, and 1000 °C) using the technique of HRS. An increase of the hyperpolarizability with the synthesis temperature is shown. This behavior can be explained by the dependence of the hyperpolarizability with the concentration of NC's (Small concentrations = large hyperpolarizabilities). When the temperature of synthesis increases, the size of nanocrystals also increases, and the concentration of NCs/ml at the suspension decreases. When we calculate the $\beta(2\omega)/V$ or $\frac{\beta(2\omega)}{unit\ cell}$, we observed that the NCs of smaller sizes have a larger value of hyperpolarizabilities per atom. This can be explained by the quantum confinement when occurring the reduction of size.

8 CONCLUSIONS AND PERSPECTIVES

The nonlinear optical properties of photonic materials with nano and submicro dimensions were characterized. Standard characterizations were performed to understand the morphology, electronic and linear optical properties of the materials studied.

Layered Transition Metal Dichalcogenides (LTMD'Ss) are 2D materials that have interesting electronic and optical properties. Second- third- and fifth-order nonlinearities were characterized for different LTMD'Ss. The second-order nonlinear optical properties were characterized in $ZrTe_2$ flakes suspended in acetonitrile using the technique of Hyper – Rayleigh Scattering (HRS). This technique is based on the effect of incoherent second harmonic generation to measure and to understand the molecular hyperpolarizability of molecules and nanoparticles. It was found a high value of the first hyperpolarizability for $ZrTe_2$ suspensions, and the polarization-resolved HRS method was applied to investigate the origin of the nonlinearity. The polar plot of the HRS intensity indicated a dipolar origin for the second harmonic generation process, suggesting large contributions from the flakes edges. The nonlinear refractive index was also determined for $ZrTe_2$ flakes using the Z-scan technique. The determination of the electronic structure by use of DFT calculation (performed by collaborators) supported the experimental results. One application of $ZrTe_2$ was performed: the use of 3D and 2D forms as scatters for a Random Laser. The gain medium used was Rh6G and the $ZrTe_2$ flakes showed good stability.

Unusual behavior for nonlinear refractive index and nonlinear absorption was found in NbS_2 flakes. A change of nonlinear refractive index from negative to positive was shown, and a transition from two-photon absorption to saturated absorption was also found. Based on previous works, the behavior of the nonlinear refractive index could be explained as RSA and ESA processes in the nanoflakes. DFT calculations (performed by collaborators) supported very well the experimental results. Nonlinear light scattering was observed and contributed to the Z-scan measurements.

The nonlinear optical properties of MoS_2, the most known and studied LTMD'S, were also investigated Despite being widely studied, we measured for the first time the presence of third- and fifth-order nonlinear refraction in MoS_2 samples. For large intensities (~70 GW/cm^2), a change in the profile of the Z-scan curve was observed, which is compatible with the presence of high-order nonlinearities. Nonlinear absorption was not observed for this sample.

Metallic Nanoclusters (MNCs) were another nanostructure that was investigated. They are aglomerates with a small number of atoms covered by molecules. We characterize the second-order nonlinear optical process of an MNC with six gold atoms protected by glutathione and mercapitopropilic acid ($Au_6(GSH)_2(MPA)_2$). A large value of the first hyperpolarizability was measured for this cluster, and an interesting property was verified: the increase of the hyperpolarizability per atom when the number of atoms in the cluster is decreased. The static hyperpolarizability was also calculated.

Graphene Quantum Dots (GQDs) is a carbon-based nanomaterial with a nonzero bandgap. The nonzero transition energy between the HOMO-LUMO levels has interesting photoluminescence properties. We characterized two different GQDs using the techniques of HRS, for second-order nonlinear optical process, and 2PAIL, to characterize the two-photon absorption cross-section. We found a good value for hyperpolarizabilities ($\sim 10^{-27}\ esu$). The 2PACS is low when compared with N-doped GQDs. Polarization resolved HRS was also employed to understand the origin of the nonlinearity; a four-lobe pattern was obtained indicating a high contribution of edges.

$NaNbO_3$ nanocrystals synthesized in differents temperatures were also investigated. An increase in the hyperpolarizability was found when the synthesis temperature is increased. This indicates an increase in the size of the nanocrystals with the temperature synthesis. On the other hand when we calculate the $\beta(2\omega)/V$ and $\frac{\beta(2\omega)}{unit\ cell}$, a decrease of these parameters is found when the temperature increase. The difference among the several samples is related to the changes in the crystalline structure of the nanocrystals.

The studies reported in this work allow evaluation of the different materials for possible applications in photonic devices. LTMD'Ss are the materials of larger interest at the present time. Future work may be dedicated to the study of the LTMD'Ss using different nonlinear optical techniques. For instance, a deeper understanding of the NbS_2 nanoflakes may be reached if an optical Kerr gate (pump-and-probe) study is performed to investigate the temporal behavior of the nonlinearity. Other interesting lines of research are for example: (*i*) the exploitation of the fifth-order nonlinearity of MoS_2 to investigate the propagation of solitons in an appropriate liquid suspension; (*ii*) the operation of Random Lasers to evaluate the efficiency of MoS_2 and WS_2 as scatters in comparison with $ZrTe_2$ already studied; (*iii*) investigation of excitonic resonances of the LTMD'Ss by characterization of their nonlinear manifestation by polarization spectroscopy.

In summary, the results herein presented open avenues for future research of basic and applied characteristics.

REFERENCES

ABBOT, E. A. *Flatland: A romance of many dimensions*. Dover, (1942).

AHMED, M. H. M. et al, *Mode-locking pulse generation with MoS_2–PVA saturable absorber in both anomalous and ultra-long normal dispersion regimes*, **Appl. Opt**. 55, 4247-4252 (2016).

ANDREWS, D. L., et al, *Theory of second harmonic generation in randomly oriented species*. **Chemical Physics**, 190, 1–9 (1995).

AUTERE, A. et al, *Optical harmonic generation in monolayer group-VI transition metal dichalcogenides*, **Phys. Rev. B** 98, 115426 (2018).

BACON, M. et al, *Graphene Quantum Dots.* **Part. Part. Syst. Charact**., 31, 415-428 (2014).

BAIN, D. et al, *Core-Size Dependent Fluorescent Gold Nanoclusters and Ultrasensitive Detection of Pb^{2+} Ion*. **ACS Sustainable Chem. Eng**., 6, 2334-2343 (2018).

BAIN, D. et al, Luminescent Au_6 and Au_8 Nanoclusters from Ligand Induced Etching of Au Nanoparticles. **Mater. Res. Express**. 2019, *6*, 124004.

BAIN, D. et al, *Opportunities and challenges in energy and electron transfer of nanocluster based hybrid materials and their sensing applications*. **Phys. Chem. Chem. Phys**., 21, 5863 (2019).

BAIN, D. *Fluorescent Metal Nanoclusters: Synthesis, Photophysical Properties and Applications*. Doctorate Thesis. **Indian Association for the Cultivation of Science – School of Materials Science** (2019).

BARBOSA-SILVA, R. et al, *First Hyperpolarizability of 1,3-Thiazolium-5-Thiolates Mesoionic Compounds*. **J. Phys. Chem. C**, 123, 677–683 (2019).

BARBOSA-SILVA, R. et al, Second-order *nonlinearity of $NaNbO_3$ nanocrystals with orthorhombic crystalline structure* **J. Lumin**., 2019, 211, 121–126.

BERA, D., et al, *Quantum Dots and Their Multimodal Applications: A Review*. **Materials**, 3(4), 2260–2345 (2010).

BERNARDI, M. et al, *Extraordinary Sunlight Absorption and One Nanometer Thick Photovoltaics Using Two-Dimensional Monolayer Materials*. **Nano Lett**., 13, 3664-3670 (2013).

BESSE, V., et al, *Fifth-order nonlinear susceptibility: Effect of third-order resonances in a classical theory*. **Physical Review A**, 92(1) (2015).

BHIMANAPATI, G. R., et al., *Recent advances in two-dimensional materials beyond graphene*. **ACS Nano** 9: p. 11509–11539 (2015).

BIKORIMANA, P. et al, *Nonlinear optical responses in two-dimensional transition metal dichalcogenide multilayer: WS_2, WSe_2, MoS_2 and $Mo_{0.5}W_{0.5}S_2$*. **Opt. Express** 24, 20685-20695 (2016).

BOKER, T. et al, *Band structure of MoS_2, $MoSe_2$, and α-$MoTe_2$: Angle-resolved photoelectron spectroscopy and ab-initio calculations*. **Phys. Rev. B** 64, 235305 (2001).

BOSCHETTI, A., et al, *Spectral super-resolution spectroscopy using a random laser*. **Nature Photonics** 14, 177–182 (2019).

BOYD, R., *Nonlinear optics*, ed. 3, **Academic Press**, (2008).

BRASSELET, S. and ZYSS, J. *Nano-Crystals for Quadratic Nonlinear Imaging: Characterization and Applications*, **Nanocrystals,** Yoshitake Masuda, IntechOpen (2010).

BREVET, P. F. *Second Harmonic Generation in Nanostructures*. **Compr. Nanosci. Technol**., *1–5*, 351–381 (2011).

BUTET, J. et al, *Multipolar second harmonic generation from metallic nanoparticles, in Metal Nanostructures for Photonics*, ed. L. R. P. Kassab and C. B. de Araújo, **Elsevier**, 2019.

CAO, H. et al. *Ultraviolet lasing in resonators formed by scattering in semiconductor polycrystalline films*. **Applied Physics Letters**, 73, 25, 656–3658 (1989).

CAO, H. *Review on latest developments in random lasers with coherent feedback.* **J. Phys. A: Math. Gen**. *38 10497* (2005).

CHEMLA, D. S. *Nonlinear Optical Properties of Organic Molecules and Crystals*; **Academic Press**: New York, (1987).

CHEN, W. et al, *Synthesis and Applications of Graphene Quantum Dots: A Review*. **Nanotech. Reviews**, 7, 157-185 (2018).

CHEN, W. Y. et al, *Synthesis of Fluorescent Gold Nanodot–Liposome Hybrids for Detection of Phospholipase C and its Inhibitor*. **Anal. Chem**., 85, 8834-8840 (2013).

CLAYS, K. et al, *in Linear and Nonlinear Optics of Organic Materials*, ed. M. Eich and M. G. Kuzyk, **Proceedings of SPIE**, 2001, vol. 4461, pp. 105–116.

CLAYS, K., and PERSOONS, A., *Hyper-Rayleigh scattering in solution*, Phys. Rev. Lett. 66, 2980 (1991).

CLAYS, K., and PERSOONS, A., *Hyper-Rayleigh scattering in solution*, **Review of Scientific Instruments** 63, 3285 (1992).

COEHOORN, R. et al, *Electronic structure of $MoSe_2$, MoS_2, and WSe_2. II. The nature of the optical bandgaps*. **Phys. Rev. B** 35, 6203–6206 (1987).

CONAN, A. et al, *Temperature Dependence of the Electrical Conductivity and Thermoelectric Power in $MoTe_2$ Single Crystals*. **Phys. Status Solidi B**, 94, 279−286 (1979).

CYVIN, S. J., et al, *Theory of Hyper-Raman Effects (Nonlinear Inelastic Light Scattering): Selection Rules and Depolarization Ratios for the Second-Order Polarizability.* **The Journal of Chemical Physics,** 43(11), 4083–4095, (1965).

DA SILVA-NETO, M. L. et al, *Hyper-Rayleigh Scattering in 2D Redox Exfoliated Semi-Metallic $ZrTe_2$ transition Metal Dichalcogenide*. **Phys. Chem. Chem. Phys**., *22*, 27845–27849 (2020).

DAS, P. K. *Chemical Applications of Hyper-Rayleigh Scattering in Solution.* **The Journal of Physical Chemistry B**, 110(15), 7621–7630 (2006).

DE OLIVEIRA, N. T. C. et al, *Light scattering, absorption and refraction due to high-order optical nonlinearities in coloidal gold nanorods*. **J. Phys. Chem. C**, 123, 12997−13008 (2019).

DHASMANA, N. et al, *Investigation of nonlinear optical properties of exfoliated MoS2 using Photoacoustic Z – scan*. **MRS Advances** 1, 3215–3221 (2016).

DIAS DOS SANTOS, F. C. et al, . *Measurement of the nonlinear refractive index of Cs D_1 line using z-scan***. Journal of the Optical Society of America B-Optical Physics,** v. 36, p. 2468, (2019).

DONG, N. et al, *Optical limiting and theoretical modelling of layered transition metal dichalcogenide nanosheets.* **Sci. Rep**. 5, 14646 (2015).

DONG, N. Y. et al, *Saturation of Two-Photon Absorption in Layered Transition Metal Dichalcogenides: Experiment and Theory,* **ACS Photonics** 5, 1558−1565 (2018).

DONG, N., et al, *Dispersion of nonlinear refractive index in layered WS_2 and WSe_2 semiconductor films induced by two-photon absorption,* **Opt. Lett**. 41, 3936-3939 (2016).

DUBOISSET, J. A. et al, *A Bottom-Up Approach to Build the Hyperpolarizability of Peptides and Proteins from their Amino Acids*. **J. Phys. Chem. B**, 117, 9877-9881 (2013).

DYBAŁA, F. et. al, *Pressure coefficients for direct optical transitions in MoS_2, $MoSe_2$, WS_2, and WSe_2 crystals and semiconductor to metal transitions.* **Scientific Reports** 6, 26663 (2016).

EDA, G and MAIER, S. A. *Two-dimensional crystals: managing light for optoelectronics* **ACS Nano** 7 5660–5 (2013).

FACURE, M.H.M. et al, *A review on graphene quantum dots and their nanocomposites: from laboratory synthesis towards agricultural and environmental applications.* **Environ. Sci.: Nano**, **7**, 3710-3734 (2020).

FAN Z. et al, *Surrounding media sensitive photoluminescence of boron-doped graphene quantum dots for highly fluorescent dyed crystals, chemical sensing and bioimaging*. **Carbon**, 70, 149-156 (2014).

FANG, Y. et al, *Structural Determination and Nonlinear Optical Properties of New 1T‴-Type MoS_2 Compound*. **J. Am. Chem. Soc**., 141, 2, 790–793 (2019).

FORCHERIO, T. et al, *Nonlinear optical susceptibility of two-dimensional WS_2 measured by hyper Rayleigh scattering*. **Opt. Lett**. 42, 5018-5021 (2017).

FORCHERIO, T. et al, *Nonlinear optical susceptibility of two-dimensional WS_2 measured by hyper Rayleigh scattering: erratum*. **Opt. Lett**. 42, 5018-5021 (2017).

FORWARD, J. M. et al, *Luminescence Studies of Gold (I) Thiolate Complexes*. **Inorg. Chem.**, 34, 6330-6335 (1995).

FOX, M. *Optical Properties of Solids.* 2nd edition. New York City: **Oxford University Press**, February 26, 2010.

FRANKEN, P. A. et al, *Generation of Optical Harmonics*, **Phys. Rev. Lett.** 7, 118, (1961).

FUJIWARA H, Principles of Optics. *Spectroscopic Ellipsometry.* 1st edition. (**John Wiley & Sons, Ltd**), 2007.

GARCÍA MEJÍA, H. A. *Espectroscopia não linear de compostos de metal de transição e um co-polímero fluoreno-benzotiadiazol*. (Tese de doutorado) **Universidade Federal de Pernambuco** – Recife: O Autor, 2012.

GHOFRANIHA, N. I. et al, *Experimental evidence of replica symmetry breaking in random lasers*, **Nat. Commun**., 6, 6058 (2015).

GIERZ, I. et al, *Snapshots of non-equilibrium Dirac carrier distributions in graphene*. **Nat Mater**, 12, 1119-1124 (2013).

GOEPPERT-MAYER, M., *Elementary processes with two quantum transitions*. **Annalen der Physik.** 18 (7–8): 466–479 – English version (2009).

GOMES, A. S. L. et al, *Observation of Lévy distribution and replica symmetry breaking in random lasers from a single set of measurements*. **Sci. Rep**. 6, 27987 (2016).

Graphene, Nanoscience, Hamburgo, 15 julho de 2012. Disponível em: http://www.nanoscience.de/HTML/research/graphene.html. Acesso em: 07/10/2019

GRIFFITHS, D., *Electrodynamics*, ed. 3. **Pearson Education**, (2011).

GU, B. et al, *Theory of Gaussian beam Z scan with simultaneous third- and fifth-order nonlinear refraction based on a Gaussian decomposition method***. J. Opt. Soc. Am. B** 22, 2651 (2005).

GUILLAMÓN, I. et al *Superconducting Density of States and Vortex Cores of 2H*-NbS_2. **Phys. Rev. Lett**. 101, 166407 (2008).

HANGYO, M. et al, *Raman spectroscopic studies of MX2-type layered compounds,* **Ferroelectrics**, *52(1), 151–15,* (1983).

HARFOUCH, E. et al, *Hyper-Rayleigh Scattering from Gold Nanorods*. **J. Phys. Chem. C**, 118, 609-616 (2013).

HE, K. et al. *Tightly bound excitons in monolayer* WSe_2. **Phys. Rev. Lett.** 113,026803 (2014).

HENDRICKX, E. et al, *Hyper-Rayleigh Scattering in Isotropic Solution*. **Acc. Chem. Res**., 31, 675–683 (1998).

HOHENBERG, P. and KOHN, W. *Inhomogeneous electron gas,* **Phys. Rev**. 136, 864 (1964).

HORNG, J. et al, *Drude conductivity of Dirac fermions in graphene* **Phys Rev B**, 83, 165113 (2011).

HUANG, C. C. et al, *Synthesis of Highly Fluorescent Gold Nanoparticles for Sensing Mercury (II).* **Angew. Chem. Int.**, 46, 6824-6828 (2007).

HUANG, Y. et al, *Luminescence Mechanisms of Ultrasmall Gold Nanoparticles*. **Dalton Trans.**, 47, 6267-6273 (2018).

HUBBARD, S. F., et al, *Spectral content and dispersion of hyper-Rayleigh scattering*. **Opt. Lett**. 21, 1774-1776 (1996).

ILIOPOULOS, K. et al, *Ultrafast third-order nonlinearities of organic solvents*. **Opt. Express** 23, 24171-24176 (2015).

JAWAID, A. et al, *Mechanism for Redox Exfoliation of Layered Transition Metal Dichalcogenides*. **Chemistry of Materials 32**, 6550 (2020).

JAWAID, A. et al, *Redox Exfoliation of Layered Transition Metal Dichalcogenides*. **ACS Nano 11**, 635 (2017).

JOULAUD, C. et al, *Characterization of the nonlinear optical properties of nanocrystals by Hyper Rayleigh Scattering*. J**. Nanobiotechnol**., 11, S8 (2013).

JU, L. et al, *Graphene plasmonics for tunable terahertz metamaterials.* **Nat Nano**, 6, 630-634 (2011).

KAISER, W. and GARRETT, C. G. B. *Two-Photon Excitation in* $CaF_2:Eu^{2+}$. **Physical Review Letters. 7** (6): 229, (1961).

KANG, X. and ZHU, M. *Tailoring the photoluminescence of atomically precise nanoclusters* **Chem. Soc. Rev**., 48, 2422-2457 (2019).

KAVITHA, M. K. et.al, Graphene: A review of optical properties and photonic applications, **Asian Journal of Physics**, 25, 7, 809-831 (2016).

KHAZAEIZHAD, R. et al. *Mode-locking of Er-doped fiber laser using a multilayer MoS2 thin film as a saturable absorber in both anomalous and normal dispersion regimes*. **Opt. Express** 22, 23732–23742 (2014).

KHEBBACHE, N. et al, Second-Harmonic Scattering from Metallic Nanoparticles in a Random Medium. **ACS Photonics**, 4, 262-266 (2017).

KHLEBTSOV, N. G., and DYKMAN L. A. *Optical properties and biomedical applications of plasmonic nanoparticles*. **Journal of Quantitative Spectroscopy & Radiative Transfer** 111, 1–35 (2010).

KIM, J. et al, *Electrical Control of Optical Plasmon Resonance with Graphene*. **Nano Lett**, 12, 5598-5602 (2012).

KIM, J. W. and LEE, H. G. *Thermal and Carbothermic Decomposition of Na_2CO_3 and Li_2CO_3*. **Metall. Mater. Trans. B Process Metall. Mater. Process. Sci**., *32*, 17–24 (2001).

KITTEL, C. *Introduction to Solid State Physics*. **John Wiley & Sons**, Inc., New York, 6th edition, (1986).

KOHN, W.; SHAM L.J.J. *Self-Consistent Equations Including Exchange and Correlation Effects.* **Phys. Rev**. 140, A1133 (1965).

KOLOBOV, A. V. and TOMINAGA, J., *Two-Dimensional Transition-Metal Dichalcogenides*, **Springer Series in Materials Science**, 1.ed, vol. 1 (2016).

KONG, D. G. et al, *The fifth-order nonlinearity of CS_2*. **J. Phys. B: Atom. Mol. Opt. Phys.** 42, 065401 (2009).

KONSTANTIN, N. et. al, *Electric Field Effect in Atomically Thin Carbon Films.* **Science** 2004: 306, 5696, pp. 666-669.

KORUZA, J. et al, *Grain-Size-Induced Ferroelectricity in $NaNbO_3$.* **Acta Mater**., 126, 77–85 (2017).

KOZAWA, D. et al. *Photocarrier relaxation pathway in two-dimensional semiconducting transition metal dichalcogenides*. **Nat. Commun.** 5, 4543 (2014).

KUMAR, N. et al. *Exciton-exciton annihilation in $MoSe_2$ monolayers*. **Phys. Rev. B** 89, 125427 (2014).

KUMARA K., et al *Third-order nonlinear optical properties of graphene quantum dots under continuous wavelength regime at 532 nm*. **AIP Conference Proceedings** 1942, 050003 (2018).

LARSON, A. C. and VON DREELE, R. B. Gsas. *Rep. lAUR* 1994, 86–748.

LATZKE, D. W. et al, *Electronic structure, spin-orbit coupling, and interlayer interaction in bulk MoS_2 and WS_2.* **Phys. Rev. B** 91, 235202 (2015).

LAWANDY, N. M., et al. *Laser action in strongly scattering media.* **Nature,** 368(6470), 436–438, (1994).

LAWRENCE, B. L. et al, *Measurements of the complex nonlinear refractive index of single crystal ptoluene sulfonate at 1064 nm*. **Appl. Phys. Lett**. 64, 2773-2775 (1994).

LEROUX, M. et al, *Traces of charge density waves in* NbS_2. **Phys. Rev. B** 97, 195140 (2018).

LETOKHOV, V. S. *Generation of Light by a Scattering Medium with Negative Resonance Absorption*. **Soviet Journal of Experimental and Theoretical Physics**, v. 26, p. 835 (1968).

LEZAMA, I. G. et al, *Surface Transport and Bandgap Structure of Exfoliated 2h- $MoTe_2$ Crystals*. **2D Mater**., 1, 021002 (2014).

LI et al, *External Electric Field Induced Second-Order Nonlinear Optical Effects in Hexagonal Graphene Quantum Dots*. **J. Phys. Chem. C**, 123, 32, 20020–20025 (2019).

LI H. et. al., *From Bulk to Monolayer MoS_2: Evolution of Raman Scattering*, **Adv. Funct. Mater.** 22, 1385–1390 (2012).

LI, B., et al, *Hydrothermal synthesis of $KNbO_3$ powders in supercritical water and its nonlinear optical properties.* **The Journal of Supercritical Fluids**, 35(3), 254–259 (2005).

LI, D. et al, *Multimodal Nonlinear Optical Imaging of MoS_2 and MoS_2-Based van der Waals Heterostructures*. **ACS Nano,** 10, 3, 3766–3775 (2016).

LI, H.-P., et al, *External Electric Field-Induced Second-Order Nonlinear Optical Effects in Hexagonal Graphene Quantum Dots.* **The Journal of Physical Chemistry C** (2019).

LI, L. et al, *Niobium disulfide as a new saturable absorber for an ultrafast fiber laser.* **Nanoscale**, ,12, 4537-4543 (2020).

LI, P. et al, *The Effects of Crystal Structure and Electronic Structure on Photocatalytic H_2 Evolution and CO_2 Reduction over Two Phases of Perovskite-Structured $NaNbO_3$.* **J. Phys. Chem. C.**, 116(14), 7621–7628 (2012).

LIMA, B., *PHOTONIC SPIN GLASS, EXTREME EVENTS AND LÉVY-LIKE BEHAVIOUR IN A CW-PUMPED ERBIUM RANDOM FIBRE LASER.* Doctorate thesis**, Universidade Federal de Pernambuco** (2019).

LIN C.-A. et al, *Synthesis and Surface Modification of Highly Fluorescent Gold Nanoclusters and Their Exploitation for Cellular Labeling*. **Proc. SPIE 7575, Colloidal Quantum Dots for Biomedical Applications V**, 757506 (2010).

LIU, H. et al, *High-harmonic generation from an atomically thin semiconductor*, **Nature Physics**, 262–265 (2017).

LIU, H., et al, *High-harmonic generation from an atomically thin semiconductor,* **Nature Physics**, 262–265 (2017).

LIU, Q. et al, *Strong Two-Photon-Induced Fluorescence from Photostable, Biocompatible Nitrogen-Doped Graphene Quantum Dots for Cellular and Deep-Tissue Imaging*. **Nano Letters,** 13(6), 2436–2441 (2013).

LUO, Z., et al, *High Yield Preparation of Macroscopic Graphene Oxide Membranes*. **J. Am. Chem. Soc.,** 131, 898-899 (2009).

LY, Y. et al, *Measurement of the optical dielectric function of monolayer transition-metal dichalcogenides: MoS_2, $MoSe_2$, WS_2, and WSe_2*. **Phys. Rev. B.**, 90, 205422 (2014).

ZHU, M. et al, *Correlating the Crystal Structure of A Thiol-Protected Au_{25} Cluster and Optical Properties*. **J. Am. Chem. Soc**.,130, 5883-5885 (2008).

MA, H. et al, *Measurements of nondegenerate optical nonlinearity using a two-color single beam method*, **Appl. Phys. Lett.** 59, 2666, (1991).

MAESTRO, L. M. et al, *CdSe Quantum Dots for Two-Photon Fluorescence Thermal Imaging.* **Nano Letters,** 10(12), 5109–5115 (2010).

MAIMAN, T., *Stimulated optical radiation in ruby*. **Nature**, 187 4736: 493–494 (1960).

MAITY, S. et al, *An Overview on the Current Understanding of the Photophysical Properties of Metal Nanoclusters and their Potential Applications*. **Nanoscale**, 11, 22685-22723 (2019).

MAK, K. F. et al *Optical spectroscopy of graphene: From the far infrared to the ultraviolet.* **Solid State Commun**, 152, 1341-1349 (2012).

MAK, K. F. et al, *Atomically Thin MoS_2: A New Direct-Gap Semiconductor.* **Phys. Rev. Lett.** 105, 136805 (2010).

MAK, K. F. et al, *Measurement of the Optical Conductivity of Graphene,* **Phys Rev Lett**, 101, 196405 (2008).

MANISH C. et.al, *The chemistry of two-dimensional layered transition metal dichalcogenide nanosheets*, **NATURE CHEMISTRY**, 5, 263 – 275, (2013).

MARDER, S. R. et al, *Approaches for Optimizing the First Electronic Hyperpolarizability of Conjugated Organic Molecules*. **Science**, *252*, 103–105 (1991).

MARKUSHEV, V. M. et al, *Powder laser*, **Zh. Prikl. Spektr**., 45: 847–850 (1986).

MCINTYRE, J. D. E and ASPNES, D. E. *Differential Reflection Spectroscopy of Very Thin Surface Films*. **Surf. Sci.** 24, 417−434 (1971).

MCMULLAN, W. G. and IRWIN J. C. *Raman scattering from 2H and 3R–NbS_2*. **Solid State Communications**, 45, 7, (1983).

MÉZARD, M. et al, *Spin Glass Theory and Beyond*. **World Scientific**, vol. 9, (1987).

MONKHORSTAND, H. J. and PACK J. D., *Special points for Brillouin-zone integrations***. Phys. Rev. B** 13, 5188 (1976).

MORRISH, R. et al, *Low-Temperature Synthesis of n-Type WS_2 Thin Films via H2S Plasma Sulfurization of WO_3*. **Chem. Mater**., 26, 3986–3992 (2014).

MOURA, A., et al, *Nonlinear effects and photonic phase transitions in Nd^{3+}-doped nanocrystal-based random lasers*, **Appl. Opt.** 59, D155-D162 (2020).

MUHAMMED, M. A. H. et al, *Bright, NIR-Emitting Au23 from Au25: Characterization and Applications Including Biolabeling* **Chem. Eur. J**., 2009, 15, 10110-10120.

NAIR, R. R. et al, *Fine structure constant defines visual transparency of graphene*. **Science**, 320, 1308 (2008).

NAITO and TANAKA, *Electrical Transport Properties in 2H-NbS_2, -$NbSe_2$, -TaS_2 and -$TaSe_2$.* J. **Phys. Soc. Jpn**. 51, pp. 219-227 (1982).

NALWA, H. and MIYATA, S. *Nonlinear Optics of Organic Molecules and Polymers*. **CRC Press** (1996).

NAPPA, J., et al, *Electric dipole origin of the second harmonic generation of small metallic particles.* **Physical Review B**, 71(16), (2005).

NASHAMIRA, S. et al, *Raman scattering from 2H-NbS_2 and intercalated NbS_2*. **Solid State Communications**, 42, Issue 8 (1982).

NEGISHI, Y. et al, *A Critical Size for Emergence of Nonbulk Electronic and Geometric Structures in Dodecanethiolate-Protected Au Clusters*. **J. Am. Chem. Soc**., 137, 3, 1206–1212 (2015).

NETO, A.C.C *et al.*: *The electronic properties of graphene*. **Rev. Mod. Phys**., 81,1, (2009).

NI, G. et al, *Tuning optical conductivity of large-scale CVD graphene by strain engineering.* **Adv Mater**, 26, 1081-1086 (2014).

NOVOSELOV, K. S. et al, *Two-dimensional gas of massless Dirac fermions in graphene.* **Nature**, 438, 197-200 (2005).

OLESIAK-BANSKA, J. et al, *Closer Look at Two-Photon Absorption, Absorption Saturation and Nonlinear Refraction in Gold Nanoclusters*. **RSC Adv.** 2016, 6, 98748−98752.

PALUMMO, M., et al, *Exciton radiative lifetimes in two-dimensional transition metal dichalcogenides*. **Nano Lett.** 15, 2794–2800 (2015).

PAULEY, M. A. et al, *Determination of first hyperpolarizability of nonlinear optical chromophores by second harmonic scattering using an external reference.* **The Journal of Chemical Physics**, *104(20)* (1996).

PAWAR, M. et al, *A Brief Overview of TiO_2 Photocatalyst for Organic Dye Remediation: Case Study of Reaction Mechanisms Involved in Ce TiO_2 Photocatalysts System.* **Journal of Nanomaterials** Volume 2018, Article ID 5953609, 13 pages (2018).

PHILIP, R., *Evolution of Nonlinear Optical Properties: From Gold Atomic Clusters to Plasmonic Nanocrystals*. **Nano Lett**. 12, 9, 4661–4667(2012).

PINCHEIRA P. I. R, et al, *Observation of photonic paramagnetic to spin-glass transition in a specially designed TiO_2 particle-based dye-colloidal random laser*. **Opt. Lett**. 41, 3459-3462 (2016).

POWERS, P. and HAUS J., *Fundamentals of Nonlinear Optics*, ed. 2, **CRC Press**, (2017).

QI, X. et al, *New Opportunities: Second Harmonic Generation of Boron-Doped Graphene Quantum Dots for Stem Cells Imaging and Ultraprecise Tracking in Wound Healing*. **Adv. Funct. Mater**., 29, 1902235 (2019).

QIU, D. Y. et al, *Optical Spectrum of MoS_2: Many-Body Effects and Diversity of Exciton States.* **Phys. Rev. Lett**. 111, 216805 (2013).

RAMAKRISHNA, G. et al, *Quantum-Sized Gold Clusters as Efficient Two-Photon Absorbers*. **J. Am. Chem. Soc.** 2008, 130, 5032−5033.

RAMASAMY, P. et al, *Size Tuning of Au Nanoparticles Formed by Electron Beam Irradiation of Au 25 Quantum Clusters Anchored Within and Outside of Dipeptide Nanotubes.* **J. Mater. Chem.**, 19, 8456-8462 (2009).

RESHEF, O., et al, *Beyond the perturbative description of the nonlinear optical response of low-index materials,* **Opt. Lett.** 42, 3225-3228 (2017).

REYNA, A. S. et al, *Nonlinear Refraction and Absorption of Ag_{29} Nanoclusters: Evidence for Two-Photon Absorption Saturation.* **J. Phys. Chem. *C*** 2018, 122, 32, 18682–18689.

RIBEIRO-SOARES, J. et al, *Group theory analysis of phonons in two-dimensional transition metal dichalcogenides*. **Phys. Rev. B** 90, 115438 (2014).

Rodriguez, E. V. et al, *Hyper-Rayleigh Scattering from $BaTiO_3$ and $PbTiO_3$ Nanocrystals*. **Chem. Phys. Lett.**, *467*, 335–338 (2009).

RUPPERT, C. et al, *Optical Properties and Bandgap of Single- and Few-Layer $MoTe_2$ Crystals.* **Nano Lett.** *2014, 14 (11), 6231−6236.*

RUSSIER- ANTOINE, et al. *Non-linear optical properties of gold quantum clusters. The smaller the better*. **Nanoscale 6**, 13572-13578 (2014).

RUSSIER-ANTOINE, I. et al, *Second Harmonic Scattering from Silver Nanocubes.* **J. Phys. Chem. C.**, 122, 17447-17455 (2018).

RUSSIER-ANTOINE, I. et al, *Tuning Ag_{29} Nanocluster Light Emission from Red to Blue With One and Two-Photon Excitation*. **Nanoscale**, 8, 2892-2897 (2016).

SAPIENZA, R. *Determining random lasing action.* **Nature Reviews Physics**, 1, 690–695 (2019)**.**

SARKAR, A. J. et al, *Spatially Dependent Replica Symmetry Breaking in an Optofluidic Random Laser*. **Frontiers in Optics**, JW3A.30 (2017).

SCHMID, W. J., & SCHRÖTTER, H. W. *Direct observation of the twisting vibration in tetrachloroethylene through the hyper-Raman effect.* **Chemical Physics Letters,** 45(3), 502–503 (1977).

SEGETS, D., et al, *Real-Time Monitoring of the Nucleation and Growth of ZnO Nanoparticles Using an Optical Hyper-Rayleigh Scattering Method.* **The Journal of Physical Chemistry C**, 113(28), 11995–12001 (2009).

SEKIMOTO, Y. et al, *Tuneable pressure effects in graphene oxide layers.* **Scientific Reports** 7, 12159 (2017).

SHAINA, P. R. and JAISWAL, M *Strain and morphology of graphene membranes on responsive microhydrogel patterns*. **Appl Phys Lett**, 105, 193103 (2014).

SHIRATORI, Y. et al, *Polymorphism in Micro-, Submicro-, and Nanocrystalline $NaNbO_3$.* **J. Phys. Chem. B**, *109*, 20122–20130 (2005).

SHIRATORI, Y. et al, *Temperature-induced Phase Transitions in Micro-, Submicro-, and Nanocrystalline $NaNbO_3$.* **J. Phys. Chem. C**, 111, 18493-18502 (2007).

SIMON, D. et al. *Electronic properties and quantum transport in Graphene-based nanostructures*, **Eur. Phys. J. B** (2009).

SLOBODENIUK A. O. and BASKO D. M., *Exciton-phonon relaxation bottleneck and radiative decay of thermal exciton reservoir in two-dimensional materials,* **Phys. Rev. B** 94, p. 205423, (2016).

SOLER, J. M. et al, *The SIESTA method for ab initio order-N materials simulation***. J. Phys.** 14, 2745 (2002).

SONG, Y., et al, *Extraordinary Second Harmonic Generation in ReS_2 Atomic Crystals*, **ACS Photonics**, 5, 3485−3491 (2018).

SPLENDIANI A., L. Sun, Y. Zhang, T. Li, J. Kim, C. Y. Chim, G. Galli, and F. Wang, "*Emerging photoluminescence in monolayer MoS_2*", **Nano Lett**. 10(4), 1271 (2010).

SU, T. T. et al, *Studies on the Thermal Decomposition Kinetics and Mechanism of Ammonium Niobium Oxalate*. **J. Therm. Anal. Calorim**., *98*, 449–455 (2009).

SUN, J. et al, *Nitrogen-doped graphene quantum dots coupled with photosensitizers for one-/two-photon activated photodynamic therapy based on a FRET mechanism*. **Chem. Commun.**, **54**, 715-718 (2018).

SUN, X. et al, *Optical Properties of 2D 3R Phase Niobium Disulfide and Its Applications as a Saturable Absorber*. **Adv. Optical Mater**., 8, 1901181 (2020).

TANG, L., et al, *Deep Ultraviolet Photoluminescence of Water-Soluble Self-Passivated Graphene Quantum Dots*. **ACS Nano**, 6, 5102-5110 (2012).

TAUC, J. et al, *Optical properties and electronic structure of amorphous germanium*. **Phys. Status Solidi** 1996, 15, 627–637.

TERHUNE, R. W., et al, *Measurements of Nonlinear Light Scattering***. Physical Review Letters**, 14(17), 681 684 (1965).

THOMAS, K. et al, *Broadband ultrafast nonlinear absorption and nonlinear refraction of layered molybdenum dichalcogenide semiconductors*. **Nanoscale** 6, 10530−10535 (2014).

TIAN, P. et al, *Graphene quantum dots from chemistry to applications.* **Materials today chemistry**, 10, 221-258 (2018).

TISSEN, V. G. et al, *Pressure dependence of superconducting critical temperature and upper critical field of 2*H-*NbS_2*. **Phys. Rev. B** 87, 134502 (2013).

TOBY, B. H. EXPGUI, a Graphical User Interface for GSAS. **J. Appl. Crystallogr**., *34*, 210-213 (2001).

TOMMASI, F. et al, *Robustness of replica symmetry breaking phenomenology in random laser.* **Sci. Rep**. 6, 37113 (2016).

TONNDORF, P. et al. *Photoluminescence emission and Raman response of monolayer MoS_2, $MoSe_2$, and WSe_2.* **Optics Express** 21, 4908-4916 (2013).

TORUN, E. et al, *Anisotropic Electronic, Mechanical, and Optical Properties of Monolayer WTe_2*, **J. Appl. Phys**., 119, 074307 (2016).

TSIPAS, P. et al, *Massless Dirac Fermions in $ZrTe_2$ Semimetal Grown on InAs(111) by van der Waals Epitaxy*. **ACS Nano**, 12, 2, 1696–1703 (2018).

UNG, T. D. T., et al, *CdTe and CdSe quantum dots: synthesis, characterizations and applications in agriculture. Advances in Natural Sciences:* **Nanoscience and Nanotechnology,** 3(4), 043001 (2012).

van LOON, E. G. C. P. et al, *Competing Coulomb and electron−phonon interactions in NbS_2.* **npj Quantum Mater**. 3, 32 (2018).

VARMA, S. J. et al, *2D TiS_2 Layers: A Superior Nonlinear Optical Limiting Material*, **Adv. Optical Mater**. 5, 1700713 (2017).

VYDROV, O. A. and VOORHIS, T. V. *Nonlocal van der Waals density functional: The simpler the better*. **J. Chem. Phys**. 133, 244103 (2010).

WALLACE, P. R, *The Band Theory of Graphite* **Phys Rev**, 71, 622-634 (1947).

WANG, G. et al, *Tunable nonlinear refractive index of two-dimensional MoS_2, WS_2, and $MoSe_2$ nanosheet dispersions [Invited]*,**Photon. Res**. 3, A51-A55 (2015).

WANG, G. et.al, *Excitons in atomically thin transition metal dichalcogenides.* **Rev. Mod. Phys.** 90, 2, (2018).

WANG, H. et al, *Magnetotransport Properties of Layered Topological Material $ZrTe_2$ Thin Film.* **ACS Nano,** 13, 5, 6008–6016 (2019).

WANG, H. et al, *Measurement of the third-order optical nonlinearities of graphene quantum dots in water at 355 nm, 532 nm and 1064 nm,* **Opt. Mater. Express** 9, 339-351 (2019).

WANG, K. et al, *Broadband ultrafast nonlinear absorption and nonlinear refraction of layered molybdenum dichalcogenide semiconductors*. **Nanoscale** 6, 10530 (2014).

WANG, L. et al, *Optical Properties and Applications of Plasmonic-Metal Nanoparticles*. **Adv. Funct. Mater.** 2005400 (2020).

WANG, Q. H., et al, *Electronics and* optoelectronics *of two-dimensional transition metal dichalcogenides.* **Nature Nanotechnology**, 7(11), 699–712 (2012).

WANG, S. et al, The toxicity of graphene quantum dots. **RSC Adv**., **6**, 89867-89878 (2016).

WANG, Y. et al, *Blue two-photon fluorescence metal cluster probe precisely marking cell nuclei of two cell lines*. **Chem. Commun**., 2013, 49, 10724.

WEAIRE, D. B., et al, *Effect of low-power nonlinear refraction on laser-beam propagation in InSb*, **Opt. Lett**., Vol. 4, 331 (1979).

WEN, X. et al, *Fluorescence Origin and Spectral Broadening Mechanism in Atomically Precise Au_8 Nanoclusters*. **Nanoscale**, *5*, 10251-10257 (2013).

WILSON, J. A. et al, *The transition metal dichalcogenides discussion and interpretation of optical, electrical and structural properties*. ***Adv. Phys.*** 18, 193–335 (1969).

WINCHESTER, A. et al, *Electrochemical Characterization of Liquid Phase Exfoliated Two-Dimensional Layers of Molybdenum Disulfide*. **ACS Appl. Mater. Interfaces** 6 (3), 2125−2130, (2014).

WU, M. et al, *Luminescent Au(I)–Thiolate Complexes through Aggregation-Induced Emission: The Effect of pH during and Post Synthesis.* **J. Phys. Chem. C**, 123,6010-6017 (2019).

WU, S., et al, *Monolayer semiconductor nanocavity lasers with ultralow thresholds*, **Nature,** 69–72 (2015).

XIA, J. *Replica symmetry breaking in FRET-assisted random laser based on electrospun polymer fiber*. **Ann. Phys**. 531, 1900066 (2019).

YAMIJALA et al, *Linear and Nonlinear Optical Properties of Graphene Quantum Dots: A Computational Study*. **J. Phys. Chem. C**, 119, 12079-12086 (2015).

YAN, C., et al, *2D Group IVB Transition Metal Dichalcogenides*, **Adv. Funct. Mater**. 28, 1803305 (2018).

YAN, Y., et al, *Recent Advances on Graphene Quantum Dots: From Chemistry and Physics to Applications*. **Adv. Mater.** 31, 1808283 (2019).

YANG, D., et al, *Lead-free antiferroelectric niobates $AgNbO_3$ and $NaNbO_3$ for energy storage applications*, **J. Mater. Chem. A**, **8**, 23724-23737 (2020).

YANKOWITZ, M. et al, *Dynamic band-structure tuning of graphene moiré superlattices with pressure*" **Nature,** 557, 404–408(2018).

YARIV, A., and YEH, Pochi., *Optical waves in crystals*, 1st ed. **John Willey & Sons**, (1983).

YARIV, A., *Quantum electronics*, ed. 3. **Wiley**, (1989).

YIN, X. et al, *Edge Nonlinear Optics on a MoS_2 Atomic Monolayer*. **Science**,344, 6183 (2014).

YOU J.W, et al, "*Nonlinear optical properties and applications of 2D materials: theoretical and experimental aspects*. **Nanophotonics**, 8(1): 63–97, (2018).

YU, X. et al, *Self-Assembled 2D WSe_2 Thin Films for Photoelectrochemical Hydrogen Production*. **Nat. Commun**., 6, 7596 (2015).

ZHAN, C. L. et al, *The high fifth-order nonlinearity in a new stilbazolium derivative:trans-1-[p-(p-dimethylaminobenzyl-azo)-benzyl]-2-(Nmethyl- pyridinium)- ethene iodide*. **Chem. Phys. Lett.** 347, 410–414 (2001).

ZHANG X. et al, "*Two-dimensional MoS_2-enabled flexible rectenna for Wi-Fi-band wireless energy harvesting*", **Nature**, 566, 368–372 (2019).

ZHANG, B. et al, Lead-Free Piezoelectrics Based on Potassium-Sodium Niobate with Giant d_{33}. **ACS Appl. Mater. Interfaces**, *5*, 7718–7725 (2013).

ZHANG, N. et al, *Saturation of two-photon absorption in layered transition metal dichalcogenides: experiment and theory.* **ACS Photonics** 5, 1558−1565 (2018).

ZHANG, S. et al, *Direct Observation of Degenerate Two-Photon Absorption and Its Saturation in WS_2 and MoS_2 Monolayer and Few-Layer Films.* **ACS Nano**, 9, 7, 7142–7150 (2015).

ZHANG, X., et al, *Two-dimensional MoS_2-enabled flexible rectenna for Wi-Fi-band wireless energy harvesting*, **Nature**, 566, 368–372 (2019).

ZHAO, W. et al, *Evolution of electronic structure in atomically thin sheets of WS_2 and WSe_2.* **ACS Nano.** 22;7(1):791-7 (2013).

ZHENG, J. et al, *Highly Fluorescent, Water-Soluble, Size-Tunable Gold Quantum Dots.* **Phys. Rev. Lett.** 93, 077402 (2004).

ZHENG, X. et al, *Z-scan measurement of the nonlinear refractive index of monolayer WS_2.* **Opt. Express** 23, 15616-15623 (2015).

ZHOU, M. et al, *Evolution of Excited-State Dynamics in Periodic Au_{28}, Au_{36}, Au_{44}, and Au_{52} Nanoclusters*. **J. Phys. Chem. Lett**., 8, 4023−4030 (2017).

APPENDIX A – CLASSICAL DESCRIPTION OF THE 5TH ORDER SUSCEPTIBILITIES

The classical description of second-and third-order susceptibilities is shown in Chapter 2. This appendix is dedicated to describe the fifth-order susceptibility (BESSE et al, 2015). Taking into account only centrosymmetric materials ($\chi^{odd} = 0$), the expansion of polarization in the power series of the optical field can be written as:

$$\vec{P} = \varepsilon_0(\vec{\vec{\chi}}^{(1)} \otimes \vec{E} + \vec{\vec{\chi}}^{(3)} \otimes \vec{E}\vec{E}\vec{E} + \vec{\vec{\chi}}^{(5)} \otimes \vec{E}\vec{E}\vec{E}\vec{E}\vec{E} + \cdots) \quad \text{(A1)}$$

where-⊗ indicates a tensorial product.

As discussed in Chapter 2, the optical susceptibilities are tensors, but in this appendix, we will consider the susceptibilities as scalar quantities. In order to obtain an expression for $\chi^{(5)}$, in terms of the anharmonic oscillator, we start writing the 2nd Newton's law in the presence of both $\chi^{(3)}$ and $\chi^{(5)}$. Then we have:

$$\frac{d^2x}{dt^2} + \Gamma\frac{dx}{dt} + \omega_0^2 x + Cx^3 + Qx^5 = -\frac{e}{m}E \quad \text{(A2)}$$

in the equation (A2), E is the electrical field, m is the electron mass, $-e$ is the electric charge, and ω_0 is the angular frequency. The potential energy for the electron is:

$$U = \frac{m\omega_0^2 x^2}{2} + mC\frac{x^4}{4} + mQ\frac{x^6}{6} \quad \text{(A3)}$$

For a monochromatic wave, $E = E_0 e^{-i\omega t} + c.c.$, where t is the temporal evolution of the electrical field and ω is the angular frequency, $c.c.$ is the complex conjugate. To guarantee the validity of the expansion in equation (A1), it was considered that the displacements of the electron are small enough and a solution for the displacement, x by using perturbation theory, $x = x^{(1)} + x^{(3)} + x^{(5)} + \cdots +$. This was shown for $x^{(1)}, x^{(2)}, and\ x^{(3)}$ in chapter two. Now, solving for $x^{(5)}$, we have:

$$\frac{d^2x^{(5)}}{dt^2} + \Gamma\frac{dx^{(5)}}{dt} + \omega_0^2 x^{(5)} = -C\left(x^{(1)}\right)^5 - 3C[\left(x^{(1)}\right)^2 x^{(3)}] \quad \text{(A4)}$$

Then, solving the equation (A4), an expression for $x^{(5)}$ can be found:

$$x^{(5)} = X^{(5)}(5\omega)e^{(-5i\omega t)} + X^{(5)}(3\omega)e^{(-3i\omega t)} + X^{(5)}(\omega)e^{(-i\omega t)} + c.c. \quad \text{(A5)}$$

identifying the terms related to terms $X^{(5)}(p\omega)$, we can write:

$$D(5\omega)X^{(5)}(5\omega) = -Q\left[X^{(1)}(\omega)\right]^5 - 3C\left[X^{(1)}(\omega)\right]^2 X^{(3)}(3\omega) \tag{A6}$$

for the fifth harmonic generation, and

$$D(5\omega)X^{(5)}(\omega) = -10Q\left[X^{(1)}(\omega)\right]^3\left[X^{(1)*}(\omega)\right]^2 - 3C\{\left[X^{(1)}(\omega)\right]^2 X^{(3)*}(\omega) + 2X^{(1)}(\omega)X^{(1)*}(\omega)X^{(3)}(\omega) + \left[X^{(1)*}(\omega)\right]^2 X^{(3)}(\omega)\}, \tag{A7}$$

for the Kerr optical effects and fifth-order nonlinear absorption.

APPENDIX B - SYNTHESIS AND CHARACTERIZATION OF LAYERED TRANSITION METALS DICHALCOGENIDES.

B.1 SYNTHESIS OF LTMD'S

Synthesis and characterization performed at Air Force Research Lab – USA

The Transition Metal Dichalcogenides characterized in this thesis were synthesized by the redox exfoliation route in the *Materials and Manufacturing Directorate of the North American Air Force Research Laboratory (RX - AFRL).* A complete description of the synthesis process and the mechanism of synthesis are available in (JAWAID et al, 2015; JAWAID et al, 2020), respectively. The approach described here was made in the MoS_2 sample but applies to any TMD of group V-VII.

Figure 88 - Redox exfoliation synthesis diagram for TMD's.

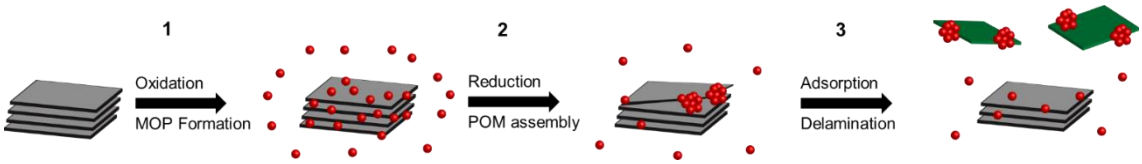

Source: Jawaid, et al (2020).

Redox exfoliation synthesis is based on the formation of peroxometalate species from the use of mild oxidants as Cumene hydroperoxide (CHP). After this step, a reducing agent, such as sodium borohydride ($NaBH_4$), is gradually added, forming polyoxemetalates (POM's) species. Because the interaction between layers in TMD's is a weak interaction (van der Walls type), Coulombic repulsion can separate the TMD's layers.

Using the MoS_2 sample as an example, the materials and the summary route used were, respectively.

B.1.1- Materials

NMethyl-2-pyrrolidona (NMP), acetonitrile (CH_3CN), dimethylformamide (DMF), ethanol (EtOH), acetone ($(CH_3)_2CO$), CHP (80%), molybdenum disulfide (IV) (MoS_2), NMP and DMF were distilled in the presence of Calcium Hydride (CaH_2) at a pressure of 300 mTorr at 60 °C. CH_3CN was distilled in the presence of CaH_2 under an argon flow. All solvents were stored in clean argon vials under active molecular sieves (3 Å). The molecular sieves were activated by heating for 24 h under vacuum (150 °C, 300 mTorr).

B.1.2 - Surface oxidation of MoS_2.

A round-bottomed balloon of three pipes was initially evacuated (300 mTorr) for 5 min and filled with argon gas. This was accomplished three times to ensure the removal of O_2. Then 0.625 mmol (100 mg) of MoS_2 suspended in 5 mL of CH_3CN was added through to the round bottom balloon and stirred at 0 °C using an ice bath. After temperature balance (30 min), 3 mmol of CHP (562 μL of 80% CHP) in 5 mL of CH_3CN were added drop by drop to MoS_2 suspension over 15 min. The mixture was stirred at 273 K (0°C) and maintained at this temperature during the addition of CHP. The suspension overhead was discolored within 60 minutes. After all the CHP was added, the ice bath was removed, and the reaction was left to stirred at 25°C for 24 hours.

B.1.3 – Example: MoS_2 exfoliation

The stirring was removed after 24 h and the MoS_2 powder was left to stand (10 min); the volume was reduced to 4 mL. The temperature was reduced to 0 °C using an ice bath and left to balance for 30 min. After balance, 50 mL of an icy aqueous solution of 0.10 M $NaBH_4$ (38 mg NaBH4, 10 mL of H_2O) were quickly added to the oxidized TMD's solution at 273 K (0°C) and stirred for 1 h. Additional 100 μL of $NaBH_4$ 0.10 M were added at 1 h intervals until a total of 350 μL was added. After the addition of $NaBH_4$, the ice bath was removed, and the solution was left in agitation for 24 h at room temperature. The viscosity of the solution increased, and the suspension went from a grayish color to a green color, indicating exfoliated material. At this point, the solution can be softened by probe (30 min) or mixed (IKA mixer, 20 000 rpm, 1 h) after the suspension has been transferred to a 20 mL vial with flat bottom. These further increases yield by approximately 2 × (solvents used: CH_3CN, acetone, ethanol). After addition of $NaBH_4$ and optional probe sonication, the stirring was removed and the large and unexfoliated flakes were left to decant. The supernatant was isolated and centrifuged at 10,000 rpm for 15 min to sediment the exfoliated flakes. The optically clear and colorless supernatant containing excess CHP and possibly unreacted molybdenites was discarded and fresh anhydrous solvent was added (e.g., CH_3CN, DMF, NMP) and the suspension was homogenized in a vortex. The suspension was subsequently centrifuged at 1500 rpm for 30 min. The resulting supernatant contained MoS_2 flakes from bulk to monolayer and was isolated for analysis by XRD, AFM, SEM and TEM. Weaker reducing agents (hydroquinone, ascorbic acid or tribasic

sodium citrate) were not able to effectively reduce the yellow peroxomolybdate complex, resulting in low yields and quality.

B.2 – CHARACTERIZATION OF LTMD's

B.2.1 - $ZrTe_2$

Transmission Electron Microscopy (TEM)

TEM and high-resolution TEM (HRTEM) images were collected on an aberration-corrected FEI Talos TEM with an accelerating voltage of 200 kV. Samples were prepared by drop-casting colloidal $ZrTe_2$ dispersions in acetonitrile (10^{-8} M) on lacey-carbon TEM grids. The solvent was wicked off with a kim-wipe after approximately 5 seconds and allowed to dry under dry N_2 (c.B. 1 hour). After drying, samples were immediately transferred to the load-lock chamber to minimize exposure to the ambient atmosphere and minimize surface oxidation due to hydrolysis.

Figure 89 – TEM images with different scales for $ZrTe_2$. a) and b) 500 nm, in different regions c) 200 nm and d) HR - TEM with a scale bar of 5 nm.

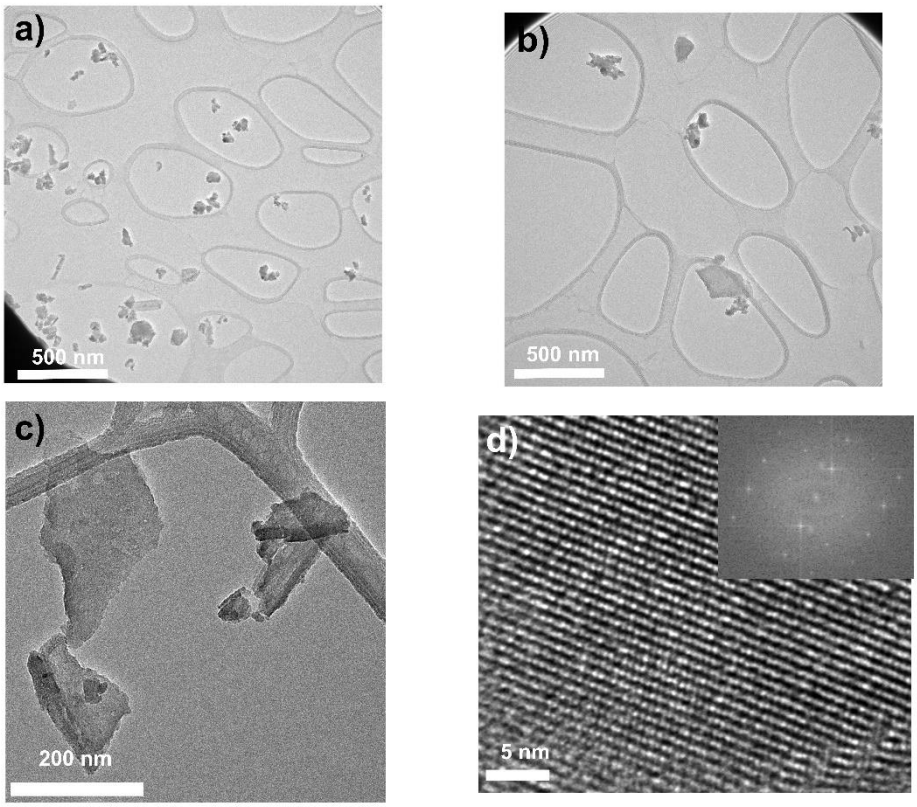

Source: The author (2021).

TEM images are shown in Figure 89. The inset in Figure 89d) shows high-resolution imaging of the basal surface of $ZrTe_2$ flakes. The hexagonal packing of the lattice is observed, and Fourier transformation of the high-resolution image indicates that single-crystalline $ZrTe_2$ domains are present.

Atomic Force Microscopy (AFM) and size distribution

Atomic force microscopy (AFM) is shown in Figure 94 of $ZrTe_2$ flakes were measured in noncontact tapping mode on a Dimension Icon (Bruker Corporation). AFM cantilevers with an aluminum reflex coating was used with a resonant frequency of 240 kHz and a force constant of 40 N/m. Samples were diluted in acetonitrile (approximately 1×10^{-9} M) and were drop-casted on Si wafers and allowed to dry under inert, anhydrous conditions. The samples were then annealed at 100 ºC under dry N_2 for 1 hour prior to imaging, to ensure complete removal of solvent.

Figure 90 - AFM a) image of the nanoflakes; lateral size (b) and height (c) distributions of ZrTe2 flakes. Note, the average height reported via AFM analysis is typically larger than the absolute particle size due to substrate-flake interactions.

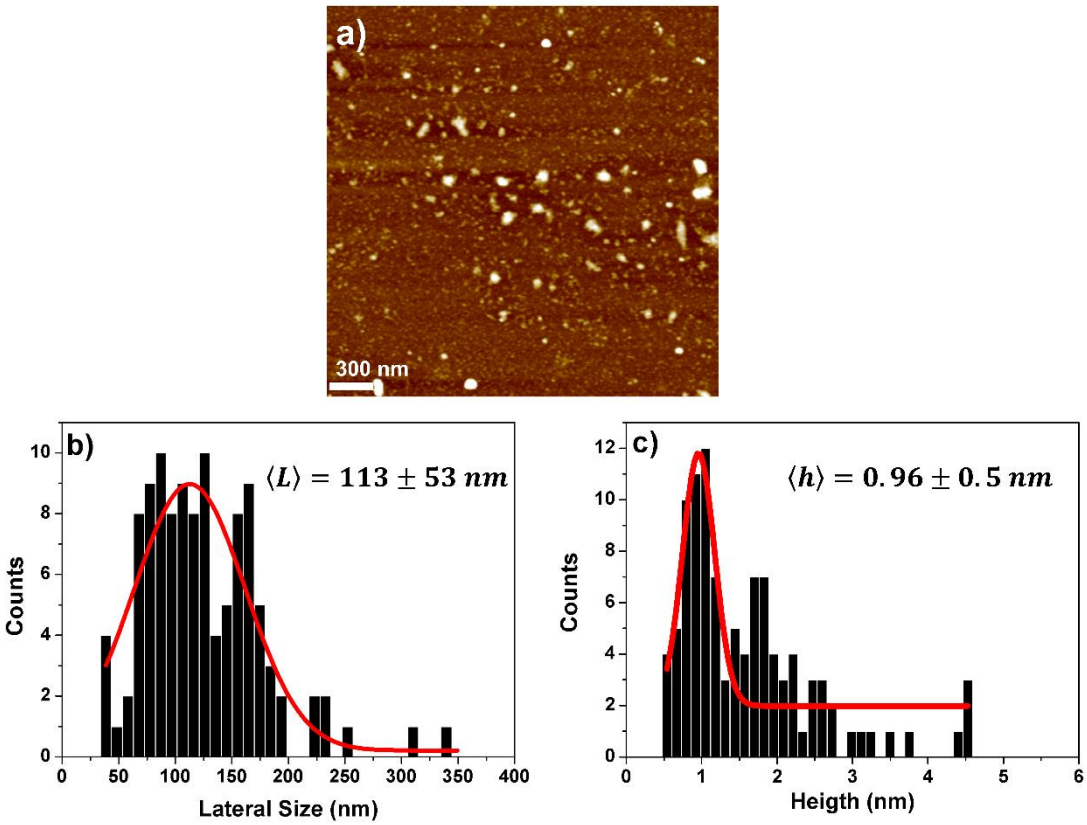

Source: The author (2021).

The Nanoscope Analysis software (Bruker Corporation) was used to determine the statistical distribution of flakes' thicknesses and lateral sizes). Figure 90a) shows the $ZrTe_2$ flakes; the scale bar is 300 nm. Figures 90b), and 90c) are shown a histogram for lateral size (90b) and height (90c). At least 100 individual flakes were analyzed. The average lateral size of 118±53 nm and the average height of 1.54±0.91 nm were obtained, with measured heights expected to be higher than the actual flakes due to substrate-flake interactions. As the out-of-plane lattice constant for $ZrTe_2$ is 0.66 nm, the measured thickness is compatible with a monolayer-rich ensemble.

X-ray Photoelectron Spectroscopy (XPS)

$ZrTe_2$ was drop-casted on silicon wafers and annealed in a thermal oven (1 hr, 100 °C) under N_2 to ensure complete solvent removal before transfer to the XPS load-lock chamber. X-ray photoelectron spectroscopic analysis was carried out using an SSI XPS System. Survey spectra were acquired using an Al Kα x-ray source (1486.6 eV) operated at 120 W (10 mA, 10 kV) with the electron analyzer operating in hybrid lens mode and an aperture size of approximately 800 μm^2. Survey data were acquired at an analyzer pass energy of 800 eV, using 1 eV step-sizes and a dwell time of 400 ms. High-resolution data of the Zr 3d, Te 3d, regions were collected using an analyzer pass energy of 30 eV and a step size of 0.1 eV.

Figure 91 - Compositional analysis of $ZrTe_2$. XPS spectroscopy of Zr_{3d} (a) and Te_{3d} (b) regions indicate the presence of compositional $ZrTe_2$.

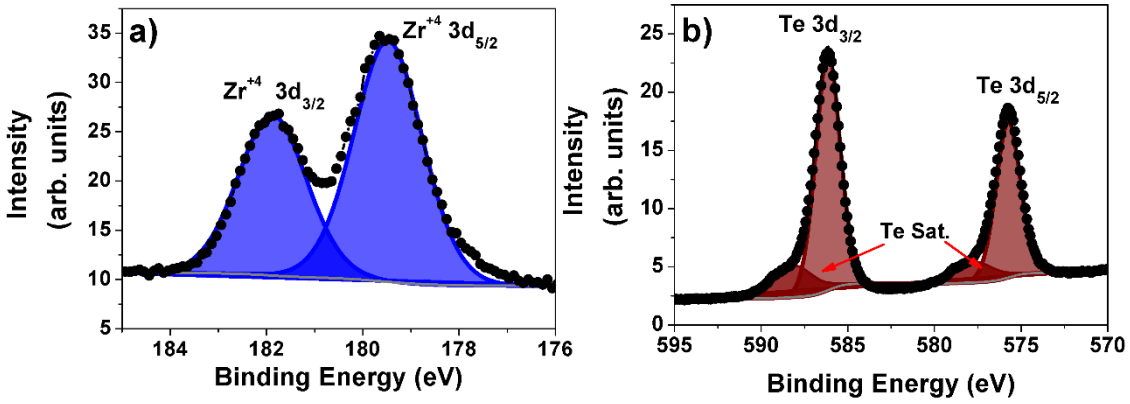

Source: The author (2021).

Data analysis was carried out using the CasaXPS software package. The XPS results are shown in Figures 91a) and 91b). The Zr region indicates no surface oxides (ZrO_2 $3d_{5/2}$ 182 eV) are present on freshly cast films (Figure 91a)). Similarly, the Te 3d region (Figure 91b))

indicates TeO_2 species are not present on the surface (Te $3d_{5/2}$ TeO_2 = 575 eV). The POM species adsorbed to the $ZrTe_2$ are not observed due to the percent atomic resolution of the XPS measurements performed.

Absorption spectroscopy

The absorption spectrum was performed in $ZrTe_2$ samples to identify optical transitions in the UV-VIS-NIR range. It can be seen that, for the $ZrTe_2$ nanoflakes concentration used in the experiments, the sample is virtually transparent in the visible and infrared ranges, with absorbances of 0.0019 and 0.0036 at 1064 nm and 532 nm (i.e., the laser's SH wavelength), respectively.

Figure 92 - Absorption spectra for Semi-metallic $ZrTe_2$.

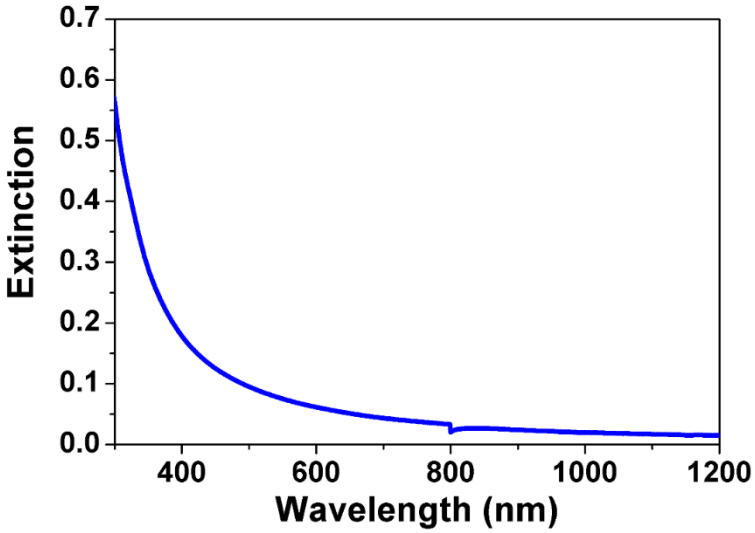

Source: The author (2021).

No absorption peaks were observed in the visible and near-infrared, indicating no electronic or excitonic transitions in this range, which is typical of metallic LTMDs. The increase in the absorbance towards the ultraviolet is attributed to electronic interband transitions in $ZrTe_2$.

Raman Spectroscopy

Raman spectra, seen in Figure 93, were collected with a Renishaw inVia confocal Raman microscope.

Figure 93 – Raman spectra of $ZrTe_2$ at 298K at room temperature.

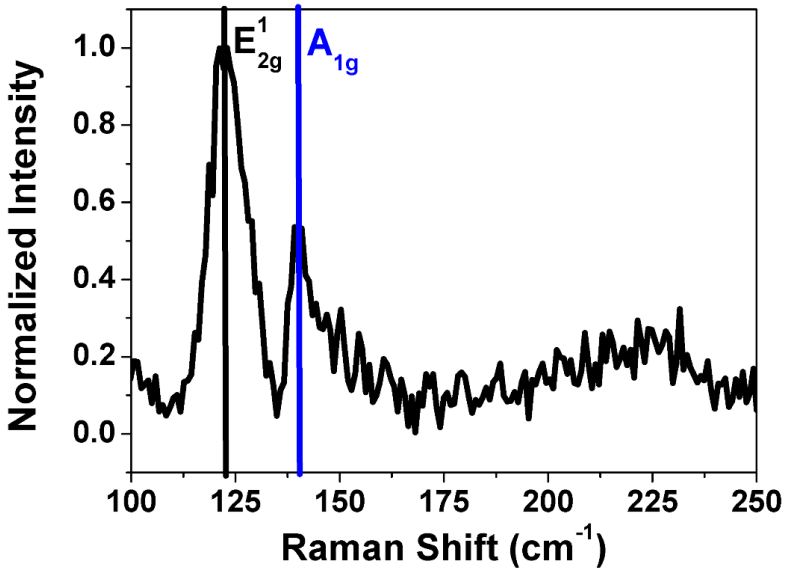

Source: The author (2021).

Samples were prepared by drop-casting on Silicon wafers and annealing in a thermal oven at 100ºC for 1 hour to ensure complete removal of solvent. After drying, samples were immediately transferred to the analysis chamber and the spectra were collected to prevent surface hydrolysis.

All spectra were collected while under ambient conditions. The excitation laser (at 514.5 nm) was focused onto the few-layered flakes with a **20** × objective lens. The power was kept to 100 μW to minimize sample heating. Spectra were collected at acquisition times between 60 – 180 s. The peaks identified in the samples (black and blue lines) correspond to the E_{2g} and A_{1g} modes of the 1T phase (HANGYO et al, 1983).

The absence of ZrO_2 features indicates that the exfoliation process does not lead to significant oxidation of the $ZrTe_2$ material provided the anhydrous sample preparation.

B.2.2 - NbS_2

Transmission Electron Microscopy (TEM)

High-resolution transmission electron microscopy (HRTEM) images were obtained using an aberration-corrected FEI Talos TEM with accelerating voltage of 200 kV.

Figure 94 – TEM for NbS_2 samples a) 200 nm and b) 200nm in different regions, c) 100 nm, and d) 200 nm in a different region of the TEM grate.

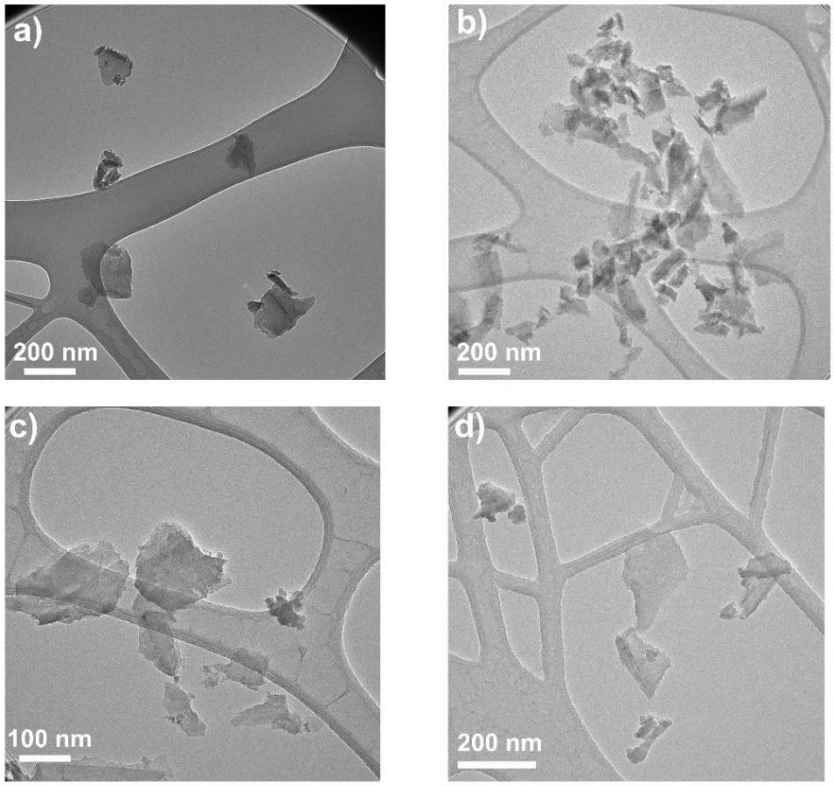

Source: The author (2021).

Figure 94 a)-d) shows the TEM images of an NbS_2 sample. The procedure for the sample preparation was the same used for $ZrTe_2$ sample and is described in the previous section.

Atomic Force Microscopy and size determination

AFM measurements were used for the determination of lateral size and height of layered NbS_2. The procedure to prepare the samples was the same used for $ZrTe_2$ and is described in the previous section.

Figure 95 – a) AFM image of NbS_2 layers, b) Lateral length, and c) height of NbS_2 layers.

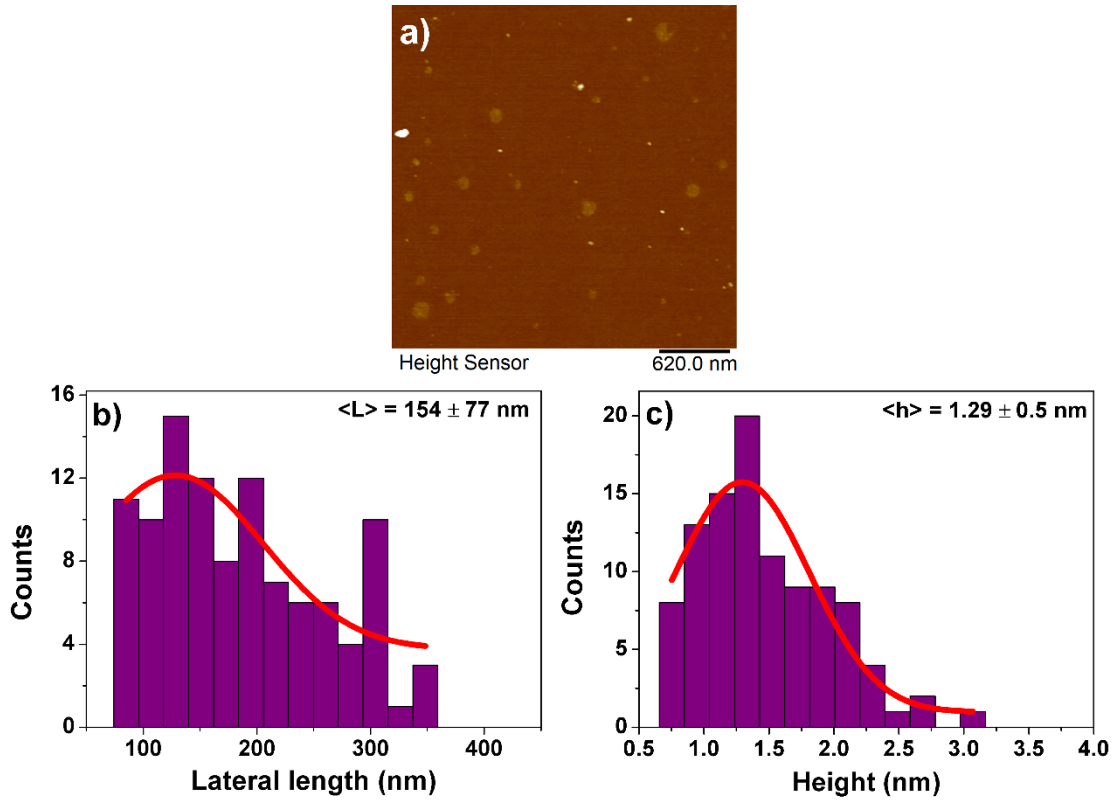

Source: The author (2021).

The lateral size is 154 nm with a Standard Deviation (SD) of 77 nm and the height is 1.29 nm with a SD of 0.5 nm. The thickness of an NbS_2 monolayer growth in an h-BN substrate is 0.6 nm, the difference between the results found in this work is due to the presence of POM species on the surface of the layers.

X-ray Photoelectron Spectroscopy (XPS)

The XPS analysis was carried out using an SSI XPS System. Survey spectra were acquired using an Al K_α X-Ray source (1486.6 eV) operated at 120 W (10 mA, 10 kV) with the electron analyzer operating in hybrid lens mode and an aperture size of approximately 800 μm^2.

Figure 96 - Compositional analysis of NbS_2. XPS spectroscopy of Nb_{3d} (a) and S_{2p} (b) regions indicate the presence of both compositional NbS_2.

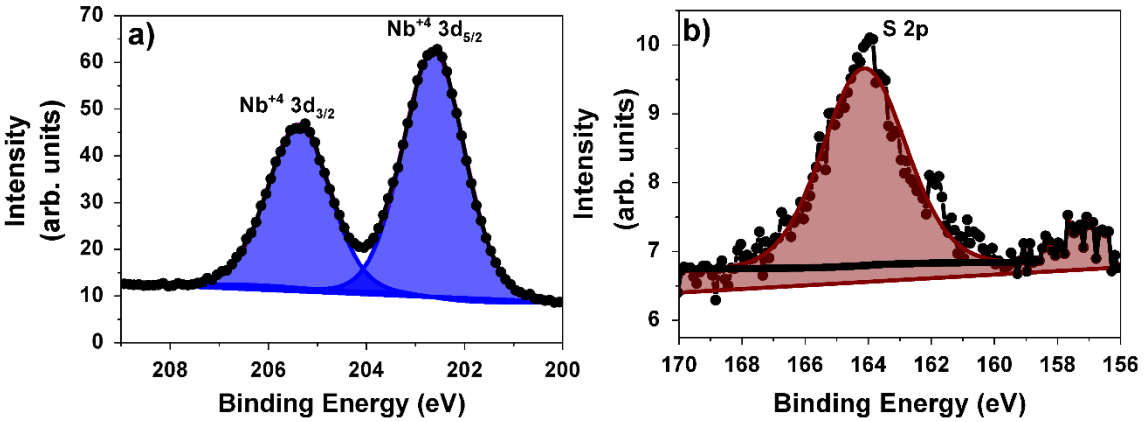

Source: The author (2021).

Figure 96 shows the results obtained from the compositional characterizations. The Nb region indicates that no surface oxides (Nb $3d_{5/2}$ 206 eV) are present (Figure 96a). Similarly, the S 2p indicates SO_x species are not present on the surface (S_{2p} SO_x = 168 eV). For the S 2p region, the small splitting of S 2p (0.92 eV) prevents the resolution of the $S2p_{1/2}$ and $S2p_{3/2}$ peaks. Thus, a single gaussian was used to fit the region (Figure 96b)).

UV-VIS-NIR Spectroscopy

Absorption spectroscopy was performed to understand possible optical transitions in metallic 2H-NbS_2. The absorption spectrum measurements were performed using a sample concentration of $5\mu g/ml$. A cell with an optical path length of 2mm was employed to perform the measurements.

Figure 97 – Extinction spectrum for NbS_2 layers.

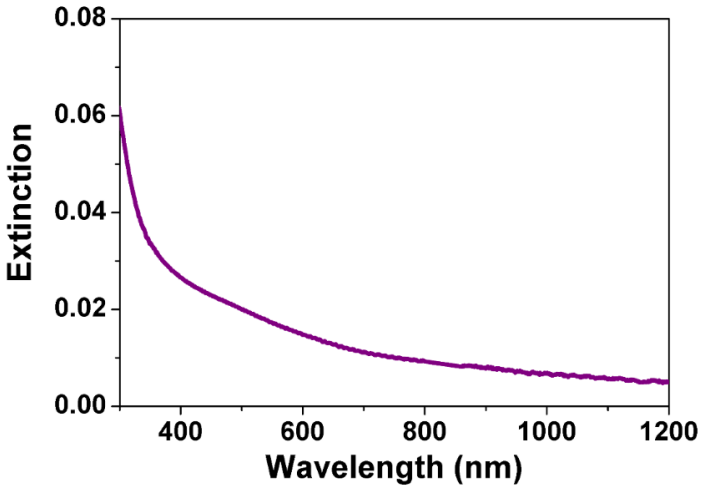

Source: The author (2021).

Figure 97 shows the extinction spectrum of NbS_2 layers. Due to the metallic character, the extinction spectrum is characterized by no excitons peaks as occur for semiconductors. A small absorption band is shown close to 500 nm and can be related to plasmon resonance.

Raman Spectroscopy:

The Raman spectroscopy characterization was carried out in dried individual redox exfoliated flakes on a SiO_2/Si substrate. Raman spectra were collected with a Renishaw inVia Raman microscope and with a WITec Alpha 300R microscope. Prior to material deposition, the substrates (SiO_2/Si) were cleaned with acetone, dried under a nitrogen stream, and immediately treated in an ozone chamber for 15 minutes to remove surface organic contaminants. This treatment creates a hydrophilic surface that allows for uniform deposition of NbS_2 solutions in acetonitrile.

Figure 98 - Raman spectra of drop casted redox exfoliated NbS_2 flakes resolve the E_{2g} and A_{1g} vibrational modes.

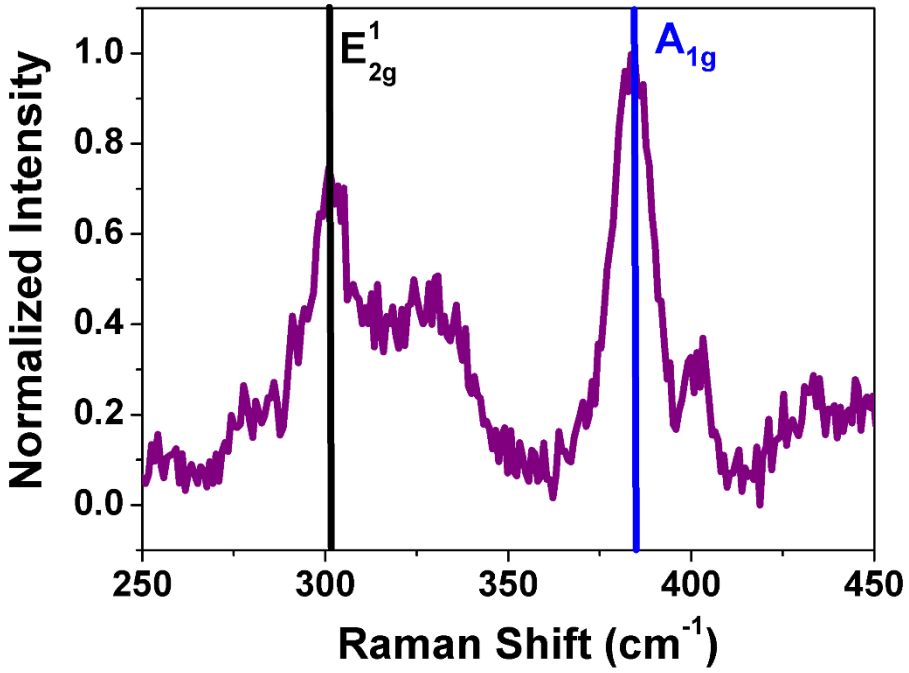

Source: The author (2021).

NbS_2 was dropcast from a solution of ACN (5 µL; 10 mg/mL NbS_2) onto cleaned wafers and allowed to dry naturally. The solution wets the substrate completely, and all solvent evaporates within 5 seconds. The samples were then immediately analyzed via Raman spectroscopy, as surface oxidation of thin NbS_2 occurs rapidly (MCMULLAN and IRWIN, 1983). The excitation laser (514.5 nm) was focused on the few-to-monolayer flakes with a 20× objective lens. The power was kept to 100 µW in order to minimize sample heating. Spectra were collected at acquisition times between 60 –180 s.

Figure 98 shows the obtained Raman spectrum. The peaks identified at 382 cm^{-1} and 401 cm^{-1} correspond to the A_{1g} vibrational mode, while the peak at 300 cm^{-1} corresponds to the E_{2g} vibrational mode (MCMULLAN et al, 1983).

B.2.3 - MoS_2

Transmission Electron Microscopy (TEM)

TEM was performed to characterize the morphology of MoS_2 flakes.

Figure 99 – TEM image for MoS_2 samples a) and b) for different regions of TEM grate.

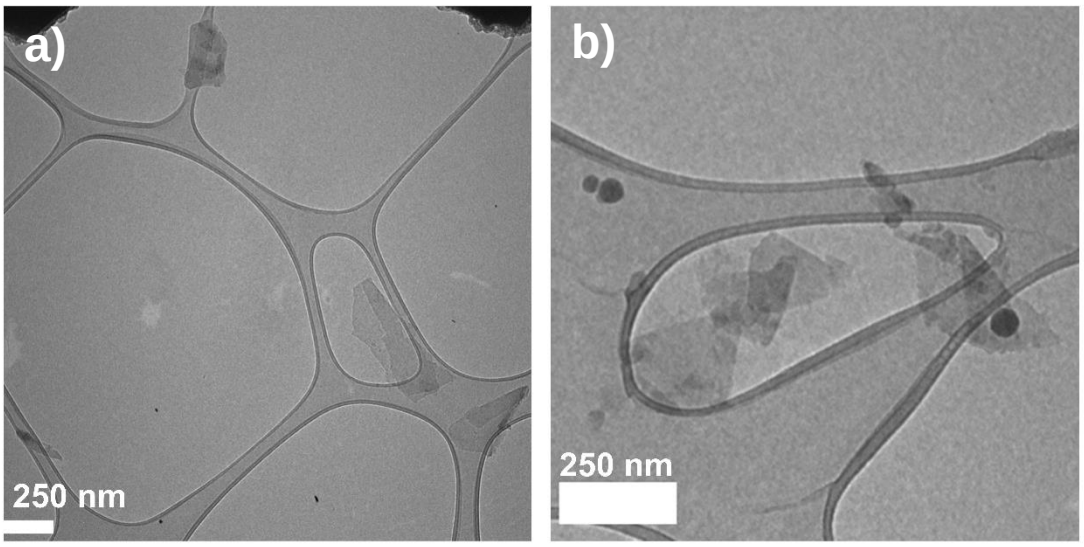

Source: The author (2021).

Figure 99 shown the TEM image for MoS_2 flakes for different regions of the TEM grating. The scale bar for both figures is 250 nm.

Atomic Force Microscopy and size determination

AFM images are performed in the same conditions to use for $ZrTe_2$ and described in the previous section.

Figure 100– a) AFM image of MoS_2 flakes, b) height and c) lateral length distribution.

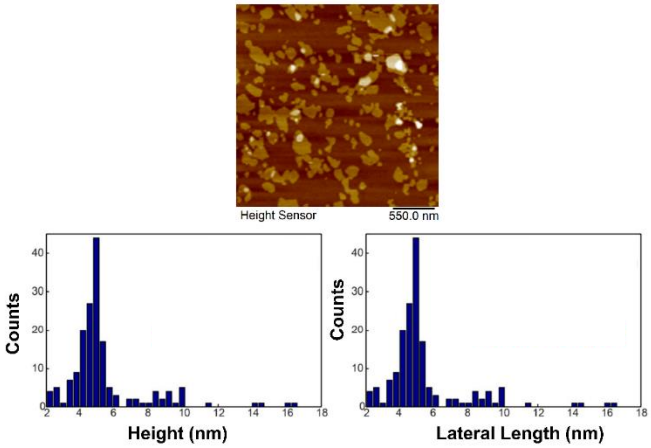

Source: The author (2021).

X-ray Photoemission Spectroscopy (XPS)

Survey data were acquired at an analyzer pass energy of 160 eV, using 1 eV step sizes and a dwell time of 400 ms. High-resolution data of the Mo_{3d}, S_{2p}. The sample preparation method was the same used for $ZrTe_2$ flakes and is described in the previous section.

Figure 101 - Compositional analysis of MoS_2. XPS spectroscopy of Mo 3d (a) and S 2p (b) regions indicate the presence of both compositional MoS_2.

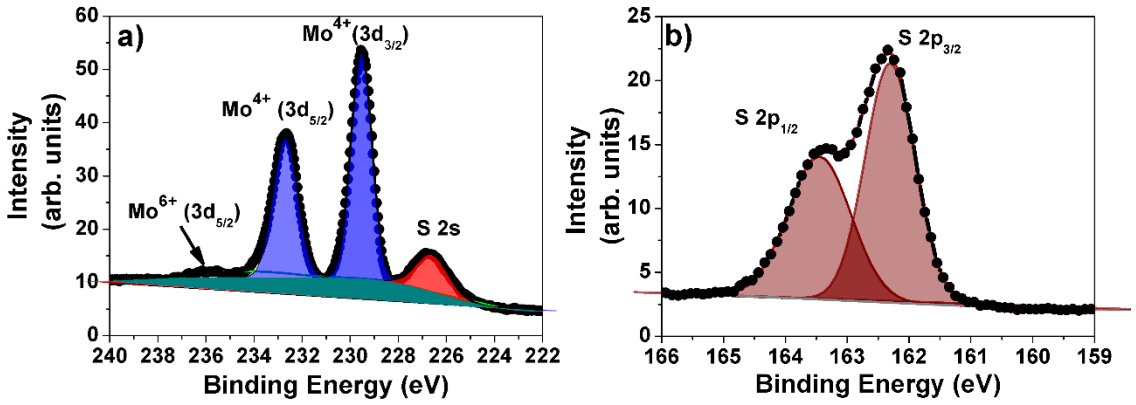

Source: The author (2021).

The Mo3d, S2s, and S2p regions of the XPS spectra for samples annealed at various temperatures are shown in Figure 101. The Mo3d spectra consist of peaks at around 229 and 232 eV that correspond to Mo^{4+} $3d_{5/2}$ and Mo^{4+} $3d_{3/2}$ components of 2H-MoS_2, respectively.

Raman Spectroscopy

Figure 102 shows the Raman spectrum of a dried MoS_2 redox exfoliated flake prepared in a similar way (532 nm excitation and a 100× objective lens, to ensure that a single flake was probed, were used in this case).

Figure 102 – Raman Spectra for MoS_2 flakes.

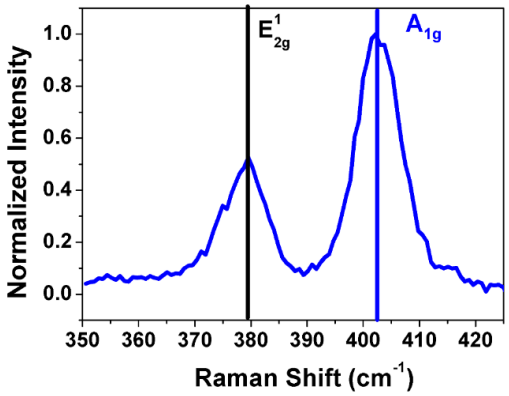

Source: The author (2021).

The ~23 cm^{-1} peak separation reveals a few-layer thickness, further confirming the effectiveness of the exfoliation and size selection procedure.

APPENDIX C - SYNTHESIS AND STANDARD CHARACTERIZATION $Au_6(GSH)_2(MPA)_2$ GOLD NANOCLUSTERS

Tetrachloroauric acid trihydrate ($HAuCl_4 \cdot 3H_2O$), 3-mercaptopropionic acid (MPA), and glutathione reduced (GSH) were purchased from Sigma-Aldrich. Tetrakis(hydroxymethyl)phosphonium chloride (THPC) and sodium hydroxide (NaOH) were purchased from Merck. Sodium phosphate dibasic heptahydrate ($Na_2HPO_4 \cdot 7H_2O$) was purchased from Spectrochem and sodium dihydrogen phosphate dihydrate ($NaH_2PO_4 \cdot 2H_2O$) was obtained from Lobachemie.

Figure 103 - Schematic representation of the synthesis of Au NCs with tunable emission via core etching as well as ligand exchange method.

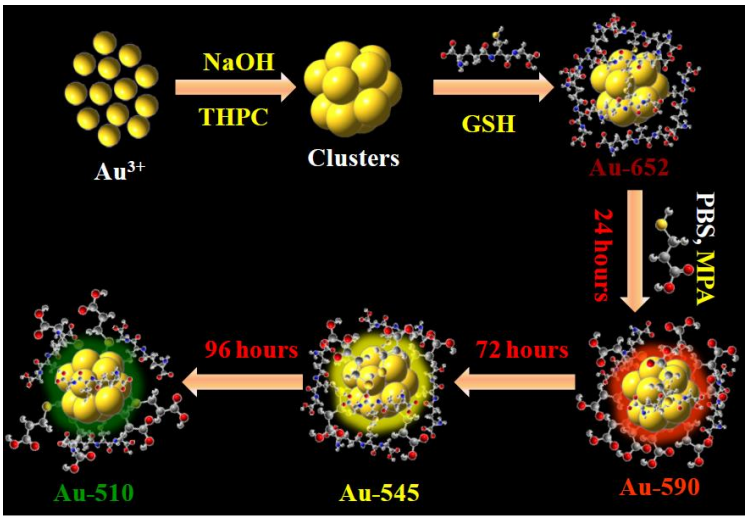

Source: Bain (2019)

The Au NC's investigated in this thesis was synthesized and characterized in the School of Materials Science - Indian Association for the Progress of Science, by the group of Professor Amitava Patra. This part is described a brief resume about the synthesis process.

The Au NCs with green fluorescence were prepared by following our previous reported procedure (BAIN et al, 2019). In a typical synthesis, 125 µL of 1 M NaOH was added to 10 mL HPLC water in a 25 mL beaker. Then 3 µL THPC solutions (80% in H_2O) was added to above solution and allowed to stirrer for minutes. Thereafter, aqueous solution of 100 µL Au^{3+} (100 mM) was added to the solution and its color immediately became light brown indicative of the Au NCs formation. The reaction was allowed to stirrer another five minutes and then 50 µL of 0.1 M glutathione was added to the reaction mixture to stabilize the as-prepared Au NCs. The as-synthesized Au NCs were kept at 4°C for further use. After aging 12 hours at 4°C, 2 mL of phosphate buffer (PBS, 50mM) of pH 9 was added to 10 mL of previously prepared Au NCs. Thereafter, 150 µL of MPA was added to the reaction mixture and the resulting mixture was

continuously stirred. The progress of the reaction was continuously monitored by UV-VIS absorption and photoluminescence (PL) spectroscopy. After 48 hours, 100 µL of MPA was added to the reaction mixture with continuous stirring. Finally, the green emitting NCs were obtained after 96 hours. The as-synthesized Au NCs were purified by centrifugation at 10,000 rpm for 10 minutes thrice to remove excess capping ligands and salts. The Figure 103 shown the schematic representation of the synthesis process.

C.1 – MALDI – TOF

The technique of MALDI – TOF was employed to measure the number of atoms in the Au_6 cluster.

The $Au_6(GSH)_2(MPA)_2$ nanoclusters consist of six gold atoms and the core is capped by two glutathione and two MPA ligands. This kind of MALDI hump is quite common for gold nanocluster in aqueous phase synthesis.

Figure 104 – MALDI – TOF Spectrometry for calculate the Au NC's mass.

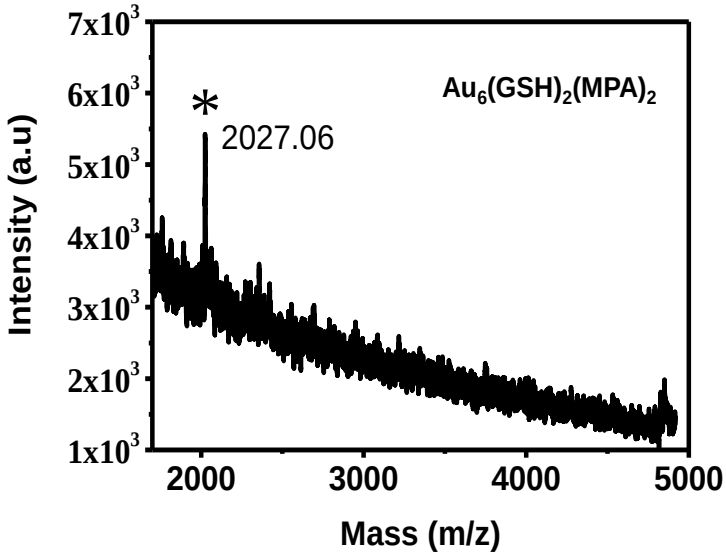

Source: Bain (2019)

Interestingly, $Au_6(GSH)_2(MPA)_2$ exhibits a single peak in its MALDI spectrum that confirms the formation of highly pure single NCs rather than the formation of mixed nanoclusters.

C.2 TRANSMISSION ELECTRON MICROSCOPY

The transmission electron microscopy (TEM) was recorded using a JEOL-JEM-2100F transmission electron microscopy system with accelerating voltage of 200 kV. Figure 105 a) displays the TEM image of the $Au_6(GSH)_2(MPA)_2$, which shows spherical size with polydispersity in nature. The average size of Au_6 NCs is 1.5 ± 0.4 nm, calculated from the

particle size distribution plots in Figure 105 b). The large size detected can be attributed to electron beam-induced aggregation as discussed by RAMASAMY, P. et al, 2009.

Figure 105 - (A) TEM image of luminescent Au NCs (B) particle size distribution curve.

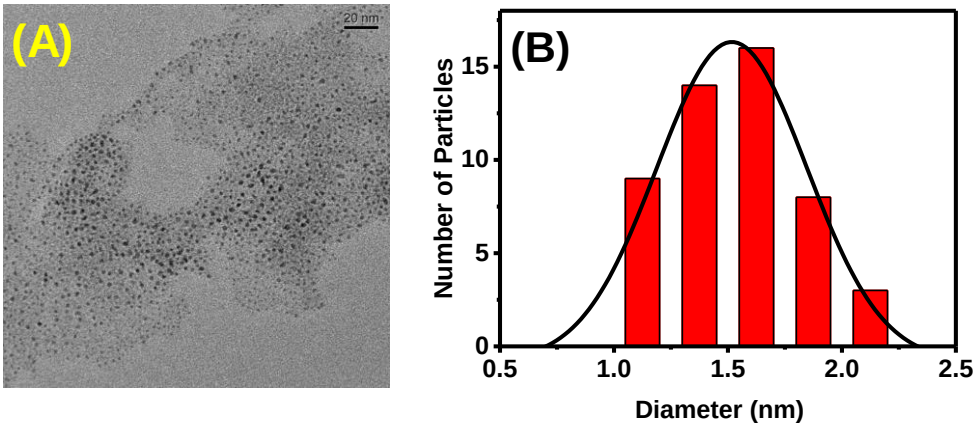

Source: Bain, et al (2019).

C.2 ABSORPTION AND PL SPECTROSCOPY

Figure 106 displays the photoexcitation spectrum that shows a peak around 394 nm resembling the absorption peak at 387 nm. The excitation-dependent emission is measured over the wavelength range 300-440 nm and there is no change in the emission band that suggests homogeneity in the emission property (BAIN et al, 2019). Notice also that the as-synthesized Au NCs show PL at 512 nm under excitation of 375 nm. The Stokes shift of 118 nm indicates that the PL of Au NCs is associated with ligand to metal charge transfer (LMCT; sulfur, S, to gold, Au). The large Stokes shift implies that a significant amount of distortion is occurring in the excited states compared to the ground state and this distortion is due to the capping ligands via LMCT (FORWARD, J. M. et al).

Figure 106 - (a) Absorption, (b) photoexcitation, and (c) photoluminescence spectra of the Au nanoclusters in water. The inset shows pictures of the NCs solution under (d) visible light and (e) UV excitation at 365 nm. The ratio between the maximum amplitudes of curves b and c is 3.93.

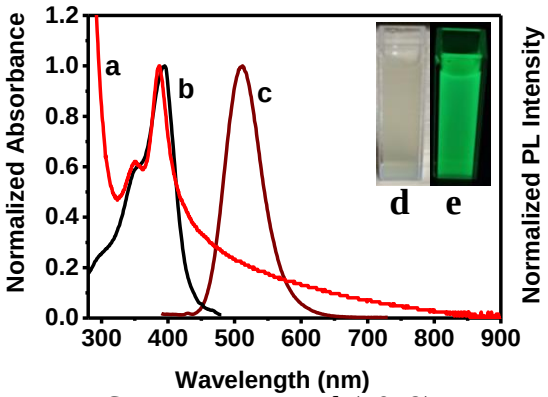

Source: Bain, et al (2019).

To further understand the LMCT process, the excited state lifetime was measured at emission 512 nm under the excitation wavelength at 371 nm and the results are shown in Figure 110(A). The decay curve is fitted with a tri-exponential having the components 29 ± 1.5 ns (38%), 201 ± 4.6 ns (42%) and 673 ± 3.6 ns (20%) and the average lifetime is 230 ns. The 29 ns component is associated with a fluorescence process (HUANG et al, 2007; HUANG et al, 2018; MAITY et al, 2019). On the other hand, the signal components at 201 ns and 673 ns are associated with triplet-to-singlet transition because during the photoexcitation process few photoexcited Au NCs go to low-lying triplet states from excited singlet states via intersystem crossing (ISC) (CHEN et al, 2013; HUANG et al, 2007). Therefore, the two longer lifetime components indicate the charge-transfer from the ligand to the gold atoms that is consistent with previous results (BAIN et al, 2018; RUSSIER-ANTOINE et al, 2016).

Furthermore, Figure 107b) illustrates the ultrafast spectroscopic study performed to understand whether there is any involvement of ultrafast relaxation processes like intraband electronic transition or solvent relaxation. For that, by exciting the Au NCs at 400 nm and monitoring the emission at 512 nm we observed molecular-like ultrafast electronic transition, how shown by ZHOU et al, 2019. The ultrafast decay is fitted with two decay components: 44.2 ps (40%) and 2.74 ps (60%). Upon photoexcitation, Au_6 NCs experience structural relaxation within 2.74 ps involving different vibrational states of the S_n states. The slower component (44.2 ps) is associated to electron acoustic phonon scattering due to surface states (WEN et al, 2013; ZHOU et al, 2017).

Figure 107 - (A) Time-resolved decay-curve of the green emitting Au NCs (excitation wavelength at 371 nm and emission at 512 nm) and (B) Ultrafast decay profile of Au NCs after excitation at 400 nm and emission monitored at 512 nm.

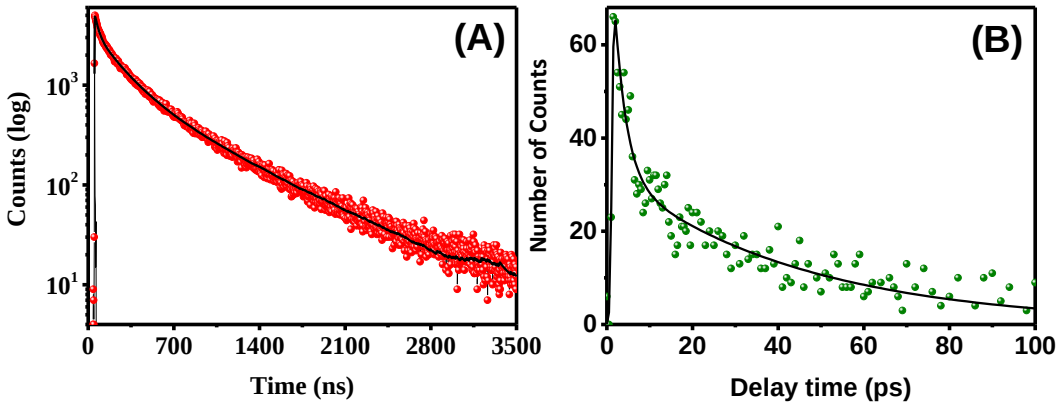

Source: Bain et al, (2019)

APPENDIX D - SYNTHESIS OF $NaNbO_3$ NANOCRYSTALS

All synthesis process was performed in the group of Professor Carlos Jacinto in the Institute of Physics, at Universidade Federal de Alagoas.

All reagents and solvents used were purchased from Sigma-Aldrich and used as obtained. The synthesis of $NaNbO_3$ nanocrystals was already reported (BARBOSA-SILVA et al, 2019) based on the Pechini's method (NOBRE et al, 1996; KUMAR et al, 1996). Briefly, acid citric ($C_6H_8O_7$) (99.5%) (19.2g) was added to 10 mL of ultrapure water under stirring and heating at 75ºC. Afterward, Ammonium Niobate Oxalate ($C_4H_4NNbO_9.xH_2O$) (99.99%) (0.1836g) was added to the reactional flask and stoichiometric amounts of sodium carbonate (Na_2CO_3) (99.999%) also was added to the flask. After 10 minutes, 5.6 mL of ethylene glycol ($C_2H_6O_2$) (99.8%) was added and all chemicals were left to react for 1 hour. Thereby, the polyestherification reaction allowed the polymerization of Niobium and Sodium Citrates. Subsequently, the mixture was cooled down to room temperature, without stirring. After this process, the mixture was placed in a furnace at 100 ºC for 72 h. This step allowed the polymerization and elimination of water to continue. As a result, a gelatinous material (gel) was obtained and heated at 400 ºC for 2 h to evaporate the organic composites. After this step, the samples were calcinated at different temperatures for 3h: sample A at 600 ºC, sample B at 700 ºC, sample C at 800 ºC, sample D at 900 ºC, and sample E at 1000 ºC. The obtained samples were in the form of white fluffy powders that were dispersed in methanol with different concentrations (nanocrystals/cm^3) for the experiments.

D.1 – STANDARD CHARACTERIZATION

The $NaNbO_3$ nanocrystals were characterized by using a scanning electron microscope (SEM), X-ray powder diffraction (XRPD), UV-VIS transmittance, Raman Spectroscopy, and hyper-Rayleigh scattering (HRS) technique.

D.1.1 - Morphological and Size Characterization.

Figure 107 shows SEM images obtained using an electron microscope MIRA3 TESCAN 25kV. Notice that the nanoparticles (NPs) present spherical shape and the increase in the calcination temperature results in the growth of the NPs, as expected (SHIRATORI et al, 2007).

Figure 108 - Morphological study of the samples. A), B), C), D) and E) correspond to the samples A, B, C, D and E, respectively.

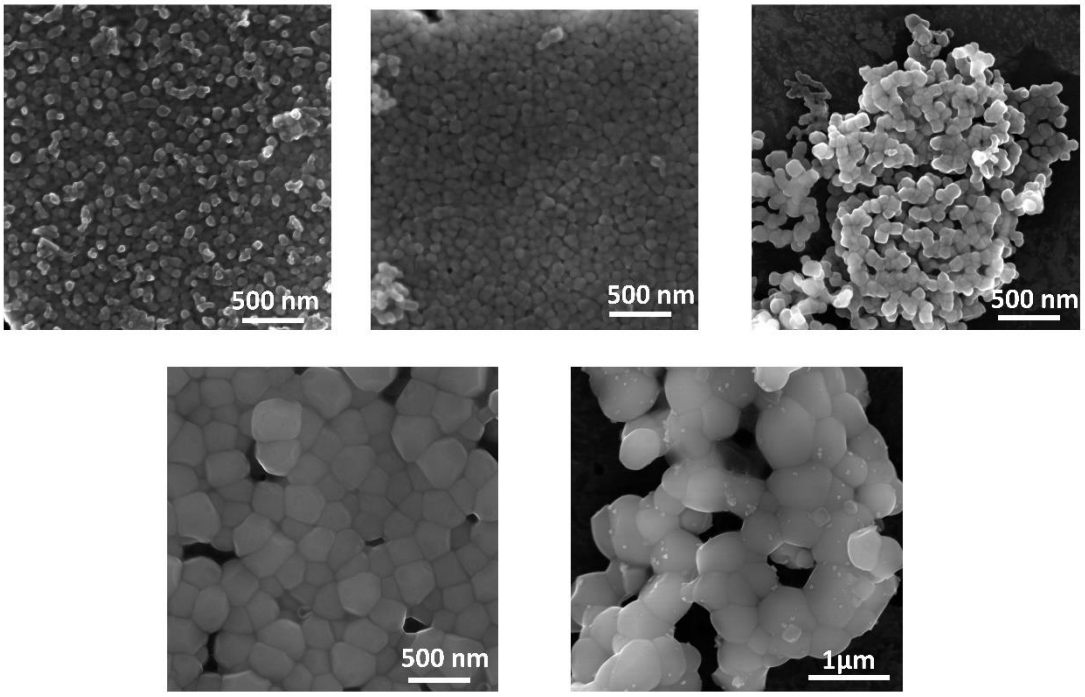

Source: The author (2021).

Figure 109 shows the size distributions of the NPs. The black lines are Gaussian fits to estimate the NPs average diameter and the standard deviation (SD) for each sample. The change in the average diameter is small from sample A to B (~18 nm) and from B to C (~20 nm), but increases drastically from C to D (~120 nm) and D to E (~320 nm).

Figure 109 - Sizes distribution of the samples: A) Sample A; B) Sample B; C) Sample C; D) Sample D; and E) Sample E. The black lines are Gaussian fits to the experimental data. The average diameters are indicated besides the histograms.

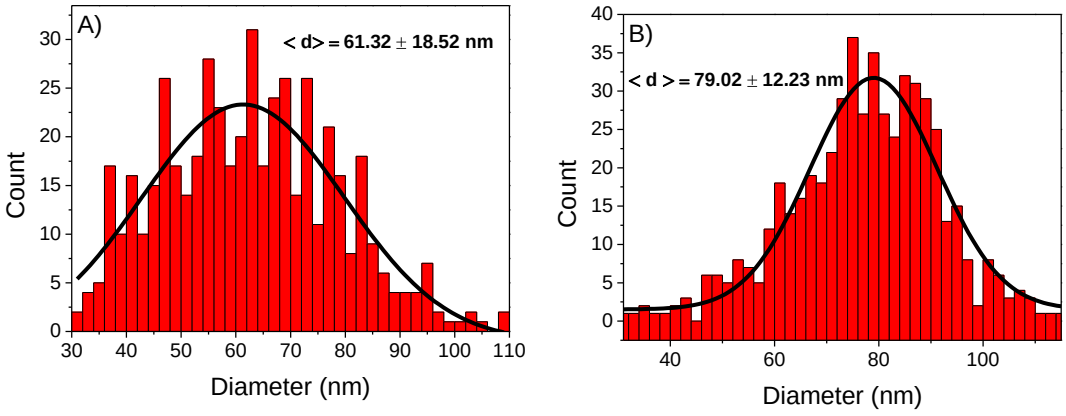

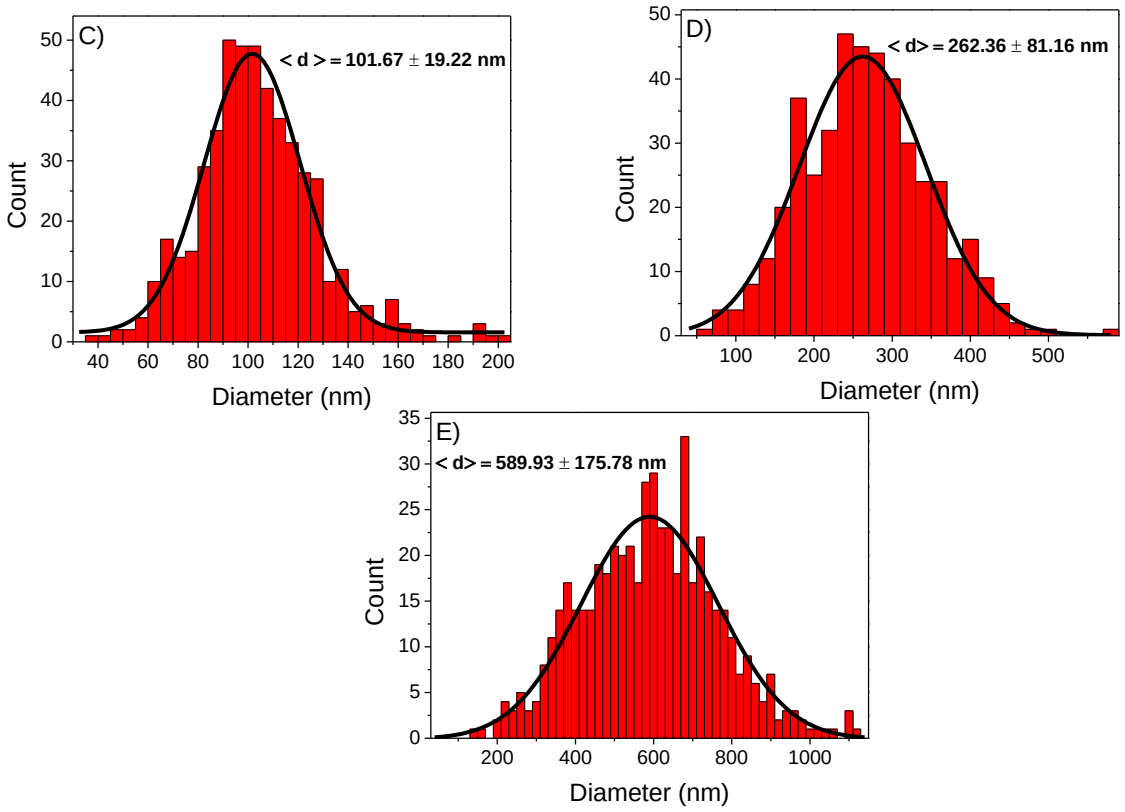

Source: The author (2021).

D.1.2 - Crystalline Structure Characterization.

The structural analysis was performed by X-ray powder diffraction (XRPD) using a RIGAKU diffractometer combined with Rietveld refinement. Figure 110 presents the results for all samples.

Figure 110- Diffractograms and results of the Rietveld refinement of the samples: A) Sample A; B) Sample B; C) Sample C; D) Sample D; and E) Sample E.

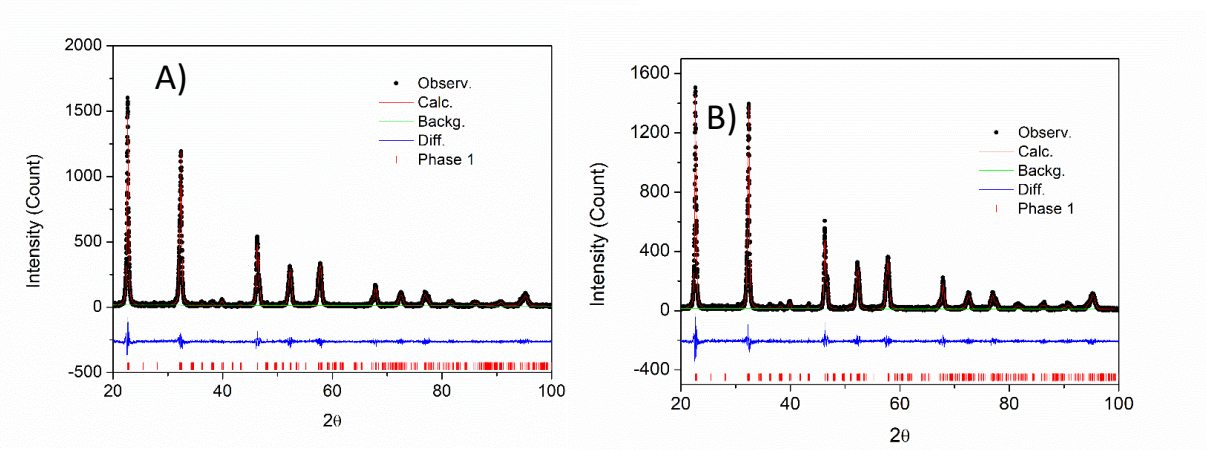

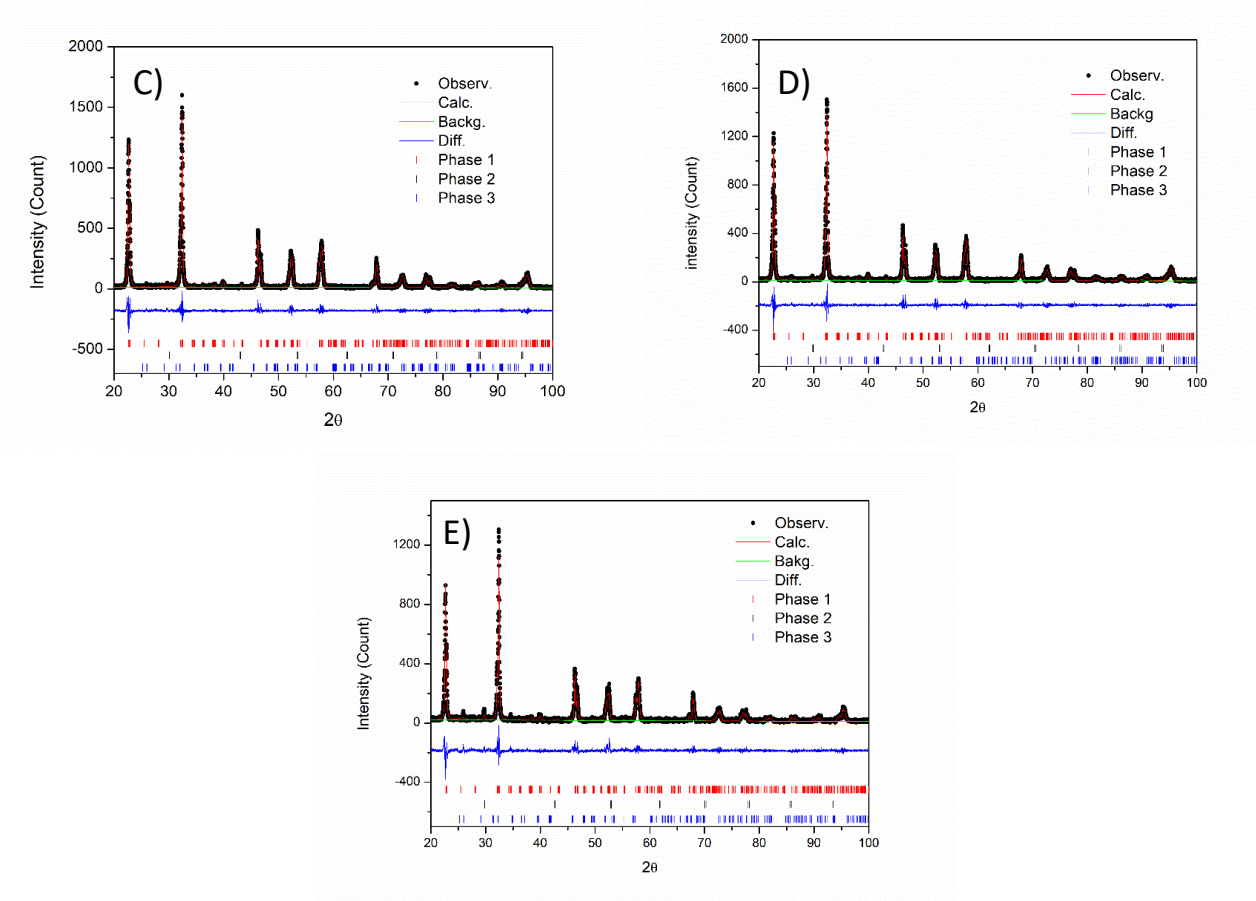

Source: The author (2021).

The refinement procedure was applied using the Experiment Graphical User Interface/General Structure Analysis System/ (EXPGUI/GSAS) (LARSON and VON DREELE, 1994; TOBY, 2001) . The weighted-profile R-factor (R_{wp}) obtained varied from 17.62 to 20.39% and the goodness of fit (S) changes from 1.112 to 1.268, in good agreement with the literature (SHIRATORI et al, 2005). No impurities were detectable in samples A and B; therefore, 100% of the NP's consist of the space group number 26 ($Pmc2_1$). This crystalline phase corresponds to an orthorhombic crystal system with an acentric lattice. In consequence of the absence of the lattice symmetry, the $NaNbO_3$ nanocrystals are ferroelectric as reported by previous authors (SHIRATORI et al, 2005; SHIRATORI et al, 2007; KORUZA et al, 2007).

Polymorphism of $NaNbO_3$ due to the different mean sizes was previously reported and the results presented in this thesis are in accordance with the literature (SHIRATORI et al, 2005; SHIRATORI et al, 2007; KORUZA et al, 2007). The predominant space group in samples C, D, and E is also $Pmc2_1$. However, the relative amount of $NaNbO_3$ is variable due to the impurities. The sub-products are Sodium (Na) and Niobium Dioxide (NbO_2). Sodium holds space group, Im$\acute{3}$m (number 229) and its origin are due to the thermal decomposition of unreacted Na_2CO_3 at high temperatures (KIM et al, 2001). On the other hand, Niobium Dioxide emerges in the samples due to the thermal decomposition of unreacted ammonium niobate

oxalate (SU et al, 2009). The NbO_2 impurities hold acentric space group number 80 (I41). The results are summarized in Table 9.

Table 9 - Summary of the results obtained from the Rietveld refinement.

Parameters \ Samples		A	B	C	D	E
R_{wp} (%)		17.62	17.83	19.12	19.21	20.39
S		1.172	1.176	1.241	1.233	1.268
Relative concentration (%)	$NaNbO_3$	100	100	91.5± 0.1	93.5± 0.1	86.6± 0.1
	Na	*	*	5.6±0.5	3.4±0.4	6.4±0.5
	NbO_2	*	*	3.0±0.2	3.1±0.2	7.0±0.4
Volume of unit cell (nm^3)	$NaNbO_3$	238.96±0.02	238.63±0.01	238.69±0.01	238.58±0.01	238.29±0.02
	Na	*	*	74.3±0.9	75.8±0.3	75.4±0.1
	NbO_2	*	*	577±3	576±4	571±2

* Not detectable.

Source: The author (2021).

D.1.3 Linear Optical Characterization

Figure 111 shows the optical transmittance of the samples. The arrows indicate the excitation wavelength (1064 nm) and the HRS signal (532 nm). It is clear the absence of absorption in the visible region and consequently, no photoluminescence is expected in this region.

Figure 111 - Transmittance of the samples versus the wavelength

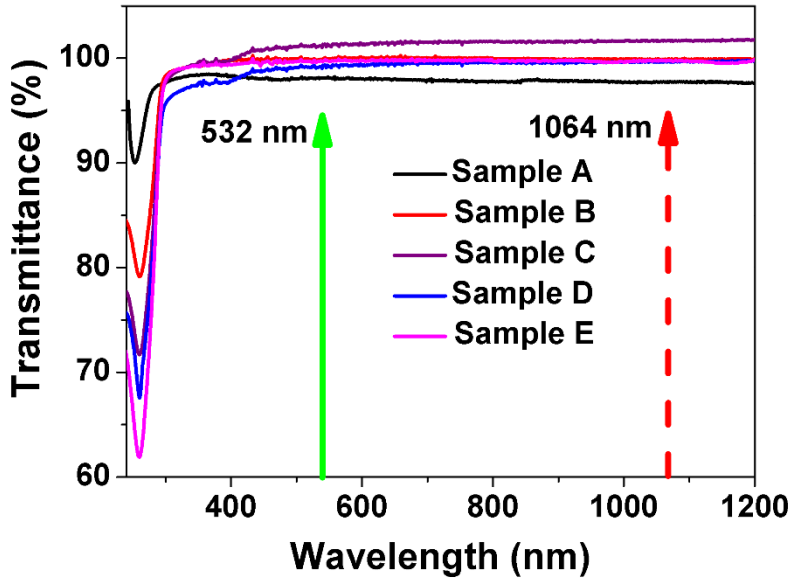

Source: The author (2021).

D.1.4 - Raman Spectroscopy

Raman spectroscopy was performed using a HORIBA IHR 320, with excitation at 671 nm. For the measurements, the powder of the $NaNbO_3$ NCs is used.

Figure 112 – Raman spectroscopy for A, B, C, D, and E samples.

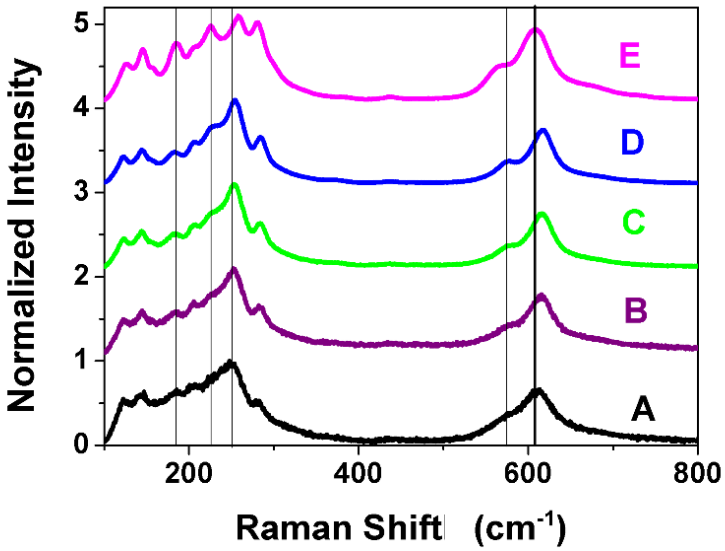

Source: The author (2021).

Figure 115 shows the Raman spectra for samples A, B, C, D, and E. The intensity is normalized and a shift for up is in the vertical direction was performed to show all spectra in only one figure notice small shifts in the Raman. More than 60 Raman modes are present at the *Pbcm* structure as shown by SHIRATORI et al, 2007.

APPENDIX E – PUBLICATIONS AND MANUSCRIPTS

E1 – MANUSCRIPTS WITH RESULTS ON THIS THESIS

1. MALDONADO, M; et al, *Femtosecond Nonlinear Optical Properties of 2D Metallic NbS2 in the Near Infrared.* ***J. Phys. Chem. C***, 124, 28, 15425–15433 (2020).
2. BARBOSA-SILVA, R.; et al, *Observation and Analysis of Incoherent Second-Harmonic Generation in Gold Nanoclusters with Six Atoms.* ***J. Phys. Chem. C***, 124, 28, 15440–15447 (2020).
3. PINCHEIRA, P. I. R., et al, *Monolayer 2D ZrTe2 transition metal dichalcogenide as nanoscatter for random laser action***. Nanoscale** 12 (29), 15706-15710 (2020).
4. da SILVA-NET**O** M. L.**,** et al, *Hyper-Rayleigh Scattering in 2D Redox Exfoliated Semi-metallic ZrTe2 Transition Metal Dichalcogenide***. Phys. Chem. Chem. Phys**., 22,27845-27849 (2020)
5. da SILVA-NETO M.L. et al**,** *Fifth-Order Optical Nonlinear Response of Semiconducting 2D LTMD'S MoS_2***. Opt. Lett.** 46, 226-229 (2021).

6. MALDONADO, M., et al, *Femtosecond Nonlinear Refraction of 2D Semi-Metallic Redox Exfoliated ZrTe2 at 800 nm.* **Appl. Phys. Lett**. 118, 011101 (2021)
7. da SILVA-NETO M.L. et al, *Second-Order Nonlinearity of Graphene Quantum Dots Measured by Hyper-Rayleigh Scattering.* Submitted to journal **Applied Optics**.

8. da SILVA-NETO M.L. et al, *Incoherent second-harmonic generation by $NaNbO_3$ nanocrystals.* **To be submitted.**

E2 – OTHER MANUSCRIPTS

1. de OLIVEIRA, N. T. C; et al *Influence of the Fifth-Order Nonlinearity of Gold Nanorods on the Performance of Random Lasers.* **J. Phys. Chem. C**, 124, 19, 10705–10709 (2020).
2. da SILVA-NETO, M. L.**;** et al, *UV random laser emission from flexible ZnO-Ag-enriched electrospun cellulose acetate fiber matrix.* **Scientific Reports**, v.9, p.1 - 9, (2019).
3. MANZANI, D. *Phosphotellurite glass and glass-ceramics with high TeO2 content: thermal, structural and optical properties*. **Dalton Transactions**, v.xx, p.xx-xxxx, 2019.

4. BAUTISTA, J. E. Q. **et al,** *Thermal and Non-Thermal Intensity Dependent Optical Nonlinearities in Ethanol at 800nm, 1480nm and 1560nm*. **J. Opt. Soc. Am. B** 38, 1104-1111 (2021).

5. PUGINA, R. S. et al, *Nd3+:YAG microspheres powders prepared by spray pyrolysis: Synthesis, characterization and random laser application***. Materials Chemistry and Physics** 269, 124764 (2021).

6. CORONEL SANCHEZ, E. D.; et al, *Simultaneous evaluation of intermittency effects, replica symmetry breaking and modes dynamics correlations in Nd:YAG random laser*. **Submitted to ACS Photonics.**

7. BAUTISTA, J. E. Q. **et al**, *Spatial self-phase modulation in liquid suspensions of MoS_2, WS_2, NbS_2 and $ZrTe_2$ monolayers with linearly and circularly polarized light*. **Submitted to Nanoscale.**

APPENDIX F – PRESENTATION IN CONFERENCES

F1 – PRESENTATION IN CONFERENCES

1. da SILVA – NETO, M. L.; et al, *Random Laser in colloidal nanocomposite Rh6G +$ZrTe_2$ Two-Dimensional Layered Transition Metal Dichalcogenide as scatterer*. Autumn Meeting, Brazilian Physical Society 2021.

2. da SILVA – NETO, M. L.; et al, *Evaluating third-and fifth order nonlinearities in metallic and semiconducting Layered Transition Metals Dichalcogenid*es. Autumn Meeting, Brazilian Physical Society 2021.

3. da SILVA – NETO, M. L.; et al, *Large First-Order Hyperpolarizability of the 2D Semi-metallic $ZrTe_2$*. OSA Siegmann School All Stars 2020.

4. da SILVA – NETO, M. L.; et al, *Unusual Behavior of Nonlinear Refraction and Absorption ofa Layered Transition Metal Dichalcogenide: Niobium Disulfide*. OSA Siegmann School All Stars 2020.

5. da SILVA – NETO, M. L.; et al, *Hyper - Rayleigh scattering in Graphene Quantum Dots*, Workshop in Materials Science 2019.

6. da SILVA – NETO, M. L.; et al, *Incoherent Second Harmonic Generation by Graphene Quantum Dots*, XXXIV NORTH AND NORTHEAST PHYSICS MEETING; Brazilian Physics Society (2019)

7. da SILVA – NETO, M. L. *Incoherent Second Harmonic Generation in Gold Quantum Clusters,* XIV Simposium on Lasers and Its Applications 2019.

8. da SILVA – NETO, M. L. *Nonlinear refraction, absorption and scattering in transition metals dichalcogenides,* Autumn Meeting, Brazilian Physical Society, 2019.